Investigation of Local and Non-Local Autoionization in Aqueous Systems

DISSERTATION

zur Erlangung des Grades eines
Doktors der Naturwissenschaften

am Fachbereich Physik
der Freien Universität Berlin

vorgelegt von
CLEMENS RICHTER

Berlin, 2020

Erstgutachter/in:	Dr. UWE HERGENHAHN
Zweitgutachter/in:	Prof. Dr. HOLGER DAU
Drittgutachter/in:	Prof. Dr. GERARD MEIJER

Datum der Disputation: 07.10.2020

Selbstständigkeitserklärung

Name: Richter
Vorname: Clemens

Ich erkläre gegenüber der Freien Universität Berlin, dass ich die vorliegende Dissertation selbstständig und ohne Benutzung anderer als der angegebenen Quellen und Hilfsmittel angefertigt habe. Die vorliegende Arbeit ist frei von Plagiaten. Alle Ausführungen, die wörtlich oder inhaltlich aus anderen Schriften entnommen sind, habe ich als solche kenntlich gemacht. Diese Dissertation wurde in gleicher oder ähnlicher Form noch in keinem früheren Promotionsverfahren eingereicht.

Mit einer Prüfung meiner Arbeit durch ein Plagiatsprüfungsprogramm erkläre ich mich einverstanden.

Datum: _____ Unterschrift: _____

_ _

Name: Richter
First name: Clemens

I declare to the Freien Universität Berlin that I have completed the submitted dissertation independently and without the use of sources and aids other than those indicated. The present thesis is free of plagiarism. I have marked as such all statements that are taken literally or in content from other writings. This dissertation has not been submitted in the same or similar form in any previous doctoral procedure.

I agree to have my thesis examined by a plagiarism examination software.

Date: _____ Signature: _____

BE EXCELLENT TO EACH OTHER.

Bill S. Preston, Esq. (Bill & Ted's Excellent Adventure)

Abstract

The irradiation of biological matter with ionizing radiation often leads to the formation of highly excited charged molecules. These systems can electronically relax through emission of a secondary electron, a process referred to as autoionization. The emitted electrons and the remaining charged species are believed to significantly contribute to the X-ray induced radiation damage in biomolecular tissue. The most established autoionization mechanism is the Auger decay, which takes place at one molecular entity. In contrast, non-local processes *intermolecular Coulombic decay* (ICD) and *electron transfer mediated decay* (ETMD), which involve at least two molecules have also been observed. The non-local decay mechanisms are associated with the emission of low energy electrons, which may cause highly damaging double strand breakage in DNA. Their potential to inflict radiation damage can be evaluated by their efficiency. In this thesis autoionization processes were investigated in different hydrogen bonded systems, such as molecular clusters, liquid water and amorphous ice, using conventional and coincident electron spectroscopy in order to assess their relevance in radiation chemistry and biology.

The ICD efficiency of pure water clusters and of mixed water-formaldehyde clusters was determined and an increase with increasing average cluster size was observed. The efficiency was limited to 10 – 50 %, likely due to photo-induced proton transfer dynamics, which close the ICD channel. This shows that ICD needs to be considered in radiation research, its capability to inflict damage is, however, greatly dependent on the flexibility of the hydrogen bond network. Metal centers in biomolecules, such as magnesium ions, show a notable susceptibility for radiation damage by X-rays. Estimation of the ETMD efficiency in aqueous solutions of magnesium salts shows an efficiency of 30 – 50 %, which is significantly increased to 75 – 90 % in fully hydrated magnesium ions. This shows that ionization of magnesium ions can lead to significant radiation damage in their immediate vicinity by non-local decay. Additionally, the possibility to utilize non-local autoionization processes as a tool to directly probe the hydrogen bond network in aqueous systems is explored. The signature of proton transfer dynamics following photoionization was investigated for amorphous ice and in binary mixtures of liquid water and cryoprotectant molecules, namely glycerol and dimethyl sulfoxide. Their presence weakens the hydrogen bond network relative to pure water, the degree of which is determined by the balance of hydrophilic and hydrophobic interactions. These results show that non-local decay phenomena indeed carry information on the chemical surrounding of the decaying molecule, specifically on the hydrogen bond network.

Furthermore, the first double ionization spectrum of liquid water was measured and compared with with the double ionization spectra of water clusters. The spectral features are separated into dicationic final states of local and non-local character. The latter is attributed to scattering of photoelectrons on the vapor phase leading to electron impact ionization and the emission of ICD electrons from the liquid phase. These results contribute to a fundamental understanding of the photoelectron spectrum of liquid water, but also make a case for the relevance of ICD in biological conditions.

Zusammenfassung

Bei der Wechselwirkung von biologischer Materie mit ionisierender Strahlung werden angeregte Molekülionen erzeugt. Diese können ihre überschüssige Energie durch die Freisetzung eines weiteren Elektrons abgeben; ein Prozess, der als Autoionisation bezeichnet wird. Die durch Autoionisation freigesetzten Elektronen und Ionen können zu den durch Röntgenstrahlung verursachten Schäden an biologischem Gewebe beitragen. Neben dem Auger-Zerfall, welcher lokal innerhalb eines Moleküls stattfindet, gibt es weitere nicht-lokale Autoionisationsmechanismen: Intermolecular Coulombic Decay (ICD) und Electron Transfer mediated Decay (ETMD). Diese beiden werden mit der Freisetzung von niederenergetischen, potentiell DNA-schädigenden Elektronen in Verbindung gebracht, wobei das Schadpotential dieser Prozesse durch ihre Effizienz bestimmt wird. Da Wasser einen Großteil biologischen Gewebes ausmacht, wurde Autoionisation in unterschiedlichen wässrigen Systemen, wie molekularen Clustern, flüssigem Wasser und amorphem Eis im Hinblick auf ihre Relevanz im Bereich der Radiobiologie mittels konventioneller und koinzidenter Elektronenspektroskopie untersucht.

Eine Bestimmung der ICD-Effizienz in Wasserclustern und Wasser-Formaldehyd-Clustern zeigte einen Anstieg der Effizienz mit ansteigender Clustergröße. Durch photoinduzierten Protonentransfer als konkurrierenden Prozess, der in der Lage ist den ICD-Kanal zu schließen, ist die ICD-Effizienz auf etwa 10 – 50 % limitert. Dies zeigt, dass der ICD Prozess als Quelle für Strahlenschäden berücksichtigt werden sollte, jedoch ist das Ausmaß stark von den Eigenschaften des Wasserstoffbrückennetzwerks abhängig. Metallionen in Biomolekülen, wie zum Beispiel Magnesium, sind besonders anfällig für Schäden durch Röntgenstrahlung. Eine Abschätzung der ETMD-Effizienz in Magnesiumsalzlösungen zeigt Werte von 30 – 50 %, die auf 75 – 90 % ansteigen können für Lösungen in denen das Magnesiumion vollständig hydratisiert ist. Durch den ETMD-Prozess können Moleküle in unmittelbarer Nähe zu Magnesiumionen beträchtlichen Schaden nehmen.

Darüber hinaus wurde die Möglichkeit verfolgt, nicht-lokale Autoionisation als Hilfsmittel für die Untersuchung des Wasserstoffbrückennetzwerks in wässrigen Systemen zu nutzen. So wurde die Signatur von photoinduziertem Protonentransfer in amorphem Eis und Mischungen aus flüssigem Wasser und Kryoprotektoren, wie Glycerol und Dimethylsulfoxid untersucht. Diese Moleküle schwächen das Wasserstoffbrückennetzwerk relativ zu reinem Wasser, wobei der Grad der Schwächung durch das Gleichgewicht von hydrophilen und hydrophoben Wechselwirkungen bestimmt ist. Diese Ergebnisse belegen die Eignung der nicht-lokalen Prozesse zur Untersuchung des Wasserstoffbrückennetzwerks.

Weiterhin wurde das erste Doppelionisationsspektrum von flüssigem Wasser aufgenommen und mit Spektren von Wasserclustern verglichen. Alle spektralen Signaturen konnten lokalisierten und nicht-lokalisierten Zuständen zugeordnet werden. Letztere entstehen zum einen durch Elektronenstoßionisation von Photoelektronen an der Gasphase und zum anderen durch ICD in der flüssigen Phase. Diese Ergebnisse tragen zum allgemeinen Verständnis des Photoelektronenspektrums von Wasser bei und bekräftigen die Relevanz von ICD unter biologischen Bedingungen.

Contents

List of Figures

List of Tables

List of Abbreviations

AES	**A**uger **E**lectron **S**pectrum
ArTOF	**A**ngle **r**esolved **T**ime **O**f **F**light (spectrometer)
ASW	**A**morphous **S**olid **W**ater
CCD	**C**harge-**C**oupled **D**evice
CIP	**C**ontact **I**on **P**air
CoESCA	**Co**incident **E**lectron **S**pectroscopy (for) **C**hemical **A**nalysis
DIE	**D**ouble **I**onization **E**nergy
DIP	**D**ouble **I**onization **P**otential
ESCA	**E**lectron **S**pectroscopy (for) **C**hemical **A**nalysis
ETMD	**E**lectron **T**ransfer **M**ediated **D**ecay
HOMO	**H**ighest **O**ccupied **M**olecular **O**rbital
IC	**I**nternal **C**onversion
ICD	**I**ntermolecular **C**oulombic **D**ecay
IMFP	**I**nelastic **M**ean **F**ree **P**ath
LEE	**L**ow **E**nergy **E**lectrons
M	**M**ol per liter (mol/L)
MCP	**M**ulti **C**hannel **P**late
MD	**M**olecular **D**ynamics
MO	**M**olecular **O**rbital
PES	**P**hoto**E**mission **S**pectroscopy
PPRE	**P**ulse **P**icking (by) **R**esonant **E**xcitation
PTM-CS	**P**roton **T**ransfer **M**ediated **C**harge **S**eparation
ROI	**R**egion **O**f **I**nterest
SFG	**S**um **F**requency **G**eneration
SR	**S**ynchrotron **R**adiation
SShIP	**S**olvent **Sh**ared **I**on **P**air
TOF	**T**ime **O**f **F**light
UHV	**U**ltra **H**igh **V**acuum
VUV	**V**acuum **U**ltra**v**iolet

Alles für die Passmann.

Chapter 1

Introduction

"So, what do you do?" A relatively simple question. Quite possibly everyone gets it occasionally in this form or any variation. In fact, it's a question I was asked on quite a regular basis during the last years. To be honest, while writing this thesis I kept asking it myself. Either actually questioning myself out of frustration or when starting a new page. In the majority of situations when someone posed this question to me, this someone had a very different scientific background, if any at all, making it inherently difficult to answer said question to a degree that satisfied everyone involved. Indeed, it took me a multitude of iterations to answer the question of what I do without going into too much detail and consequently losing my interlocutor's attention. This in turn resulted in me being upset about the continuing inability to communicate the work I am excited about and should feel proud of. By the time I had written about 90 % of this thesis, I found myself talking to a tailor, a make-up artist and a medical doctor trying to come up with a simplified but accessible explanation of the things I do:

> *I investigate processes called autoionization.*
> This is a rather unfamiliar word and I rarely expect anyone to have a connection to it. But I do kind of like it, so I continue to use it.
> *When someone is getting an X-ray taken, the interaction of the X-ray radiation with the matter making up the body can trigger multiple processes, among them also the ones called autoionization. Those are particularly interesting as it was discovered that they produce a number of very reactive species which in turn are prone to inflict damage to the biological tissue e.g., break DNA. The research I do essentially serves to characterize these processes. How efficient are they? How can they be influenced? Since the body is in large parts comprised of water, my research focuses on these autoionization processes in water and mixtures of water of increasing complexity. In the end, we hopefully have a better understanding of these processes, ideally even controlling them for things like radiotherapy.*

This is certainly not the most sophisticated description of my work, but nevertheless it seemed to spark a bit of genuine interest in my counterpart. A reaction I was very grateful for as I invested quite some time and effort into producing results, understanding and communicating them.
At this first page, I took the liberty to put a more personal note on the otherwise rather detached and scientific tone of a doctoral thesis. Judging from other dissertations I have read,

this might be an unusual approach, but rather than struggling for days this gave me an entry into the topic of this thesis. For the remainder of this work I will try to answer the question of what I do with a compilation of results produced in numerous experiments in the time as a doctoral student, which the scientifically trained reader might find more illustrative.

Autoionization. In chemistry, a word usually associated with the spontaneous dissociation of water molecules in liquid water [1]:

$$H_2O + H_2O \rightleftharpoons H_3O^+ + HO^-.$$

This chemical equilibrium is a fundamental reaction called autoprotolysis in acid-base chemistry and is typically used to determine and explain the pH of water. Here, small energetic fluctuations lead to the dissociation of an OH bond and the abstraction of a proton (H^+) leaving a hydroxide ion (OH^-) behind. The proton is transferred to a neighboring water molecule to form H_3O^+. This is a very specific example of an autoionization process and does not represent the processes investigated in this work. However, it shall be revisited at a later point.
A more general definition of autoionization is given in the the IUPAC Compendium of Chemical Terminology [2]:

> *[Autoionization] occurs when an internally supra-excited atom or molecular moiety loses an electron spontaneously without further interaction with an energy source.[...]*

In other words, it describes the change of the initial charge state of an excited atom or molecule from Z to $Z + 1$ by emission of an electron. In physics, specifically in the field of photoemission spectroscopy, the word is often synonymous to the Auger decay as a well established process [3]. The Auger decay is an electronic relaxation process of a core-excited atom or molecule by ejection of an outer shell electron. In comparison to the Auger decay, which has been described for the first time in the early 1920s [4, 5], there is a relatively young class of electronic decay channels further expanding the concept of autoionization. The most important difference between Auger and this newer class of autoionization phenomena is their localization. While Auger decay takes place locally within a single atom or molecule, be it in the gas phase or in a solid material, in which the individual atoms are indistinguishable, the other autoionization phenomena are a direct consequence of the discernability of individual entities. These processes are therefore classified as non-local autoionization processes. The two most prominent examples of this category are Interatomic/Intermolecular Coulombic decay (ICD) and Electron transfer mediated decay (ETMD) [6, 7], which will be the main focus of this thesis. In a given system consisting of a minimum of two distinct entities an electron vacancy with an energy above the double ionization threshold can decay by transition into a doubly ionized final state. The two positive charges are distributed over different sites in the system. At small system sizes the repulsion between the charges may lead to a Coulombic explosion.
Over the last years, many theoretical and experimental investigations on these phenomena

have been performed and captured in a recent review article [8]. It could be well substantiated that these processes are of a general nature in weakly bonded systems, such as van-der-Waals clusters and hydrogen bonded systems. While the majority of studies has been performed on van-der-Waals bound systems, such as rare gas clusters, hydrogen bonded systems are of particular interest since the hydrogen bond constitutes one of the most often found intermolecular interactions in biological matter. It is the essential part in forming the double helix structure of DNA [9] and the origin of many of the anomalous properties of liquid water [10]. So, due to the ubiquity of the hydrogen bond in biochemistry, non-local processes like ICD are likely to happen in organic matter containing hydrogen bonded macromolecules. It is, however, difficult to study these phenomena in macromolecular systems using the techniques established in the community, such as electron spectroscopy, ion spectroscopy and charged particle coincidences [8]. Smaller molecular systems are, however, accessible and the first observation of ICD in water clusters [11, 12], as the most prominent hydrogen bonded system, demonstrated the relevance of these processes in radiobiology. In water clusters inner valence ICD was observed to lead to the emission of low kinetic energy electrons. These low-energy electrons are a highly reactive species, prone to inflict damage to macromolecular assemblies e.g., by causing DNA strand breaks [13]. Since water makes up on average 60 % of the human body [14], exposition of biological matter to ionizing radiation will likely induce these decay process in the vicinity of other biomolecules. In order to compare non-local decay processes to other pathways of radiation damage, it is necessary to quantify their efficiency and characterize the influence of the chemical surrounding on the process itself. Therefore, a significant part of this thesis is dedicated to the quantification of non-local electronic decay in an aqueous environment.

While ICD is the most recognized one among the non-local autoionization processes, the ETMD process also deserves significant attention in terms of radiation damage. A recent theoretical study showed that X-ray irradiation of metal complexes results in intricate and highly efficient deexcitation cascades involving ETMD [15]. At the end of the cascade the charge state of the metal center is seemingly unaltered, but in the course of deexcitation not only a number of reactive electrons are emitted but also the metal's solvation shell is critically changed. In fact experimental studies also show that metal centers of proteins are particularly sensitive to X-ray radiation and are damaged by relatively low doses long before the remainder of the macromolecule is affected [16]. Organometal complexes, especially magnesium complexes, play an important role in the human body for instance as active site in various enzymes [17]. Due to this abundance a fundamental understanding of the high efficiency of non-local electronic decay at metal centers is highly desirable, with the prospect of deliberately utilizing the chemical specificity of the decay for radiotherapeutic applications.

Another aspect of post-ionization processes discussed in this thesis is the photoinduced protolysis of water upon X-ray irradiation. Similar to the previously introduced spontaneous autoprotolysis in liquid water, the core-level excitation/ionization results in the dissociation of an OH bond followed by a proton transfer to the neighboring water molecule, ultimately

producing the species H_3O^+ and OH^+. A spectroscopic signature of this protolysis was recently identified as a non-local contribution in the O 1s Auger electron spectrum of liquid water [18]. Since this signature requires the existence of an hydrogen-bonded environment, it supposedly carries information on the quality of said environment. With this in mind, the non-local autoionization signature opens up the possibility to investigate the hydrogen bond network of water in presence of other species such as ions or organic molecules.

Briefly, on the following pages a collection of results on non-local autoionization phenomena in the hydrogen-bonded environment of condensed water is presented. These results were obtained in different electron spectroscopic experiments on clusters, ice layers and solutions using synchroton radiation. While each experimental chapter discusses an individual autoionization process specific to the investigated system, the recurring theme is that the hydrogen bond, respectively the hydrogen bond network, is responsible for its existence and influences its qualities.

Chapter 2

Concepts

2.1 Photoionization

Light–matter interaction with an isolated atom or molecule (M), enables various processes to occur. Among them is the emission of an electron, which is called photoionization, with the emitted electron called the photoelectron $e^-_{h\nu}$:

$$M + h\nu \longrightarrow M^+ + e^-_{h\nu}. \tag{2.1}$$

The so-called photoelectric effect was first described experimentally by Hertz [19] and shortly after theoretically explained by Einstein [20]. The latter formulated a fundamental rule: the kinetic energy E_{kin} of the photoelectron is determined as the difference of the incoming photon energy $h\nu$ (h is the Planck constant and ν is the photon frequency) and a binding energy E_B:

$$E_{kin} = h\nu - E_B. \tag{2.2}$$

This simple relationship has strong implications, since the binding energy E_B is a characteristic quantity of the studied system. In a first approximation, termed Koopmans' Theorem, these binding energies correspond to the energy eigenvalues ϵ of the Hartree-Fock orbitals which describe the electronic structure of atoms or molecules [21]:

$$E_B = -\epsilon. \tag{2.3}$$

The experimental technique used to study these electrons is called *photoemission spectroscopy* or *photoelectron spectroscopy* (PES). In the approximation of Koopmans' Theoerem, photoelectron spectroscopy measures orbital energies and helps understanding the electronic structure and reactivity of chemical compounds. Figure 2.1(a) illustrates a typical PES experiment: A photon source delivers a photon $h\nu$ which ionizes a gas phase sample. The emitted photoelectron enters an electron analyser, where its kinetic energy E_{kin} can be determined. Depending on the incident photon energy $h\nu$, different parts of an atom's or molecule's electronic structure can be probed, as schematically depicted in figure 2.1(b). Here, the energy level diagram of the occupied molecular orbitals of water is shown. The orbitals can be separated into valence levels and core levels. The energetic positions of the valence levels are essential in the understanding of a molecule's chemistry, as the outermost orbitals typically

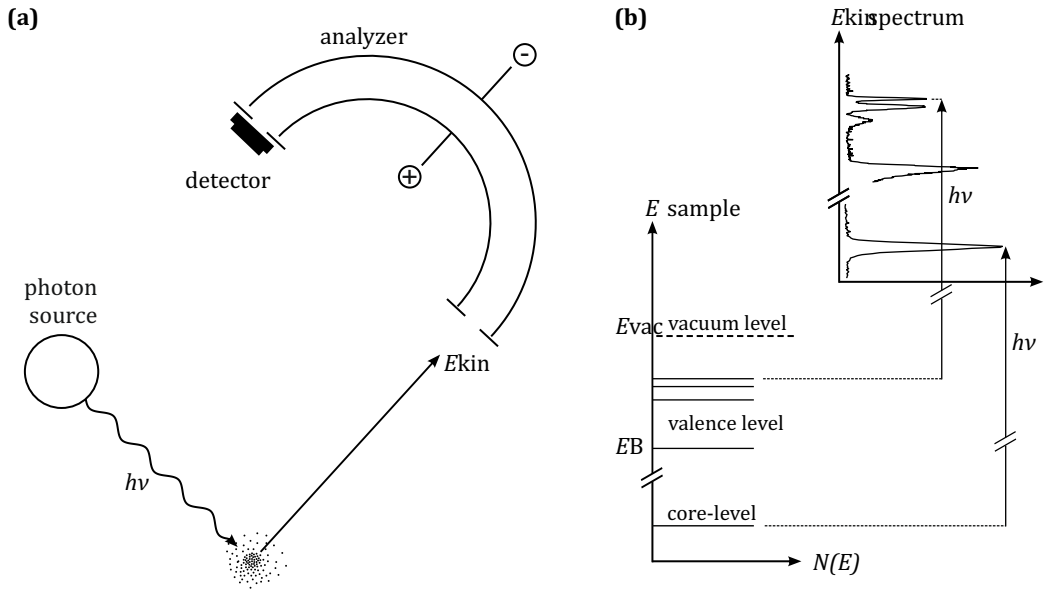

Figure 2.1: (a) Principle of photoelectron spectroscopy on a gas phase sample. (b) Schematic view of the photoemission process. The figure was adapted from ref. [22].

take part in chemical reactions. They are, however, close in energy, which potentially complicates their interpretation in more complex systems. The energetics of the core levels carry information of a molecule's chemical surrounding and its charge state (by chemists often referred to as oxidation state). They are typically well separated in energy, which makes them easier accessible for interpretation. Hence, core-level photoelectron spectroscopy of molecules in the gas phase or adsorbed on surfaces is also referred to as *electron spectroscopy for chemical analysis* (ESCA)[23]. The appropriate choice of photon energy $h\nu$ then delivers the photoelectron spectrum, also shown in figure 2.1(b).

While this basic concept of PES is readily accessible, its theory is more complex and the accurate calculation of photoelectron spectra of compounds with more than a few atoms is demanding. Even in the simplest case of the photoionization of an isolated system, such as an ideal monoatomic gas, and using the simplification of non-interacting electrons, the resulting photoelectron spectrum depends on various factors. The ionization process can be described as a transition, promoted by an interaction operator $\hat{H}$, from an N electron initial state $|i_N\rangle$ into an ionic final state $\langle f_{N-1,e}|$, with $N-1$ being the number of electrons of the ion and e the photoelectron.

$$\langle f_{N-1,e}| \hat{H} |i_N\rangle \tag{2.4}$$

Expression 2.4 is often called the matrix element, which has to be different from zero for the respective transition to be visible in a spectrum. The probability of this transition $\Gamma_{i\to f}$, which is a measure for the intensity of the photoelectron signal, is formulated in Fermi's Golden rule and is proportional to the absolute square of the matrix element and the density of available final states $\rho(E_f)$:

$$\Gamma_{i\to f} \propto |\langle f_{N-1,e}| \hat{H} |i_N\rangle|^2 \rho(E_f). \tag{2.5}$$

The operator $\hat{H}$ is the Hamiltonian describing the perturbation of the initial state by the incoming photon,

$$\hat{H} = \vec{A} \cdot \vec{p}, \tag{2.6}$$

where $\vec{A}$ is the vector potential of the photon field and $\vec{p}$ is the momentum of the photon.
It is usually assumed that the promotion of the system $i \rightarrow f$ is instantaneous and the outgoing photoelectron does not interact with the remaining cationic system. This approximation, however, is designed for emission of high energy photoelectrons and breaks down for photoelectrons with lower kinetic energy of only few electronvolts or the emission of second order electrons. Quantification of the limits in which the approximation is valid is difficult and strongly depends on the investigated system. For instance, in atomic and molecular systems the electron-hole interaction can be neglected at kinetic energies of tens of eV of the photoelectron, whereas for solid metallic systems the number is in the keV regime [24].
From the transition matrix elements other factors determining the photoemission process can also be derived, such as the photoionization cross section $\sigma_{h\nu}$ or the asymmetry parameter β, which describes the angular dependence of the photoelectron's emission directions. Since these factors are not central to the work presented in this thesis, they are not discussed here. For a more detailed description it is referred to the literature e.g., reference [25].

Apart from the general mechanism of photoionization, there is another key characteristic which needs to be considered when dealing with photoelectron spectra specifically obtained from condensed phase systems. Photoelectron spectroscopy is an inherently surface sensitive technique, due to the *inelastic mean free path* (IMFP) of electrons. The IMFP is a quantity that describes the mean distance an electron can travel before undergoing inelastic scattering processes, which cause the loss of kinetic energy and thus the loss of information about the initial binding energy. The IMFP depends on the sample's density n and the inverse of the scattering cross section σ^{-1}. In the case of a dilute gas phase sample inelastic scattering can be neglected, but needs to be taken into account when probing condensed phase samples such as solids or liquids. The information obtained typically originates from the first two to three atomic layers at the surface.
For completeness, also the *elastic mean free path* (EMFP) should be mentioned. The EMFP, is analogous to the IMFP, describing the mean distance an electron of specific kinetic energy can travel until experiencing elastic scattering processes. In contrast to inelastic scattering, in elastic scattering processes the electron's kinetic energy is conserved, but its propagation direction is changed. In photoionization, elastic scattering of the emitted photoelectron is reflected in its angular distribution, described by the anisotropy parameter β. As elastic scattering is not within the scope of this this thesis, it is referred to the literature for a discussion of its effects on photoionization [26, 27].

2.2 Double Photoionization

Photoionization is not restricted to the emission of a single photoelectron. Upon absorption of a photon of sufficient energy it is also possible to emit two electrons, leaving the respective target molecule in a doubly charged final state M^{2+}:

$$M + h\nu \longrightarrow M^{2+} + e^-_{h\nu 1} + e^-_{h\nu 2}. \tag{2.7}$$

As in photoionization the energy of the incoming photon must exceed the *double ionization potential* (DIP). The DIP can be estimated by the empirical 'rule of thumb':

$$DIP = 2.8 \cdot E_{B,HOMO}, \tag{2.8}$$

where $E_{B,HOMO}$ is the binding energy of the HOMO and the empirical factor 2.8 reflects the increased energy to remove a second electron and afford the Coulomb repulsion of the 2h final state [28].
Experimentally, electron spectra as a function of *double ionization energy* (DIE) are accessible by the coincident detection of two electrons. The DIE is defined by equation 2.9:

$$DIE = h\nu - (E_{kin}(e_1) + E_{kin}(e_2)). \tag{2.9}$$

The double ionization process can take place in a direct or indirect fashion. In the direct pathway the available excess energy is shared in a stochastic fashion, in which one electron can have any energy from zero up to a maximum kinetic energy $E_{kin,max} = h\nu - DIE$; the second electron will then have a complementary energy of $E_{kin}(e_2) = E_{kin,max} - E_{kin}(e_1)$. In the indirect process, however, the single photoionization process leads to a singly charged short-lived excited state, which sequentially emits a second electron. In this case, the kinetic energy of the second electron is determined by the energy difference of the singly charged intermediate state and the doubly charged final state.
The spectroscopy of single photon double ionization is a relatively new field of electron spectroscopy, which gained some momentum with development of coincident detection schemes, such as *cold target recoil ion momentum spectroscopy* (COLTRIMS) and magnetic bottle *time-of-flight photoelectron photoelectron coincidence* spectroscopy (TOF-PEPECO). Double photoionization is used to investigate electron correlation effects in atoms and molecules.

2.3 Autoionization

Photoionization of an atom or molecule leads to a singly charged excited state, which will dissipate its excess energy. This section introduces possible electronic relaxation processes which can be summarized under the term *autoionization*. In the context of this thesis autoionization describes processes in which the sample is initially photoionized into a charged excited state capable of reducing its internal energy by emission of at least one more electron, in which case autoionization can also be regarded as indirect double ionization. Relaxation

mechanisms involving the emission of photons[1] or resonantly excited processes will not be discussed. In the following sections the different autoionization mechanisms will be distinguished by the localization of the positive charges in their respective final states.
Based on the localization the spectral signature of autoionization mechanisms can provide insight in e.g., the chemical surrounding or molecular dynamics. Interpretation of this type of experimental data is not straightforward, and requires close collaboration with theory.

2.3.1 Auger Decay

The Auger decay is the most well-known autoionization process in electron spectroscopy. In the Auger process, formulated here for a molecular entity M, a photon $h\nu$ leads to emission of a photoelectron $e^-_{h\nu}$ and subsequently an Auger electron e^-_{Auger}:

$$M + h\nu \longrightarrow M^{2+} + e^-_{h\nu} + e^-_{Auger}. \tag{2.10}$$

As a result the molecule is left in a dicationic state with two positive charges residing on a single molecular entity. In the literature this state is often referred to as a two-hole (2h) final state. An illustrative description of the Auger decay is depicted in figure 2.2, showing the

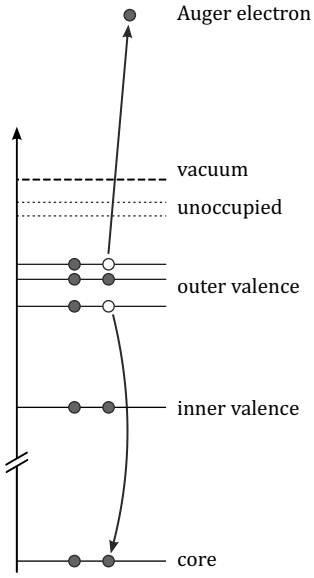

Figure 2.2: Principle of Auger decay following core-level ionization.

molecular orbital diagram after the removal of a core-level electron. The resulting core-hole is filled by an outer valence electron and the energy gained by this transition is simultaneously transferred to a second outer valence electron which is emitted into the vacuum. This step-wise process of creating a 2h final state can also be described as the prime example of an indirect double photoionization. The kinetic energy of the Auger electrons is typically high and can be estimated by the binding energies of the orbitals involved in the decay.

$$E_{kin}(e_{Auger}) \approx E_{B,core} - E_{B,valence1} - E_{B,valence2} \tag{2.11}$$

[1] The core-hole decay of lighter elements of atomic number $Z \lessapprox 40$ is dominated by relaxation via Auger decay [3]. It is therefore reasonable to neglect radiative decay for the samples covered in this thesis.

This approximation provides a rough estimate, as it does not include contributions from screening, the Coulomb repulsion between the two produced positive charges or nuclear dynamics. Multiple combinations of $E_{B,valence1}$ and $E_{B,valence2}$ are possible, and as a result the kinetic energy distributions of Auger electrons is extended over a wide range. Whereas the kinetic energy of photoelectrons depends on the initial photon energy, the Auger electrons always appear at fixed energy. In this work we focus on the KLL-Auger and the effects of hydrogen bonding on the Auger electron distribution.

2.3.2 Intermolecular Coulombic Decay

Intermolecular Coulombic decay (ICD), which was theoretically predicted by Cederbaum and co-workers in 1997, is an autoionization mechanism leading to non-local final states [6]. In this process a weakly interacting system, such as a molecular dimer $M \cdots M$ is photoionized and subsequently emits a photoelectron $e^-_{h\nu}$ and an ICD electron e^-_{ICD} resulting in a doubly charged final state:

$$M \cdots M + h\nu \longrightarrow M^+ + M^+ + e^-_{h\nu} + e^-_{ICD}. \tag{2.12}$$

The secondary step of this process, following the initial photoionization, is depicted in the energy diagram in figure 2.3. The diagram shows the occupancy of energy levels of a weakly

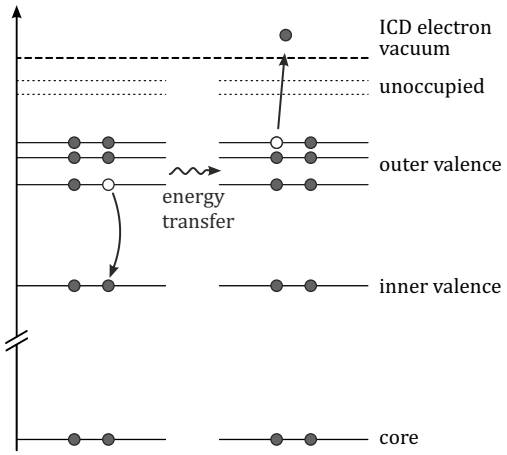

Figure 2.3: Intermolecular Coulombic decay (ICD) following inner valence ionization.

interacting dimer after inner-valence ionization. The inner valence hole is filled by an outer valence electron of the same molecule and the energy of this transition is transferred to the neighboring molecule from where an outer valance electron can be emitted.
Compared to the double ionization potential (DIP) in single atoms or molecules, the DIP of correlated systems, such as clusters, decreases. If the cluster DIP is lower in energy than the ionization potential (IP) of an inner valence excited state, this state can decay into the doubly ionized state. One reason for the lowering of the DIP in clusters is the significant reduction of the repulsive Coulomb interaction when the positive charges of the final state are distributed over separate molecular units. The leading term of the matrix element to

describe this process is:

$$V_{k,i,ov_1,ov_2} = \int\int k^*(\vec{r}_1) v_i^*(\vec{r}_2) \frac{1}{|\vec{r}_1 - \vec{r}_2|} v_{ov_1}(\vec{r}_1) v_{ov_2}(\vec{r}_2) d\vec{r}_1 d\vec{r}_2. \tag{2.13}$$

Here $v_i(\vec{r}_2)$ is the orbital of the initial vacancy, $k(\vec{r}_1)$ is the wave function of the ejected electron and $v_{ov_1}(\vec{r}_1)$ and $v_{ov_2}(\vec{r}_2)$ are the outer valence orbitals at the sites $\vec{r}_1$ and $\vec{r}_2$. Equation 2.13 essentially describes the Coulomb interaction of all states involved in the decay, hence the name "Coulombic" decay.
A more detailed derivation of Eq. 2.13 is given in references [7], [29], and [30]. Due to the anti-symmetry of the electronic wave function, the matrix element of the form V_{k,i,ov_1,ov_2} can be partitioned into a direct term and an exchange term, where the direct term is typically the dominant term to describe the ICD process:

$$|V_{k,i[ov_1,ov_2]}|^2 = |V_{k,i,ov_1,ov_2} - V_{k,i,ov_2,ov_1}|^2 . \tag{2.14}$$

The essential characteristics of ICD were summarized in the reviews by Hergenhahn and Jahnke [31, 32] and summarized as below:

- The ICD rate depends strongly on the intermolecular distance R between the two entities involved. Without taking into account overlap of the orbitals $v_{ov_1}(\vec{r}_1)$ and $v_{ov_2}(\vec{r}_2)$ the rate is proportional to R^{-6}, which is characteristic of a dipole-dipole interaction. Taking into account finite overlap, however, the rate increases much faster than R^{-6}.
- The R^{-6} dependence is comparable to Förster resonance energy transfer (FRET), which also is a process mediated by dipole-dipole coupling [33]. In both processes the energy transfer can be explained by the exchange of a virtual photon. ICD, however, does not require a resonance condition between the virtual photon and discrete electronic states and is therefore a more general mechanism.
- The number of nearest neighbors greatly influences the ICD rate. Usually, the probability for the decay increases with the number of neighbors.
- As can be seen in the detailed theoretical description in ref. [29], ICD is mediated by electron correlation effects.

2.3.3 Electron-Transfer Mediated Decay

As an additional result of the detailed interpretation of Eq. 2.13 in References [29] and [7], a further non-local decay mechanism was identified in electronically excited clusters. Unlike in ICD, in which an energy transfer takes place between two monomer units within a cluster, electronic de-excitation can also be achieved by an electron transfer step, mediated by the exchange term[2]. In the case of electron-transfer mediated decay (ETMD) a photon

[2]For completeness it should be mentioned that the exchange term also contains the *exchange* ICD process (eICD) involving an electron transfer. The two processes ETMD and eICD can then be distinguished by their different localization of the final state holes [34].

$h\nu$ is absorbed e.g., by a molecular dimer $M \cdots M$, and subsequently a photoelectron $e^-_{h\nu}$, an ETMD electron e^-_{ETMD} and a doubly charged dimer $M \cdots M^{2+}$ are produced:

$$M \cdots M + h\nu \longrightarrow M \cdots M^{2+} + e^-_{h\nu} + e^-_{ETMD}. \tag{2.15}$$

In analogy to the previous scheme for ICD, a graphical description is shown in Figure 2.4. The energy diagram shows a molecular dimer after inner valence photoionization. The

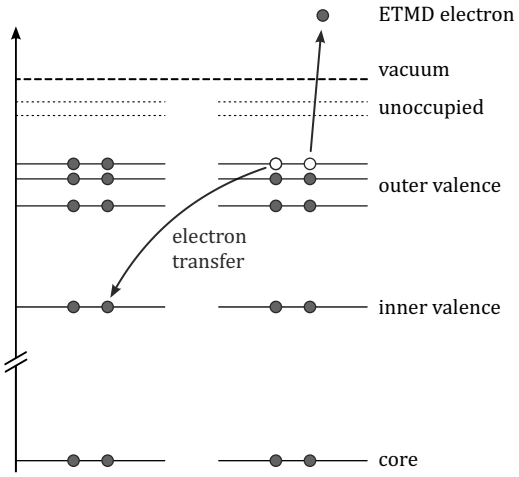

Figure 2.4: Electron transfer mediated decay (ETMD) following inner valence ionization.

initial vacancy is filled via electron transfer of an outer valence electron of the neighboring molecule. An additional electron is emitted from the outer valence state of the second molecule, leaving the neighboring molecule in a doubly charged state.
Additionally, ETMD is not restricted to two units taking part in the decay process, also decay processes can take place involving three molecules (ETMD(3)). The corresponding equations can be written as:

$$M \cdots M \cdots M + h\nu \longrightarrow M^+ \cdots M \cdots M^+ + e^-_{h\nu} + e^-_{ETMD}. \tag{2.16}$$

Here, the center molecule gets ionized, but ends in its initial state due to electron transfer from one of the neighboring molecules. The final charges are separated over two neighboring molecules, leading to even lower final state energies. The most important aspects of ETMD can be compiled as follows:

- Analogous to ICD, ETMD is mediated by electron correlation.
- Partitioning of the matrix element $V_{[k,i]ov_1,ov_2}$ (compare eq. 2.13 and 2.14) delivers in the exchange term the theoretical description of ETMD.
- Unlike intermolecular Coulombic deay, ETMD crucially depends on orbital overlap, which leads to faster decrease in the ETMD decay width, with increasing intermolecular distance between the relevant entities [35].
- Due to the required overlap and finite time for an actual electron transfer, rather than a virtual photon transfer, the ETMD process is typically less efficient than ICD. However,

when more directional interactions between the participating entities are present the electron transfer mediated decay can be enhanced, leading to compatible or greater efficiency than ICD.

So far, the introduced non-local autoionization processes, namely ICD and ETMD[3], were discussed subsequent to an inner valence photoionization event. However, both processes also occur after core-level excitation or ionization, in which case there is a competition between the local and non-local decay modes. This topic will be discussed in more detail in Section 4.2.1.

2.4 Water and Hydrogen Bonding

The electronic relaxation processes introduced in the preceding section 2.3 all result in the emission of a secondary electron of discrete kinetic energy ranging from few electronvolt in the case of inner valence ICD/ETMD to hundreds of electronvolt in the case of KLL-Auger. In the case of inner valence ICD the emitted low kinetic energy electrons are highly reactive and capable to inflict severe damage to biological samples [13]. This indicates that the non-local autoionization mechanisms are a potential pathway for radiation damage — a point emphasized early on in the research on non-local electronic relaxation phenomena. The majority of investigations were done on homogeneous and inhomogeneous rare gas systems, respectively clusters, since they represent a prototypical environment, in which individual distinguishable atoms interact weakly with one another via van-der-Waals interactions. However, the combination of radiation damage and non-local decay processes requires studies on biologically relevant systems. While a theoretical and experimental investigation of biomolecules like small DNA fragments, proteins or even cells is challenging, to say the least, it is possible to investigate the matrix in which biomolecules are typically embedded. This matrix is water.

Water is most certainly one of the most studied molecules, as it is an integral part in many scientific fields such as chemistry and biology as a universal solvent. It has a simple structure, built-up of one oxygen (O) and two hydrogen (H) atoms combined in the H_2O molecule in C_{2v} symmetry. Yet, its properties in the condensed state are highly complex and regarded as anomalous compared to other liquids. The origin of its anomalous properties, such as expansion upon freezing [36], high viscosity [37] or high melting and boiling point [38] are still not fully understood. They have, however, been linked to water's ability to form strong intermolecular hydrogen bonds [10].

The hydrogen bond is a type of molecular interaction defined by the IUPAC Compendium of Chemical Terminology [2] as:

[3] Since the first description of ICD and, soon after, ETMD a number of similar processes have been theoretically and experimentally described which are mechanistically closer to one or the other. Since for the work summarized in this thesis those processes are of minor interest they are not discussed. For further reading it shall be referred to references [31, 32] and the upcoming review [8].

> *A form of association between an electronegative atom[4] and a hydrogen atom attached to a second, relatively electronegative atom. It is best considered as an electrostatic interaction, heightened by the small size of hydrogen, which permits proximity of the interacting dipoles or charges.[...]*

The hydrogen bond itself is classified as a weak interaction with bond formation enthalpies in the range of hundreds of millielectronvolt [39]. However, formation of multiple hydrogen bonds, as for instance in liquid water, can lead to an overall strong interaction due to cooperative effects. The literature on theoretical and experimental efforts to understand the intricacies of the hydrogen bond network of water on a fundamental level is vast. The focus lies particularly on the local to extended structure of solvation shells dependent on temperature or solute within the network [10]. Although a discussion of the complex behavior of the condensed water's hydrogen bond network is exceptionally interesting, it would drift away from the actual focus of this work. Therefore, only the most important characteristics of water and the hydrogen bond will be mentioned here. Upon condensation water forms hydrogen bonds with its neighboring molecules. Due to the pronounced directionality of the hydrogen bond along the a linear O-H$\cdots$O axis, which in part stems from the slightly covalent character of the interaction [40], the water molecule is capable to form a maximum of four hydrogen bonds. Of these four bonds, two are called "donor" bonds, in which the water molecule's two H atoms engage in the hydrogen bond formation, and the other two are called "acceptor" bonds, resulting from the interaction of the oxygen lone pair's interaction with neighboring water molecules. The formation of these hydrogen bonds leads to the tetrahedral hydration shell surrounding each water molecule. A schematic drawing of this structure is depicted in figure 2.5. In this hydrogen-bonded structure the molecules retain

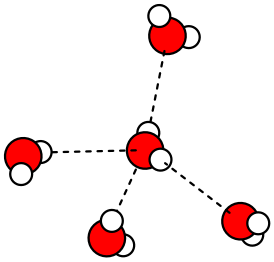

Figure 2.5: Drawing of the tetrahedral solvation shell structure of condensed water made up of hydrogen bonded water units. The central water molecule donates two hydrogen bonds via the OH groups and accepts two via its oxygen lone pairs.

their identities as individual molecules, although the hydrogen bond presents an attractive intermolecular interaction, the covalent O-H bonds are not broken. Within the framework of non-local autoionization processes the preservation of molecular distinguishability is a key feature of hydrogen bonding, as these processes explicitly require the distinguishability of molecular or atomic units. In fact, the first theoretical description of the non-local ICD process in weakly bound systems was given for small molecular clusters of water $(H_2O)_n$ and of hydrogen fluoride $(HF)_n$ [6], which both represent the text book examples of hydrogen bonding.

[4] Often, the electronegative atoms are N, O or F, so atoms from the first row of the Periodic Table.

Chapter 3

Experimental Methods

3.1 Synchrotron Radiation

The different photoemission experiments presented in this thesis were performed utilizing a tunable light source, namely an electron storage ring or synchrotron radiation facility. *Synchrotron radiation* (SR) was first theoretically predicted in 1945 by Iwanenko and Pomeranchuk and shortly after experimentally verified in 1947 by Elder et al. [41, 42]. Originally observed in the field of particle physics it was considered an unwanted energy loss mechanism of accelerated charged particles.
Generally SR can be described as a modulated emission pattern of electromagnetic radiation by accelerated charged particles, such as electrons or positrons. If a charged particle traveling at velocity v is entering a magnetic field perpendicular to its direction the Lorentz force causes a circular trajectory. This situation is shown fig. 3.1 for two cases (a) and (b). Here the magnetic field vector is perpendicular to the electron orbit (dashed line) with the

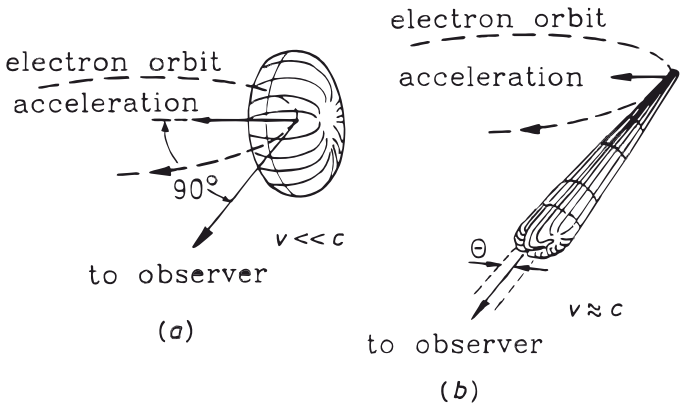

Figure 3.1: Emission pattern of an electron on a circular orbit with velocity v: (a) $v/c \ll 1$ and (b) $v/c \approx 1$. (Taken and modified from ref. [43].)

directionality of the velocity $\vec{v}$ indicated by arrows. The acceleration is also perpendicular to the magnetic field pointing toward the center or the electron orbit. At velocities far below the speed of light c the electromagnetic radiation emitted by the particle follows a toroidal pattern, as was previously observed for the dipole radiation of antennas (see fig. 3.1(a)). At relativistic velocities i.e., when $\beta = v/c \approx 1$, the observed radiation is emitted within a narrow cone into the forward direction, sometimes pictorially described as searchlight effect (see fig. 3.1(b)). Additionally, from the perspective of the observer the emitted radiation

is significantly blue-shifted. This cone can be described in terms of its opening angle θ, respectively its reciprocal value γ, and is usually on the order of a fraction of mrad:

$$\theta = 1/\gamma = \sqrt{1-\beta^2} = \frac{m_e c^2}{E}. \tag{3.1}$$

It is this radiation of relativistic particles that is referred to as synchrotron radiation.
Modern synchrotron sources consist of a closed particle orbit comprised of linear sections connected by dipole magnets. The linear sections are equipped with other tunable magnet structures, the so-called insertion devices, namely wigglers/undulators.[1] Figure 3.2 shows a schematic drawing of an undulator insertion device. Unlike the spectrally continuous radia-

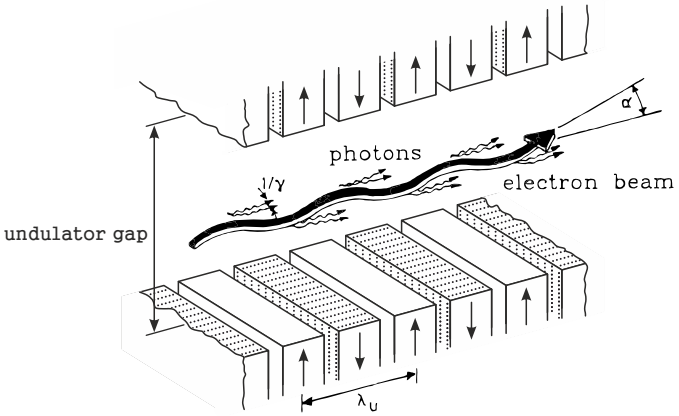

Figure 3.2: Schematic drawing of an undulator insertion device with magnet arrays of alternating polarity, providing a magnetic field with period λ_u. The electron beam passes this field and is forced on a horizontally undulating trajectory. The maximium deflection angle α and the photon emission angle $1/\gamma$ at the stationary point of the oscillation of the electron beam are shown. (Figure taken and modified from ref. [44].)

tion produced by a bending magnet or a wiggler, the undulator radiation exhibits characteristic maxima in its spectral distribution, which are a consequence of its magnetic structure. The undulator consists of an array of magnets of alternating polarization which creates a transversely undulating magnetic field with N periods of length λ_u. The electron beam centrally passes the undulator and is forced on a horizontally oscillating trajectory. At every deflection of this trajectory a searchlight cone, indicated in fig. 3.2 with their opening angle $1/\gamma$, is emitted. In an undulator the deflection is small and conditions for constructive interference of the emitted radiation can be met which leads to a sharp increase in brilliance. The requirement for constructive interference is that the time difference between the electron traveling the undulator period λ_u and the emitted light to travel the same distance must equal $n\lambda/c$, where n is an integer, indicating the occurence of higher harmonics. The emitted wavelength λ_n can be calculated with the so-called *undulator equation*:

$$\lambda_n = \frac{1}{n}\frac{\lambda_u}{2\gamma^2}\left[1 + \frac{K^2}{2} + \gamma^2\left(\Theta^2 + \Psi^2\right)\right]. \tag{3.2}$$

[1] Of course, the synchrotron also contains a section, in which the electrons are initially injected and a radio frequency cavity, responsible to re-accelerate the particles after each revolution.

Here, n denotes the nth harmonic of the undulator ($n = 1$ is called the fundamental radiation), K is the dimensionless undulator parameter, and Θ and Ψ are the angles with respect to the undulator axis describing the emission in the horizontal and vertical direction, respectively. For the undulator parameter holds

$$K \propto B_0 \lambda_u, \tag{3.3}$$

which makes it the crucial quantity to tune the emitted photon energy by opening or closing the undulator gap to vary the magnetic field strength B_0.
Based on the preceding description, the light is linearly polarized in the plane of the synchrotron ring. Other polarization states e.g., linear vertical or circular, are possible by employing more complex magnet arrangements.
Some of its key features are briefly summarized as follows:

- SR has a very broad energy spectrum ranging from the far infrared to hard X-ray region. In combination with suitable monochromators, it represents a tunable photon source for diverse experiments in multiple scientific disciplines, such as physics, chemistry and biology.
- SR typically has a high photon flux compared to X-ray tubes used in lab-based experiments, which was drastically increased with the development of second generation synchrotrons. The high photon flux allows for the operation as a user facility in which experiments can be carried out within a reasonable amount of time.
- SR has a high brilliance i.e., it is highly collimated with small divergence and small source size, similar to laser light.
- SR has a pulsed time structure, which can be varied by changing the fill pattern (see below) thereby enabling experiments requiring pulsed light as well as quasi-cw light.
- Modern-day synchrotron facilities have precise control over the particles trajectories which lead to the high spatial stability of the light source.
- SR can be produced in any polarization state, linear or circular depending on the shape of the employed magnetic field in the undulator.

All measurements presented in this thesis were done using synchrotron radiation produced at undulator beamlines for VUV and soft X-ray radiation, namely the beamlines U49-2-PGM-1, UE52-PGM, UE52-SGM, UE56/2-PGM-1 or UE112-PGM-1 at BESSY II as well as the PLÉIADES beamline at Soleil.

3.2 The Liquid Microjet

The development of photoelectron spectroscopy in the late 1950's to early 1960's [45, 46] the technique was restricted to solid or diluted gaseous samples due to the required vacuum conditions. From a chemist's point of view the electronic structure of molecules and

ions in solution or the solution itself is of utmost importance since the majority of chemical reactions occur in a liquid environment — predominantly in liquid water. First attempts on performing XPS or ESCA on liquids were carried out by Hans and Kai Siegbahn on submilimeter-sized beams of low vapor pressure liquids where the gas phase between spectrometer aperture and sample could be maintained at levels of low scattering probability i.e., the electron signal is not significantly attenuated by scattering at the gas phase [47]. Although these experiments were successful, due to the technical challenges photoelectron spectroscopy was primarily applied to solid surfaces and molecules in the gas phase for the years to come. However, the key requirements for a stable liquid beam in vacuum, which were formulated in reference [47], were later met by Faubel et al. who introduced the liquid micro-jet technique and demonstrated its application to photoelectron spectroscopy on liquid water and organic solvents [48, 49]. The idea is the introduction of a liquid sample into the vacuum in the form of a fast-flowing cylindrical micrometer-sized jet with a diameter comparable or smaller than the molecular mean free path under equilibrium vapor pressure ($d_{jet} \lessapprox \lambda_{gas}$). Although most liquids freeze when exposed to vacuum due to evaporative cooling resulting from the sudden pressure drop, the high flow rate of the jet ensures the existence of liquid–gas interface over a short distance. Furthermore the possibility of beam damage or decomposition due to X-ray irradiation is diminished by continuously replenishing the sample. A schematic drawing of such jet is shown in figure 3.3. The jet is produced by

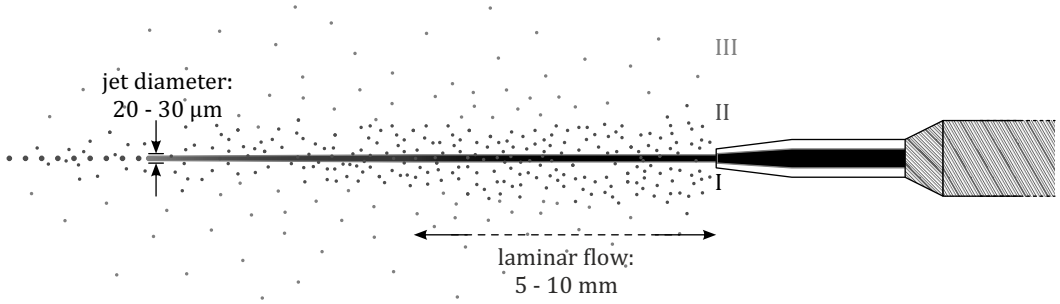

Figure 3.3: Schematic of a cylindrical liquid micro-jet. I is the bulk liquid phase, II is the collisional vapor phase due to immediate evaporation upon entering the vacuum and III is the collision-free gas phase.

pushing a liquid, usually water, through a tapered glass capillary with a micrometer-sized orifice. In the context of this work nozzles of 20 – 30 μm diameter were used and the flow rate of around 1 ml/min was achieved by pressurizing the water using a high-performance liquid chromatography (HPLC) pump, yielding a jet velocity around 40 m/s.[2] Under these conditions a region of laminar flow is formed over the length of 5 to 10 mm immediately behind the orifice. Beyond the laminar region the jet forms a break-up region of turbulent flow which ends in the formation of droplets. Specifically, the area of laminar flow, as illustrated in fig. 3.3, can be partitioned into the actual liquid phase I, a collisional vapor phase II and the collision-free gas phase III [48, 50]. For electron spectroscopic experiments it is beneficial to reduce the size of region II, which can be realized by a reduction of the jet diameter and

[2]The jet velocity v_{jet} was estimated using the equation $v_{jet} = F/(\pi r_0^2)$, with F being the flow rate and r_0 the jet radius [50].

by introduction of a skimmer into region II. In this case, skimmer refers to a small orifice introducing a pressure differential into a region of lower pressure. This does not reduce the physical size of region II, but effectively shortens the path length emitted electrons have to travel before entering the collision-free gas phase III. While a smaller jet diameter reduces the vapor phase contribution it also leads to lower stability against turbulences e.g. air bubbles in the tubing. In a typical liquid jet photoemission experiment the spectrometer entrance acts as a skimmer for the vapor phase thus leading to a $1/r^2$ dependence of the radial vapor density, instead of a $1/r$ dependence without a skimmer, with r describing the distance from the jet surface.
All photoelectron spectroscopic measurements take place within the laminar region, as it can be considered as the least disturbed surface of the liquid jet. Since most liquids are insulators, X-ray irradiation leads to charging. The addition of salt e.g., 0.05 mol/l NaCl, makes the sample conductive, thus prevents/minimizes said charging of the liquid jet. Additionally, to ensure stable operation over multiple hours the liquid sample needs degassing prior to operation of the jet in vacuum.

3.3 Molecular Clusters

In the realm of physics and chemistry one typically differentiates between the investigation of properties of individual atoms or molecules in the gas phase and the investigation of condensed matter in a liquid or solid state, which can be treated as a system of infinite size. There is however a state of intermediate finite size — the cluster. The term is generally described by the Concise Oxford Dictionary as *a group of similar things positioned or occurring closely together*. In more scientific terms a cluster constitutes an aggregate of atoms or molecules intermediate in size and exhibiting intermediate properties [51]. They consist of N monomer units with N ranging from 2 to $\sim 10^5$, thus taking on physical sizes on the nanometer scale [52]. Such small sizes lead to a high ratio of surface to bulk constituents which can induce higher reactivity than the bulk material. This is often observed for metal clusters in the field of catalysis [53]. In general, physical and chemical properties of clusters are strongly dependent on their size and will gradually approach those of the bulk material as is schematically shown in fig. 3.4. While clusters are of general interest in their own

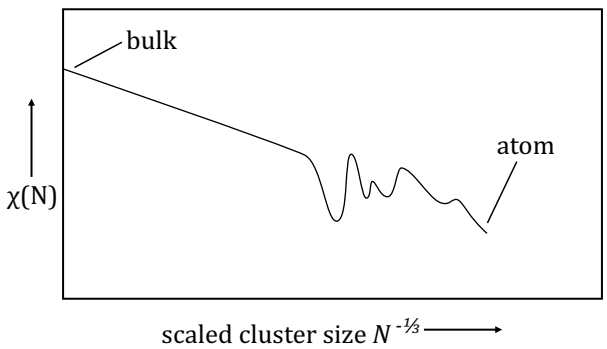

Figure 3.4: Arbitrary cluster property $\chi(N)$ as a function of the scaled cluster size $N^{-1/3}$, proportional to the inverse cluster radius. Modified from reference [52].

right, they are often used to study the emergence of bulk properties from single molecules. This is best demonstrated in theoretical studies, in which the bulk system of interest is reduced to clusters of varying size in order to make the study computational feasible. For completeness, however, it should be mentioned that there are indeed systems, in which no correspondence between cluster and bulk properties can be found, as was seen for small clusters of aluminum oxide. A theoretical and experimental investigation of $(Al_2O_3)_4^+$ clusters identified a structure as the global-minimum, which has no equivalent in the known bulk phases of aluminum oxide [54].
Depending on the cluster constituents, which can be almost any atom or molecule, there are different types of clusters categorized by their primary binding interaction. Table 3.1 gives an overview of the different types of clusters. Since the processes discussed in this thesis are

Table 3.1: Classification of clusters based on the type and strength of binding interactions between its constituents. Modified from reference [52].

cluster type	mean binding energy in eV	ionization induced bonding change	appearance in periodic table and examples
metallic cluster development of band structure delocalized electrons	0.5 - 3	barely	metallic elements Al_N, Cu_N, Fe_N, Pt_N
covalent cluster sp-hybridization directional bonding via electron pairs	1 - 4	little	B, C, Si, Ge
ionic cluster Coulomb interaction between ions	2 - 4	little	metals with electronegative elements $(KF)_N$, $(CaI_2)_N$
hydrogen-bonded cluster strong dipole-dipole interaction	0.15 - 0.5	strong	closed shell molecules containing H and electronegative elemens (F, O, N)
molecular cluster like *vdW-cluster* plus weak covalent interaction	0.3 - 1	strong	organic molecules and closed shell molecules $(I_2)_N$, $(As_4)_N$, $(S_8)_N$, (org. molecule)$_N$
van-der-Waals-cluster induced dipole interaction between closed shell atoms and molecules	0.001 - 0.3	strong	rare gases, closed shell atoms and molecules (rare gas)$_N$, $(H_2)_N$, $(CO_2)_N$

specifically properties of weakly interacting systems, we only focus on clusters bound by dispersion forces and hydrogen bonds — corresponding to the last three entries in table 3.1. For the preparation of clusters three different kind of sources are mainly employed, namely *supersonic jets*, *gas aggregation sources* and *surface sources*. In the experiments discussed in this thesis neutral molecular clusters were produced by continuous adiabatic expansion in a supersonic jet. In the following the basic principles of this process shall briefly be discussed. For a more extensive description of cluster production I refer to references [51] and [52]. In such a jet, a gas is adiabatically expanded from a reservoir with stagnation pressure p_0 and temperature T_0 into vacuum through an orifice of diameter d. Under these conditions the expansion can be described by:

$$T^{\kappa}\, p^{1-\kappa} = T_0^{\kappa}\, p_0^{1-\kappa} = const., \tag{3.4}$$

with the exponent κ being the ratio of the specific heat capacity of a gas at constant temperature and pressure. From eq. 3.4 it follows that the temperature of the gas is reduced upon expansion into the vacuum. Mechanistically this occurs by conversion of undirected motion of gas particles into a directional motion. At elevated pressure in the reservoir the mean free path λ is smaller than the orifice diameter ($\lambda < d$). Under such conditions the gas flow into the vacuum is viscous leading to a greater density and a higher number of collisions between the particles. The momentum transfer in this collisions leads to the conversion of transversal velocity components of the particles into longitudinal velocity. Slow particles thereby increase their velocity and *vice versa*. The velocity distribution of particles in the jet becomes very narrow and exceeds the local speed of sound c at the orifice, hence the term supersonic expansion. Since the resulting molecular beam is directional and the relative velocity between particles is small, the beam is considered as translationally cold. This refers to the local beam temperature within the moving frame. To initialize cluster formation the local beam temperature ($k_b T$, with k_b being the Boltzmann constant) must be lower than the binding energy of the respective molecular dimer. If this condition is fulfilled, three-body collision can lead to the production of dimers illustrated in eq. 3.5:

$$M + M + M \longrightarrow M + M_2. \tag{3.5}$$

The cluster subsequently grows by additional collisions with monomers or small clusters (eq. 3.6). In this process a broad distribution of cluster sizes is produced which is typically characterized by the mean cluster size $\langle N \rangle$.

$$M_N + M_1 \longrightarrow M_{N+1} \tag{3.6}$$

It was shown by Hagena et al. [55, 56] that the mean cluster size, specifically of rare gas and metal clusters, shows a dependence on experimental parameters such as the diameter of the orifice, the stagnation pressure and the nozzle temperature. He summarized this relation in an empirical scaling law, showing that for a given nozzle diameter the mean cluster size increases with increasing pressure and decreasing nozzle temperature.

For water clusters, Bobbert et al. [57] determined a revised scaling law analogous to references [55] and [56]. The mean cluster size $\langle N \rangle$ for water clusters can be determined by eq. 3.7:

$$\langle N \rangle = 11.6 \left(\frac{p_0 \, d_{eq}^{q} \, T_0^{q-3}}{1000 \, k_B \, T_0 (r_{ch} \, T_{ch})^{q-3}} \right)^{a}, \tag{3.7}$$

with the stagnation pressure p_0 in Pa, the temperature of the nozzle T_0 in K, the equivalent diameter of a conical nozzle d_{eq}[3] in μm, the characteristic radius of water $r_{ch} = 3.19$ Å and temperature $T_{ch} = 5684$ K. The exponents q and a were determined from fitting experimental data as $q = 0.634$ and $a = 1.886$. In the supplementary material of ref. [59] a critical analysis of the scaling law can be found. Therein, the mean cluster sizes $\langle N \rangle \approx 5-108$ estimated using eq. 3.7 were subject to a systematic uncertainty on the order of 35 %. The majority of cluster sizes reported in sections 4.1 and 4.1.2 fall into this range which makes them consistently too small or too large by about 35 %. For clusters significantly exceeding the nominal size of 108 molecules the systematic uncertainty might be greater. Nevertheless, the empirical scaling law gives a reasonable estimation of the magnitude of $\langle N \rangle$ as a function of few input parameters.

For completeness, other methods for the determination of the cluster size should be mentioned. A number of sizing methods use time-of-flight mass spectrometry to record the size distribution of a cluster beam. The prerequisite for mass detection is the presence of charged clusters, ions. The choice of the ionization is what distinguishes different mass spectrometry based sizing methods. For instance, many standard mass spectrometers used for the measurement of the residual gas in UHV experiments use electron impact ionization. This can be regarded as relative harsh ionization method, which can lead to fragmentation. Photoionization is an alternative ionization method which can lead to less fragmentation. Cluster size distributions of protonated water clusters have been measured using tunable VUV radiation [60]. It was observed that the detected cluster size distribution is dependent on the photon energy. Another approach makes use of a dopant atom in the cluster. In reference [61] a neutral beam of water clusters is guided through a sodium oven, where the cluster can pick up a sodium atom. Subsequently the sodium can be selectively ionized using UV radiation below the ionization threshold of water. Thereby even less fragmentation is observed allowing for a more refined determination of the mean cluster size from the measured size distribution. Other methods using for example light scattering [62] are available for larger clusters of several tens or hundreds of nanometers in size.

The clusters discussed in this thesis were produced using the cluster source constructed and later adapted by the previous PhD students Silko Barth and Marko Förstel; detailed descriptions of the source can be found in reference [58] and [63], respectively. In principle the cluster source contains a reservoir which can be filled with approximately 30 ml water. The reservoir temperature can be controlled with via resistive heating thus changing the equilibrium vapor pressure and allowing control over the stagnation pressure p_0. The gas

[3] The equivalent diameter d_{eq} of a conical nozzle is defined as $d_{eq} = 0.736 d / tan\alpha$, with d representing the smallest diameter and α being the half opening angle. A more detailed description of the properties of a conical nozzle is given in ref. [58].

expands through a conical nozzle of diameter d_{eq} which can be heated separately. The resulting mean cluster sizes $\langle N \rangle$ range from small clusters of approximately five molecules to bigger clusters of about 250 molecules, estimated using eq. 3.7. The source worked reliably and produced interesting results, correlating the energy difference of the cluster and gas phase HOMO to mean cluster size $\langle N \rangle$ in the photoelectron spectrum [59] and it lead to the first observation of ICD in biologically relevant systems [12].

3.4 Magnetic Bottle Electron Time-of-Flight Spectrometer

The main body of experimental work presented in this thesis was performed using a magnetic bottle electron time-of-flight (TOF) spectrometer. The particular properties of this type of electron analyzer, compared to a conventional hemispherical electron energy analyzer, will be introduced in more detail.

The magnetic bottle is based on the magnetic mirror concept, which was studied extensively for its application in nuclear fusion and plasma physics with the prospect to trap charged particles [64]. The first combination of a magnetic mirror with a time-of-flight electron spectrometer was realized by Kruit and Read in the early 80's with the intent to optimize the accurate measurement of photoelectrons emitted from a very weak source [65]. Kruit and Read were aiming for a maximum increase in the collection efficiency for laser multi-photon ionization experiments on gases by greatly increasing the acceptance angle of their spectrometer. They were typically suffering from relatively low target densities and a limited laser flux due to possible space charge effects. In their experiments only a low number of photoelectrons were emitted into the direction of the spectrometer aperture. With the adoption of the magnetic bottle field they enhanced the acceptance angle of their spectrometer to 2π sr. The name 'magnetic bottle' stems from the visual appearance of the magnetic field lines comprised of a strong inhomogeneous field and a weak homogeneous field. This situation is depicted in figure 3.5. Here, B_i denotes the strong inhomogeneous (initial) magnetic

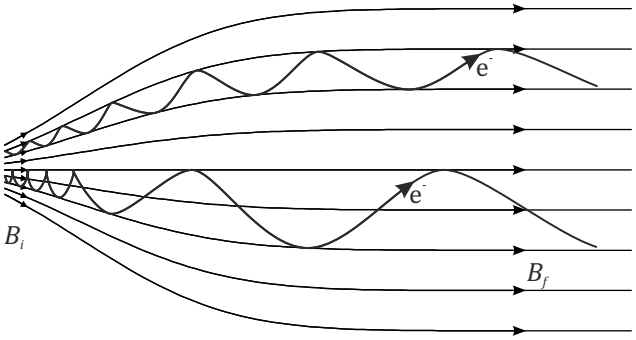

Figure 3.5: Schematic diagram of the diverging magnetic bottle field which changes gradually from a strong inhomogeneous field B_i to a weaker homogeneous field B_f. Electrons e^- emitted in B_i engage on a helical trajectory along the magnetic field lines.

field, which is positioned in the interaction region in front of the electron analyzer and B_f is the weak homogeneous (final) magnetic field in the electron detector. An electron with energy E emitted at an arbitrary angle to the magnetic field lines at B_i will undergo a helical

motion circulating in the magnetic field due to the Lorentz force $e\,\vec{v} \times \vec{B}$. Under adiabatic conditions, meaning that the change of the magnetic field strength during one revolution of the cyclotron motion is negligible compared to the overall magnetic field strength, angular momentum L and the total energy E are conserved. E can be partitioned into a parallel energy $E_{\parallel}$ and a transverse energy $E_{\perp}$:

$$E = E_{\parallel} + E_{\perp} : \tag{3.8}$$

The conservation of angular momentum,

$$L = \frac{2m_e E_{\perp}}{qB}, \tag{3.9}$$

where m_e is the mass and q is the charge of the electron, requires that the partitioning between $E_{\parallel}$ and $E_{\perp}$ follows changes in the magnetic field i.e., a decrease in $|B|$ along the diverging magnetic field will lead to a decrease in $E_{\perp}$ and an increase in $E_{\parallel}$. This means that all electrons emitted at an angle of less than 90 ° to the horizontal axis — a cone angle of 2π sr — will be guided by the magnetic field lines into the electron spectrometer. Thus, the magnetic bottle spectrometer combines a substantial increase in detection efficiency and good transmission, especially for low energy electrons, with the loss of angular information. Kruit and Read initially used a strong electromagnet to produce the inhomogeneous field B_i. The spectrometer design was subsequently altered, replacing the electromagnet with strong permanent magnets, to simplify the operation and make the B_i region more accessible [66, 67]. Magnetic bottle spectrometers of this type were used to conduct measurements of gases, clusters, liquid jets and solid samples [68–71]. In the context of this work two different magnetic bottle spectrometers were used, one for experiments on molecular clusters with an increased acceptance angle of 4π sr, described in detail in reference [72] and a similar spectrometer adapted for the use with a liquid jet, equipped with a much smaller entrance aperture and additional turbomolecular pumps attached to the drift tube, briefly described in reference [73].

In contrast to a hemispherical analyzer, in a time-of-flight spectrometer charged particles, such as electrons, are recorded at the detector as a function of their arrival time which is inversely proportional to their kinetic energy. The advantage of a time-of-flight spectrometer is their capability to record the whole photoelectron spectrum of a sample rather than just a specific energy region, as is the case in a hemispherical analyzer, and the possibility of a very high resolution, specifically for low kinetic energies [22][4]. Since the arrival time of an electron at the detector needs to be referenced to the time of ionization, it is essential to use a pulsed light source with a sufficient pulse-to-pulse temporal separation. For the time-of-flight electron spectra presented in this thesis, the electron storage ring BESSY II in *single bunch operation* mode delivered light pulses with a pulse duration < 100 ps and a repetition rate of 1.25 MHz of tunable photon energy in the VUV and soft X-ray range.

[4] It should be noted that in a magnetic bottle time-of-flight electron spectrometer the resolution is traded for a significant increase in collection efficiency.

The electron spectra were measured in time-of-flight defined by the time difference between a trigger signal, the so-called bunchmarker, provided by BESSY and the arrival time of an electron at the MCP detector. For conversion of the time domain spectra to the energy domain, a calibration of the time-of-flight spectrometer was necessary. Practically, this was accomplished by measuring a set of time-of-flight spectra of a known kinetic energy. Since the kinetic energy is determined by the relation $E_{kin} = h\nu - E_B$ (eq. 2.2), a photoline of well known binding energy E_B is required, as well as knowledge of the correct photon energy $h\nu$. Since it is possible, that the nominal photon energy provided by a synchrotron beamline does not reflect the actual photon energy, a photon energy calibration is essential. This photon energy calibration can be performed, for instance, by measuring of well defined *X-ray absorption spectra* (XAS). The position of an XAS signal as a function of the nominal photon energy provided by the beamlime relative to its literature value can then be used to correct for a possible offset. The relation between kinetic energy and flight time was then determined using equation 3.10:

$$E_{kin} = \frac{m_e}{2}\frac{l^2}{(t-t_0)^2} + eU. \tag{3.10}$$

Where m_e is the electron mass, l is the length of the drift tube, t is the recorded time-of-flight with respect to the bunchmarker, t_0 is time-zero i.e., the time offset between the bunchmarker and the actual light pulse, and eU is an offset potential resulting from the electric field along the electron trajectory.

The *t-E* calibration procedure is an essential part of every set of experiments and has to be performed for every distinct parameter set of the magnetic bottle.[5] The procedure is briefly outlined in the following paragraphs. Figure 3.6(a) shows selected time-of-flight spectra of a magnesium salt solution at photon energies of 70 to 100 eV recorded in 5 eV steps and at a retardation voltage of -10 V at the spectrometer drift tube. The signal of interest in the spectra is the Mg 2p photoline of binding energy at 55.72(48) eV in a $MgCl_2$ aqueous solution [74]. The calibration points, shown in 3.6(b), are determined by the center of gravity of the Mg 2p peak for all spectra. Subsequently, these calibration points are fitted using eq. 3.10 with l, t_0 and eU as free parameters.

Due to the non-linear relationship between energy and flight times ($E \propto 1/t^2$), the point spacing between energy increments is decreased with increasing kinetic energy, which leads to higher weighting of the signal originating from high kinetic energy electrons. For area conservation in the time-to-energy conversion of the spectra the following operation had to be performed at every point in the spectrum:

$$I(E) = I(t)\frac{dt}{dE}. \tag{3.11}$$

Where $I(E)$ is the intensity in the energy domain, $I(t)$ is the intensity in the time domain, as measured and dt/dE is the Jacobian factor required for the coordinate transformation. An

[5] The experiment-specific adjustable parameters of the magnetic bottle spectrometer include the position of the permanent magnet in front of the spectrometer entrance, the current of the solenoid creating the homogeneous magnetic field B_f and the voltage on the drift tube used to accelerate or decelerate the electron signal.

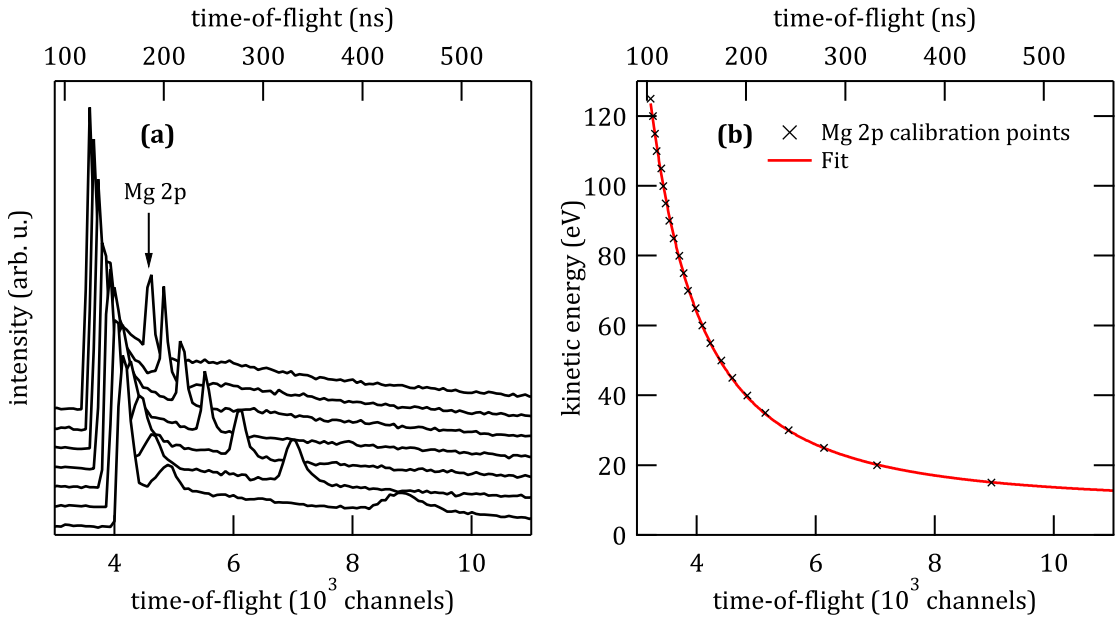

Figure 3.6: Example for the energy calibration of the magnetic bottle time-of-flight spectrometer for a magnesium salt solution and a retardation voltage of −10 V along the drift tube. (a) shows selected time-of-flight spectra of photon energies from 70 to 100 eV in 5 eV steps. (b) shows the whole set of calibration points of the respective spectrometer settings including the fit according using eq. 3.10.

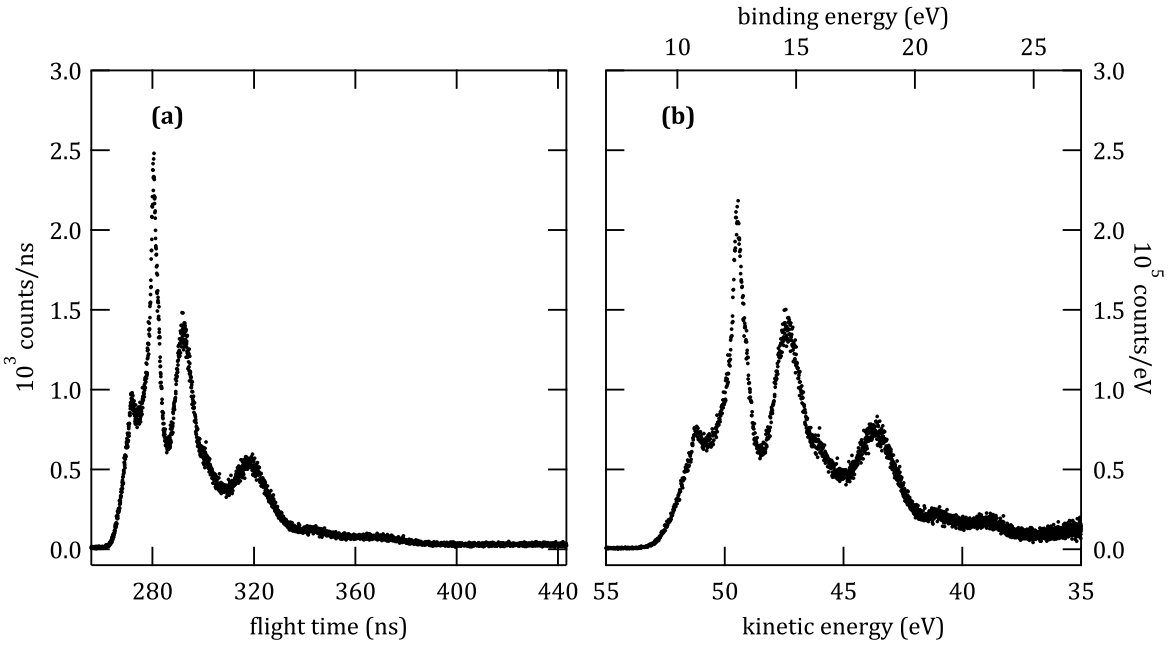

Figure 3.7: Example for the energy conversion of Water-Formaldehyde-cluster recorded with $h\nu = 62\,eV$. (a) Time-of-flight-data (b) Photoelectron spectrum after energy conversion.

example of a raw and *t-E* converted spectrum is displayed in figure 3.7. The figure shows outer valence spectra of water-formaldehyde-clusters recorded at 62 eV photon energy as a function of (a) flight time in ns and (b) kinetic energy and apparent binding energy in eV.

3.4.1 Coincident Electron Detection

An additional advantage in the use of a time-of-flight spectrometer is the ability to record multiple electrons within a set time interval given by the repetition rate of the light pulses produced by the electron bunches in the electron storage ring. The BESSY II single bunch repetition rate is 1.25 MHz, which corresponds to a time window of 800 ns between two consecutive bunches.
Events in which n electrons — with $n > 1$ — hit the detector within one single bunch revolution period are classified as a coincidence. The flight times of all electrons are stored in list mode. From these lists two-dimensional maps can be constructed which reveal correlations between two emitted electrons. A schematic example of an electron correlation map is displayed in figure 3.8. This artificial map shows the correlation of two electrons as a function

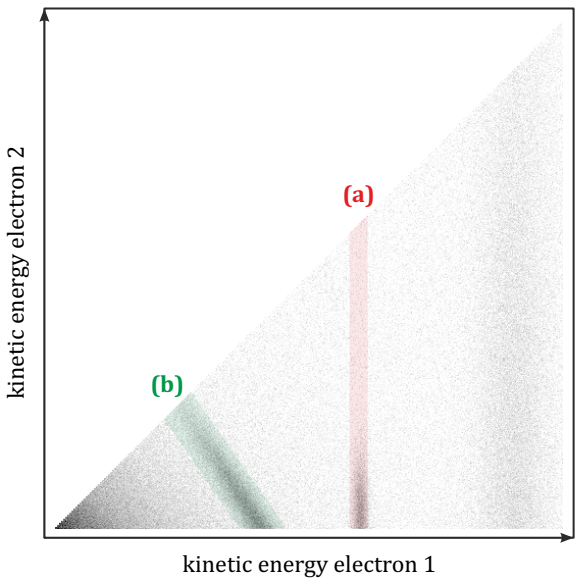

Figure 3.8: Schematic two-electron coincidence map in energy space.

of increasing kinetic energy. Here, the horizontal axis corresponds to the faster electron e.g., the photoelectron and the vertical axis is the secondary electron axis. Due to the relation $e_1 \geq e_2$ the sector above the diagonal contains no electron events at all.
The two highlighted signatures (a) and (b) in figure 3.8 illustrate an example of the most important features observed in this work. (a) is indicative of a process in which photoionization produces an intermediate state of finite life time, which can decay further by emission of a second electron, so in other words: an autoionization process. (b) is commonly associated with a single photon double ionization event resulting in the simultaneous emission of two electrons stochastically sharing their energy (see Section 2.2).
The map also shows slightly enhanced intensity at higher kinetic energies of electron 1 (on the righthand side of (a)), which stems from random coincidences of photoelectrons emitted from valence states with either slow electrons created in a previous bunch, secondary electrons which lost their energetic information due to inelastic scattering or a valence photoelectron from a different molecule within the illuminated sample volume. These random coincidences can obscure real coincident events and therefore should be avoided or at least

reduced, for instance by reducing the photon flux to conditions in which less than one ionization event occurs per light pulse. Inelastic scattering, however, cannot be avoided, when a condensed matter sample is investigated e.g., a liquid jet. The intensity of inelastically scattered electrons can be seen at low kinetic energies of electrons 1 and 2 in the correlation map 3.8 (on the lefthand side of (b)).
The measurement of these electron correlation maps within a reasonable amount of time is only feasible using a spectrometer with a high acceptance angle. Therefore, the combination of the TOF electron spectrometer with the magnetic bottle guiding field offers the ideal conditions to record electron-electron coincidence events. For instance, measurements of molecular water clusters of mean cluster size $\langle N \rangle = 67$ (see section 4.1.1) were performed at 62 eV photon energy with non-coincident count rate of 22.5 kHz, a coincident count rate of 3.2 kHz within an acquisition time of 10 min.
In this thesis, electron-electron coincidence detection was used to distinguish the low kinetic energy signal of non-local autoionization processes, such as ICD and ETMD, from a background of secondary electrons. However, it is a more versatile technique which also enables the measurement of molecular double ionization spectra [28] or ultrafast conformational and nuclear dynamics of molecules upon core ionization [75].

3.5 Experimental Setups

This section comprises a brief overview on the experimental setups used to collect the data presented in this thesis. While the principle of photoelectron spectroscopy, as introduced in section 2.1, applies to all experiments, different electron analyzers were used to investigate different samples and their spectral signatures.

3.5.1 Experiments with Magnetic Bottle Electron Spectrometer

For the measurements of coincident electron-electron spectra, two different experimental setups were used for experiments on liquids and clusters, respectively. Figure 3.9 shows schematic drawings of the two different experiments. Their common feature is the use of a time-of-flight electron spectrometer of the magnetic bottle type, as described in section 3.4.
The liquid jet experiment consists of a cubic interaction chamber with a differential pumping section towards the beamline on a movable aluminum frame. As indicated in fig. 3.9 the experiment is arranged along three orthogonal axes. The light propagation axis and the liquid jet axis span a horizontal plane with the spectrometer axis perpendicular. The intersection of the three axes is in the interaction region. The main chamber is pumped by a 1450 l/s turbo-molecular pump downstream of the light propagation axis. The spectrometer can be sealed off using a gate valve in case venting of the main chamber is required. The magnetic bottle consists of two solenoids creating a weak magnetic guiding field and two SmCo permanent magnets terminated with a soft iron cone opposite the spectrometer's $\sim$ 6 mm aperture mounted on an XYZ-manipulator to ensure optimization of the magnetic bottle settings. The magnetic field strength of the permanent magnet and the guiding field

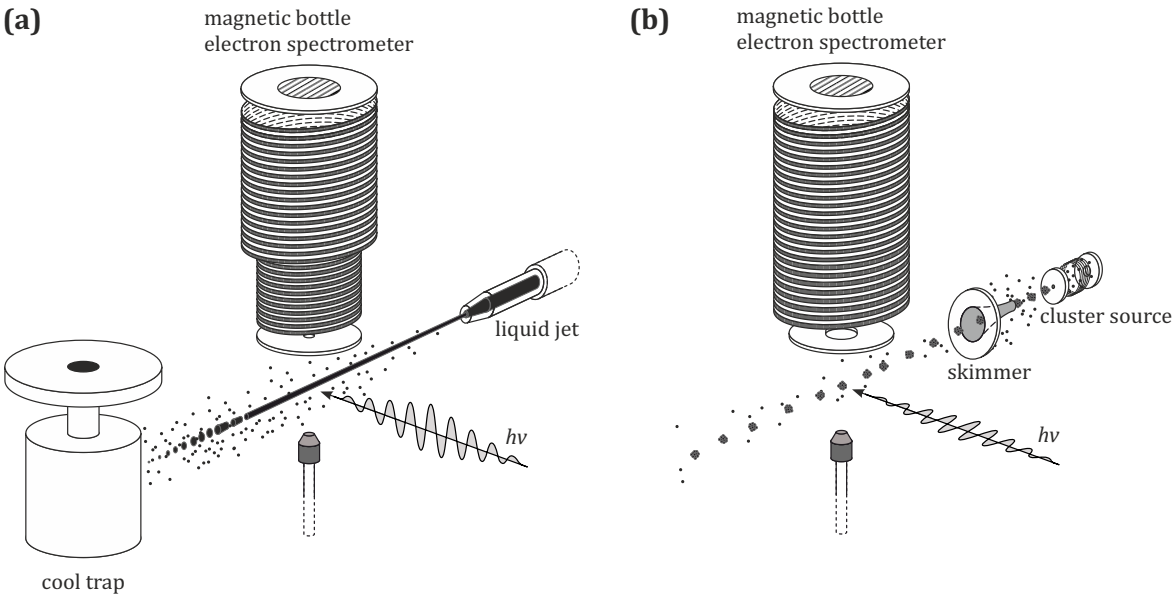

Figure 3.9: Schematic drawings of the electron-electron coincidence experiments with a magnetic bottle time-of-flight spectrometer. (A) Shows the experiment measurements using a liquid jet and (B) shows the experiment on a cluster jet.

are approximately 0.15 T and 0.5 mT, respectively. The spectrometer's drift tube is terminated with a copper mesh and subsequently capped with a detector assembly comprised of an MCP double stack and a fluorescence screen. The spectrometer drift tube is housed in μ-metal. It is pumped using two turbo-molecular pumps, which maintain the pressure in the mid 10^{-6} mbar regime in the drift tube and the detector under operating conditions. The liquid jet is inserted horizontal to the synchrotron beam with a liquid nitrogen filled cylindrical cool trap on the opposite side for additional cryogenic pumping and to freeze out the liquid. During operation of the liquid jet the main chamber pressure can be maintained at 10^{-4} to 10^{-3} mbar for multiple hours.

For coincidence experiments on clusters depicted in fig. 3.9(b) a second setup of analogous geometry was used. This setup is described in great detail in the PhD thesis of Melanie Mucke [63]. Briefly, it consists of two separate chambers divided by a gate valve along the cluster jet axis into spectrometer chamber and expansion chamber. The expansion chamber can be equipped with different cluster sources for the production of rare gas clusters or molecular clusters via supersonic expansion. The produced cluster jet is guided through a conical skimmer of 1 mm opening into the spectrometer chamber, where it is overlapped with the incoming light below the spectrometer's 25 mm aperture. The spectrometer consists of a 600 mm drift tube with a single solenoid outside of the vacuum tube wrapped with two layers of μ-metal to shield off external magnetic fields. The solenoid length is 600 mm with approximately 270 turns, creating a guiding field of about 0.5 mT at an applied current of 1 A. A detailed description of the spectrometer and its characteristics is given in ref. [63, 72].

3.5.2 Experiments with the Hemispherical Electron Analyzer

Photoemission experiments focusing on autoionization processes resulting in electrons of higher kinetic energy were performed with hemispherical electron analyzers since the magnetic bottle electron spectrometer, described above, was not designed for detection of electrons with several hundreds of electronvolt kinetic energy. The general working principle is illustrated in figure 2.1(a). Photoelectrons produced in the interaction region in front of the analyzer aperture are focused — via an electrostatic lens — onto the entrance slit of the hemisphere, which consists of two concentric electrodes. The electrons are then deflected by the electric field in the hemisphere and follow a curved trajectory onto an electron detector e.g., a combination of MCP, fluorescence screen and CCD camera. The electrostatic potential between the hemispherical electrodes leads to a dispersion centered around electrons with a specific kinetic energy, the so-called pass energy. With a hemispherical analyzer, in fixed mode, it is only possible to measure the spectral distribution within a certain energy window of $\pm 4\,\%$ of the pass energy. The choice of the pass energy is typically a compromise between high spectral resolution at lower pass energy and high transmission at higher pass energy.

For measurements of high-kinetic energy electrons from a liquid jet, the SOL^3 experimental station at BESSY II was used [76]. It is an experimental station specifically designed to perform photoemission spectroscopy on liquid samples and solid/liquid interfaces. The setup is illustrated in figure 3.10(a). In this setup, the liquid jet, the hemispherical analyzer, and

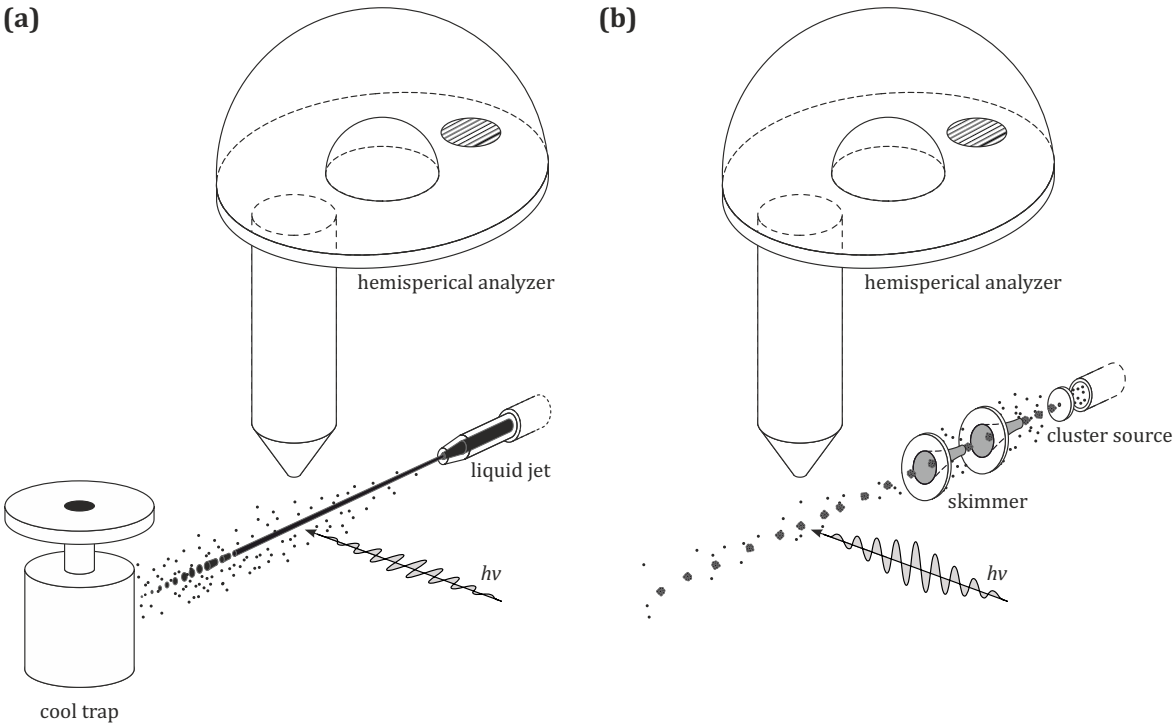

Figure 3.10: Schematic drawings of experiments with a hemispherical analyzer. (A) Shows the experiment using a liquid jet and (B) shows the experiment on clusters.

the synchrotron light span an orthogonal basis with the interaction region at the center. The SOL^3 endstation itself consists of three integral components: (1) the electron analyzer, (2) the

interaction chamber and (3) a differential pumping stage between the interaction chamber and the beamline. The analyzer is a Scienta Omicron R4000 HiPP-2 built for high resolution photoelectron spectroscopy at excitation energies ranging from the UV to tender X-ray (5 - 6000 eV). The electrostatic lens section of the analyzer is equipped with differential pumping sections to enable measurements at near ambient pressure conditions up to tens of millibars in the interaction region. The interaction chamber is equipped with two liquid nitrogen cool traps and a 1600 L/s turbomolecular pump. In normal vacuum operation of the SOL^3 the combination of cool traps and turbo pump allows for operation of the liquid jet at a chamber pressure of 10^{-4} mbar for more than ten hours. The pressure differential between the interaction chamber and the beamline, which is operated at 10^{-8} mbar or lower at the last segment, is bridged with a three-stage differential pumping chamber equipped with a cool trap and three 250 L/s turbomolecular pumps. A more detailed description of the SOL^3 experimental station and its specifications can be found in ref. [76].
Additionally, figure 3.10(b) shows a simple schematic drawing of experiments performed on molecular clusters using a hemispherical analyzer. In this experiment the molecular cluster beam, the electron analyzer and the synchrotron beam also provide an orthogonal system with the interaction region in its vertex. Molecular clusters are produced by supersonic expansion in an adjoining expansion chamber and pass through two conical skimmers before entering the interaction region. This experiment is a permanent endstation at the VUV/soft X-ray beamline PLEIADES at the SOLEIL synchrotron, France. A detailed description of the experimental setup is given in ref. [77]. Briefly, it consists of a multipurpose chamber equipped with a Scienta Omicron R4000 hemispherical electron analyzer and an adjoining expansion chamber, which can be supplied with different sources for low density samples, namely a source for aerosol nanoparticles or a source for molecular clusters. In the context of this work, the latter was used to produce clusters of small molecules like water or methanol. The clusters were produced by flowing a carrier gas, such as N_2, through a heated reservoir of water or methanol and subsequently adiabatically co-expanding the mixture through a converging-diverging nozzle. The cluster's size could then be estimated from energy difference of the gas phase and cluster HOMO signal in the valence electron spectra [59].

3.5.3 Experiments on the CoESCA Setup

For photoemission measurements on ice surfaces the CoESCA endstation at the UE52-PGM beamline at BESSY II was used. The permanent endstation is primarily intended for experiments on solid surfaces under UHV conditions. It is equipped with a separate sample preparation chamber which is connected to the analysis chamber by a sample transfer hub. The analysis chamber is subdivided into an upper part for additional sample preparation or surface analysis and a lower part housing two electron spectrometers in a plane with the synchrotron beam. A schematic drawing of the parts of the endstation used in the experiments presented in this thesis is displayed in figure 3.11. The sample was mounted on a sample holder incorporated into a cryostat and could be positioned using a 5-axis manipulator. In the upper part of the analysis chamber a doser was mounted consisting of a guiding tube and a gas reservoir separated by a 5 μm pinhole. The doser was used to produce ice

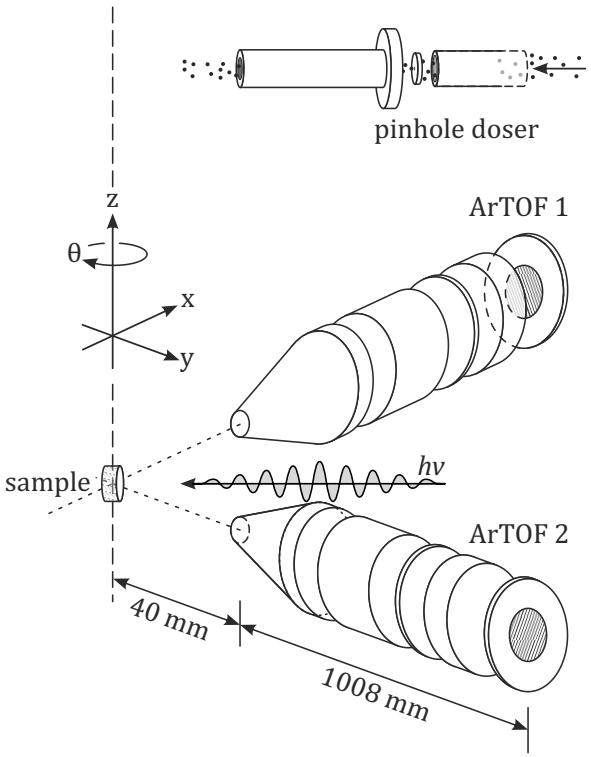

Figure 3.11: Schematic drawings of experiment at the CoESCA end station using one or two Ar-TOF's.

films on the metal sample at temperatures of approximately 98 K. During dosing the upper and lower part of the chamber were separated with a gate valve to minimize contamination of the lower chamber.[6]

The electron spectrometers are the recently developed Scienta Omicron ArTOF 2 and its prototype ArTOF 1. These spectrometers combine a time-of-flight based detection scheme with an electrostatic lens system to perform angular resolved photoelectron spectroscopy. A detailed description of the ArTOF is given in reference [78]. Briefly, in the ArTOF the drift tube of a conventional time-of-flight spectrometer is replaced by an advanced electrostatic lens system which projects the emission cone of electrons with a fixed center energy onto the 2D sensitive detector behind the focal plane. The advantage of such a lens system is that photoelectrons of a certain kinetic energy and emission angle create a unique position at the focal plane. The ArTOF measures the arrival times of electrons and their x and y coordinates on the 2D detector. Since the electrostatic potentials of the lens are pre-set, it is possible to calculate the trajectories of electrons at a certain kinetic energy and translate measured arrival times into the energy domain and the respective x and y coordinates at the 2D detector into angular information.

The time-of-flight detection scheme requires a pulsed photon source which in the case of the CoESCA end station could be realized by the use of single bunch operation of the storage ring or in conventional multi-bunch operation with the recently implemented *pulse picking by resonant excitation* (PPRE) [79]. Briefly, a laser pulse is used to excite a single electron

[6] Upon dosing the pressure in the preparation chamber was as high as 10^{-4} mbar, while the analysis chamber was maintained in the range of 10^{-8} mbar.

bunch out of the multi-bunch pattern which results in a horizontal divergence of its respective synchroton radiation wavelet. With the use of knife-edge apertures it is possible to block photons emitted by the multi-bunch train to only select light of the excited electron bunch, thus providing a quasi-single bunch in standard operation mode.
The experiments presented here were the first user experiments other than the commissioning of the CoESCA setup. They were performed using the PPRE bunch within the multi-bunch operation mode. In the course of two consecutive beamtimes measurements were performed with either ArTOF 2 or ArTOF 1 and both simultaneously. In addition, coincident measurements using both spectrometers were attempted (see chapter 8). The respective Auger electron spectra presented in section 4.2.1 were obtained at count rates of 1.5 to 2.7 kHz and acquisition times of 4 to 12 min.[7] Core level spectra were acquired at 5 to 7 kHz whitin 2 to 3 min. A critical aspect during the measurements was the temperature control using the flow cryostat and the resistive heating at the CoESCA endstation. After careful cooling of the sample from room temperature to about 98 K, the sample temperature was stable for multiple hours, enabling preparation and measurement conditions of amorphous ice layers. Using the resistive heating, the preparation of crystalline ice was attempted by annealing of the amorphous layers. However, these attempts were unsuccessful, due to insufficient temperature control, which could not be overcome within the time alloted for the experiments.

3.5.4 Energy Axes

This work comprises results of different electron spectroscopic experiments, such as conventional photoemission spectroscopy, Auger electron spectroscopy and coincident electron spectroscopy. Each of these experiments focuses on different features in the photoemission signal of the respective sample. Typically, these features are interpreted within a certain framework, in which it might be beneficial to exchange the experimental energy axis. For instance, in conventional photoemission spectroscopy the data is interpreted in terms of electronic structure on the binding energy scale i.e., the binding energy referenced to the vacuum level which approximately corresponds to the energy eigenvalue of the Hartree-Fock orbitals (see section 2.1). Throughout this thesis different types of electron spectra are presented and interpreted using either kinetic energy, binding energy or double ionization energy.

The kinetic energy axis corresponds to the actual quantity measured in a photoemission experiment, the excess energy of any emitted electron following photoionization. Autoionization signatures of the Auger decay, ICD and ETMD exhibit an electron distribution independent of the incident photon energy and are therefore only displayed as a function of their kinetic energy.
The binding energy axis (E_B) is derived from the kinetic energy (E_{kin}) by the relation:

$$E_B = E_{kin} - h\nu,$$

[7] The count rates refer to the respective energy window of the Auger or core level spectra.

with $h\nu$ being the incident photon energy.[8]
The double ionization energy axis is used to display spectral intensity of states, from which two electrons were removed by a single photon. In this work, these double ionization spectra are constructed from two coincident detected electrons (see section 3.4.1). The double ionization energy (DIE) is derived from the sum of the kinetic energy of the coincident event:

$$\text{DIE} = (E_{kin}(e_1) + E_{kin}(e_2)) - h\nu.$$

In the photoemission signal all the signatures, which are best described by individual energy axes, are simultaneously present, which naturally makes the kinetic energy the only correct axis when displaying electron spectra. Therefore, the electron spectra shown in this thesis are displayed as a function of the kinetic energy as principle energy axis (the bottom axis). Whenever it is beneficial for the interpretation or explanation of the electron signal the binding energy is displayed as a second energy axis (the top axis). Double ionization spectra are displayed in a similar fashion with the $(e_1 + e_2)$ sum kinetic energy as the principle energy axis (bottom axis) and the derived double ionization energy as a second energy axis (bottom axis).[9]

[8] see section 2.1 for a more extensive description of the photoionization process.
[9] Exceptions are made for reference spectra taken from the archive of digital spectra provided by ref. [28].

Chapter 4

Non-local Autoionization in Hydrogen Bonded Systems

In the following chapter the results on different aspects of non-local autoionization processes in hydrogen-bonded systems will be presented and discussed. The first part concentrates on intermolecular Coulombic decay (ICD) following inner-valence ionization in an aqueous environment. The second part focuses on non-local autoionization after core-level ionization. In both cases the hydrogen bond network influences the spectroscopic signature of the respective processes.

4.1 Inner Valence ICD in Molecular Clusters

When Cederbaum and co-workers predicted the existence of a non-local autoionization mechanism in excited weakly bound systems, namely intermolecular Coulombic decay (ICD), they specifically used small water clusters to introduce this concept [6]. The general nature of this mechanism was emphasized early on [80]. In a weakly bonded system such as a *van-der-Waals*- or molecular cluster an inner shell electronic vacancy can be filled by an electron of lower binding energy from the same atom or molecule. The energy thereby obtained is transferred to an adjacent atom or molecule from were a second electron is liberated. This secondary electron typically is of low kinetic energy, on the order of few electronvolt. While the first experimental results focused on rare gas clusters [81–84], the experimental observation of ICD after inner-valence ionization of water dimers and medium-sized water clusters [11, 12] lead to the recognition of ICD and related processes as a source for highly reactive species in a biologically relevant environment. A study by Boudaïffa and co-workers unambiguously attributed the origin of single- and double-strand breaks in DNA molecules to very low kinetic energy electrons of about 3 – 30 eV and their transient reaction products [13]. Although there are multiple radiation induced processes capable of producing potentially harmful low energy electrons, most of them are indirect, involving inelastic scattering events whereas ICD gained recognition as a direct source of these electrons [85]. Recently, Ren and co-workers reported the first experimental observation of ICD in a hydrated biomolecule [86]. Therein, they observed the break-up of water-tetrahydrofuran dimers after electron impact in a reaction microscope. Tetrahydrofuran can be regarded as a surrogate of desoxyribose in the backbone of DNA strands. The break-up

could be traced back to the Coulomb explosion after inner-valence ionization of water in the dimer. It has also been shown that the presence of water can lead to increased damaging effects to DNA by dissociative electron attachment promoted by low energy electrons [85]. The natural abundance of water, specifically in the aqueous environment in living cells, together with the general nature of the ICD process and its associated highly reactive final state species calls for a quantitative description of the process in water in order to evaluate its relevance in the field of radiation chemistry and biology. Therefore, one of the main topics of this thesis is the determination of the efficiency of the inner valence ICD process in water clusters of increasing size.

Mucke *et al.* have previously identified the ICD signature in photoelectron spectroscopic measurements of pure water clusters [12]. Figure 4.1 shows the full valence photoelectron spectrum of water clusters with a mean clusters size $\langle N \rangle = 98$ taken with a conventional hemispherical analyzer at 60 eV photon energy. The spectrum resembles the valence spec-

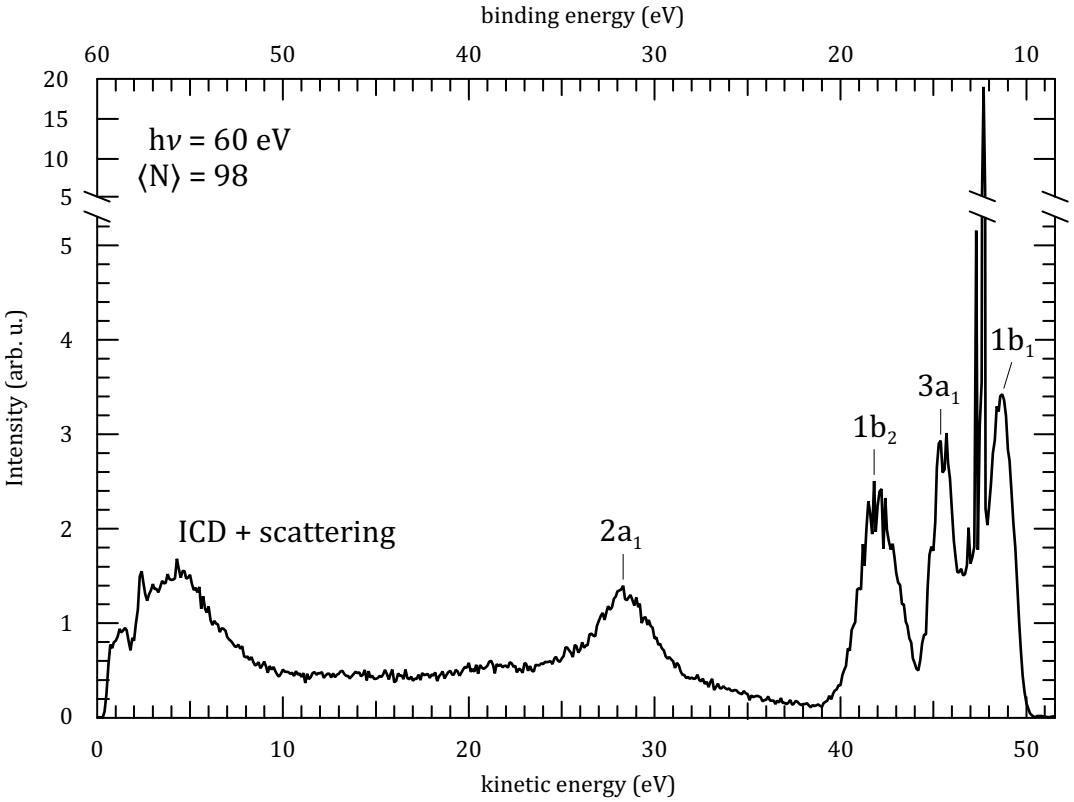

Figure 4.1: Photoelectron spectrum of water clusters $\langle N \rangle = 98$ recorded with a conventional hemispherical analyzer. Taken from reference [58].

trum of liquid water [87] with the labels denoting the occupied molecular orbitals of water $1b_1$, $3a_1$, $1b_2$ and $2a_1$. Analogous to the first observation of ICD in neon clusters [82] a signal corresponding to the ICD electron distribution could be observed in the scattering background.

An unambiguous identification of ICD from the one-dimensional photoelectron spectrum is not possible. Therefore in this work coincident electron detection (see chapter 3.4.1 and ref. [11, 12] for more detail) was employed to separate the ICD signal from the inelastic scattering background. An exemplary two-dimensional coincidence spectrum of medium-sized

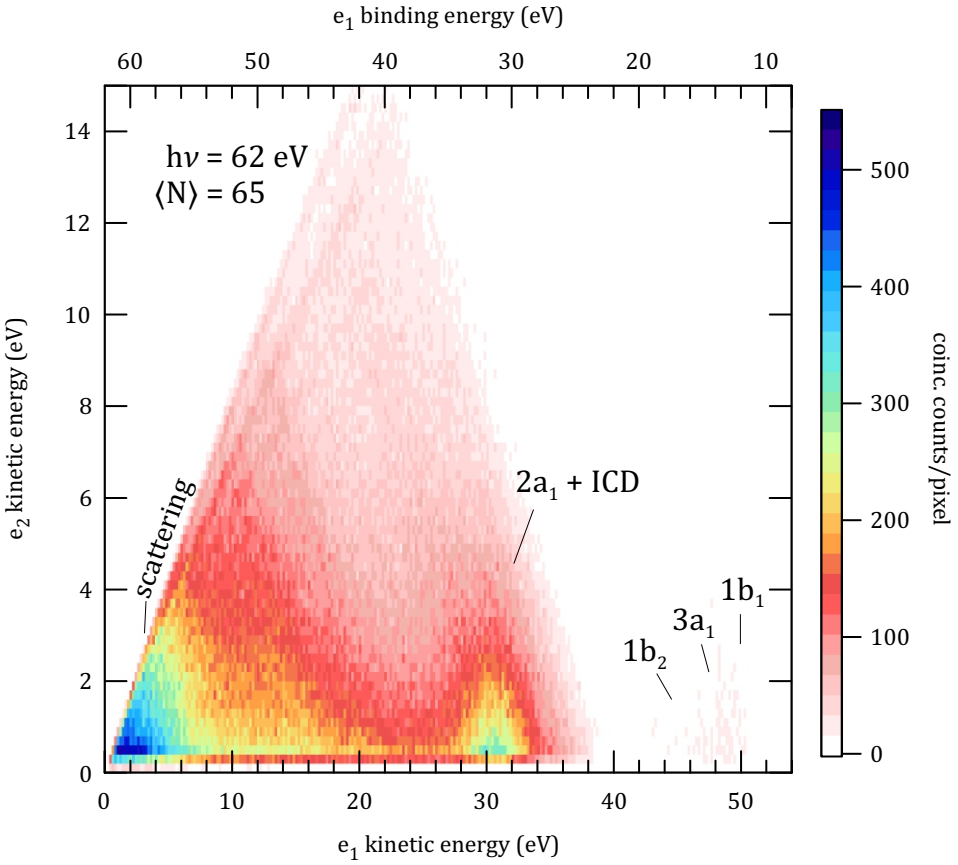

Figure 4.2: Coincidence spectrum of water clusters $\langle N \rangle = 65$ recorded with a magnetic bottle time-of-flight electron spectrometer.

water clusters ($\langle N \rangle \approx 65$) at 62 eV photon energy is displayed in fig. 4.2. The figure shows the coincident intensity of two electrons arriving at the detector within one period of the BESSY II storage ring in single bunch operation. The horizontal axes correspond to the kinetic energy (bottom) and binding energy (top) of the photoelectron e_1 in a comparable interval as in figure 4.1. The vertical axis denotes the kinetic energy of the secondary electron e_2. In the coincidence spectrum the signal of the outer valence states $1b_1$, $3a_1$ and $1b_2$ is weak and can be assigned to random coincidence events. The correlation of $2a_1$ photoelectrons with secondary electrons of low kinetic energy can be assigned to the ICD process. This coincident $2a_1$ signal is absent in the gas phase coincidence electron spectra reported in references [12, 68] as well as in the more extensive investigation of the water molecule by Reedy and co-workers [88]. Analogous to the one-dimensional photoelectron spectrum, coincident intensity at low energies of both e_1 and e_2 corresponds to inelastic scattering.

4.1.1 Inner Valence ICD Efficiency in Water Clusters

The following section focuses on a quantitative description of the inner valence ICD process. The ICD efficiency is determined by its decay rate relative to other accessible relaxation mechansims, such as radiative decay, involving the emission of a photon, or radiationless deexcitation processes, such as internal conversion (IC) or intersystem crossing (ISC). In homonuclear and mixed rare gas clusters the ICD lifetime, or inverse decay rate, after inner-valence ionization was found to be on the order of tens to hundreds of femtoseconds [89–91]. At this ultrafast time scale radiative transitions can usually be neglected. This is one of the reasons for the ICD mechanism to quench other decay pathways in rare gas clusters and to exhibit an efficiency close to unity i.e., every inner-valence vacancy decays by ICD [92, 93]. On the other hand, on the femtosecond scale substantial nuclear motion can occur in molecular systems. In gase phase spectroscopy this femtosecond nuclear motion is called ultrafast dissociation [94]. Specifically for water this process has been shown for the gas phase [95] and in liquid water [96, 97]. Therefore, the description of the ICD process requires consideration of nuclear dynamics. A coupling between nuclear and electron dynamics was recognized for instance in Ne-He dimers [98] but also after core level ionization in aqueous solution [18, 99]. Depending on the particular potential energy landscape of the system, the nuclear dynamics may suppress or even enhance the non-local autoionization process.

Water clusters were chosen as an experimental environment to study ICD in a size-selective manner and to provide some link from very small systems to bulk water [59, 100]. The ICD process after inner-valence photoionization of the $2a_1$ molecular orbital can be described as follows:

$$H_2O\cdots H_2O \xrightarrow[-e_1]{h\nu} H_2O\cdots H_2O^+(2a_1^{-1}) \xrightarrow[-e_2]{} H_2O^+\cdots H_2O^+ \longrightarrow H_2O^+ + H_2O^+. \quad (4.1)$$

Since experimental and theoretical results indicate that core level [101] and valence ionization [102] in water can initiate proton transfer along the hydrogen bond coordinate, this scenario must be considered as well:

$$H_2O\cdots H_2O \xrightarrow[-e_1]{h\nu} H_2O\cdots H_2O^+ \longrightarrow H_3O^+\cdots OH. \quad (4.2)$$

Given these two equations, two questions arise: Does inner valence $2a_1$ ionization also induce a proton transfer? Is there interference between the ICD process and the proton transfer? There are in fact indications of an interference between the processes hinting towards a reduced efficiency of ICD. Svoboda *et al.* [102] compared the simulated abundance of H_2O^+ fragments after ionization of water dimers by electron impact on water clusters [103] and argued that some formation of water cations via ICD takes place, but likely only for a fraction of these ionized states. In references [18] and [102] proton transfer processes faster than the measured ICD rate for the isoelectronic neon dimer[1] could be identified. Therefore, it does

[1] In the ICD community, the rare gas atom neon is often taken as a reference point due to its isoelectronic structure to water.

Table 4.1: Compilation of expansion conditions for cluster production, and calculated mean cluster size $\langle N \rangle$. All experiments used a conical nozzle with 80 μm smallest diameter and a 15° half opening angle. The stagnation pressure p_0 was derived from the vapour pressure of water at the reservoir temperature T_r. The nozzle temperature T_0 was set independently from T_r. The H_2O/D_2O comparison was measured in a separate beamtime.

Species	T_r (°C)	p_0 (mbar)	T_0 (°C)	$\langle N \rangle$	$\langle N \rangle^{-1/3}$ (Å^{-1})[2]
H_2O	76.6	413	144	5	0.576
	87.5	637	144	12	0.439
	99.5	994	144	27	0.332
	114	1630	144	67	0.246
	115	1690	144	75	0.238
	123	2210	144	123	0.201
	131	2740	144	186	0.175
	135	3150	144	241	0.161
H_2O	104	1180	102	75	0.237
H_2O	102	1085	102	64	0.250
H_2O	104	1180	104	72	0.241
D_2O	102	1080	102	64	0.250
D_2O	104	1180	104	72	0.241
D_2O	107	1280	104	84	0.229

seem plausible that proton transfer plays a role in the electronic inner-valence relaxation of water dimers or cluster, respectively.

Experiments were performed using an experimental setup combining a cluster source with a magnetic bottle electron spectrometer as described in section 3.9 which allowed coincident electron detection required to unambiguously identify electrons emitted in the autoionization process. Cluster ensembles were probed with VUV synchrotron radiation provided by the BESSY II storage ring. The photon energies were chosen to ensure initiation of the ICD process i.e., $h\nu$ exceeding the binding energy E_b of the $2a_1$ level, which is at 32.0 eV for $\langle N \rangle = 100$ clusters [59]. The cluster jet, produced by supersonic expansion of pure water vapor, typically contains clusters with a broad size distribution which can be characterized by the mean size $\langle N \rangle$. $\langle N \rangle$ was estimated from the expansion parameters with the empirical relation given in ref. [57], yielding mean sizes ranging from 5 to 241 water molecules. The expansion parameters and respective cluster sizes of the water clusters are compiled in Table 4.1. The estimated cluster sizes are subject to a systematic uncertainty on the order of 35% as discussed in section 3.3, including 7% uncertainty in the reference temperature of the

[2]While $\langle N \rangle$ is a dimensionless quantity $\langle N \rangle^{-1/3}$ can be given in Å^{-1}, as it is proportional to the effective cluster radius r_N. The relation $r_N = r_s \cdot N^3$ with r_s being the Wigner-Seitz-radius gives a simple estimate of the size of a clusters assuming spherical shape [104].

thermocouple used to measure the reservoir temperature T_r. The remainder is attributed to inherent limitations of the empirical model. This systematic uncertainty should be common to all data points, rendering all calculated cluster sizes consistently too small or too large.
For a conclusive interpretation of the experimental results, the energetics of the inner-valence ionized water dimer were calculated. The water dimer can be regarded as the simplest water cluster and serves as a model system which allows the accurate calculation of the energetics of the $2a_1$ singly ionized and doubly ionized states. Experimental observation of inner valence ICD in water clusters by Mucke *et al.* [12] and in the water dimer by Jahnke *et al.*[11], in which related spectral signatures could be identified, suggest that the dimer is in fact a suitable system for the investigation of ICD and related processes. Calculations on the water dimer presented in this thesis were performed in a collaborative effort by the groups of Petr Slavíček from the University of Chemistry and Technology Prague and the group of Nicolas Sisourat from the Sorbonne Université Paris. Since the present work is of experimental nature, only the results of these calculations will be discusses in detail. Briefly, water dimer energetics and trajectories along a reaction coordinate were computed using second order perturbation theory and *ab initio* molecular dynamics simulation by Daniel Hollas of the Slavíček group. Electronic decay rates of the dimer were determined using the Fano-CI method by Tsveta Miteva from the Sisourat group. For a comprehensive description of the computations, including the respective basis sets, employed programs, and benchmarking of the energetics the reader is referred to reference [105], its supplementary material and the references therein.

Coincident electron detection was applied to the water clusters compiled in table 4.1 to detect electron pairs, consisting of a $2a_1$ photoelectron together with a pertaining ICD electron. The correlation between the two electrons is visible in two-dimensional histograms for all cluster sizes, as seen in figure 4.2. From these spectra, the ICD efficiency α_{ICD} could be extracted, defined as the fraction of inner valence states decaying by ICD. This approach is consistent with earlier work on coincident spectra of Ne clusters, in which the efficiency α_{ICD} after 2s inner-valence ionization was found to be 0.99(11) [92]. The analysis follows the assumption that under ideal conditions α_{ICD} is described by the ratio of coincident electron pairs $P(E_{\mathrm{ph}}, E_{\mathrm{ICD}})$ to the total number of electrons detected from the $2a_1$ state $p(E_{\mathrm{ph}})$:

$$\alpha_{\mathrm{ICD}} = \frac{P(E_{\mathrm{ph}}, E_{\mathrm{ICD}})}{p(E_{\mathrm{ph}})}. \tag{4.3}$$

Here P denotes the coincident detection rate of electrons with kinetic energies E_{ph} and E_{ICD}, and p is the non-coincident detection rate of photoelectrons of energy E_{ph} (with or without a secondary electron). The precondition for this approach is the distinguishability of the photoelectron and secondary electron, $E_{\mathrm{ph}} \neq E_{\mathrm{ICD}}$, which can experimentally be realized by tuning the photon energy. In the experiments, the photon energy was always chosen to ensure $E_{\mathrm{ph}} > E_{\mathrm{ICD}}$, designating the photoelectron and ICD electron as 'first' (e_1) and 'second' (e_2) electron arriving at the detector, as labeled in figure 4.2.
Under actual experimental conditions several corrections to the measured data must be

taken into account, modifying eq. 4.3 to:

$$\alpha_{\mathrm{ICD}} = \frac{P(E_{\mathrm{ph}}, E_{\mathrm{ICD}})}{p(E_{\mathrm{ph}})} \frac{1}{c\,\gamma(E_{\mathrm{ICD}})}, \tag{4.4}$$

in which the parameter c describes the degree of condensation in the cluster jet and $\gamma(E_{\mathrm{ICD}})$ is the detection efficiency for secondary electrons of energy E_{ICD}. Both parameters can be determined experimentally. A detailed derivation of eq. 4.4 and discussion of the experimental parameters is given in the supporting information of reference [105].
The detection efficiency $\gamma(E_{\mathrm{ICD}})$ was determined by comparison of photoelectron and coincident Auger electron count rates of Xe gas. Coincidences of Xe 4d photoelectrons with Xe $N_{4,5}OO$ Auger electrons [106] were used for this purpose as previously described in references [72] and [92].
The degree of condensation c of the cluster jet is required because the $2a_1$ inner valence photoline does not allow a successful separation of monomer and clusters. To experimentally assess c, outer valence spectra were taken of every cluster size before and after measuring the ICD spectra. In reference [59] it was shown that cluster and monomer signals for the HOMO can be distinguished. Under the assumption that the photoionization cross sections are equal for both signals, the following expression is used:

$$c = \frac{p(E_{\mathrm{HOMO,c}})}{p(E_{\mathrm{HOMO,c}}) + p(E_{\mathrm{HOMO,m}})} \tag{4.5}$$

Where $p(E_{\mathrm{HOMO,c}})$ and $p(E_{\mathrm{HOMO,m}})$ are the detection rate of the cluster signal and monomer signal, respectively. The cluster and monomer signal were determined from least squares fits to the outer valence spectra taken at 62 eV photon energy and a retardation voltage of $V_{ret} = -15\,\mathrm{V}$ set to the spectrometer drift tube to improve the energy resolution. Figure 4.3 shows an example of an outer valence spectrum of a cluster jet with $\langle N \rangle = 76$ water molecules. The fit requires six Gaussian components to yield consistent and satisfactory results for all measured cluster sizes. The components 'g1' and 'g2', shown as green shaded curves, are assigned to the $1b_2$ and $3a_1$ molecular orbitals. Compared to a gas phase spectrum the signals are broadened but a clear distinction of the spectral contribution from the two phases is not possible. Component 'g4' (red shaded curve) is attributed to the gas phase $1b_1$ molecular orbital, corresponding to the oxygen lone-pair, with the small auxiliary 'g3' (red shaded curve) tentatively being attributed to its vibrational component. This auxiliary peak is required to reproduce the assymmetry of the $1b_1$ signal. High resolution photoelectron spectra of gas phase water clearly show a vibrational progression at low kinetic energy side (higher binding energy) of the leading peak [107]. Karlsson *et al.* assigned the vibrational progession of the $1b_1$ state to the v_1 and v_2 modes of the water molecules [108]. The additional Gaussians 'g5' and 'g6' displayed as blue shaded curves represent the cluster $1b_1$ at the given spectral resolution. To determine the degree of condensation c according to eq. 4.5 'g3' and 'g4' were summarized as $p(E_{\mathrm{HOMO,m}})$ and 'g5' and 'g6' as $p(E_{\mathrm{HOMO,c}})$, respectively. The resulting values of c for all measured cluster sizes are presented in table 4.2.
It can already be inferred from one- and two-dimensional spectra shown in figures 4.1 and

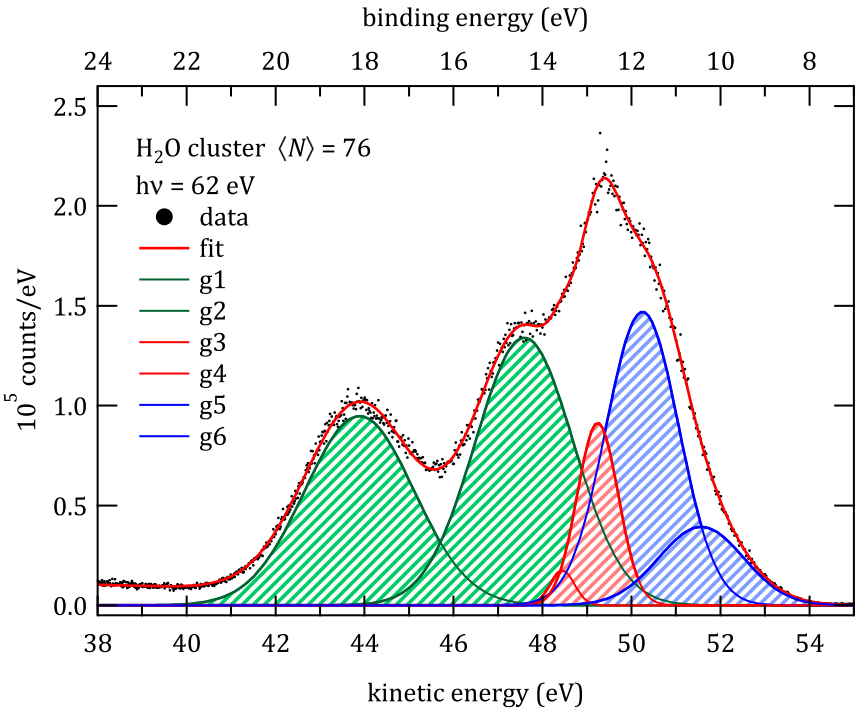

Figure 4.3: Outer valence photoelectron spectrum of a jet of $\langle N \rangle = 76$ water clusters at $h\nu = 62$ eV. Components of a least squares fit to disentangle cluster and monomer intensity are also shown. The components 'g5' and 'g6' are assigned to the cluster HOMO component, components 'g3' and 'g4' are assigned to the monomer $1b_1$, 'g3' tentatively to its vibrational component. A number of constraints were applied to produce consistent and well-defined fit results over the whole series of cluster sizes.

Table 4.2: Degree of condensation c for water clusters of varying mean sizes $\langle N \rangle$. The table distinguishes between the clusters measured in a size dependend matter and a comparison of the isotope effect in H_2O and D_2O measured in a separate beamtime.

size dependence			isotope effect		
Species	$\langle N \rangle$	c	Species	$\langle N \rangle$	c
H_2O	5	0.44(5)	H_2O	75	0.76(3)
	12	0.68(5)	H_2O	64	0.74(3)
	27	0.73(5)	H_2O	72	0.75(3)
	67	0.75(5)	D_2O	64	0.74(3)
	75	0.76(5)	D_2O	72	0.75(3)
	123	0.78(5)	D_2O	84	0.72(3)
	186	0.78(5)			
	241	0.78(5)			

4.2, that a background correction is essential when determining the non-coincident and coincident detection rates $p(E_{ph})$ and $P(E_{ph}, E_{ICD})$. The background signal contains inelastically scattered electrons as well as electron intensity from direct and indirect double ionization of the gaseous water molecules in the cluster jet [68, 88, 109] and overlaps with both the inner

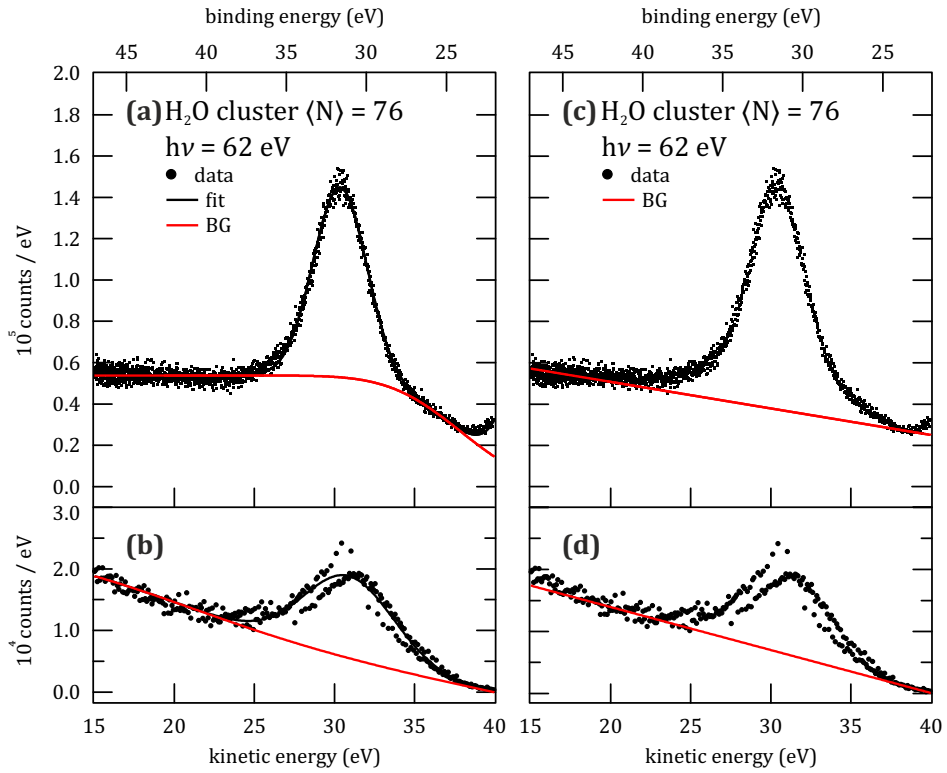

Figure 4.4: Coincident and non-coincident electron spectra of $\langle N \rangle = 76$ water clusters recorded at $h\nu = 62$ eV. Panels (a) and (c) show $p(E_{\mathrm{ph}})$, the intensity of photoelectrons detected in the region of $2a_1$ binding energies; panels (b) and (d) show the integral of $P(E_{\mathrm{ph}}, E_{\mathrm{ICD}})$ over an interval of 0 – 5 eV for E_{ICD}. The black solid traces correspond to the fit of the photoline with background and are shown to guide the eye. The red solid traces in (c) and (d) indicate a linear background below the $2a_1$ peak, while panels (a) and (b) show a curved, Shirley-type background.

valence peak and the ICD signature.

An overview of the applied background correction to the non-coincident and coincident $2a_1$ peaks is given in figure 4.4 for a cluster jet of $\langle N \rangle = 76$ taken at 62 eV photon energy. The panels (a) and (c) display the non-coincident intensity of the photoelectrons $p(E_{\mathrm{ph}})$. The corresponding coincident spectrum $P(E_{\mathrm{ph}}, E_{\mathrm{ICD}})$ integrated over an interval of 0–5 eV of E_{ICD} is shown in (b) and (d). Experimental data, shown as black circles, in the left and right hand side panels are identical, but different approaches for peak-to-background separation were employed. The background is indicated as a solid red curve in both cases. While the applied background on the right side stems from a simple linear model similar to the analysis in reference [92], the left side shows the results of a more sophisticated fit to the data comprised of Gaussian distributions on a linear baseline, thus recreating a curved Shirley-type background. Both approaches to peak-to-background separation to the spectra are reasonable and no distinct argument can be made in favor of any of the two. The two variants likely mark the largest and smallest choices for the ratio $P(E_{\mathrm{ph}}, E_{\mathrm{ICD}})/p(E_{\mathrm{ph}})$ that are compatible with the data and in this way will contribute to the experimental uncertainty of the resulting efficiency α_{ICD}.

After assessing the parameters c, $\gamma(E_{\mathrm{ICD}})$ and the peak-to-background separation the results of the inner valence ICD efficiency α_{ICD} in water clusters can be summarized in figure 4.5. In figure 4.5 the data in panels (a) and (b) corresponds to $p(E_{\mathrm{ph}})$ and $P(E_{\mathrm{ph}}, E_{\mathrm{ICD}})$ after

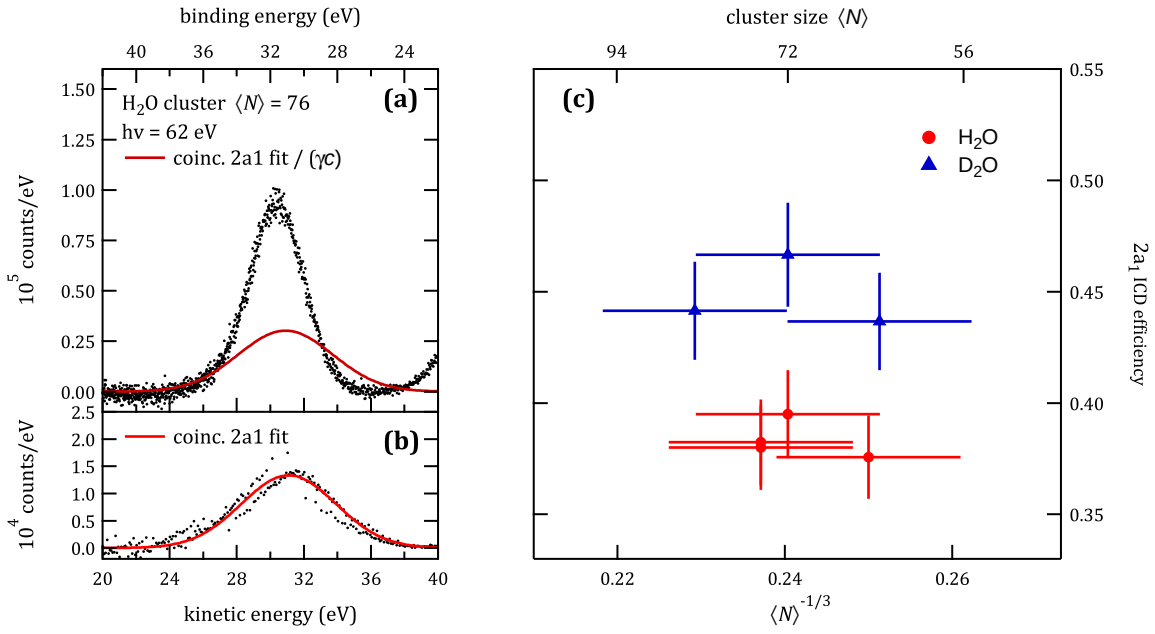

Figure 4.5: Efficiency of ICD after $2a_1$ ionization of water clusters. (a) $2a_1$ photonemission spectrum of a water cluster jet of mean cluster size is $\langle N \rangle = 76$ recorded $h\nu = 62\,\mathrm{eV}$. A linear background was subtracted. (b) Coincident electron spectrum of a $2a_1$ photoelectron and an ICD electron, after background subtraction. (a) and (b) are derived from the same data set. The solid trace in (b) is a fit to the coincident data. For comparison with the undiscriminated data, the curve is multiplied by the inverse of the detection efficiency $\gamma(E_{\mathrm{ICD}})$ and the degree of condensation c, with values of 0.58(4) and 0.76(5) in this example; the result is shown in (a) (solid trace). (c) Effect of isotopic substitution on the ICD efficiency, measured at $h\nu = 60\,\mathrm{eV}$. Error bars shown here represent the standard deviation due to stochastic errors.

subtraction of a curved background[3] for a cluster jet of $\langle N \rangle = 76$ water clusters at 62 eV photon energy. For an ideal detector (or after correction for its finite detection efficiency γ), a fully condensed cluster jet, and ICD efficiency of one, the two panels (a) and (b) would be identical. This was shown for rare gas clusters in references [92] and [69]. Any mismatch in the non-coincident and coincident data after accounting for the correction parameters can be interpreted as inner-valence ionization events not resulting in the emission of an ICD electron. This situation is shown in figure 4.5(a) in the comparison between the dotted photoline and the solid red curve which results from a Gaussian fit to the coincidence data devided by $c\,\gamma(E_{\mathrm{ICD}})$. From this comparison, one can directly infer that the ICD efficiency in water clusters is lower than unity.

Figure 4.5(c) shows values for the $2a_1$ ICD efficiency quantitatively assessed according to eq. 4.4. Here, results for clusters made up of 'normal' water (H_2O) and isotopically substituted 'heavy' water (D_2O) are compared. The clusters were produced under identical

[3] The data shown in fig. 4.5 (a) and (b) correspond to spectra shown in fig. 4.4(a) and (b).

settings of the cluster source (see table 4.1) and are comparable in size. These experimental results clearly allow two main conclusions: Firstly, the efficiency of the ICD process in medium sized water clusters is well below unity. Secondly, the ICD efficiencies display an isotope effect, with D_2O clusters exhibiting higher ICD efficiencies. These results indicate that there is another dynamic process competing with the electronic ICD process on the same time scale.

The resulting efficiencies of the size dependent ICD measurements are compiled in figure 4.6 for mean sizes ranging from 5 to 241 water molecules, taken at photon energies of 62 and 80 eV. The efficiency is displayed as a function of the mean cluster size $\langle N \rangle$ on the top

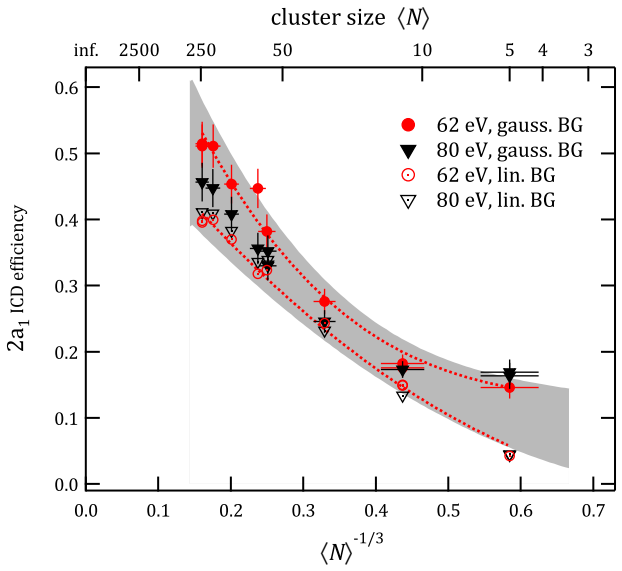

Figure 4.6: The efficiency of the decay of $2a_1$ vacancies by ICD as a function of mean cluster size $\langle N \rangle$ (top axis) or $\langle N \rangle^{-1/3}$ (bottom axis, with $\langle N \rangle^{-1/3} \propto$ to effective cluster radius). Empty and filled symbols represent different methods of background subtraction. Error bars shown for some of the data represent the standard deviation due to stochastic errors. Dotted lines show polynomial fits to the 62 eV data sets, to guide the eye. The effect of systematic error on these two curves is shown by the shaded region.

axis or as $\langle N \rangle^{-1/3}$ on the bottom axis which is proportional to the inverse cluster radius. The different routines for background correction shown previously in figure 4.4 were applied in the analysis resulting in the empty and filled symbols with the colors black and red representing the photon energy 62 and 80 eV, respectively. The two approaches to the peak-to-background separation approximately represent the lower and upper limits for the ICD efficiency. This systematic uncertainty stemming from the respective background model is highlighted as the grey shaded area. In general, the ICD efficiency increases from values of 0.05 and 0.2 at the smallest sizes to about 0.4 and 0.5 for larger clusters. It remains, however, well below unity.

Since the ICD process is the only electronic relaxation channel energetically accessible upon

inner-valence ionization of water and the ICD efficiency shows the distinct isotope dependence, proton transfer dynamics is the primary candidate for a competing relaxation pathway. The proton transfer reaction initialized after water valence ionization takes several tens of femtoseconds in liquid water [110] as well as in molecular clusters [102] while it is much faster upon core ionization [18]. In the latter case a signature of proton transfer dynamics could be identified in the Auger distribution of liquid water, within the core hole lifetime of about 4 fs [99]. A more detailed description of the underlying processes will be given in section 4.2.1.

While it was already established for liquid water and water clusters that core level and valence ionization leads to a dissociative final state that can initialize proton transfer, the situation for inner-valence ionization was subject to speculation. The potential energy curves shown in figure 4.7 calculated for the water dimer suggest the proton transfer reaction is indeed energetically favorable upon inner-valence ionization. The figure presents the dimer's

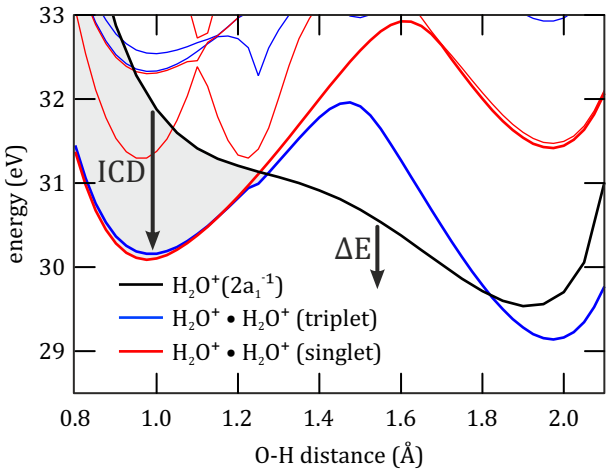

Figure 4.7: The potential energy curves of the singly (black) and doubly ionized singlet (red) and triplet (blue) states for the water dimer shown along the proton transfer coordinate. The shaded area denotes the region in which ICD is energetically allowed and arrows indicate relaxation via ICD or radiationless deexcitation ΔE, respectively.

potential energy curves along the proton transfer coordinate i.e., the O-H distance. The black trace denotes the singly ionized $2a_1^{-1}$ state with an initial energy of ca. 32 eV above the neutral ground state. The negative slope of the curve is a clear indicator of the open proton transfer channel. Furthermore, the figure shows the lowest singlet and triplet doubly ionized states as red and blue traces, respectively. A hole population analysis shows the two positive charges in these states are separated, a situation often denoted as 1h1h state. Both singlet and triplet doubly ionized states correspond to the final states of the ICD process. The 1h1h potential curves contain two local minima thus taking a double-well shape. The left minimum is located at the ground state geometry of the water dimer at $r(\mathrm{OH}) \approx 0.97$ Å and corresponds to the $H_2O^+ \cdots H_2O^+$ structure whereas the right minimum represents the fully proton transferred $HO^+ \cdots H_3O^+$ structure. The maximum of the curves depicts the transient $HO \cdots H^+ \cdots H_2O^+$ species. From the energy of the 1h initial state and the two

lowest 1h1h final states at the ground state geometry it is immediately clear that autoionization is energetically favourable. Yet, a moderate geometry change along the O-H axis induces a crossing of the singly and doubly ionized states at a crossover distance of ≈ 1.3 Å, thereby closing the ICD channel. Thus it can be established that the proton transfer is indeed a competing mechanism for the ICD process. The grey shaded area indicates the region in which ICD is energetically allowed.

The excess energy of the ICD electron corresponds to the energy difference between the $2a_1^{-1}$ state and the 1h1h final state. From the potential curves of figure 4.7 an ICD electron distribution of about 0 to 2 eV can be estimated which is in good agreement with the experimental results on the water dimer reported by Jahnke *et al.* [11]. Indication of a closing of the ICD channel has previously been observed in the electron-ion-ion coincidence experiments by Jahnke and co-workers as they detected no ICD-induced break-up into a $HO^+ \cdots H_3O^+$ structure.

In order to gain more insight into the relaxation dynamics following the $2a_1$ ionization, additional *ab initio* molecular dynamics simulations of the water dimer were performed. This was necessary as one-dimensional cuts through the potential energy surface, while especially in the present example being remarkably helpful in understanding the underlying mechanism, often provide a biased view on the dynamics of a system. The distinctive feature of the water dimer system compared to higher order clusters is the distinguishability of the two water molecules into the proton donating and proton accepting unit. In the calculations, the focus lies on the photoinduced dynamics of the proton donating unit, as in larger clusters up to liquid water essentially all water units will act partially as hydrogen bond donors. The *ab initio* MD simulations show that upon $2a_1$ inner-valence ionization on the proton donor, the proton transfer takes places for all trajectories and is completed after $\approx$ 8 fs. The impact of said trajectories is summarized in figure 4.8. The figure shows the

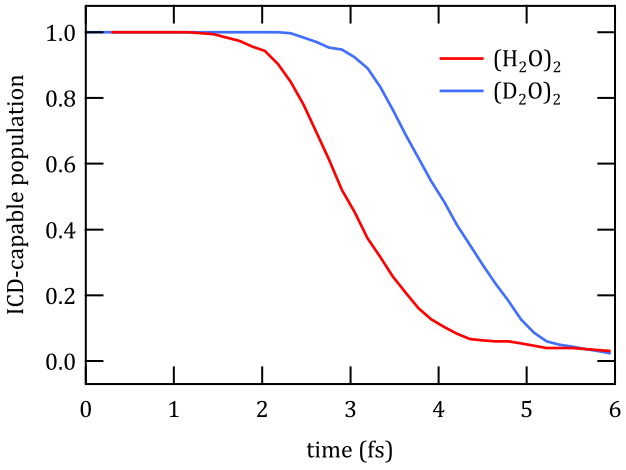

Figure 4.8: Closing of the ICD channel as a function of time after inner-valence ionization for the regular and deuterated water dimer. Fraction of *ab initio* molecular dynamics trajectories in which the ICD process is energetically allowed.

decline of the ICD-capable population as a function of time. This population is defined as the fraction of $2a_1^{-1}$ excited state structures higher in energy than the doubly ionized ICD

final state. The key message of figure 4.8 is that the time available for the system to undergo ICD is restricted to a few femtoseconds. For further discussion this time dependence can be approximated by a step function with a characteristic time t_{open}, which corresponds to the time at which the ICD-capable population dropped to 0.5. For the two traces shown the opening time t_{open} is $\approx$ 2.9 fs for regular and $\approx$ 4.0 fs for deuterated water dimers. These theoretical results can immediately be related to the isotope effect observed in the experimental ICD efficiencies. In deuterated water clusters the ICD channel stays open over an extended time, thereby significantly enhancing the efficiency of decay process.

Combining the experimental ICD efficiencies with the calculated proton transfer kinetics an estimate of the ICD lifetime can be made. In this approach the smallest measured cluster size, with on average five water molecules per cluster, is compared to the calculations of the water dimer. Assuming that the ICD process can be described by an exponential law with a characteristic lifetime τ_{ICD} and the opening time t_{open}, the ICD efficiency is related to these quantities by:

$$\alpha_{\text{ICD}} = 1 - \exp\Big(- t_{\text{open}} / \tau_{\text{ICD}} \Big). \tag{4.6}$$

The experimental efficiency α_{ICD} of the smallest H_2O clusters containing about five water molecules per cluster is between 0.05 to 0.22. With the opening time $t_{\text{open}} = 2.9$ fs the resulting ICD lifetime τ_{ICD} is about 57 to 12 fs. This ICD lifetime should not depend on the isotopic substitution as the decay process is of purely electronic nature. Therefore, when using the ICD lifetime evaluated from the H_2O clusters together with the elongated opening time $t_{\text{open}} = 4.0$ fs for deuterated water the ICD efficiency according to eq. 4.6 is $\approx$ 1.35 times larger. This increase in efficiency is in the same range, although somewhat larger, than the measured ICD enhancement for the deuterated cluster shown in figure 4.5(c) with $\langle N \rangle = 60-80$. For said deuterated clusters the enhancement factor is between 1.18 and 1.27, depending on the applied background correction. Given the simplicity of this estimation and the fact that the ICD rate depends on the geometry of the system, which most likely differs significantly between dimers and clusters of $\langle N \rangle = 60-80$ units, the enhancement factors match quite well.

Additionally, the ICD rates were directly estimated from the equilibrium geometry of the water dimer using the Fano-CI theory. This theory allows the calculations of decay widths and rates of resonance transitions, such as Auger decay or ICD, at relatively low computational costs. A comprehensive introduction into the Fano-CI theory is given in reference [111] and a brief description of the calculations for water clusters is given in the computational methods section of reference [105] and its respective supporting information. Assuming the water dimer only has one singlet and one triplet final state accessible for the decay, an ICD lifetime of 72 and 131 fs was obtained for the donor and acceptor water molecules, respectively. These values are compatible with the experimental values of 150 ± 50 fs reported for ICD in the isoelectronic neon dimer [89]. From these considerations, an estimated lifetime in small water clusters can be extrapolated under the idealized assumption that each water molecule forms two donor and two acceptor bonds. The summation of the respective decay rates results in a total ICD lifetime of about 23 fs. Although this is a very simple estimate, the value is in good agreement with the ICD lifetime of 12-52 fs

for the smallest water clusters extracted from the combination of experiment and molecular dynamics simulation. A further extrapolation from the Fano-CI results indicates that with the availability of additional final states in clusters of increasing size and higher ICD efficiency the ICD lifetime drops to only few fs. [105].

The results unequivocally show that proton transfer strongly competes with the ICD process, thereby limiting it to the first few fs after the initializing inner-valence ionization event. The electronic ICD lifetime is significantly longer than the opening time for the process to occur, which is reflected in a limited efficiency of the ICD process in finite size water clusters. An overview of these competing processes following the $2a_1$ inner-valence ionization in the water dimer is illustrated in figure 4.9. The figure should help to put the results into

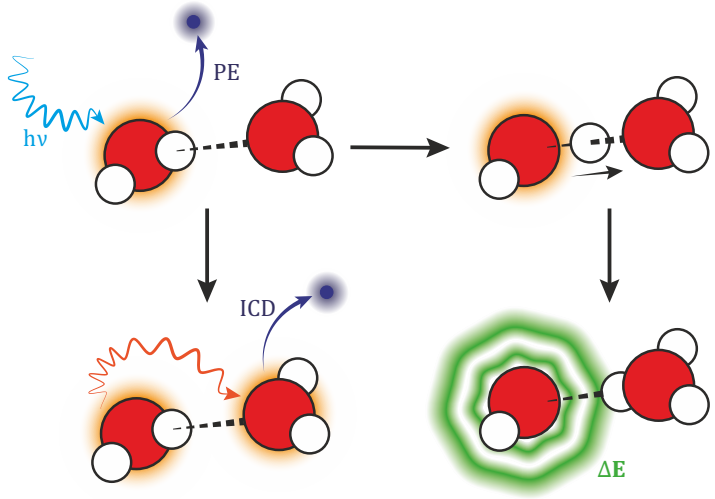

Figure 4.9: Photoinduced processes of the water dimer. The $2a_1$-ionized water dimer energetically relaxes by emission of a secondary electron in the ICD process and at the same time undergoes proton transfer dynamics along the OH coordinate. The nuclear dynamics inhibit the ICD process and dissipation of excess energy is likely achieved by radiationless deexcitation ΔE.

the context of radiation chemistry. In this field, the creation of charged particles on time scales at which ICD and proton transfer are completed is of importance. While the ICD releases the highly reactive ICD electron it also creates two excited cations which will react further with surrounding water molecules to produce OH radicals and H_3O^+. After proton transfer the system remains singly charged with a highly excited OH neutral radical and the charge transferred H_3O^+ species. The excited OH radical will likely dissipate its excess energy by radiationless deexcitaion and dissociate further releasing a hydrogen atom. The oxygen atom will react with surrounding water forming either two OH radicals or hydrogen peroxide. The final products of the two processes are thus similar with the main difference being the highly damaging low energy electron [13] for ICD and the hydrogen atom with low potential for biological damage for the proton transferred structure. Although these considerations are of speculative nature for the ICD process they are reasonable as those products are typically encountered in the radiolysis of water [112]. The results indicate that

small strongly hydrogen-bonded systems are less susceptible to damage from autoionization products after irradiation than previously thought.

In the following paragraphs, the cluster size dependence of the ICD efficiency shown in figure 4.6 will be addressed. As already pointed out the graph shows an increase of the ICD efficiency from 0.05 – 0.2 to 0.4 – 0.5 with decreasing values of $\langle N \rangle^{-1/3}$ i.e., with increasing cluster size. This behavior can be explained by the combined effect of several factors:
The experiments of Barth *et al.* have shown that with increasing cluster size, electron polarization effects lead to a shift of the excited state towards lower binding energy [59]. This shift is larger for doubly ionized molecules and results in an increased energy difference between singly and doubly ionized states [113]. In the present case a greater energy difference between the singly and doubly charged excited states stretches the opening time t_{open} of the autoionization channel and additionally offers more doubly charged states to decay into. Consequently the ICD lifetime τ_{ICD} decreases. To substantiate this claim, the potential curves of the singly and doubly ionized water dimer previously shown in figure 4.7 were embedded in a dielectric continuum approximately mimicking a larger water aggregate such as liquid water. The resulting curves are depicted in figure 4.10. Here the solid

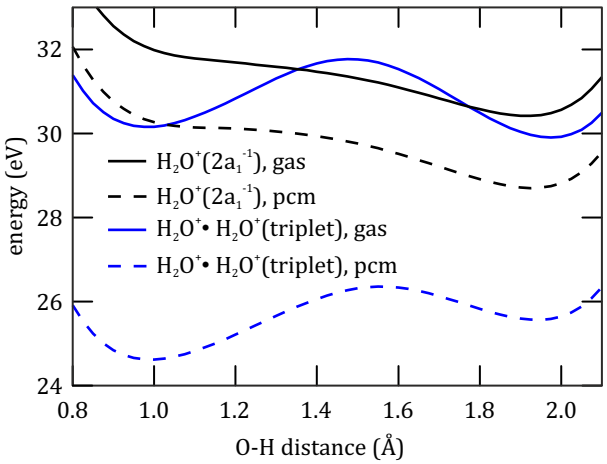

Figure 4.10: Calculated potential curves are shown for a gas phase dimer (solid lines) and for the same dimer embedded in a polarizable continuum (dashed lines). The blue lines depict the lowest doubly ionized triplet state, while the black lines depict the $2a_1$ singly ionized state.

lines correspond to the 1h inner valence state (black) and 1h1h triplet final state (blue) of the free dimer in the gas phase. The dashed curves correspond to the same 1h and 1h1h states in the polarizable continuum model. Clearly, the inital and final state curves are qualitatively similar to the gas phase, except both curves are shifted to lower energies, as the solvent effectively stabilizes the positive charges. The figure undoubtly shows the degree of stabilization is more pronounced for the doubly charged final state, which ultimately results in ICD electrons with higher kinetic energy. It should be noted that these results suggest that the ICD channel never closes in liquid water, thus implying an ICD efficiency of unity. However, the underlying model is rather crude and experimental validation is required. A

detailed description of the computations and a critical discussion of the polarizable continuum model is presented in the supplementary material of ref. [105].
Nonetheless, the widening of the energy gap between the ICD initial and final states is reflected in the experimental data. Figure 4.11 displays the ICD electron distribution for mean cluster sizes 5 to 241 water molecules as a function of kinetic energy. The spectra were

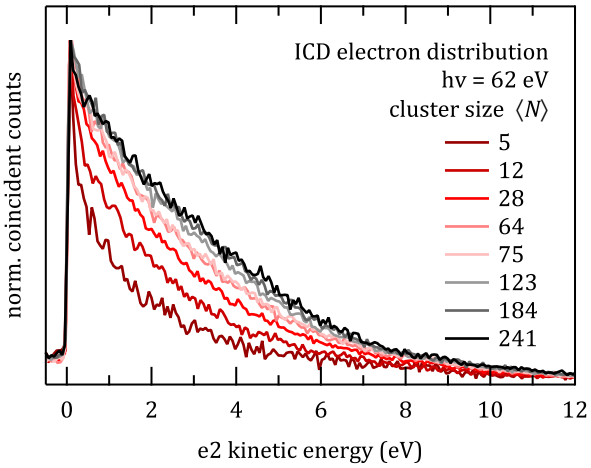

Figure 4.11: Energy distribution of ICD electrons. Experimental data for all mean cluster sizes measured, normalized to the same height and without background subtraction. Coincident counts were summed up between 26 and 35 eV photoelectron kinetic energy corresponding to the $2a_1$ photoline at 62 eV photon energy.

obtained by integrating the coincident events $P(E_{\mathrm{ph}}, E_{\mathrm{ICD}})$ over E_{ph} and for better comparison all traces were normalized to maximum intensity. For the smallest clusters of about five molecules the ICD electron distribution is very narrow with a width of approximately 2 eV. This situation strongly resembles the energetics presented in figure 4.7 and the coincident electron spectra of the water dimer by Jahnke *et al.* [11]. With growing cluster size higher kinetic energies of the ICD electrons are observed, indicating an increase of the gap between the $2a_1$-ionized and the lowest doubly ionized states. From the polarizable continuum model a bulk limit of approximately 6.5 eV for said gap could be estimated which is in reasonable agreement with the trend observed in figure 4.11. Given these theoretical and experimental results the mechanism of increasing polarization screening due to increasing cluster size could be confirmed.
Additionally, two other factors are noteworthy: The increased number of accessible ICD final states is not only due to the energetic shifts, but also due to an increasing number of neighboring water units for water centers in a larger cluster. For instance, theoretical results on rare gas clusters predict a drastic decrease of the ICD lifetime with increasing system size [30, 114]. In water, which can be at most fourfold coordinated, the number of neighboring molecules in the network reaches an average of 3.2 bonds per molecule for water clusters up to 21 molecules [115], which would lessen the effect of the number of neighbors compared to rare gas clusters.
Finally, with increasing system size the hydrogen bond length decreases. Diffraction experiments showed a O-O distance of 2.8 Å between water molecules in bulk water in contrast

to 2.9 Å in the water dimer [116]. This should in principle lead to a faster ICD process due to larger orbital overlap and faster proton transfer as well. Fano-CI calculations for the dimer with reduced O-O distance however did not result in changes in the ICD lifetimes within the error of the method [111].
The combination of these three effects is what has been observed experimentally in the size dependence of the ICD efficiency. However, a quantification of the degree as to which the individual mechanisms influence the efficiency is not possible at this point and would require further studies.
An intriguing follow-up experiment on ICD in water would be the observation of said process in liquid water. The respective experiments require the combination of the coincident electron detection scheme of a magnetic bottle spectrometer with the liquid microjet [117]. First attempts on this combination have been published in reference [73] and will be further discussed in chapters 5 and 6.

In conclusion, it was unambiguously demonstrated that the efficiency of ICD in water clusters after inner-valence ionization is substantially lower than unity, contrary to the results observed in Ne_N, which is isoelectronic to water. Comprehensive calculations of the water dimer suggest proton transfer dynamics between neighboring water molecules as a competing mechanism, taking place within a few femtoseconds after ionization. This scenario involving nuclear dynamics is supported by experimental results with isotopically substituted water clusters $(D_2O)_N$. Combination of coincident electron spectroscopy and *ab initio* molecular dynamics simulation further allows an estimation of the ICD lifetime in small water clusters, putting it in the range of 12 to 52 fs. Explicit lifetime calculations with the Fano-CI method are consistent with these values. Additionally, size dependent measurements show that the ICD efficiency increases for larger water clusters.

4.1.2 Inner Valence ICD Efficiency in Mixed Clusters

With the first observation of ICD in inner-valence ionized water dimers and medium-sized to larger clusters by Jahnke *et al.* [11] and Mucke *et al.* [12] the non-local autoionization mechanism could be established as a possible source for radiation damage due to the production of slow electrons. These slow electrons are highly reactive and, within a biological environment, lead to the deterioration of organic molecules [13]. In a biological environment, such as human tissue, a variety of molecules is in close proximity to water, as it makes up on average 60 % of the human body [14]. While biologically relevant molecules are typically rather complex, their attractive interaction with the surrounding water is usually dominated by hydrogen bonding with their functional groups. Therefore, a first attempt to estimate the relevance of ICD in aqueous biosystems was performed by Stoychev and co-workers [118] by calculation of a hydrogen-bonded dimer consisting of water and small molecules, mimicking functional groups common to biomolecules. Their selection contained molecules such as formaldehyde, formaldimine, ammonia and hydrogen sulfide, so molecules containing elements C, N, O, and S which make up more than 99 % of the mass of most cells [119]. The results of high precision *ab initio* calculations of the single- and

double-ionization spectra of the respective complexes show that the non-local electronic relaxation process after inner-valence ionization is possible in all systems.
In the following section, the theoretical results for the water-formaldehyde dimer will briefly be summarized [118]. This theoretical investigation has no direct connection to this thesis. However, it suggested the binary system of water and formaldehyde ($H_2O\cdots HCHO$) as a viable example for experiments on inner valence ICD in a heteromolecular environment.
The formaldehyde molecule represents the simplest example of a carbonyl group, one of the most abundant functional groups in organic molecules. Stoychev *et al.* used high level *ab initio* methods to optimize the geometry of the dimer and further calculated the respective single and double ionization spectra. These spectra are displayed in figure 4.12. The

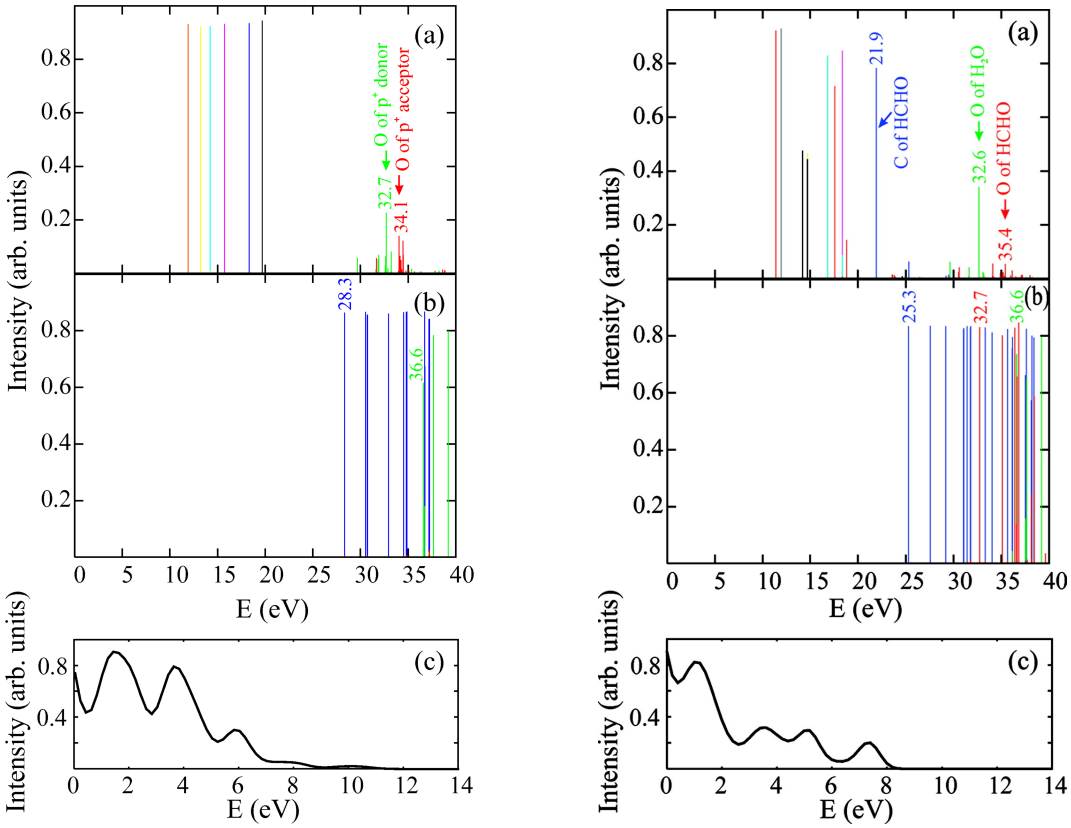

(A) $H_2O\cdots H_2O$ (B) $H_2O\cdots HCHO$

Figure 4.12: (a) and (b) are the computed single and double ionization spectra of $H_2O\cdots H_2O$ and $H_2O\cdots HCHO$ in their equilibrium geometry. (c) shows the kinetig energy distribtion of ICD electrons. The colors in (b) indicate different kind of dicationic states with the 1h1h states depicted in blue and the 2h states in green ($H_2O^{2+}\cdots H_2O$) and red ($H_2O\cdots HCHO^{2+}$). Taken from ref. [118].

figure is divided in two parts: (A) on the left displays the results for the water dimer as an established benchmark and (B) on the right displays the corresponding single and double ionization spectra (a and b) of the water-formaldehyde dimer in its ground state equilibrium geometry; (c) depicts the kinetic energy spectrum of the secondary electron. The situation in the water dimer (A) is the same as discussed in detail in section 4.1.1 but in this case different *ab initio* methods were used without incorporating nuclear dynamics. In the single ionization spectrum (a) the green and red lines correspond to the $2a_1$ inner valence state of O 2*s*

character at around 32 eV. The blue lines in the double ionization spectrum (b) were assigned to dicationic states of 1h1h character i.e., the two charges are separated. Noticeably, the first doubly ionized state at 28.3 eV is lower in energy than the inner valence state, hence the ICD channel is open. The ICD electron distribution in (c) is obtained as the energy difference between the singly ionized inner valence states and the 1h1h final states convoluted with a Gaussian function to account for vibrational broadening of the individual lines. Figure 4.12(B) analogously shows the same type of spectra for the water-formaldehyde dimer. The inner valence state is broadened and contains contributions of both molecules' O 2*s*-type orbitals, marked by the green and red arrows. Again, the double ionization spectrum (b) shows that the onset of double ionization is below the singly ionized inner valence states. However, while the majority of dicationic final states are of 1h1h character (blue), one 2h final state with both charges located on the formaldehyde entity is lower than its respective O $2s^{-1}$ state. The electronic relaxation processes after initial inner-valence ionization based on the energetics of the singly and doubly ionized states are summarized in table 4.3. As elaborated in section 4.1.1 for the water dimer, the only accessible electronic relaxation

Table 4.3: Possible inter- and intramolecular decay modes of the inner-valence ionized states of the $H_2O\cdots H_2O$ and $H_2O\cdots HCHO$ dimers. $*$ Process with low probability. IA refers to an intramolecular autoionization process. Taken from ref. [118].

H-bonded system (p-donor$\cdots$p-acceptor)	open relaxation channels p-donor	p-acceptor	products of decay	energy range of emitted e^- (eV)
$H_2O\cdots H_2O$	ICD		H_2O^+/H_2O^+	0-10
		ICD	$H_2O\cdots H_2O^{2+}$	0-11
$H_2O\cdots HCHO$	ICD		$H_2O^+/HCHO^+$	0-8
	ETMD*		$H_2O\cdots HCHO^{2+}$	0
		IA	$H_2O\cdots HCHO^{2+}$	0-4
		ICD	$H_2O^+/HCHO^+$	0-10

process is ICD, which is, however, affected by photoinduced proton transfer dynamics. The process is allowed for both water units in the dimer, the proton-donor and -acceptor. The accessible electronic relaxation channels in the water-formaldehyde dimer are, however, more diverse.

In the hetero-molecular dimer both entities can be distinguished, with the water molecule acting as the proton-donor and formaldehyde the proton acceptor. Ionization of the water unit, analogous to the pure water dimer, allows for the electronic relaxation into the $H_2O^+\cdots HCHO^+$ final state corresponding to the ICD process. Additionally, due to the existence of the $H_2O\cdots HCHO^{2+}$ doubly ionized state electron-transfer mediated decay (ETMD) is also energetically possible, leading to emission of a secondary electron of close to zero eV kinetic energy. This process, however, has a low probability in this system. The processes subsequent to inner-valence ionization of the water unit can be written in short as:

Step 1: inner-valence ionization of the proton donor

$$H_2O\cdots HCHO \xrightarrow{h\nu} H_2O^+(2a_1^{-1})\cdots HCHO + e_{h\nu} \tag{4.7}$$

Step 2.1: intermolecular Coulombic decay (ICD) including the Coulomb explosion

$$H_2O^{+*}\cdots HCHO \longrightarrow H_2O^+\cdots HCHO^+ + e_{ICD} \longrightarrow H_2O^+ + HCHO^+ \tag{4.8}$$

Step 2.2: electron transfer mediated decay (ETMD)

$$H_2O^{+*}\cdots HCHO \longrightarrow H_2O\cdots HCHO^{2+} + e_{\mathrm{ETMD}} \tag{4.9}$$

Upon ionization of the formaldehyde unit the energetics permit ICD as well. In addition another decay channel into the $H_2O\cdots HCHO^{2+}$ final state is accessible. This decay is similar to the local Auger decay after core level ionization. It is therefore denoted as *intramolecular autoionization* (IA). Analogously, the processes initiated by inner-valence ionization of the formaldehyde unit can be summarized in the following equations:

Step 1: inner-valence ionization of the proton acceptor

$$H_2O\cdots HCHO \xrightarrow{h\nu} H_2O\cdots HCHO^+(O\,2s^{-1}) + e_{h\nu} \tag{4.10}$$

Step 2.1: intramolecular autoionization (IA) of the formaldehyde unit

$$H_2O\cdots HCHO^{+*} \longrightarrow H_2O\cdots HCHO^{2+} + e_{\mathrm{IA}} \tag{4.11}$$

Step 2.2: ICD and Coulomb explosion of the dimer

$$H_2O\cdots HCHO^{+*} \longrightarrow H_2O^+\cdots HCHO^+ + e_{\mathrm{ICD}} \longrightarrow H_2O^+ + HCHO^+ \tag{4.12}$$

Stoychev *et al.* suggest that these electronic relaxation processes, specifically the non-local decay phenomena, take place in a biochemical context in which a larger biomolecule is surrounded by water. The electronic decay in this environment would proceed similarly to the investigated dimers, with the exception of the charge separation via Coulomb explosion, rather the local bond would be broken. Any excess energy of the final states can potentially be dissipated to the high number of vibrational states in a system of greater complexity, thus leading to a 'heating' of the system. Further reactions damaging the biochemical system can be induced by the low energy electrons (LEE) and the excited radical cations.
In the following section, experimental results on the binary system of water and formaldehyde will be presented. This investigation is focused on the effect of the carbonyl function on the ICD efficiency, since it is one of the most common functional groups in organic molecules.

Within an experimental beamtime at the BESSY II synchrotron radiation facility, electron-electron coincidence experiments were performed on mixed clusters of water and formaldehyde at the former UE56/2-PGM1 beamline using VUV and soft X-ray radiation. Measurements were performed with the setup consisting of an expansion chamber housing a cluster source and an interaction chamber with the magnetic bottle electron time-of-flight spectrometer described in the methods section 3.5 and references therein. Analogous to the experiments of pure water clusters, the clusters were produced by supersonic expansion. In this case however, the reservoir of the cluster source was filled with a volumetric 1:1 mixture of highly purified water and formaldehyde solution. The reservoir and nozzle of the cluster source were heated to achieve cluster production by expanding the resulting gas mixture into vacuum. A formaldehyde solution typically contains fair amounts of water and very few percent methanol as stabilizer to prevent polymerization and precipitation of paraformaldehyde. Formaldehyde is able to accept at least one hydrogen bond and is in general soluble in water. Therefore, it was speculated that addition of formaldehyde to a surplus of water does not drastically change the condensation behavior upon supersonic expansion and that the cluster size estimation based on the stagnation conditions using the scaling law by Bobbert *et al.* [57] is still applicable, given the inherent uncertainty of the model. The expansion parameters were set to produce clusters of small to medium size, comparable to the pure water clusters presented in section 4.1.1. The expansion parameters are compiled in table 4.4 together with the estimated mean size $\langle N \rangle$ of the cluster ensemble. Also shown is the scaled cluster size $\langle N \rangle^{-1/3}$, which is proportional to the inverse cluster radius, assuming a spherical cluster shape. For the size estimation given in the table, the stagnation pressure p of pure water was used. The vapor pressure of pure formaldehyde ranges between 4378 to 4420 mbar at 20°C [120]. Mixtures of water and formaldehyde, however, exhibit a vapor pressure much closer to the values of pure water. The authors of reference [121] report a vapor pressure of 306 mbar at 70°C for a binary mixtures, which is close to the vapor pressure of 312 mbar for pure water at the same temperature. It was therefore assumed that stagnation pressure of pure water represents a reasonable estimate of the expansion conditions, given the excess of water in the mixtures and the uncertainties inherent to the scaling law.

Table 4.4: Expansion parameters of the cluster source and resulting mean cluster sizes $\langle N \rangle$. All experiments used a conical nozzle with 80 μm smallest diameter and a 15° half opening angle. The stagnation pressure p was derived from the vapour pressure of water at the reservoir temperature T_r. The nozzle temperature T_n was set independently from T_r.

Species	T_r (°C)	p (mbar)	T_n (°C)	$\langle N \rangle$	$\langle N \rangle^{-1/3}$ (Å^{-1})
H_2O/HCHO	77.1	422	144	5	0.579
	99.5	995	144	27	0.332
	109	1380	144	51	0.270
	123	2210	144	123	0.201

For all clusters in the table a set of photoelectron spectra were taken focusing on the outer

valence region, the inner valence region and the O 1*s* core level. The outer valence and core level spectra were used to monitor the production of clusters and to assess the degree of condensation in the cluster beam, whereas the inner valence spectra, specifically the coincident electron spectra, were used to investigate the occurrence of electronic relaxation processes, such as the predicted ICD, ETMD, and IA. Furthermore, in order to investigate the impact of a heteromolecular environment on the accessible autoionization processes the efficiency of the decay was determined. For this purpose the ratio of coincident and non-coincident electron detection rate given by equation 4.4 was determined, as introduced and described in detail for the ICD efficiency in pure water clusters (see section 4.1.1).

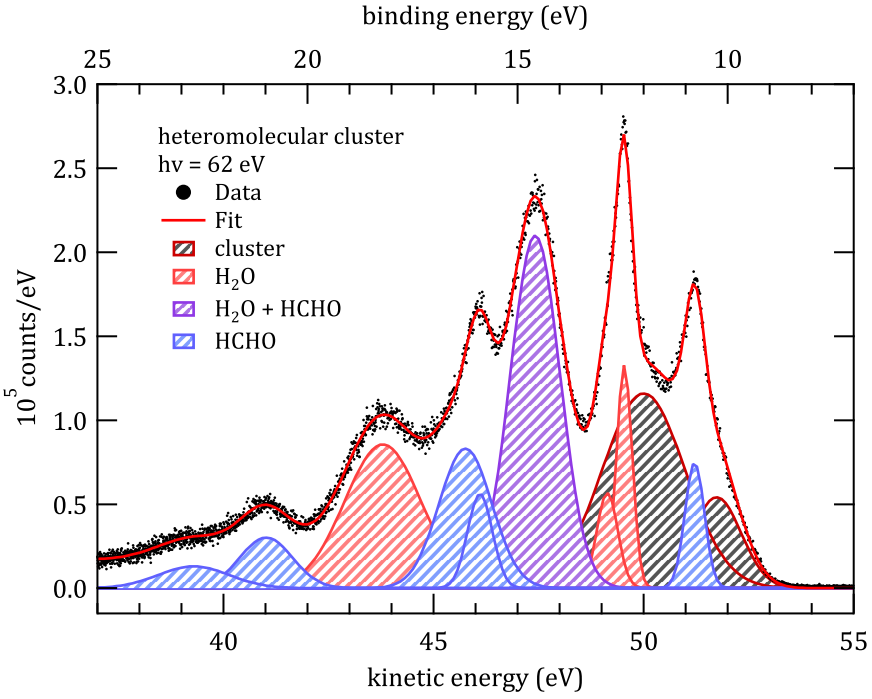

Figure 4.13: Fitted outer valence spectrum of mixed water-formaldehyde clusters. The spectrum was measured at $h\nu = 62$ eV and a nominal cluster size $\langle N \rangle = 27$.

An example of an outer valence spectrum is displayed in figure 4.13 exhibiting the coexistence of water and formaldehyde in the molecular beam. The spectrum was recorded at expansion conditions yielding a mean size $\langle N \rangle$ of about 27 molecules at a photon energy of 62 eV and applying a retardation voltage of -30 V to the drift tube to obtain a better energy resolution. The data was fitted with multiple Gaussians and a step function, modeling the background of inelastically scattered electrons. The number of Gaussian distributions is based on the outer valence states expected for water and for formaldehyde as well as two additional Gaussians describing the respective HOMO of the condensed phase. Based on the gas phase and cluster spectra of water [59, 87] and the respective gas phase spectra of formaldehyde[107, 122], the composition of the cluster beam can be reasonably well described by the applied fit function. In Figure 4.13 the blue shaded area is attributed to the

signal contribution of formaldehyde molecular orbitals (MO) $2b_2$, $5a_1$, $1b_2$ and the inner valence states mostly localized at the carbon atom (in the order of increasing binding energy). The red shaded area can be assigned to the water MO's $1b_1$ and its vibrational component, and $1b_2$. The purple area constitutes the overlapping $3a_1$ of water and $1b_1$ of formaldehyde. The two additional Gaussians shown as black shaded areas are assigned to formaldehyde $2b_2$(c) and water $1b_1$(c). From this fit a relative composition of the cluster beam can be estimated based on the ratio of HOMO signals of the two molecules. These compositions are summarized in table 4.5 for all measured cluster sizes. The data suggests that there is an

Table 4.5: Chemical Composition of the cluster beam.

$\langle N \rangle$	gas phase H_2O : HCHO	cluster H_2O : HCHO
5	8.8 : 1	7.1 : 1
27	2.3 : 1	3.6 : 1
51	6 : 1	3.3 : 1
123	5.4 : 1	2.6 : 1

excess of water molecules in the gas phase and condensed phase of the molecular beam. Therefore the clusters formed in the beam are assumed to resemble the amorphous water clusters discussed in section 4.1.1 with some of the water units replaced by formaldehyde.
As a brief reminder, the parameters required to determine the ICD efficiency are the coincident and non-coincident count rates of the inner valence state ($P(E_{\mathrm{ph}}, E_{\mathrm{ICD}})$ and $p(E_{\mathrm{ph}})$) , the degree of condensation in the cluster beam c and the detection efficiency $\gamma(E_{\mathrm{ICD}})$.
For the detection efficiency $\gamma(E_{\mathrm{ICD}})$ a value of 0.58(4) was used, which was determined for the measurements of pure water clusters under comparable experimental settings within the same beamtime. The stability of these settings was verified by determining of detection efficiency of Ar 2p-Auger coincidences in calibration spectra of Ar gas, measured immediately following the series of water-formaldehyde clusters.
In previous experiments on pure water clusters c was determined by the ratio of cluster HOMO signal to total HOMO signal. However, due to the strong overlap of the water cluster $1b_1$ with the gas phase $2b_2$ of formaldehyde, O $1s$ core level spectra were recorded for this purpose. A core level spectrum is shown in figure 4.14 for a mixed-cluster jet with a mean size $\langle N \rangle = 27$ at $h\nu = 560$ eV and -15 V retarding voltage. Two different fit models were employed consisting of either three gaussians (fig. 4.14(a)) and two gaussians (fig. 4.14(b)) on a step-like background. Figure 4.14(a) considers a distinct gas phase contribution of water and formaldehyde and a strongly overlapping condensed phase peak at lower binding energy, whereas in fig. 4.14(b) the two gas phase contributions strongly overlap as well. While both fits give qualitatively similar results, the residuals suggest a slightly better agreement for fig. 4.14(a). The O 1s binding energy of the gas phase is at 539.9 eV for water and at 539.42 for formaldehyde according to reference [123]. In fig. 4.14(a), the apparent binding energy (top axis) is shifted by about 300 meV, but the splitting between the two peak centers is

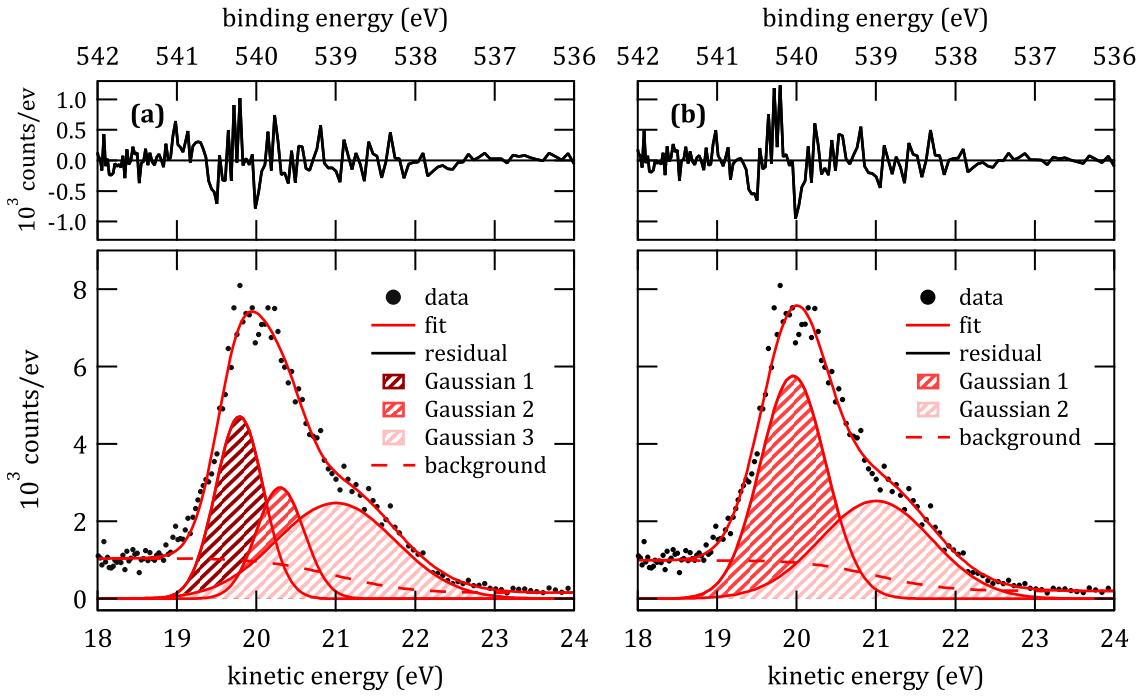

Figure 4.14: Example fit of the O 1s spectra to determine the degree of condensation of the cluster jet, measured at $h\nu = 560$ eV and a nominal cluster size $\langle N \rangle = 27$. In (a) three Gaussians are used to account for the gas phase contribution of H_2O and HCHO, whereas in (b) two Gaussians are used.

well reproduced by the fit. The energy splitting between the assigned gas phase and cluster components is comparable to the values given for pure water clusters (1.3 eV) in ref. [124]. Both fitting procedures were performed for the O 1*s* spectra of all measured cluster sizes ranging from 5 to 123 monomer units per cluster and were used to determine the degree of condensation c according to eq. 4.13:

$$c = \frac{p(E_{\mathrm{O}\,1s})_{cluster}}{p(E_{\mathrm{O}\,1s})_{total}}, \tag{4.13}$$

where $p(E_{\mathrm{O}\,1s})_{cluster}$ are the O 1*s* photoelectrons of the cluster and $p(E_{\mathrm{O}\,1s})_{total}$ the total O 1*s* photoelectrons of the cluster and gas phase. The resulting degrees of condensation are displayed in figure 4.15 as a function of the mean cluster size $\langle N \rangle$ (top) and $\langle N \rangle^{-1/3}$ (bottom). The solid and open symbols are the results of the fits employing three and two Gaussians, respectively. Both fits give similar estimates for c except for the smallest clusters of $\langle N \rangle \approx 5$ molecules. For the calculation of the ICD efficiency (eq. 4.4) the fit results employing three gaussians are used, due to the slightly higher fit quality and their reasonable agreement with the gas phase references. The results using two gaussians are considered as contribution to the uncertainties of the ICD efficiency.

Analogous to the procedures outlined in section 4.1.1 and reference [92], the coincident and non-coincident count rates ($P(E_{\mathrm{ph}}, E_{\mathrm{ICD}})$ and $p(E_{\mathrm{ph}})$) were determined from photoelectron spectra of the inner valence state. Example inner valence spectra are displayed in fig. 4.16.

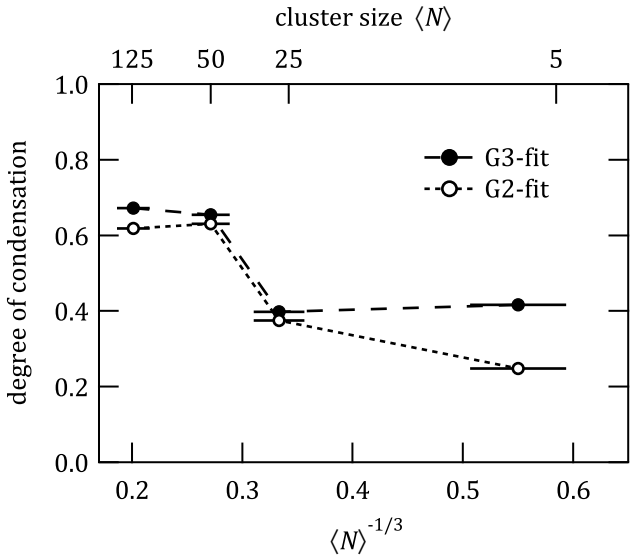

Figure 4.15: The degree of condensation c is shown as a function of mean cluster size $\langle N \rangle$ (top axis) and $\langle N \rangle^{-1/3}$ (top axis). The solid symbols are derived from the fit shown in fig. 4.14(a) and open symbols correspond to fig. 4.14(b).

Here the inner valence photoelectron signal (a) and coincident signal integrated over an interval of 0 – 5 eV for e_{ICD} (b) are shown for mixed clusters with $\langle N \rangle = 27$ recorded at $h\nu = 62$ eV and + 3.4 V acceleration voltage. The states in this energy region are primarily composed of the O 2s orbitals of water and formaldehyde, respectively. A Shirley-type background was subtracted from the data as established in section 4.1.1. The solid trace in (b) represents a Gaussian fit to the coincident signal. For a quantitative comparison with the photoelectron data (a) the fit curve is corrected by the detection efficiency γ and the respective degree of condensation c. From the comparison of the coincident and non-coincident data it is immediately obvious that the ICD efficiency in these clusters is much lower than unity.

This procedure has been applied to the different cluster sizes and the resulting ICD efficiencies based on equation 4.4 are displayed in figure 4.17. The results for the mixed clusters are shown as red markers. For direct comparison, the efficiency of pure water clusters of same or similar size is shown in black. The depicted error bars represent the standard deviation due to stochastic errors, taking into account contributions of the peak-background separation and the degree of condensation in the cluster jet. It is immediately seen that the efficiency in mixed water-formaldehyde clusters is drastically lower for clusters of approximately 25 or more molecules. In the case of smaller clusters ($\langle N \rangle \lessapprox 25$) the efficiency appears to be equal to pure water clusters within the error bars. The reason behind the large error bars for small water-formaldehyde clusters is twofold. First, the gas phase contribution of formaldehyde double ionization, specifically the leading peak associated with an intramolecular electronic decay of the excited molecule, overlaps with the lower binding

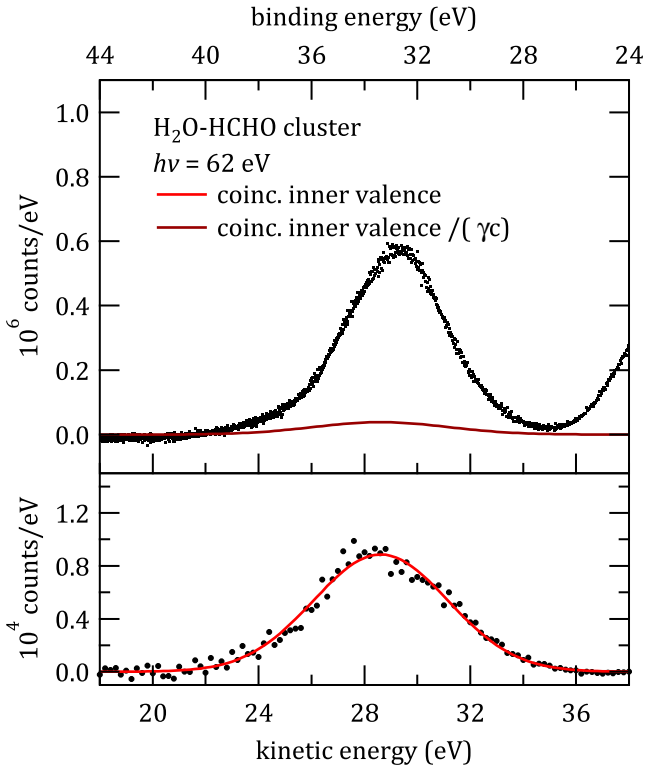

Figure 4.16: Inner valence photoelectron signal used to determine the ICD efficiency. The spectra were measured at $h\nu = 62$ eV and a nominal cluster size $\langle N \rangle = 27$. (a) shows the intensity of photoelectrons $p(e_{h\nu})$ in the region of the O 2*s*-like inner valence states. (b) shows the integral of $P(e_{ICD}, e_{h\nu})$ over an interval of 0 – 5 eV for e_{ICD}. The solid trace in (b) is a fit to the coincident data. For comparison with the undiscriminated data, the curve is multiplied by the inverse of the detection efficiency $\gamma(E_{\mathrm{ICD}})$ and by the inverse degree of condensation c, with values of 0.58(4) and 0.40(3) in this example; the result is shown in (a) (solid trace).

energies of the ICD relevant inner valence region [125]. This overlap complicates the determination of the background. Second, the two applied fit models for the degree of condensation c (see fig. 4.15) gave varying results. It is reasonable to assume that the total error of the efficiency is greater when considering sources of systematic errors which would be common to all data points. As shown for pure water clusters, the separation of non-coincident and coincident inner valence signal from the background considerably affects the experimental error of the efficiency (see section 4.1.1). Another source of systematic error is the estimation of the cluster size with the scaling law of Bobbert *et al.*[57], assuming similar cluster formation as in pure water clusters. It is possible that the formation of clusters is less efficient in the binary mixture and the presented sizes are slightly overestimated.

Similar to what was seen before for pure water clusters, in which ultra fast proton transfer limits the efficiency of the ICD process, these mixed cluster results also suggest a competing relaxation mechanism after inner-valence ionization. With regard to what was suggested by the theoretical results on water clusters, there are several scenarios to consider. First, the influence of proton transfer might be more prominent for mixed clusters. Let us assume the

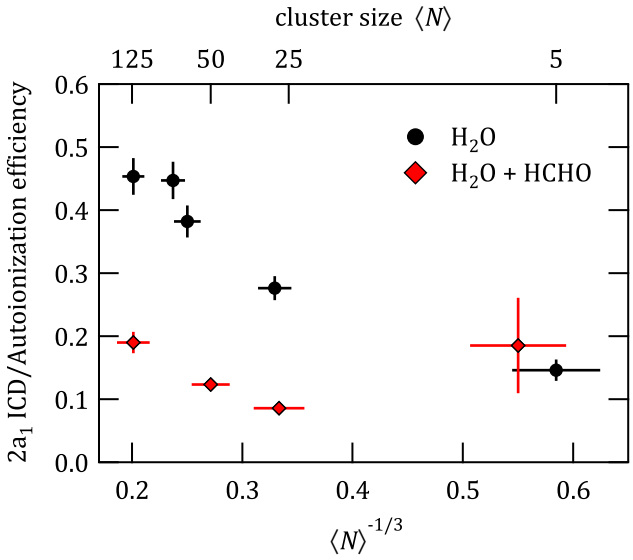

Figure 4.17: Comparison of ICD efficiencies in pure water and water-formaldehyde clusters as a function of cluster size $\langle N \rangle$ (top) and $\langle N \rangle^{-1/3}$ (bottom) , measured at $h\nu = 62$ eV. Error bars shown here represent the standard deviation due to stochastic errors.

dimer situation presented by Stoychev *et al.*[118] with water as proton donor and formaldehyde as proton acceptor. Undergoing proton transfer after inner-valence ionization might drastically change the electronic structure, potentially leading to a geometry in which ICD is not allowed even for small geometry changes. Previous theoretical studies investigated the molecular interactions of small formaldehyde-water clusters in order to describe the solvent effects on the carbonyl group in an aqueous environment. The structures of lowest energy indicated the hydrogen bonding between water (donor) and formaldehyde (acceptor) as the favorable interaction between the two [126, 127]. Similar hydrogen bonding behavior was found in calculations on microsolvated clusters of formic acid [128]. Experimental results are limited to matrix isolation IR spectroscopic measurements on the water-formaldehyde dimer, but also these investigations corroborate the hydrogen bonding interaction between the two molecules [129, 130]. Therefore, it is likely that changes in the hydrogen bonding interaction, and suspectedly proton transfer dynamics, play a crucial role in the lower autoionization efficiency. Second, the influence of other deexcitation processes might be more pronounced. As was seen in the calculated potential energy curves for the water dimer, the ICD relevant states were embedded in a high number of states. While the formaldehyde molecule is only slightly bigger in size, the complexity of the potential energy curves for the mixed system might be noticeably increased. The extended gas phase spectrum of formaldehyde already shows a significant number of peaks [125]. A third mechanism to influence the ICD efficiency in mixed clusters might be fluorescence. For example, in gaseous formaldehyde fluorescence as well as photodissociation has been observed after photoexcitation with VUV light[131]. Such a radiative decay is unlikely to affect the autoionization, as both processes take place at different time-scales, but nevertheless it should be mentioned for completeness.

So, what is the consequence of this investigation? In principle, inner valence ICD, which is acknowledged as a source of radiation damage, could be experimentally observed in the binary model system of water and formaldehyde, mimicking the interaction of water with the carbonyl groups of larger organic molecules in a heterogeneous environment. While this emphasizes the universality of this non-local electronic relaxation process, the decay efficiency is decisive for its relevance in radiation damage. A comparison of the ICD efficiency in mixed clusters with that of pure water clusters showed a significant decrease of the efficiency in the binary system. As hydrogen bonding is the favorable interaction between the two molecules, the decay efficiency is likely limited by proton transfer dynamics induced by the initial photoionization. In pure water it was shown, that moderate geometry changes along the proton transfer coordinate of the system lead to the ICD channel being energetically closed (see section 4.1.1). For the water-carbonyl interaction seemingly even smaller geometry changes might prohibit this process. In that sense, the proton transfer potentially averts the production of highly reactive low energy electrons in the immediate vicinity of a carbonyl containing compound.

4.2 Proton Transfer Mediated Charge Separation

The content of the following section is part of a collaboration with the research group of Olle Björneholm at the Uppsala University, Sweden. As such, the presented results are part of the recently published Doctoral thesis of Clara-Magdalena Saak [132].
The research compiled in section 4.2.1 was initiated by the supervisor of this thesis, Uwe Hergenhahn, and me, and the respective experiments were conducted with the support of Clara-Magdalena Saak. Also the data analysis was performed by myself.
As for the results of section 4.2.2, the scientific project was initiated, proposed, designed and conducted by Clara-Magdalena Saak and myself based on our mutual interest in physical chemistry, specifically intermolecular interactions in water and photoelectron spectroscopy. The data analysis shown here was carried out by Clara-Magdalena Saak and the results were interpreted in close colaboration between the two of us.
While in Clara-Magdalena Saak's thesis [132] the overall focus lies on the reaction of the hydrogen bond network in water towards inorganic ions as well as organic molecules in an atmospheric chemistry context, the work presented in this thesis is motivated by gaining a general understanding of non-local electronic decay phenomena in a molecular environment.

As of now the discussion of non-local autoionization phenomena in hydrogen bonded systems was focused on electronic relaxation processes induced by inner-valence photoionization. In the following sections, the emphasis lies on the accessible electronic decay processes subsequent to core level ionization. Complementary to the previous analysis on ICD after $2a_1$ photoionization of water clusters, in which nuclear dynamics along the hydrogen bond coordinate within the lifetime of the inner-valence excited state could be identified as key result, in this section a particular focus lies on the influence of hydrogen bonding on the decay mechanisms.

Typically, in an atomic or molecular system the resonant photoexcitation or photoionization of a core level will leave the system in a highly excited state, which can either relax radiatively[4] or dissipate its excess energy by emission of a high energy electron in a *core-valence-valence* (KVV) Auger decay [5]. The Auger process is very well established [133], but was up until the 60s/70s mostly investigated in surface science as a tool to identify the elemental composition of a material's surface [134]. With the advent of high resolution electron analysers and the ESCA technique [23], molecular species could be investigated, exploiting the sensitivity of Auger spectra to the individual chemical environment. Among the first molecules gas phase water was studied [135, 136]. Figure 4.18 exemplarily shows the Auger electron spectrum (AES) of water vapor, specifically the gaseous phase surrounding a water liquid jet, as a red trace. The AES of the liquid jet vapor phase is congruous with the molecular spectra reported by the groups of Moddemann [135] and Siegbahn [136]. The leading

[4] Radiative decay by release of a X-ray photon is a process of low probability for lighter elements with atomic number $Z < 40$ [3].

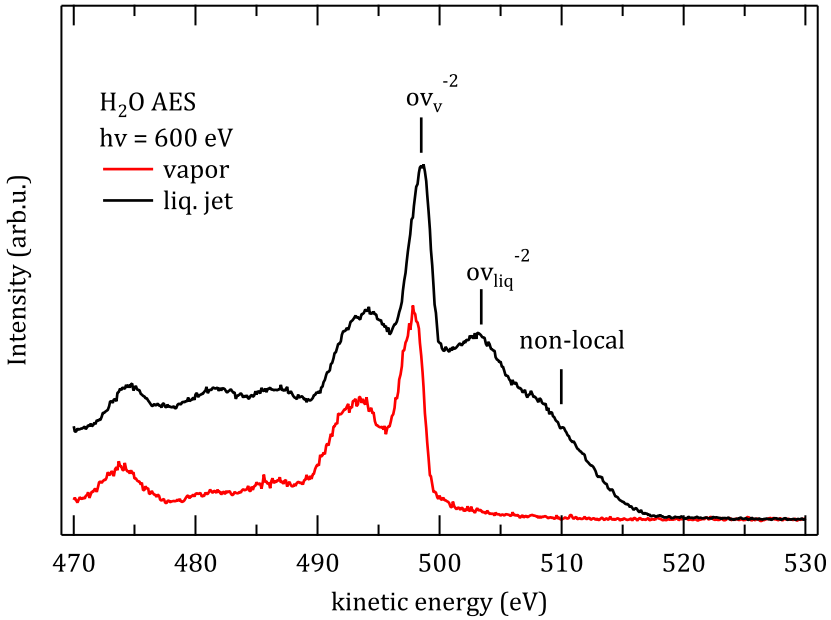

Figure 4.18: Auger electron spectra (AES) of water vapor and a water liquid jet.

peak in the molecular AES corresponds to decay of the O 1s core hole by filling the vacancy with an outer valence electron and concerted emission of a second outer valence electron. The label ov_v^{-2} denotes the molecular final states of $1b_1^{-2}$ and $3a_1^{-1}1b_1^{-1}$ configuration, which are close in energy. The signatures of lower kinetic energy amount to the progression of two-hole final states comprised by the combination of outer and inner valence orbitals of the water molecule i.e., $1b_1$, $3a_1$, $1b_2$ and $2a_1$.

In addition, fig. 4.18 shows the condensed phase AES of a water liquid jet as black trace. Upon comparing the two traces a strong vapor phase contribution is obvious in the liquid jet spectrum[5]. The leading peak of the liquid phase is labeled as ov_{liq}^{-2} and it is well separated from the molecular high energy peak by about 4.8 eV kinetic energy which is in line with the observations in references [124] and [138]. The shift and significant broadening of the liquid phase peak is a result of polarization screening [139], which describes the stabilization of the final state hole by the electron density of the surrounding molecules. The liquid water AES displays an additional shoulder at the high energy flank of the ov_{liq}^{-2} peak. In a carefully conducted comparison of the AES of molecular water and different sized water clusters Öhrwall and co-workers could assign this additional intensity to the emergence of delocalized doubly charged final states in the condensed phase [124]. These delocalized contributions to the condensed phase AES were more thoroughly investigated by Thürmer *et al.* for liquid water by experimental and theoretical methods [18]. The authors measured the AES of a liquid jet containing normal water (H_2O) and heavy water (D_2O) and could

[5]The spectra were taken at the UE52-SGM beamline [137] employing the SOL^3 end station [76], in which the interaction region of the liquid jet with synchrotron radiation is approximately 15 cm behind the beamline focus. This geometry results in a much bigger spot size, much larger than the $\sim$ 30 μm size of the liquid jet. The photoelectron spectra recorded under these conditions naturally exhibit a rather noticeable vapor phase contribution.

identify a distinct isotope effect in the high energy flank of the AES associated with delocalized final states. Due to the isotope effect Thürmer and co-workers concluded that the Auger electron distribution in liquid water is affected by nuclear dynamics taking place within the short lifetime of the O 1s core-hole of $\sim$ 4 fs [140]. This interpretation was corroborated by calculations of the dynamics following core-ionization of a water dimer. These calculations unambiguously identified the O-H distance as the crucial coordinate of the potential energy surface of said dynamics. As a descriptive example, a replication of the experimental results in reference [18] is shown in figure 4.19. The Figure displays the AES of liquid water

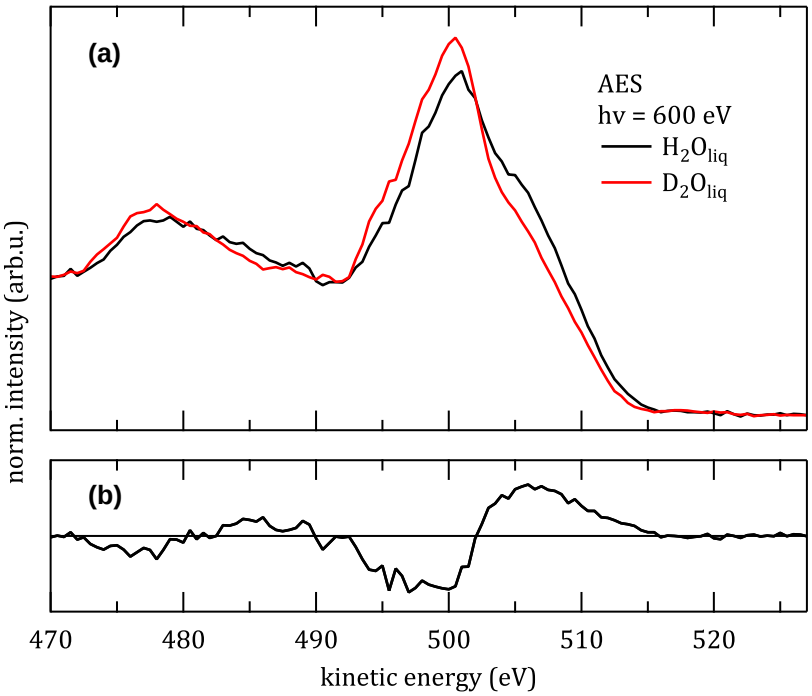

Figure 4.19: (a) exemplarily shows the isotope effect in the AES of liquid H_2O and D_2O. (b) displays the (H_2O - D_2O) difference spectrum.

after carefully subtracting the gas phase contribution. The black solid trace corresponds to normal water H_2O and the red trace is the spectrum of heavy water D_2O at identical conditions. At first glance, there is a noticeable difference between the two spectra visible in the leading peak of the AES. In the spectrum of normal water the high kinetic energy shoulder, associated with delocalized final states, exhibits a higher intensity and in deuterated water the most intense peak around 500 eV kinetic energy has higher intensity than normal water. This isotope effect is more apparent in the black solid trace in (b), which is obtained as the difference of the two spectra ($H_2O - D_2O$).

In reference [18] the character of the dicationic final states resulting in the autoionization process were thoroughly investigated, identifying two distinct mechanisms contributing to the spectral signature. The first process is the Auger decay. The second process is the related intermolecular Coulombic decay (ICD) in which the initial core vacancy is filled by a local valence electron but the energy gained by this transition is transferred to a neighboring molecule from where a second valence electron is emitted. Consequently the two processes

lead to two different dicationic final states:

Auger decay following core ionization

$$H_2O\cdots H_2O \xrightarrow{h\nu} H_2O^{+*}\cdots H_2O + e_{h\nu} \longrightarrow H_2O^{2+}\cdots H_2O + e_{\text{Auger}} \tag{4.14}$$

Intermolecular Coulombic decay following core ionization

$$H_2O\cdots H_2O \xrightarrow{h\nu} H_2O^{+*}\cdots H_2O + e_{h\nu} \longrightarrow H_2O^{+}\cdots H_2O^{+} + e_{\text{ICD}} \tag{4.15}$$

The equations 4.14 and 4.15 illustrate the X-ray induced processes in a water dimer at energies capable to photoionize a core electron. The water dimer is used here as a proxy for the condensed phase encountered in the liquid jet experiments, since the dimer is the smallest unit of interacting molecules. Evidently, in the two equations the two positive charges in the final states are differently distributed. While the vacancies are localized on the initially ionized site in the case of the Auger decay, for ICD the holes are delocalized over two separate water units. This charge separation leads to the emission of secondary electrons of higher excess energy i.e., the non-local ICD process contributes to the intensity of the high kinetic energy flank of the AES.
Unlike in the case of ICD after inner-valence ionization, in which the decay pathway is open if the binding energy of the inner valence state exceeds the double ionization threshold, the non-local ICD process is always open in the case of core level excitation or ionization, but is in direct competition to the local Auger decay. Since the ICD process requires two water molecules in close proximity, the Auger decay supposedly is the dominating decay mechanism, although the branching ratio between the two is not clear. However, the relative probabilities of the decay processes should not depend on the isotopic substitution. The fact that the two liquid jet spectra of normal and heavy water show a significant isotope effect under otherwise identical experimental conditions suggest that significant nuclear dynamics are taking place within the short life time of the core-excited state.
A detailed computational investigation of the excited state dynamics of the water dimer, specifically along the O-H bond distance, was able to describe the isotope effect. The essence of these investigations is summarized in the energy diagram in figure 4.20. Shown here is a schematic potential energy curve of the water dimer ground state, excited state and the lowest final states of the Auger and ICD process as a function of the O-H distance i.e., the hydrogen bond coordinate. In addition the wave packets of the ground state molecular structure are shown in red for the normal (protonated) water and blue for the heavy (deuterated) water dimer. In the experiment, this wave packet is vertically promoted into the core-excited state by absorption of a photon $h\nu$ indicated by the green arrow. The nature of the excited state is defined by having one hole in the O 1s level ($1h_{O\,1s}$). Unlike for the non-interacting water molecule in the gas phase, where the $O\,1s^{-1}$ state is not dissociative [140], in the condensed phase the same state is in fact dissociative i.e., the wave packet will follow the slope of the potential curve. The $1h_{O\,1s}$ excited state can relax via Auger decay or ICD into the

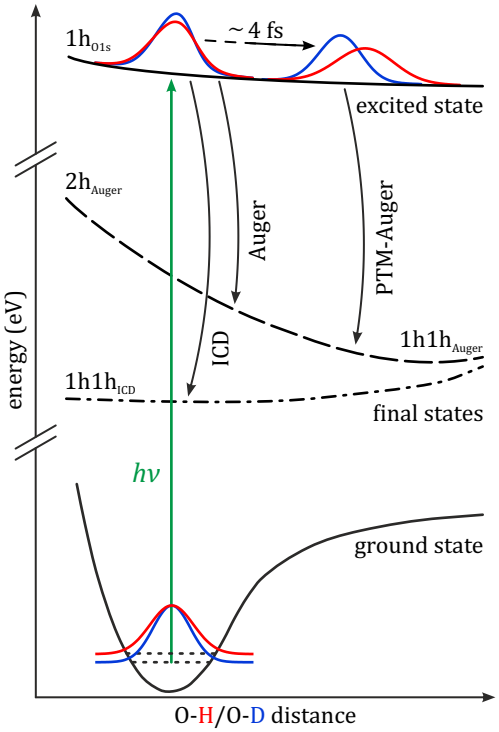

Figure 4.20: Energy diagram of the PTM-CS process adapted from ref. [18]

doubly charged final states $2h_{Auger}$ or $1h1h_{ICD}$, which could be distinguished by analysing the hole locations of all calculated final states[6]. From the transitions indicated with black arrows labeled "ICD" and "Auger" it is immediately clear that around the ground state geometry of the water dimer the excess energy of the emitted Auger electron is lower than that of the ICD electron — ~500 and 510 eV, respectively. However, a significant proportion of the excited state wave packet will travel along the O-H bond coordinate within the O 1s core hole lifetime of ~4 fs before the system relaxes. As clearly visible, the doubly charged final states are also dependent of the O-H bond coordinate. While the potential curve of the Auger final states shows a steep dissociative slope the ICD final states are relatively flat. With increasing O-H distance the final states become closer in energy. Transitions occuring at greater O-H distance will result in secondary electrons of higher kinetic energy i.e., higher signal intensity on the high kinetic energy flank of the AES. Now considering the H_2O and D_2O dimers, statistically the excited state wave packet of the lighter isotope will travel further along the O-H bond coordinate than the heavier analog before it relaxes into the final state, thus leading to the isotope effect in the spectra. The final states at larger O-H distance are of 1h1h character as the positive charges can be separated along the O-H bond. The equations 4.14 and 4.15 can be reformulated to include the photoinduced nuclear dynamics:

Auger decay with nuclear dynamics

$$H_2O\cdots H_2O \xrightarrow{h\nu} HO^*\cdots H^+\cdots H_2O + e_{h\nu} \longrightarrow HO^+\cdots H^+\cdots H_2O + e_{Auger} \qquad (4.16)$$

[6]In the energy diagram only the 2h and 1h1h final states of lowest energy are depicted. For a complete picture it is referred to reference [18] and the corresponding supporting information.

Intermolecular Coulombic decay with nuclear dynamics

$$H_2O\cdots H_2O \xrightarrow{h\nu} HO^*\cdots H^+\cdots H_2O + e_{h\nu} \longrightarrow HO\cdots H^+\cdots H_2O^+ + e_{ICD} \qquad (4.17)$$

The species $HO^*\cdots H^+\cdots H_2O$ formed upon photoionization is a Zundel-like cationic excited state [141] in which the positive charge can be considered as located on the proton taking part in a hydrogen bond between the two water molecules. As the proton moves along the O-H bond coordinate it separates the positive charge from its molecular origin. The isotope effect observed in the O 1s autoionization spectrum of liquid water was therefore termed *proton-transfer mediated charge separation* (PTM-CS). The name suggests that PTM-CS is a general process to be observed in a hydrogen bonded network in which a proton transfer can take place. This was further underpinned in two follow-up publications focusing on aqueous solutions of hydrogen peroxide [142] and ammonium salts [113] as well as in theoretical investigations of the water pentamer [99]. Additionally, in two recent publications describing the systematic investigation of the Auger spectra of different solvent clusters of water, methanol and dimethyl ether, and on liquid methanol, it was unambiguously demonstrated that the PTM-CS is a signature exclusive to hydrogen bonded systems [143, 144].
As the overarching theme of this work is the experimental investigation of non-local autoionization processes in a hydrogen bonded environment, specifically in water, it should be clarified how to fit the PTM-CS process into the collection of related electronic decay mechanisms, namely the Auger decay, ICD and ETMD. As previously mentioned, in the case of core level photoionization the relaxation via Auger decay, ICD and also ETMD is energetically feasible, therefore all processes can be expected to contribute to the AES. Since the Auger decay is a local decay mechanism which only involves one molecular site it is the process with the largest decay amplitude i.e., the highest probability. The other two processes are non-local, involving two or three weakly interacting molecular sites in close proximity. It was shown that the non-local processes ICD and ETMD have comparable decay probability [99]. The PTM-CS process, which essentially describes the influence of ultra fast nuclear dynamics on the charge separation on the final state energy, is predominantly dependent on the Auger final states, as the other two process are already of non-local character and their potential energy curves are relatively flat. In other words, the PTM-CS is a property of the hydrogen bond network in the core-excited state, which leads to an isotope effect in the Auger decay.

In the work compiled in this thesis, the generality of the PTM-CS process was further verified and tested for its possibility to be used as a spectroscopic tool to investigate hydrogen bonding in different systems. For this purpose two different sets of experiments were performed. In the following sections 4.2.1 and 4.2.2 these experiments are briefly introduced followed by a comprehensive discussion of the results.

4.2.1 Proton Transfer Mediated Charge Separation in Amorphous Ice

Water in its metastable glassy phase is likely the most prevalent form of water in the universe e.g., in cosmic dust particles and bulk material of comets [145]. This form of water is also called *amorphous solid water* (ASW) as it lacks long range order, resembling the structure of liquid water [146]. In laboratory experiments ASW can be formed by vapor deposition onto a substrate at $T < 130\,\mathrm{K}$. The thereby produced amorphous ice layers are often used as a model for liquid and supercooled liquid water in the controlled environment of a surface science experiment [147]. These experiments cover a wide rang of scientific subjects, for example fundamental properties and transitions in the complex phase diagram of water [148, 149]. Further examples are reactions of molecules adsorbed on ice surfaces [145, 150, 151], and solvation dynamics of charged particles in water, respectively, at water/metal and water/metal oxide interfaces [152, 153]. In ASW the degrees of freedom of the water molecules, specifically the position of the oxygen atoms, are reduced compared to liquid water due to the cryogenic temperatures, however the hydrogen bond network is regarded as intact. The strong similarities between liquid water and its proxy suggest that photoinduced processes connected to the hydrogen bond network are also in place in ASW. Therefore, it was attempted to investigate the AES of amorphous water ice surfaces and compare the results with the recent findings on PTM-CS in the AES of liquid water.

The experiments were carried out at the BESSY II synchroton radiation facility using the CoESCA endstation, which was described in section 3.5, at the UE52-PGM soft X-ray beamline. The setup hosts two ArTOF electron analyzers, of which predominantly the Scienta ArTOF2-EW analyzer with an angular acceptance of 56° was used to ensure a high electron collection efficiency. The beamtimes took place during multi bunch operation mode of the BESSY II storage ring and the pulsed light required for the operation of the ArTOF spectrometer was produced using the pulse picking by resonant excitation (PPRE) scheme, yielding an effective quasi-single bunch operation mode with a repetition rate of 1.25 MHz [79]. This procedure strongly reduces the overall available photon flux to about 0.5 % of the multi bunch flux, which is beneficial for electron spectroscopic experiments on radiation sensitive or insulating materials like ice films.
Ice samples were prepared on a Au(111) single crystal using the dosing system specifically set up for the experiments at the CoESCA end station. Initially, the Au crystal was cleaned by several cycles of Ar sputtering and annealing until no carbon could be observed in the core level spectra. The Au sample served as a well defined substrate, which could be temperature controlled using a liquid nitrogen cryostat. Subsequently, the ice films were produced with established surface science methods described in detail in [154] and [155] and references therein. Briefly, the crystal was cooled to about 98 K and H_2O/D_2O, which was previously purified in freeze-pump-thaw cycles, was dosed with the pinhole doser directly onto the single crystal for 5 min. The pressure in the reservoir of the dosing system was stabilized to about 3 mbar. This procedure resulted in thick ice films, which was verified by the absence of an Au 4f photoelectron signal from the substrate. The actual coverage of the produced films could not be determined, as the geometry of the chamber and the time

alloted for the experiments did not allow for a characterization by temperature controlled desorption (TPD) [156]. However, the preparation procedure was unchanged for the entirety of the project giving consistent photoelectron and Auger electron spectra, therefore it was concluded that the prepared ice layers were sufficiently thick to decouple the ice surface from the metal substrate.

An essential difference between photoelectron spectroscopic experiments on ASW and the ones performed on the liquid jet is that the ice layers form a stationary sample in contrast to the steadily replenished surface of the jet. Water, or ice, is an insulator and sample charging has been noted very early in its investigation by photoelectron spectroscopy [157, 158]. It leads to a reduction in electron kinetic energy, or an increase in apparent binding energy, due to the buildup of positive charge at the irradiated surface. This is consistent with findings reported by Moon and Kang [159]. In their experiments on ASW and crystalline ice surfaces they observed the production of long-lived (minutes to hours) H_3O^+ complexes as the product of the irradiation with UV light. In the experiments conducted at the CoESCA endstation the effect of sample charging could be observed in the core level spectra. With the efficient data acquisition by the ArTOF it was possible to quantify the buildup of the surface charge as a function of time. For this purpose the O 1s spectra of ASW were recorded in fixed mode before and after each series of Auger spectra. In all cases, a single O 1s photoline was observed. From these measurements the center-of-gravity of the photoline was determined for time intervals of 10 s length. The resulting evolution of the core level shift as a function of experimental time is shown in figure 4.21. The relative core level shift is defined as the displacement of the O 1s peak at a distinct time increment of the overall experimental time,

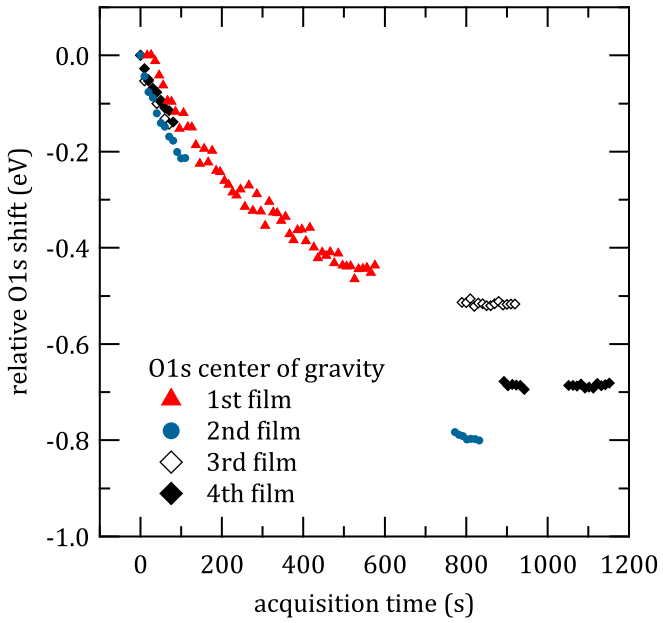

Figure 4.21: Relative kinetic energy of the O 1s photoelectron line of amorphous ice during soft X-ray irradiation at $h\nu = 700$ eV as a function of irradiation time.

with the starting value being the first 10 s of exposure. The zero of the time axis was determined with an accuracy of a few seconds by opening the beam shutter at the start of the data acquisition. It essentially marks the first time the ice film is irradiated with synchrotron light. As a function of time, the shift develops as a negative exponential converging to a plateau at values between -0.5 and -0.9 eV. The O 1s shift can be fully reversed by halting the irradiation for some minutes or choosing a fresh sample spot. Results in fig. 4.21 have been acquired on three different days of the same beamtime and two different substrates, an amorphous Cu plate[7] and the Au(111) single crystal. Regarding the spread in the magnitude of the core level shift, there are two possible explanations. One of them is the photon flux, which is sensitive to the PPRE and beamline settings. The second explanation rests in the unknown thickness or exact morphology of the ice films. For instance, a slightly thinner ice film most likely leads to a less pronounced shift upon continuous irradiation, as the coupling between the charged surface and the metal substrate might be stronger enabling a more effective charge transport. For all core level spectra that were evaluated no appreciable change in the spectral shape or width was found. From this it is assumed that charging of the sample is the dominant effect produced by the irradiation, and that actual X-ray induced chemical transformation probably requires higher radiation doses to become observable in the photoelectron signal.

After characterization of the surface charging the main focus was on the Auger electron spectrum of H_2O-ASW and its deuterated analog. AES of the two different ice layers are shown in figure 4.22. Both spectra were recorded under equivalent experimental conditions at a photon energy of 700 eV in swept mode using a step size of 0.5 eV and are comprised of several sweeps. Within this accuracy, no energy shift between the sweeps was observed. Therefore, charging of the amorphous ice layers was not expected to affect the comparison of the two isotopologues. In fig 4.22(a) the black trace corresponds to the AES of H_2O-ice and the red trace to D_2O-ice. The spectrum of normal ASW compares well with an early publication of Coulman and co-workers [160]. However, no isotope effect was reported therein. The two traces were normalised to equal area to enable comparison, a procedure which was introduced in the work of Thürmer *et al.* [18]. Upon comparing the two traces in (a) a significant surplus of intensity is observed in the high kinetic energy flank of the spectrum in H_2O-ASW compared to D_2O-ASW, analogous to the observations for liquid water [18]. The isotope effect between the spectra is better visible in the (H_2O-D_2O) difference spectrum in fig. 4.22(b). As the overall intensity is normalized, the difference trace essentially shows the redistribution of AES intensity due to the isotopic substitution. Positive values in the difference trace refer to a higher electron intensity of the normal ASW and indicates a higher degree of photoinduced charge separation in the PTM-CS process i.e., a higher number of delocalized states has been populated. Whereas negative values correspond to higher intensity in the deuterated ASW and indicate a higher propensity of decay processes close to the ground state geometry. This demonstrates that the proton transfer is active under cryogenic conditions in amorphous ice, similar to the results reported for liquid water.

[7] The Cu plate was used as dummy sample to test the cryostat and the dosing equipment, which were installed immediately before the beamtime, while the Au(111) sample was cleaned in a separate preparation chamber.

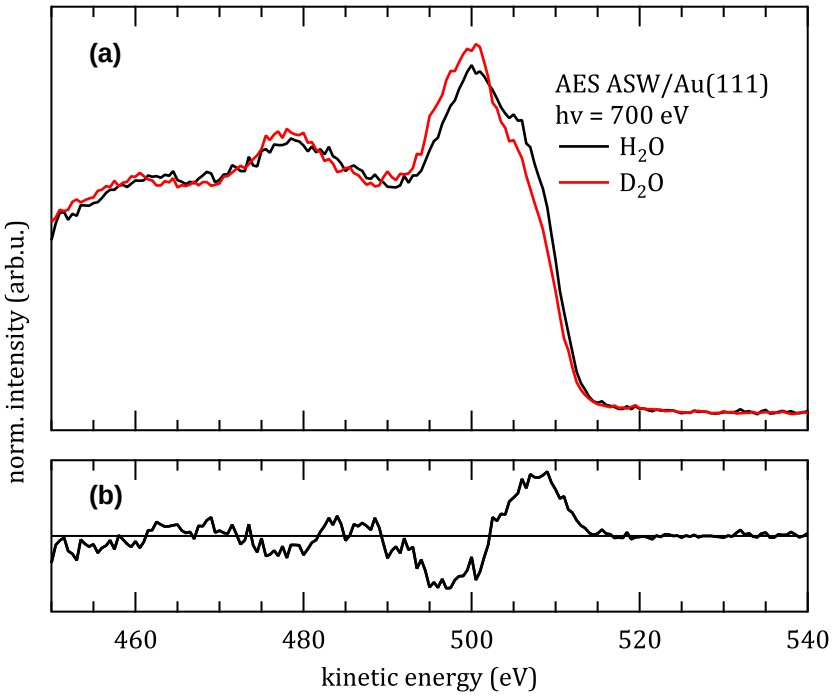

Figure 4.22: (a) shows the AES of amorphous H_2O-ice and D_2O-ice showing an isotope effect. (b) displays the (H_2O - D_2O) difference spectrum, the PTM-CS signature.

The following paragraph is an attempt to put the results of this study into perspective and give an outlook on possible follow-up experiments. The sensitivity of the Auger spectral shape on the geometrical arrangement of the molecules' surrounding the ionized center has been targeted in ref. [99]. It can be inferred that Auger spectroscopy, more specifically the observation of the PTM-CS feature, might be a new handle to elucidate information about differences in the local structure between different modifications of ice. The most obvious example would be the comparison of amorphous and crystalline I_h ice. Considering the geometries of the two phases, one would expect an increase of the PTM-CS signature in the crystalline hexagonal form of ice due to the highly directional character of the hydrogen bond. In the I_h lattice every water molecule takes part in four hydrogen bonds. Whereas in amorphous ice, which is considered to have a geometry closer to the fluctuating hydrogen bond network in liquid water, the average number of hydrogen bonds is < 4, due to hydrogen bond defects such as dangling O-H bonds. In the context of this project studies on crystalline ice produced by annealing an amorphous film [161] were indeed attempted. They were, however, unsuccessful.

The resemblance of the recorded PTM-CS signature with the results initially reported by Thürmer *et al.* [18] can be regarded as an argument for using amorphous ice as a model system to study the properties of liquid water in a controlled surface science experiment.

4.2.2 Proton Transfer Mediated Charge Separation in Mixtures of Water and Organic Solvents

Based on the observation of PTM-CS in amorphous ice and aqueous solutions [18, 113, 142], it was speculated whether the PTM-CS signature could be used as a spectroscopic tool to investigate the hydrogen bond network of aqueous mixtures of organic solvents. Water has a number of unique properties which have been traced to its ability to form hydrogen bonds. The hydrogen bond in itself is defined as a weak interaction (see sections 3.3 and 2.4). Within a hydrogen bond network, however, the high number of hydrogen bonds enables strong intermolecular interactions. In liquid water, these hydrogen bond interactions are constantly formed and broken on an ultrafast timescale. The average lifetime of a hydrogen bond in water is 1.4 ps [162]. Therefore the intermolecular network can be regarded as highly fluctuating making it inherently difficult to understand or probe its properties.
Hydrogen bonding is also essential to understand the solvation and mixing behaviour of polar/protic liquids. The interaction of solutes with the liquid network can be manifold. For instance the solute can form a strongly hydrogen bonded solvation shell with water [163], which can indirectly strengthen or weaken the water-water hydrogen bonds [148, 164]. When these effects are summed up, they can significantly affect the macroscopic properties of the liquid, such as its viscosity [165, 166], freezing point [167, 168] or thermal properties [169].
One class of molecules known to strongly affect the macroscopic properties of water are cryoprotectants, which are frequently used in cellular biology to preserve the integrity of organic samples during the freezing and thawing processes necessary for cryogenic preservation [170]. As hydrogen bonding predominantly governs the intermolecular interactions in liquid water and cryoprotectants have a pronounced colligative effect on the freezing behavior of water, their influence on the hydrogen bond network of water should be measurable.
It was initially presumed that cryoprotectant molecules hinder ice formation by disrupting the hydrogen bond network of water and hampering the formation of the its tetrahedral structure. It was, however, shown that water principally maintains the tetrahedral structure even at high cryoprotectant concentrations and the changes in the hydrogen bond environment are much more subtle [171]. Glycerol, a regularly used additive in cryopreservation, has been found to affect the structure of liquid water similar to an increase in pressure, which also decreases its freezing point [172]. In water-glycerol mixtures, water's tetrahedral structure is maintained but the distance to its second hydrogen bonded neighbor i.e., it second solvation shell, is decreased. So, a vital aspect to understand the effects of solutes and co-solvents on macroscopic properties of the aqueous system is the extended hydrogen bond network rather than only the first solvation shell.
The PTM-CS signature in the KVV-Auger spectrum of water can be regarded as a feature of its hydrogen bond network. As such, it should be inherently sensitive towards changes in said network. In order to test this hypothesis and contribute to the discussion about solute-induced structural change in liquid water, electron spectroscopic experiments were performed on mixtures of water and two frequently used cryoproctectants, glycerol ($C_3H_8O_3$)[173] and dimethyl sulfoxide ($(CH_3)_2SO$, DMSO)[174]. Their respective

glycerol dimethyl sulfoxide (DMSO)

Figure 4.23: Lewis structures of the cryoprotectant molecules glycerol and DMSO.

Lewis structures are depicted in figure 4.23. Glycerol is able to form up to nine hydrogen bonds with surrounding water molecules due to its three hydroxyl groups (-OH) [171]. The hydroxyl group can accept two hydrogen bonds via the oxygen lone pairs and donate one hydrogen bond itself. Whereas DMSO is not capable to donate a hydrogen bond, but can accept accept two at the oxygen site [175]. Due to the different capabilities to engage in hydrogen bonding and results of previous work on binary mixtures [171, 175–178] of water with glycerol and DMSO, respectively, varying impacts on the global hydrogen bond network were expected, which raised the question whether this behavior is discernable in the PTM-CS signature.

The measurements presented in this section were performed at the UE52-SGM soft X-ray beamline [137] at the BESSY II synchrotron facility using the mobile SOL^3 endstation, which is specifically designed for liquid jet photoelectron spectroscopy [76]. The sample was a liquid jet of about 25 μm diameter, at a flow rate of 1 ml/min. The jet was mounted vertically to the synchrotron plane, intersecting the soft X-ray beam at a 90 ° angle. The hemispherical electron analyzer was positioned within the synchrotron plane. Electrons were detected at 90 ° with respect to the linear polarization of the synchrotron radation. In this setting photoelectron spectra of pure water, water-glycerol and water-DMSO mixtures, and their deuterated counterparts where measured at 600 eV photon energy. 50 mM NaCl[8] was added to all solutions to avert electrokinetic charging of the jet as well as charging due to continuous ionization. The jet was then connected to the ground of the setup via a small gold wire a few centimetres upstream of the fused silica nozzle.
In the aforementioned setting, data sets consisting of O 1s core-level and Auger spectra were recorded for: (i) liquid and vapor-phase water, (ii) 6 mol% glycerol in water, (iii) 11 mol% glycerol in water, (iv) 10 mol% DMSO in water and (v) 50 mol% DMSO in water. The same measurements were repeated with the equivalent deuterated samples. The chemicals D_2O and DMSO were used without further purification[9]. For the solutions with normal water, glycerol[10] was also used without purification, while for the deuterated solutions it was transformed into d3-glycerol by mixing with D_2O in a 1:3 ratio, leading to fast proton/deuterium exchange of the glycerol's OH groups. Subsequently the residual water was extracted using a rotary evaporator. This exchange procedure was performed three times, resulting in d3-glycerol with 7.3 % water content (H_2O/D_2O) and 90 % deuteration, as determined by NMR-spectroscopy.

[8] NaCl: purity > 99.8 %, Sigma Aldrich
[9] D_2O: purity 99.8 % Atom D, Acros Organics; DMSO: purity ≥ 99.5 %, Carl Roth
[10] glycerol: purity ≥ 99.5 %, Carl Roth

The O 1s spectra were used to calibrate the binding/kinetic energy axis (see eq. 2.2 for relation of the two energy axes). The calibration was done by fitting the core-level spectra, which yielded the center energy of the water O 1s. Any deviation from the literature value of 538.1 eV [179] was corrected. This calibration is typically used to determine and counteract any photon energy offset of the beamline. Furthermore, this procedure also corrects for effects of residual streaming potential [180] of the liquid jet surface, which has been observed to affect the apparent binding energy [87, 181, 182]. An overview of the O 1s spectra of all measured samples is given in figure 4.24. The spectra are aligned on the O 1s core

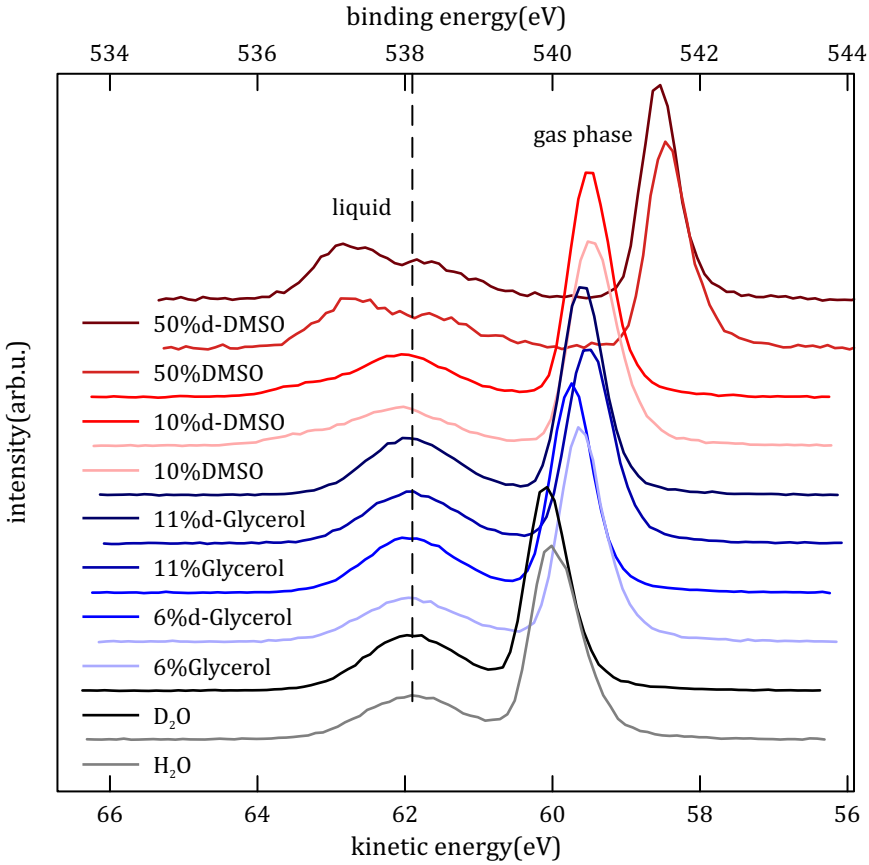

Figure 4.24: O 1s spectra of water-cryoprotectant mixtures

level of liquid water, indicated by the dashed vertical line. Each spectrum is composed of the condensed phase signal between 536 to 539 eV binding energy and a gas phase peak of evaporating water at higher binding energy. The spectral contributions of the different condensed phase components overlap significantly. Especially in the case of water-glycerol mixtures the two contributions cannot be separated. In comparison of the light and heavy solutions e.g., H_2O and D_2O, no isotope effect was observed in the O 1s spectra.

It can be immediately recognized that the vapor phase contribution to the overall signal intensity is relatively high. This is due to the experimental geometry special to the combination of the SOL^3 endstation and the UE52-SGM beamline. The interaction region spanned by the liquid jet, the synchrotron light and the axis of the electron analyzer is placed approximately 15 cm behind the beamline focus which results in a relatively big spot size in contrast to the liquid jet of few tens of micrometers. Due to the nature of the liquid jet discussed in

section 3.2, this geometry leads to a significant contribution of the surrounding vapor phase in all recorded spectra.
Noticeably the water O 1s gas phase signal is shifted for every spectrum. These shifts are a result of differences in the potential environment around the liquid jet. While the aforementioned procedure of energy calibration corrects for the effect of varying surface charges of the liquid jet, it cannot correct for the gas phase peak as this should not be subject to surface charge effects. However, due to the existence of the liquid jet surface in close proximity to electrons emitted from a water molecule in the gas phase surrounding the jet, the electron experiences a potential which is dependent on the distance to said jet surface, the streaming potential and molecular composition of the surface i.e., the surface dipole.
The recorded Auger electron spectra contained a considerable vapor phase contribution, similar to the O 1s spectra. Therefore, the vapor phase was carefully subtracted from all spectra, which is justified as the main focus of this project was an investigation of the PTM-CS signature i.e., the dynamics of the hydrogen bond network upon core level de-excitation, which is a feature solely associated with the condensed state. An example of the vapor phase subtraction is given in figure 4.25 for the Auger spectrum of pure water. Here, three

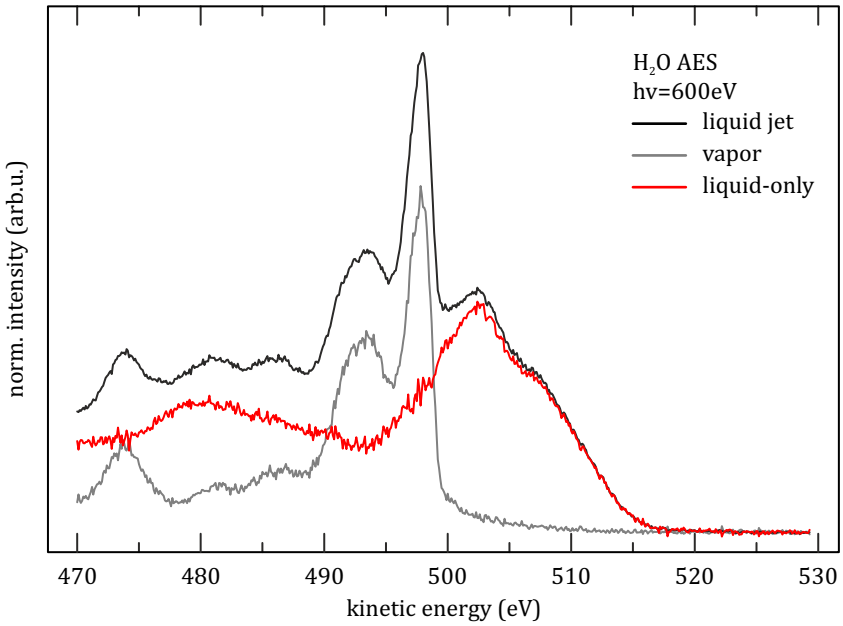

Figure 4.25: Vapor phase subtraction from the Auger electron spectrum of a water liquid jet. The original spectrum is displayed in the black, vapor phase spectrum in grey and the liquid-only trace in blue.

traces are shown consisting of the raw liquid jet spectrum in black, the respective vapor phase spectrum in grey, obtained by moving the liquid jet out of the beam, and the so-called *liquid-only* trace in red. The latter is obtained by subtracting the grey trace from the raw data. The subtraction procedure consisted of aligning the vapor phase spectrum (grey trace) with the vapor phase contribution of the liquid jet spectrum (black trace), subsequently, the leading vapor phase peak of the liquid jet and vapor phase spectra were fitted to determine the area ratio between the two peaks as an initial correction factor. Subsequently this factor was manually varied to achieve a smooth low kinetic energy flank of the leading condensed

phase peak in the range of 495 to 500 eV. The liquid-only spectra are in good agreement with the liquid jet spectra presented in the work of Thürmer *et al.* [18], where the vapor phase contribution is considerably smaller. Furthermore, the liquid-only spectra strongly resemble the Auger spectra of amorphous ice depicted in the preceding section and in ref. [160].

In the following paragraphs the liquid-only Auger spectra of the different solutions will be discussed in detail. These spectra are compiled in figure 4.26. The spectra can be partitioned

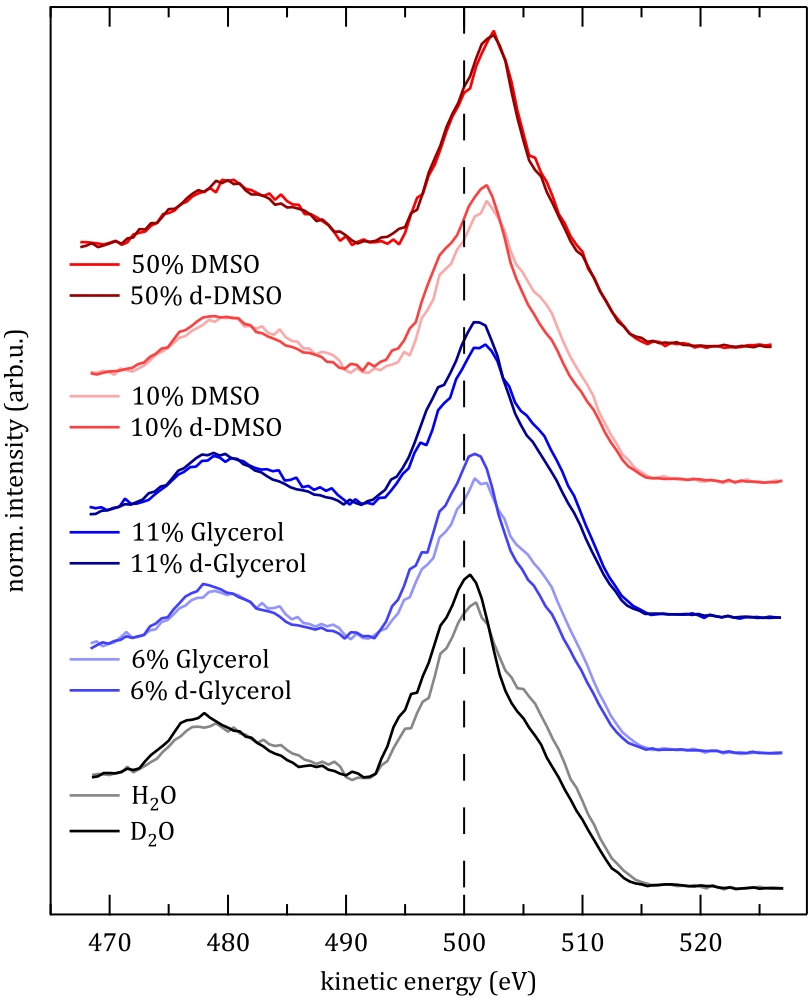

Figure 4.26: Liquid-only Auger spectra of pure water and mixtures of water with two cryoprotectants at different concentration. For each system, traces of the normal and deuterated components were measured under identical conditions, and are compared in the graph. All spectra have been normalised to unit area. The dashed line indicates 500 eV KE.

into a region of higher intensity between 495 – 515 eV kinetic energy and a second region of lower intensity between 470 – 495 eV. In comparison with the Auger spectrum of the water vapor/gas phase (see fig. 4.25) the condensed phase contributions are significantly broadened and shifted to higher kinetic energy, due to the changes in the polarization screening in the different intermolecular geometries encountered in the liquid phase. As emphasized earlier, the condensed phase Auger spectra also involve non-local transitions ascribed to

ICD and ETMD, which typically result in secondary electrons of higher kinetic energy. It is therefore likely that the liquid-only spectra of the binary systems contain a signal contribution of the non-local processes between water and glycerol or water and dmso, respectively, in addition to the contributions of the individual molecules. In general, all liquid spectra shown in fig. 4.26 are very similar in appearance. The O 1s Auger spectrum of alcohol hydroxyl groups has been reported to be very similar to water, with the most significant deviation being a shoulder at higher kinetic energy than the main line [183]. The liquid phase O 1s Auger spectrum of methanol, as the simplest alcohol, closely resembles the spectrum of liquid water and shows a significant non-local decay contribution [144].
For DMSO, so far no O 1s Auger spectrum has been reported. However, the Auger spectra of the SO_2 molecule, which exhibits a chemical environment of the oxygen groups similar to DMSO, have been described in the literature [184]. Therefore, the spectral shape of the O 1s Auger decay of DMSO should resemble the one reported for SO_2.
The individual spectral contributions to the mixed condensed phase spectra are very broad and strongly overlap. A separation is consequently not viable in the conventional one-dimensional electron spectroscopic approach. It is however possible to point out changes to the apparent main peak and the relative intensity of the non-local decay shoulder with respect to the pure water reference spectrum. The Auger spectra of the different mixtures show small differences from pure water, which can be attributed to an increased contribution of the glycerol or DMSO component. In both regions of lower and higher kinetic energy, the apparent maximum of the traces appears at successively higher kinetic energy with increasing concentration of the respective organic solvent. Additionally, the high kinetic energy shoulder at $\sim$ 505 eV, corresponding to the non-local final states, becomes less pronounced relative to the main peak.
For all binary mixtures shown in fig. 4.26 measurements of the normal and deuterated species are depicted. In every case an isotope effect is observed, suggesting that proton transfer dynamics take place in the core-excited state. As expected, the protonated systems show a more pronounced signal intensity at high kinetic energy side of the main peak ($>$ 503 eV), which is accompanied by a reduction of signal intensity on the lower kinetic energy side. This effect can also be observed for the region at lower kinetic energy but of lower magnitude. This isotope dependent redistribution of signal intensity is attributed to the PTM-CS process. The PTM-CS signature supposedly enables conclusions about the ionization-induced nuclear dynamics of the hydrogen bond environment. This signature of intensity redistribution is most noticeable in the difference traces of the protonated and deuterated systems displayed in figure 4.27. 4.27(a) shows the difference traces of the two glycerol solutions in comparison to water. (b) analogously shows the comparison for DMSO solutions with pure water. (c) displays the absolute values of the area described by the difference traces normalized to the value of pure water. The numerical values of the normalized areas are summarized in table 4.6. The isotope effect relative to water is referred to as Δ_{PTM-CS}. Error bars for Δ_{PTM-CS} capture the noisiness/uncertainty of the difference traces in fig. 4.27(a) and (b). It was obtained by fitting the normalized difference traces with four Gaussians and subsequently quantifying the spread of data points around the baseline of the fit

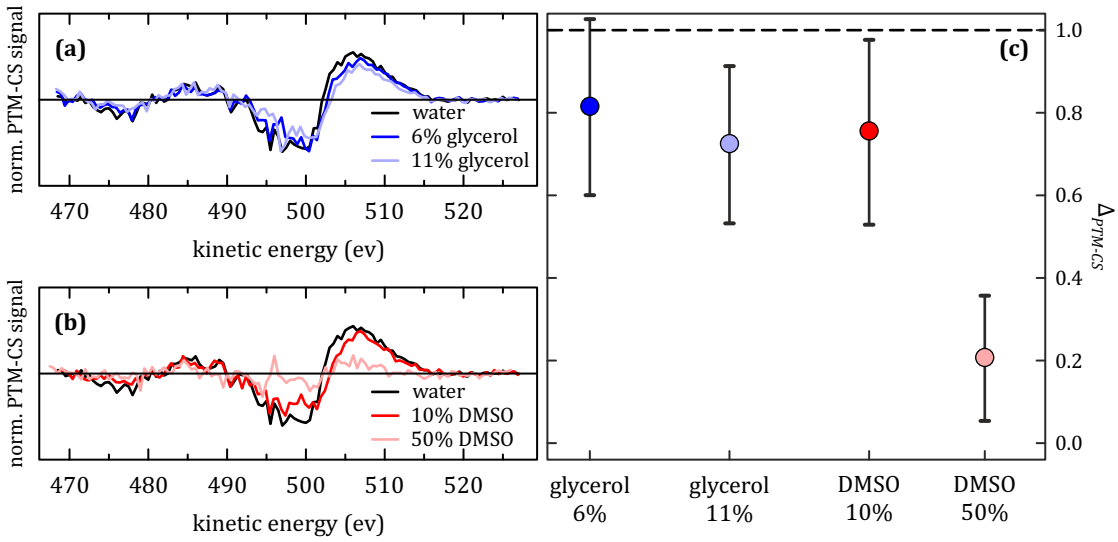

Figure 4.27: Difference in the O 1s Auger spectra between several deuterated aqueous mixtures and their non-deuterated analogues. Panel (a) shows the glycerol-water mixtures, and panel (b) the DMSO-water mixtures. In both panels, the pure water trace is shown in dark blue. Panel (c) summarizes the relative isotope effect ($\Delta_{PTM.CS}$).

Table 4.6: Summary of sample composition and experimental results. X refers to the co-solvent in the individual mixtures, either DMSO or glycerol, and O(X) to the oxygen atoms of the co-solvents. The first two columns show the composition of the mixed samples in molar fractions of the co-solvent and the molar fraction of the number of total oxygen atoms that are part of the co-solvent molecules. The freezing points of the mixtures were taken from the literature [167, 168]. Δ_{PTM-CS} is the relative isotope effect that we determined experimentally. Δ_{OH} is the fractional decrease of hydrogen bonds due to the loss of hydroxyl groups in the mixed systems, and Δ_S is the steric effect the apolar groups exert on the hydrogen bond network.

System	X (mol%)	O(X) (atom%)	Freezing Point (°C)	Δ_{PTM-CS}	Δ_{OH}	Δ_S
Water	0	0	0	1	1	1
Glycerol (aq)	6	16	-6	0.82(21)	0.92	0.89
Glycerol (aq)	11	27	-12	0.72(19)	0.86	0.84
DMSO (aq)	10	10	-17	0.75(22)	0.90	0.83
DMSO (aq)	50	50	-45	0.21(15)	0.50	0.42

residual using the width σ of a single Gaussian distribution. Changes in the isotope effect are interpreted as changes in the propensity of the PTM-CS to occur i.e., overall changes in the strength of the hydrogen bond network relative to that of liquid water.

It is clearly visible in the difference traces in fig. 4.27(a) and (b) that the addition of cryoprotecting molecules affects the magnitude of Δ_{PTM-CS}. The shape of the PTM-CS signature, however, is unaffected. For all traces the relative intensity on the high kinetic energy side of each region, associated with the non-local transitions, is higher for the light (H) system than for its heavy (D) equivalent. Conversely, predominantly local transitions of lower kinetic energy show more intensity in the deuterated solutions. In solutions of 6 and 11 mol% glycerol, Δ_{PTM-CS} decreases slightly with increasing concentration of glycerol relative to the

nominal value of 1 for pure water to a fraction of 0.82(21) and 0.72(19), respectively. In the 10 mol% DMSO solution, the reduction of Δ_{PTM-CS} is with a value of 0.75(22) of the same magnitude. A more drastic change is observed at higher concentration of DMSO (50 mol%), in which case Δ_{PTM-CS} is decreased to 0.21(15) relative to liquid water.

The reduction of the isotope effect in the binary mixtures is most likely associated with the reduction of possible O-H$\cdots$O hydrogen bonds that can be formed per oxygen site. A single water molecule is capable to donate and accept hydrogen bonds via the two O-H groups and the two oxygen lone pairs, respectively. The resulting maximum number of hydrogen bonds formed by an individual water molecule in the condensed phase is four — four bonds per molecule and per oxygen atom. The glycerol molecule contains three hydroxyl groups that can each donate one hydrogen bond and accept two [171, 178]. In contrast, DMSO, with its sulfoxide group S = O, is not able to donate any hydrogen bonds but can accept two [185]. From this follows that the number of hydrogen bond acceptors via the oxygen lone pairs is greater than the number of hydrogen bond donors i.e., accessible hydroxyl groups -OH, in the mixtures. It is therefore sensible to concentrate on the accessible hydroxyl groups to estimate the reduction in the number of possible hydrogen bonds. The number of possible hydrogen donor bonds in the mixed system relative to pure water can be estimated stoichiometrically. It is given as Δ_{OH} in table 4.6. These values were calculated per average oxygen atom, since the normalization procedure of the Auger spectra also relates the relative intensity to the number of oxygen atoms in the probed volume.

For completeness, it should be addressed that even in pure liquid water the average number of hydrogen bonds formed by an individual molecule is lower than the four possible hydrogen bonds, as the characteristic fluctuations of hydrogen bond formation and disruption are inherent to the liquid phase. In contrast to the fluctuating disordered liquid, in the ordered structure of hexagonal crystalline ice every water molecule is part of a rigid tetrahedral environment of hydrogen bonds.

In the framework of the applied explanatory model, the values of Δ_{PTM-CS} and Δ_{OH} should be very close or equal if the reduced number of accessible hydrogen bonds in the binary mixtures would predominantly be a stoichiometric effect. This is, however, not the case as immediately discernible from table 4.6. The experimentally determined isotope effect Δ_{PTM-CS} in the mixed system is stronger than the stoichiometrically predicted reduction of accessible hydrogen bonds Δ_{OH}. This indicates the contribution of additional co-solvent induced effects acting on Δ_{PTM-CS} which lead to a further reduction of the fraction of possible hydrogen bonds formed in the liquid. The reduction of Δ_{PTM-CS} beyond Δ_{OH} is likely caused by the disruption of the water hydrogen bond network by the introduction of the apolar functional groups of the cryoprotectants. These groups, like the dimethyl sulfur groups (-S(CH_3)$_2$) in DMSO and the hydrocarbon backbone of glycerol, disturb the formation of hydrogen bonds and thus reduce the effective number of hydrogen bonds which can be formed. A reduced number of effective hydrogen bonds consequently reduces the number of oxygen sites capable to undergo the ionization induced proton transfer reaction, which is reflected in the lowering of the observed isotope effect. The influence of the hydrocarbon groups can be referred to as the steric effect Δ_S of the apolar/aprotic sites in the solution. In

the simplest approach it can be defined as the ratio of the observed isotope effect (Δ_{PTM-CS}) and the reduced number of possible hydrogen bonds (Δ_{OH}):

$$\Delta_S = \frac{\Delta_{PTM-CS}}{\Delta_{OH}} \tag{4.18}$$

In table 4.6 it can be seen that the steric effect Δ_S is similar for lower cryoprotectant concentrations of 6 to 11 mol%. However, in the case of high DMSO concentration (50 mol%) Δ_S reduces to 0.42.

The interpretation of Δ_S is not straightforward but depends on the individual mechanism affecting the magnitude of the PTM-CS signature in the mixture. Based on the assumption that Δ_{PTM-CS} is proportional to the average number of hydrogen bonds per oxygen in reference to pure water, Δ_S can be considered as the fraction of effectively formed hydrogen bonds. At this point it is not well known how strongly the PTM-CS effect reacts to the weakening of the hydrogen bonds. It is likely that the slope of the dissociative core-excited state (see energy diagram in fig. 4.20 for graphical representation) is sensitive to the strength of the hydrogen bond. Taking this into account, Δ_{PTM-CS} is better described as a convolution of the relative number of formed hydrogen bonds and the strength of said bonds. In that sense the value of Δ_S indicates the steric contribution to the weakening of the hydrogen bond network relative to the reference system of pure water.

Any co-solvent induced disorder into the system likely results from steric hindrance by any functional groups that can not, or only weakly, engage in hydrogen bonds. The term 'steric hindrance' includes any effect that impede hydrogen bond formation by disallowing any molecular trajectories which bring the donor and acceptor groups into spatial proximity, due to e.g. cavity formation around the apolar groups. The excluded volume of these cavities depends on the hydrophobicity of the apolar groups. These apolar groups can either be integrated in the hydrogen bond environment as monomers or they can form larger agglomerate or clusters. These different molecular structure motifs can affect the overall hydrogen bond network in different ways, making the manner in which the apolar moieties arrange themselves in the liquid phase relevant beyond their concentration. For instance, clustering has been observed at concentrations as low as 5 mol% in mixtures of water and glycerol [172] leading to the formation of micro-domains in the liquid phase. The lower concentrations measured for the binary water-cryoproctant mixtures were on the same order of magnitude. This effect has been studied in detail for alcohols [186, 187] but is generally present in many binary mixtures.

It is speculated that the hydrogen bond network itself drives the cluster formation by optimizing its structure for water-hydroxyl interactions and excluding hydrophobic groups [171]. The reduction of hydrogen bonding due to the co-solvent is therefore smaller in the clustered geometry compared to a homogeneous distribution of the co-solvent molecules. Conversely, the better the interaction of a co-solvent with water i.e., its capability to from hydrogen bonds, the smaller is the number of clusters in solution.

In the case of glycerol, it has been shown that even at only 5 mol% concentration only 40 % of the glycerol molecules are found as monomers, with the remainder forming dimers or

larger clusters [172]. The molecules forming these clusters maintain strong hydrogen bonds with the surrounding water via their hydroxyl groups and arrange their hydrophobic backbone towards the center of the aggregates [171].
In mixtures of DMSO and water similar effects were observed. Here, complexes are formed in which the DMSO molecules align along their S=O bond and the oxygen sites take part in hydrogen bonds with water, whereas the hydrophobic $S(CH_3)_2$ assemble together [188] interacting only weakly with the surrounding water molecules [177]. In ref. [175] it was shown that in the 10 mol% DMSO solution the majority of DMSO molecules accept one hydrogen bond from water. However, at the higher concentration of 50 mol% the self-interaction between DMSO molecules dominates, leading to the formation of dimers that only interact with each other via intermolecular O$\cdots$S interactions. These dimers or higher order aggregates do not participate in any hydrogen bonds with water [175], but rather exclude themselves from the aqueous phase forming DMSO clusters or domains. This domain formation can therefore lead to the formation of a surface-like layer of water molecules around the hydrophobic clusters [189, 190]. At these hydrophilic–hydrophobic phase boundaries interfacial water molecules can form dangling -OH bonds, due to the inabillity to form hydrogen bonds [191, 192]. At the high DMSO concentration where self-interaction of the two respective solvents is the dominating interaction such hydrophilic-hydrophobic interface is formed and accompanied by a strong increase in the steric hindrance, as seen in Δ_S.
The influence of both co-solvent molecules on water diffusion has been studied by Schrader *et al.* in the bulk liquid and on the surface of a biological membrane [193]. Schrader and co-workers show that in solutions of up to 7.5 mol% DMSO and glycerol similarly affect the bulk diffusivity of water. An analogous behavior at low concentration was observed for Δ_{PTM-CS} in the present study. Further, the authors also report that the behavior of the two cryoprotectants diverges at the membrane surface. They suggest that glycerol and water are more compatible i.e., glycerol can be better integrated into a hydrogen bond network, whereas DMSO is less compatible due to its structure and its intermolecular interactions. The results of the present investigation likely represent another facet of the difference in intermolecular interaction between water-glycerol and, on the other hand, water-DMSO, namely the pronounced self-interaction of DMSO at higher concentrations as also discussed in ref. [175].
It is possible to tentatively relate the results directly to the cryoprotective properties of the two molecules. The studied mixtures have a freezing point significantly lower than that of the pure systems (see table 4.6). While it is known from the literature that most water molecules maintain a tetrahedral hydrogen bond environment in the studied mixtures, the experimental results are consistent with the observation of an overall weakening of the network. It is reasonable to assume that this weakening is caused by a distortion of the extended hydrogen bond network to accommodate the apolar groups of the cryoprotectants. In the liquid jet experiment the sample is subject to significant evaporative cooling. The hydrogen bond network probed in the Auger spectra can therefore be considered close to the freezing point of water. Without further experiments, however, no statement can be made about ice crystallization in water-glycerol and water-DMSO mixtures.

In conclusion, the photoinduced proton dynamics occurring within the lifetime of the O 1s core-excited state were employed to the hydrogen bond network of binary mixtures of water with glycerol and DMSO — two frequently used molecules for cryopreservation. These molecules lead to a reduction in the isotope effect observed in the O 1s Auger spectra i.e., the PTM-CS effect, of the liquid solution relative to pure water. This reduction can be related to an overall weakening of the hydrogen bond network formed in the liquid, which can be attributed to a combination of two different effects:
Firstly, a reduction in the maximum possible number of hydrogen bonds that can be formed in the system, due to the replacement of water with molecules of reduced hydrogen-bonding ability and secondly, a so-called steric effect herein defined as describing the disruption of the extended hydrogen bond network by introduction of the apolar functional groups in glycerol and DMSO. The steric effect can be thought to reduce the number and strength of the formed hydrogen bonds. It is particularly pronounced for 50 mol% DMSO solutions, since the high concentration of DMSO shifts the solution into a regime in which the molecules preferentially self-interact to form aggregates no longer engaging in hydrogen bonds with the water domains [175].
The presented investigation constitutes the first time that the ultrafast PTM-CS process has been used to systematically study the influence of co-solvents on the global hydrogen bond network strength in aqueous mixtures. A similarly systematic study was performed on unimolecular clusters of different sizes and hydrogen bonding capability [143] in preparation of the present investigation of binary mixtures. In reference [143] the strength of the PTM-CS signal of small and large molecular clusters was compared to the bulk liquid following the buildup of an extended hydrogen bond network. The reported dependence on the average system size indicates that confinement effects due to differences in surface-to-volume ratio have a considerable impact on the overall strength of the hydrogen bond network. Furthermore, it could be established that in a hydrogen bond network of methanol the PTM-CS effect is about half as strong as in liquid water due to the substitution of a -OH function with a methyl group. These observations are directly applicable to the binary mixtures studied in this thesis. So it can be concluded that the non-local PTM-CS process is indeed an attractive spectroscopic tool to investigate hydrogen bonding interactions in more complex systems beyond water.

Chapter 5

Double Ionization and the Elusive ICD Signature in Liquid Water

The double ionization of atoms and molecules and the investigation of non-local electronic decay processes, such as ICD, are closely related as they are both governed by electron correlation effects and the respective final states are of dicationic character.
In the following section, the signatures of doubly-ionized states of the inner valence region in the electron spectrum of water are discussed in pursuit of identifying the signature of ICD in liquid water. For this purpose, the individual double ionization contributions were determined starting with the non-interacting water molecule in the gas phase followed by water clusters and the condensed phase: liquid water. As water is ubiquitous and part of numerous biologically relevant processes a detailed understanding of the interaction of water with radiation, especially ionizing radiation, is essential since the products of the interaction are typically highly reactive species, such as fast and slow electrons as well as excited ions and radicals. While the main focus of the present work is the investigation of non-local decay phenomena in aqueous systems after initial photoexcitation it will become clear that with increasing condensation a clear separation of double ionization and non-local decay becomes increasingly challenging.

The double ionization of the water molecule in the gas phase has been intensively studied using different experimental approaches utilizing either photons or projectiles, such as electrons or ions, to induce ionization followed by the detection of the emitted electrons or the fragment ions [136, 194–196]. The most recent experiments on water double ionization employed techniques such as electron-electron coincidence spectroscopy, threshold photoelectron spectroscopy and cold target recoil ion momentum spectroscopy (COLTRIMS) [68, 88, 109]. Especially the results of Eland and co-workers are directly comparable to the data recorded in the context of this work as both were obtained using time-of-flight photoelectron-photoelectron coincidence spectroscopy (TOF-PEPECO). In figure 5.1 the double ionization spectrum of the free water molecule in the gas phase is displayed for reference. The double ionization spectrum was taken from the archive of digital spectra provided by ref. [28]. It was recorded at 110 eV photon energy using synchrotron light, thus accessing an extended energy range. In general, the spectrum strongly resembles the Auger spectrum of gas phase water [136]. The individual peaks in fig. 5.1 are labeled according to the *molecular orbitals*

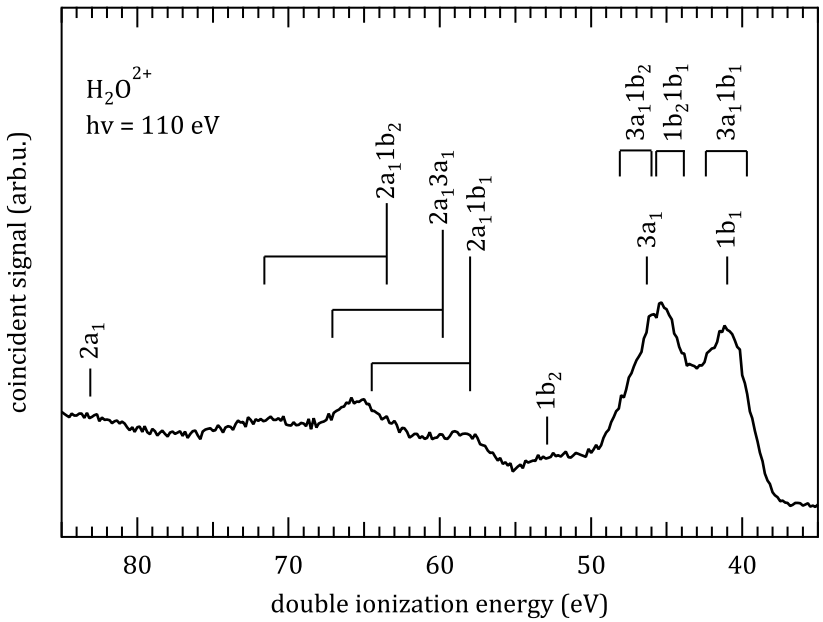

Figure 5.1: TOF-PEPECO spectrum of molecular water at 110 eV photon energy. The peaks are assigned according to the molecular orbital from which the electrons are removed. The spectrum and assignments were taken and modified from ref. [28] and therein.

(MO) carrying the two positive charges in the final state. Where the label consists of a single MO, both detected electrons where emitted from the same orbital. In cases of states corresponding to two MO's two spin multiplicities are possible, with the states of lower double ionization energy corresponding to a triplet final state and the other to a singlet state.
With regard to the coincident measurement of water clusters described in section 4.1.1 and the coincidence experiments on a liquid jet the leading double ionization peaks between 35 to 50 eV are the most important spectral features as they are always observed in the spectra due to the presence of gas phase molecules in the cluster beam and respectively around the liquid jet, as described in section 3.2. For molecules, such as water, the dicationic state (H_2O^{2+}) is not stable but rather dissociative, immediately leading to the separation of the two positive charges. In a comprehensive study around Reedy and co-workers the double ionization induced dissociation of the water molecule was investigated using theoretical methods and COLTRIMS [88]. Their results show that the first and second double ionization peak can be assigned to distinct two-body and three-body-breakup channels of the water molecule, respectively. The first peak is attributed to the two-body-breakup of the form:

$$H_2O + h\nu \longrightarrow H^+ + OH^+ + 2e^-. \tag{5.1}$$

This dissociation channel is in agreement with the peak assignment in fig. 5.1. Removal of an electron from the non-bonding $1b_1$ and from the bonding $3a_1$ or $1b_2$ MO weakens the bonding interaction between one of the hydrogen atoms and oxygen thus enabling dissociation. Additionally, a second process is observed for the first double ionization peak:

$$H_2O + h\nu \longrightarrow H^+ + OH^* + e^- \longrightarrow H^+ + OH^+ + e^-, \tag{5.2}$$

where OH^* is in an excited state which can subsequently autoionize yielding OH^+ and a second electron of near zero kinetic energy [197].
The second double ionizaton peak is attributed to the three-body-breakup:

$$H_2O + h\nu \longrightarrow 2H^+ + O^* + 2e^-, \tag{5.3}$$

matching the simultaneous removal of two electrons from the $3a_1$ or the $3a_1$ and $1b_2$, respectively, thus breaking both OH bonds.
So far, double ionization of an isolated non-interacting water molecule was discussed. The spectral features are those of 2h final states with both charges localized on the same molecule. As interactions with neighboring molecules are introduced by condensation the double ionization potential is subject to changes, analogous to the single ionization potential in the condensed phase. The effect of condensation on the double ionization potential of the water dimer was discussed by Cederbaum and co-workers [6] and gave rise to the investigation of ICD and related phenomena. Specifically for small water clusters, calculated single and double ionization spectra showed a dependence on the number of neighboring water molecules [198].
In general, once a second water molecule is introduced and both molecules interact weakly via a hydrogen bond, the double ionization potential is reduced due to the emergence of new final states of 1h1h character. These final states are energetically lower than the $2a_1$ inner valence state, thus giving rise to ICD as an electronic relaxation process. This situation is displayed in figure 5.2. Panel (a) shows the conventional photoelectron spectrum of small water clusters with a mean cluster size $\langle N \rangle = 5$ recorded with a magnetic bottle electron spectrometer at 62 eV photon energy. This spectrum, occasionally referred to as the single ionization spectrum, consists of the outer valence peaks corresponding to the molecular orbitals $1b_1$, $3a_1$ and $1b_2$ and the inner valence signal of the $2a_1$ orbital. Panel (b) shows the corresponding double ionization spectrum of the water clusters as solid black trace. In addition, the dashed trace corresponds to the reference spectrum of gas phase water (see fig. 5.1). Clearly, the double ionization spectrum of the cluster beam includes a considerable amount of signal from gaseous water as indicated by the two intense peaks between 35 to 50 eV double ionization energy aligned with the reference spectrum. Further, the bars indicate the energetic position of the first doubly ionized states of 2h (black) and 1h1h (red) character calculated for a water tetramer [198]. The intensity in the double ionization spectrum between 25 to 35 eV double ionization energy is assigned to autoionization by ICD initiated after $2a_1$ photoionization. In the work by Müller and co-workers [198], the double ionization spectra of a single water molecule up to the tetramer were calculated and characterized regarding the localization of the holes in the final states. A general trend observed in small water clusters is the continuous lowering of the double ionization potential, with the 1h1h states lowest in energy. The states with both final state charges localized at a single site are close to the values observed in the experimental gas phase double ionization spectrum.

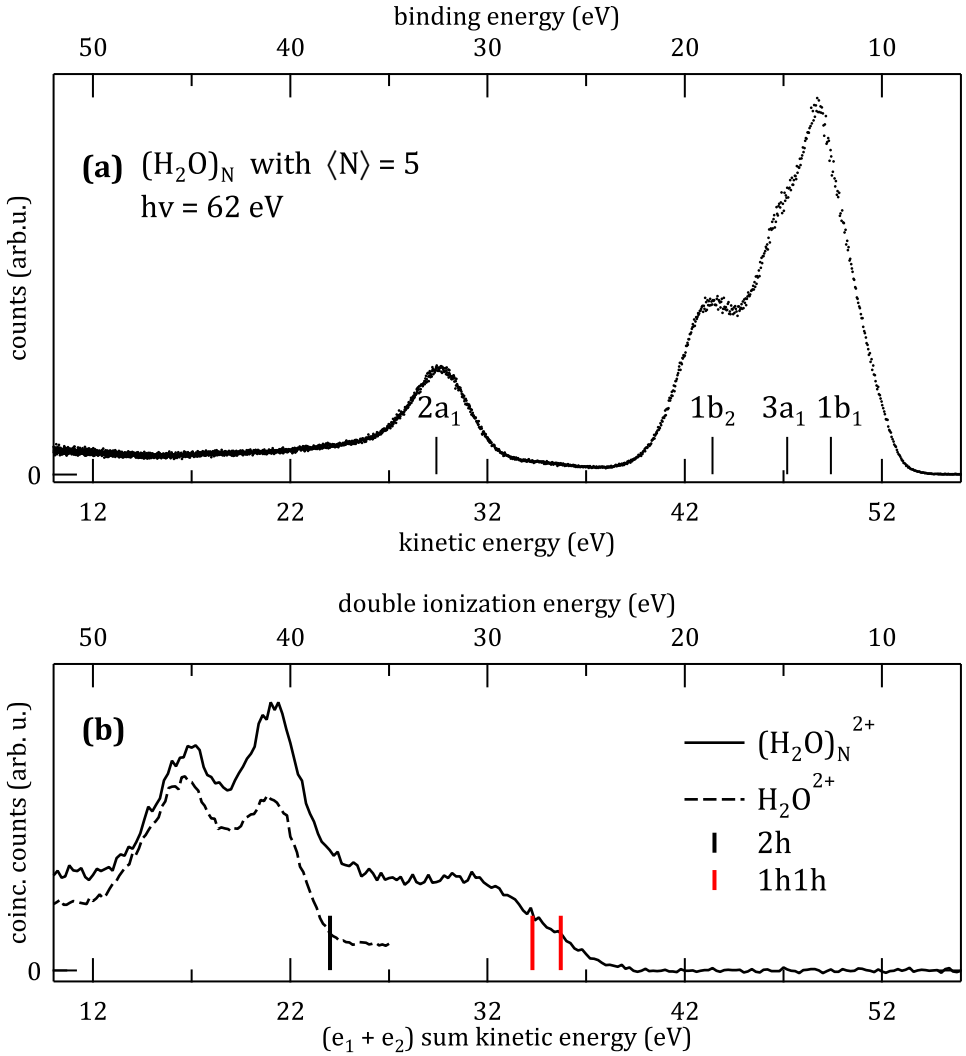

Figure 5.2: (a) conventional photoelectron spectrum and (b) double ionization spectrum of a molecular beam containing small water clusters with mean size $\langle N \rangle = 5$ and a significant gas phase contribution. The dashed line in (b) corresponds to the leading double ionization peaks of molecular water [28]. Additionally, the lowest double ionization states of 2h and 1h1h character, calculated for the water tetramer [198], are indicated as black and red ticks, respectively. Considering the energetic position of singly and doubly ionized states, it is immediately clear that $2a_1$ ionization allows subsequent autoionization into the 1h1h doubly ionized states (ICD).

The data presented in this chapter was recorded in separate beamtimes at the BESSY II synchrotron radiation facility employing the two experimental setups described in section 3.5 containing a magnetic bottle time-of-flight electron spectrometer. The two setups enable the measurement of coincident electron spectra of molecular clusters and of a liquid jet, respectively. The spectra of water clusters are part of the data set presented in section 4.1.1. Briefly, the measurements were performed at the UE56/2-PGM1 beamline using VUV radiation. A molecular beam of water clusters of varying mean cluster size $\langle N \rangle$ was produced via supersonic expansion. The expansion parameters leading to the respective clusters sizes are given in table 4.1 in section 4.1.1. Coincidence measurements of the liquid jet were conducted with synchrotron radiation in the VUV and soft X-ray regime provided by the UE56/2-PGM1 and

UE112-PGM-1 beamlines. The sample solution was a 50 mM solution of NaCl in ultrapure water. The small amount of salt ensures the conductivity of the sample solution. Magnetic bottle electron spectrometers are frequently combined with liquid jets containing various aqueous solutions [181, 199, 200]. However, no coincidence data acquisition has been reported, other than the work in reference [73], which was part of this thesis. Coincident electron detection enables the investigation of doubly ionized states resulting from either direct double ionization processes or from electronic decay processes such as ICD.

While a coincident detection scheme is conceptually readily accessible, the quantitative measurement of the double ionization energy or, respectively, the generation of double ionization spectra from the actual measurement is not as straightforward as in conventional photoemission spectroscopy. In order to ensure the understanding of double ionization spectra and to show how the double ionization spectra relate to conventional photoelectron spectra, figure 5.3 shows an illustrative example. In panel (a) the two-dimensional coincident electron spectrum of a water cluster beam of mean size $\langle N \rangle = 5$ and in (b) and (c) two distinct one-dimensional spectra derived from the electron correlation map. The two- and one-dimensional spectra displayed here correspond to the same measurement of small water clusters recorded at 62 eV photon energy shown in the previous figure 5.2. (a) is the correlation map of two electrons e_1 and e_2 emitted within the time of two consecutive photon pulses. Here, e_1 is assigned as initial photoelectron as a function of kinetic energy (bottom)

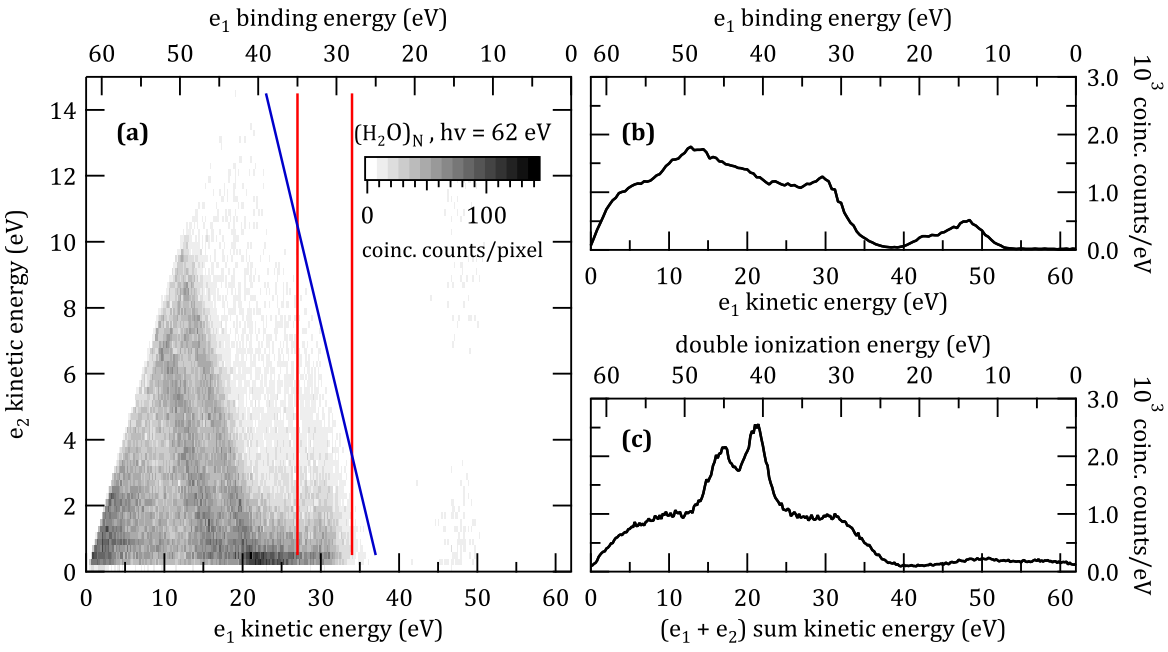

Figure 5.3: Coincident electron spectra of small water clusters, with $\langle N \rangle = 5$, recorded at 62 eV photon energy. (a) is the two-dimensional correlation map of electrons e_1 and e_2 emitted after irradation. (b) displays the coincident e_1 electron spectrum and (c) the double ionization spectrum. The ICD signature in the correlation map is enclosed by the two red lines. Coincident events of constant final state energy, but arbitrary energy sharing of the two electrons, such as molecular double ionization, is found parallel to the blue line.

and binding energy (top) and e_2 is a secondary electron also given in kinetic energy. The correlation map consists of three distinct features which are in the order of decreasing e_1 kinetic energy: the $2a_1$ ICD signature around 30 eV, the gas phase double ionization signature between 10 – 20 eV kinetic energy and the signature of inelastically scattered electrons underlying the other features, with its main intensity close to 0 eV kinetic energy. In fig. 5.3(a) the ICD signature is enclosed by the two red lines indicating its coincidence signal is composed of a $2a_1$ photoelectron of $\sim$ 32 eV binding energy and a secondary ICD electron of near zero to $\sim$ 4 eV kinetic energy. The molecular double ionization signature of gas phase water in the cluster beam on the other hand is visible as two diagonal lines parallel to the solid blue line.

The trace in figure 5.3(b) correspond to the coincident e_1 electron spectrum, in which all coincident events are projected onto the horizontal axis. It can be displayed as a function of e_1's kinetic energy (bottom) and its binding energy (top).

Figure 5.3(c) shows the double ionization spectrum, which corresponds to the coincident events of constant final state energy. It is generated as a histogram of the sum of kinetic energies of the e_1,e_2-coincidences. It is therefore displayed as a function of $(e_1 + e_2)$ sum kinetic energy (bottom) and the double ionization energy (top), derived according to equation 2.9 (see section 2.2).

Obviously, the two types of spectra contain the same information although some features are obscured in one or the other. For instance, the coincident $2a_1$ peak at $\sim$ 32 eV binding energy, which has been used for the quantitative determination of ICD (see section 4.1.1), is clearly visible in the dashed trace. In the double ionization spectrum the $2a_1$ ICD signature is broadened with its maximum at $\sim$ 31 eV DIE. The same holds for the intensity between 10 – 20 eV binding energy which is attributed to random coincidences of an outer valence electron with a secondary electron of arbitrary energy. In the double ionization spectrum these random coincidences are washed out over the range of 0 to about 20 eV DIE[1]. As for the gas phase double ionization signal, it can be seen in the e_1 coincident spectrum as broad asymmetric peak between 40 – 55 eV binding energy. However, it consists of two well separated peaks at $\sim$ 41 and $\sim$ 46 eV double ionization energy. Hence, depending on the choice of the one-dimensional representation it is possible to identify and emphasize different spectral signatures in the coincident electron spectrum.

In coincidence experiments on a molecular cluster beam it is possible to follow the double ionization spectrum of water as a function of mean cluster size i.e., as a function of progressing condensation. The measurements were performed for water clusters with mean sizes $\langle N \rangle$ of 5 to 241 molecules at 62 and 80 eV photon energy. The resulting double ionization spectra are compiled in figures 5.4(a) and (b), respectively. In both panels the spectral intensity is normalized at the leading gas phase double ionization peak at 41 eV double ionization energy to enable the comparison of the spectra. The mean cluster size is indicated by the color gradient of the traces with dark red representing small clusters and black denotes

[1] As these random outer valence coincidences do not have a physical meaning, they were subtracted in subsequent double ionization spectra.

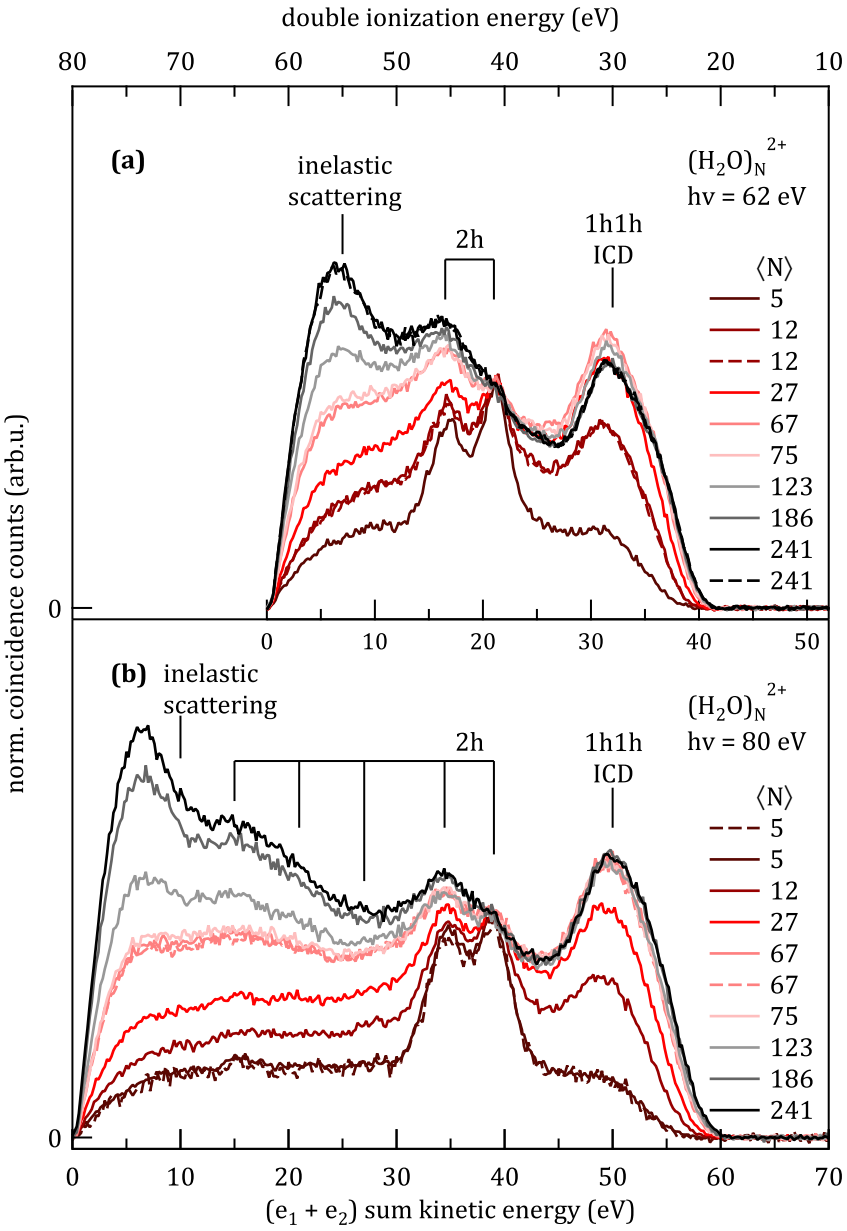

Figure 5.4: Double ionization spectrum of water clusters of increasing mean size ranging from 5 to 241 molecules on average recorded at (a) 62 and (b) 80 eV photon energy. Labeled are the 1h1h final states of the ICD process, the 2h states of the gaseous water molecules present in the cluster beam and the signal of inelastically scattered electrons. Upon increasing cluster size and increasing degree of condensation the signal of inelastic scattering increases, whereas the intensity of molecular double ionization is reduced.

larger clusters of 241 molecules on average. In the spectra three distinct features are visible: the 1h1h dicationic final states corresponding to the ICD process, the 2h states of the free water molecules in the cluster beam and the signature of inelastically scattered electrons. With increasing cluster size the intensity of the 2h states is reduced, which is in line with the increased degree of condensation in the cluster beam (see table 4.2 in section 4.1.1). In turn, the coincidence intensity of the 1h1h states increases with increasing cluster size as

the efficiency of the ICD process i.e., the probability of populating the 1h1h final states, increases. Additionally, the intensity of the inelastically scattered electrons, which constitutes the background under the double ionization peaks, increases as well.
The coincidence counts leading to the 1h1h states around 31 eV double ionization energy can be analyzed with regard to the energy sharing ratio of the two coincident electrons e_1 and e_2. For this purpose the coincident e_1 electron spectrum is fitted with a Gaussian distribution to determine the position and width of the signature on the e_1 kinetic energy axis. Subsequently, all coincident events whose $e_1 + e_2$ sum kinetic energy lies within the range defined by the fit, are selected for further analysis. This subset corresponds to 1h1h coincident events following the diagonal i.e., states of constant $e_1 + e_2$ sum kinetic energy, in the two-dimensional correlation map (see figure 5.3(a)) with a width of about 8 eV. The energy sharing ratio is obtained by division of the e_1 kinetic energy by the sum kinetic energy of the electron pair: $e_1/(e_1 + e_2)$. The resulting energy sharing ratios for the size dependent measurements of water clusters are shown in figure 5.5. The color gradient of the traces is

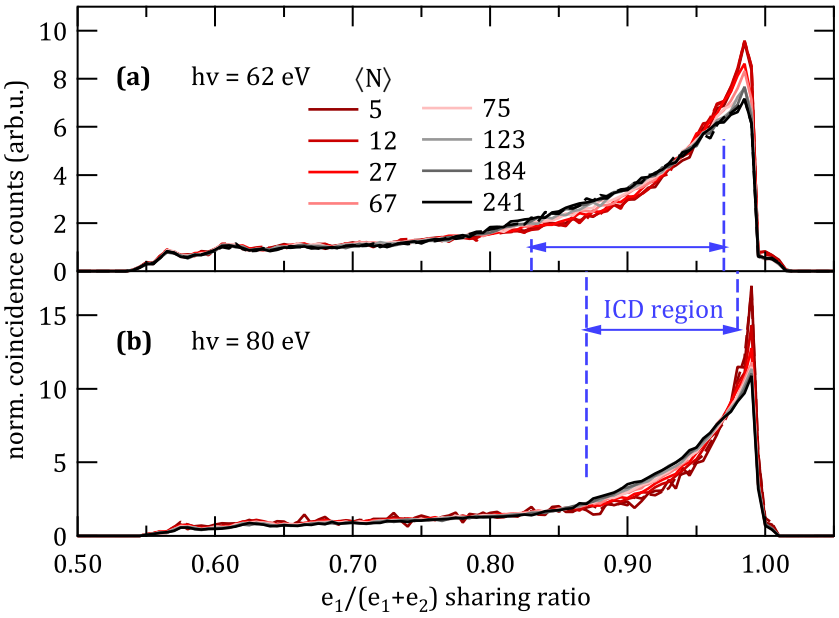

Figure 5.5: $e_1/(e_1 + e_2)$ energy sharing ratio of the electrons corresponding to the first double ionization state of water clusters of 5 to 241 molecules for coincident electron spectra taken at (a) 62 and (b) 80 eV photon energy. For comparison the traces are normalized to unit area. The area between the blue dashed lines corresponds to the region in which coincidences $P(e_{h\nu}, e_{ICD})$ of $2a_1$ photoelectrons and ICD electrons of $1-6]$ eV energy occur.

the same as before ranging from dark red for small clusters to black for larger clusters. The traces are normalized to unit area to enable comparison within the data set. By definition the energy sharing is asymmetrical with e_1 possessing more energy than e_2 (see section 3.4.1). This asymmetry is found to increase with increasing incident photon energy. The region between the two blue dashed lines denoted as the *ICD region* corresponds to electron pairs with e_1 having a kinetic energy of 31 or, respectively 49 eV kinetic energy (corresponding to the $2a_1$ inner valence state measured at 62 and 80 eV photon energy) and e_2 in an interval of

1 to 6 eV kinetic energy. It can be recognized that upon increasing the average cluster size the energy sharing distribution is flattened due to an increase of the ICD intensity. This observation is analogous to the broadening of the ICD electron distribution presented in figure 4.11. Flattening of the energy sharing distribution is present in both data sets recorded at different photon energies. It is therefore possible to infer information on the presence of ICD from double ionization spectra, specifically from the energy sharing ratios of a coincidence pair leading to the same double ionization energy.

After analyzing the coincident electron spectra of water clusters, analogous measurements were attempted in combining the water liquid jet with a magnetic bottle electron spectrometer. Figure 5.6 shows two coincidence spectra from these experiments comparing the spectrum of (a) the water liquid jet and (b) the water vapor phase surrounding the liquid jet. Analogous to the measurements on water clusters, a small acceleration voltage of +3 V was

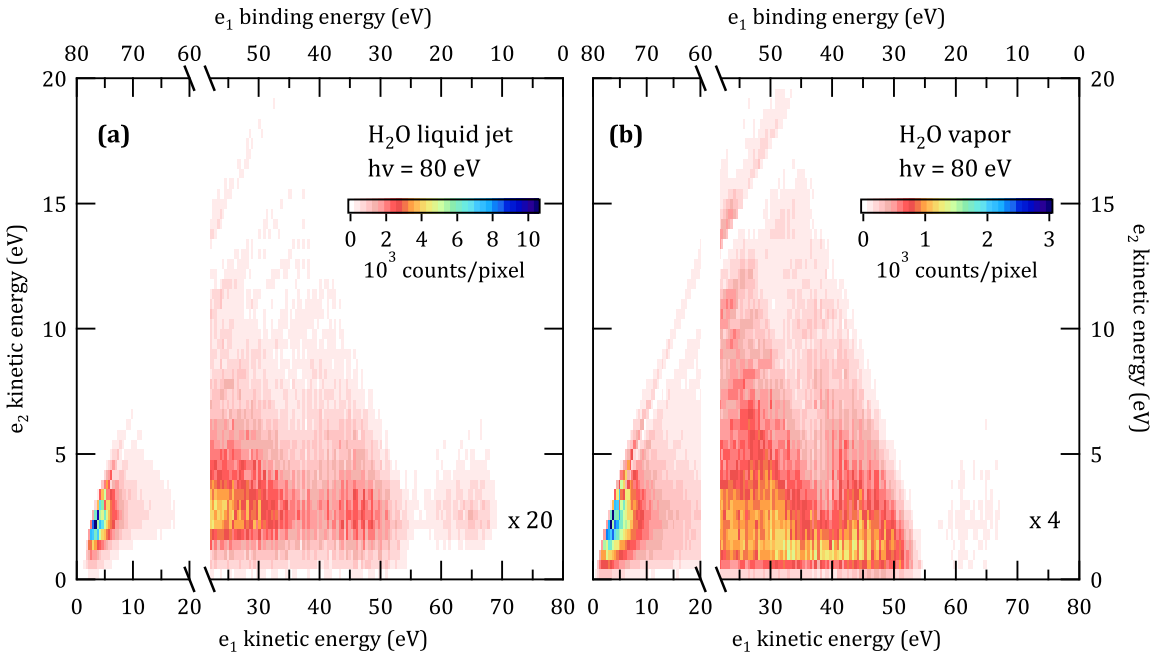

Figure 5.6: Electron correlation map of (a) liquid water and (b) water vapor evaporating of a liquid jet recorded at 80 eV photon energy. The experiments on the liquid jet were conducted analogous to previous investigations of water clusters [12, 105].

applied to the spectrometers drift tube and −2 V to the permanent magnet to ensure that electrons of about zero kinetic energy can be detected. Additionally, the liquid jet itself was biased at −2 V relative to the ground potential of the chamber and the analyzer. The liquid jets' electron correlation map in fig. 5.6(a) closely resembles the two-dimensional spectra of water clusters. The signature of inelastic scattering, however, is much stronger and the signal intensity in the region of 0 to 58 eV e_1 binding energy needs to be enhanced by a factor of 20 for proper visualisation. The intensity between 40 to 60 eV binding energy can be assigned to double ionization from the vapor phase around the liquid jet and the intensity around 32 eV binding energy resembles the signature of 1h1h final states occupied in the ICD process. The latter feature is of particular interest here.

Figure 5.6(b) is an analogous electron correlation map of the water vapor surrounding the liquid jet. In conventional liquid jet photoelectron spectroscopy the spectra of the vapor phase are often used to identify features that are unique to the condensed phase. For this purpose, the liquid jet is lowered by several millimeters so that the volume probed by the light only contains water molecules evaporated from the liquid jet. Surprisingly, the two-dimensional spectrum of water vapor shows a considerable amount of coincidence intensity around 32 eV e_1 binding energy. This intensity follows a diagonal path parallel to the gas phase double ionization signature in the coincidence map. For more insight into the observed features, the coincidence signal is projected onto the sum kinetic energy axis i.e., the double ionization axis. Such double ionization spectra are displayed in figure 5.7 for water vapor measured at 62 and 80 eV photon energy. The gas phase spectrum measured at 110 eV

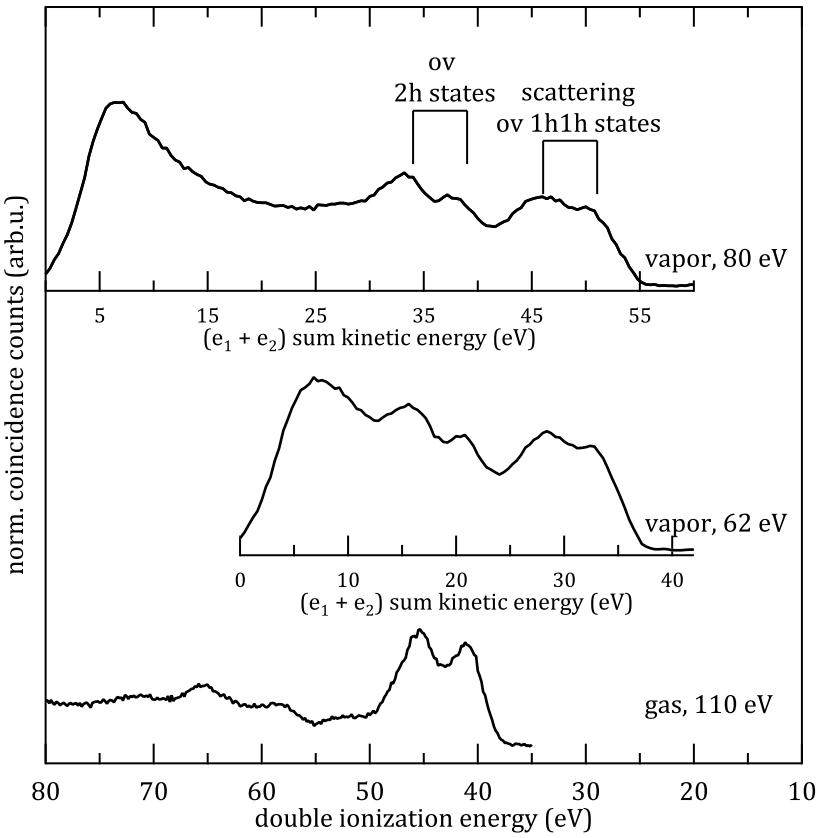

Figure 5.7: Double ionization spectra of water vapor at 62 and 80 eV as well as the double ionization spectrum of gaseous water at 110 eV photon energy for reference [28]. The spectra are aligned on the double ionization energy scale. For the vapor phase traces the individual sum kinetic energy axes are displayed as additional bottom axes.

photon energy is added as a reference. In this representation the double peak structure of the gas phase double ionization is well resolved and lines up with the reference spectrum. This double peak structure is also reflected in the signal between 25 to 35 eV double ionization energy. In contrast to the gas phase reference, the vapor spectra presented here contain a relatively prominent contribution of inelastically scattered electrons. From the intense inelastic scattering background, it can be assumed that the vapor phase is much more dense than in

ref. [28]. Electrons emitted from one water molecule therefore undergo scattering processes on water molecules in the vicinity. In fact, the newly observed double peak structure between 25 to 35 eV can be explained by assuming two singly ionized non-interacting water molecules. In this case, the final states can be assigned analogous to the gas phase double ionization spectrum with the respective molecular orbitals e.g., $1b_1^{-1}1b_1^{-1}$ or $3a_1^{-1}1b_1^{-1}$, but they are of 1h1h character with the positive charges well separated from each other. The process is illustrated in figure 5.8. Here, a photon ionizes a water molecule from which elec-

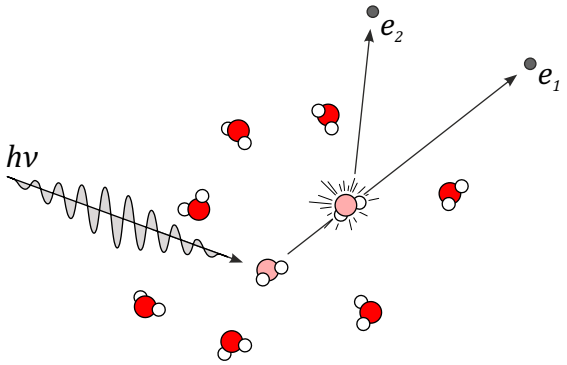

Figure 5.8: Double ionization in dense vapor phase by intermolecular scattering of the initial photoelectron e_1. e_1 acts as a projectile and leads to emission of e_2 from a neighboring water molecule by electron impact ionization.

tron e_1 is ejected. The outgoing photoelectron with tens of electron volt kinetic energy acts as a projectile and leads to emission of a second electron e_2 from water a molecule in the vicinity by electron impact ionization. The underlying mechanism is likely a "knock-out" process known from electron impact ionization experiments [201].

Similar to the Auger decay after initial photoexcitation or -ionization, ICD as a non-local electronic decay mechanism involving neighboring atoms or molecules is thought to be a very general process occuring in weakly bound systems held together by van-der-Waals interactions or hydrogen bonds. While most experimental systems in the research on non-local decay phenomena were performed on atomic or molecular clusters, it could already be shown that non-local channels are active after core-level excitation or ionization in liquid water and aqueous solution [18] (see previous chapter). Therefore, it is a reasonable assumption that in liquid water the ICD process is also allowed after inner valence ionization analogous to water clusters. Coincident electron spectroscopic measurements should allow the detection of ICD electrons of very low kinetic energy emitted in coincidence with inner valence electrons. These coincidences are, however, hard to identify. Additionally, it could be shown that the respective energy window overlaps with the signature of 1h1h double ionization states formed by photoelectron impact ionization in the vapor phase. Since all contributions to the coincidence electron spectrum of a liquid jet are known, a tentative analysis of the double ionization spectra of water vapor compared with liquid jet data should give new insights into the occurrence of ICD. Figure 5.9 shows such analysis of (a) water vapor and (b) liquid water double ionization spectra taken at 80 eV photon energy. The vapor phase spectrum in (a) is shown as lines and markers. It was fitted in the interval

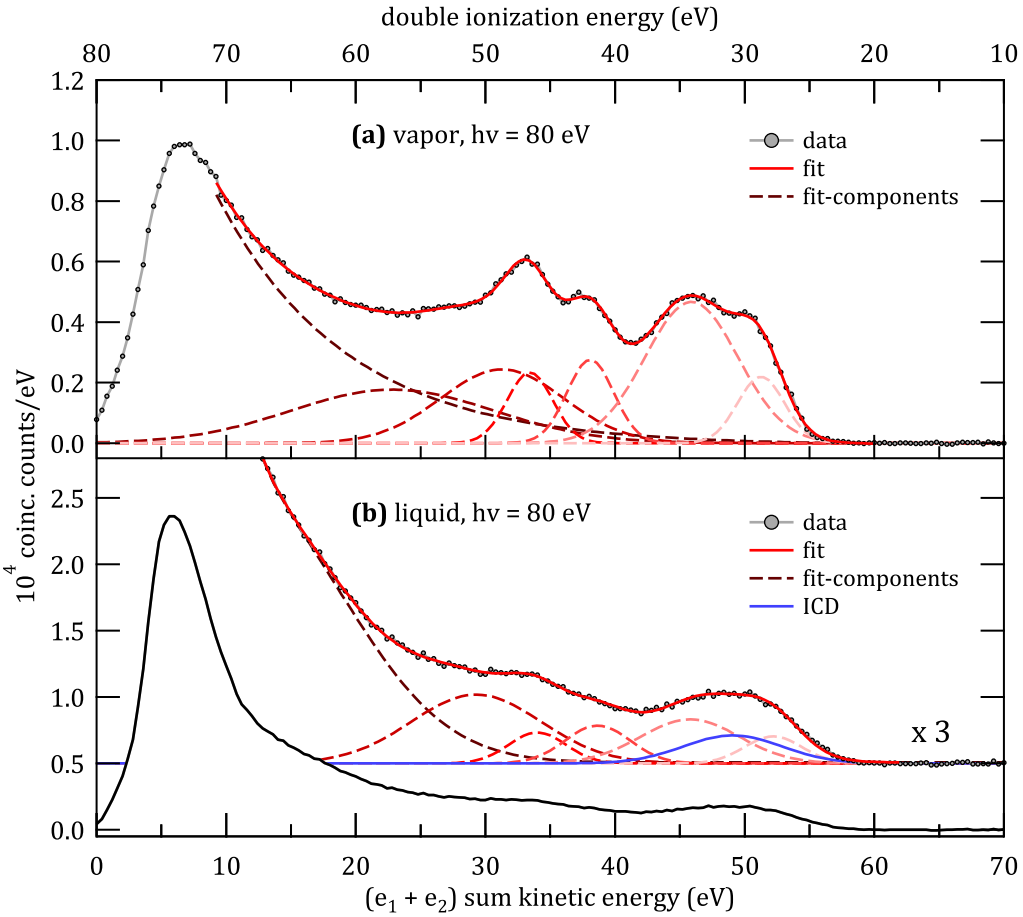

Figure 5.9: Detailed comparison of the double ionization spectra of (a) water vapor and (b) liquid water taken at 80 eV photon energy. In both spectra the first double ionization signal is visible at around 30 eV. Fitting of the spectra was tentatively attempted to identify the individual signal contributions. The fits are shown as solid red traces with its individual components shown as dashed 'reddish' traces. For the liquid jet spectrum (b) an additional peak was required to obtain reasonable results. This additional intensity could be assigned to 1h1h doubly ionized states corresponding to the ICD process.

of 10 to 60 eV sum kinetic energy using a model consisting of an exponentially decaying curve and six Gaussian distributions. The fit is shown as a solid red trace and its individual components as dashed traces. The fit function was based on the number of distinguishable peaks observed in the gas phase reference over the respective energy window on the double ionization energy scale (see fig. 5.1) plus two additional Gaussians for the newly identified 1h1h scattering states. The four leading peaks of highest kinetic energy corresponding to the doubly ionized 1h1h and 2h outer valence states are well resolved. The lower lying doubly ionized states are rather broad and of lower intensity and therefore merge with the inelastic scattering background.

Figure 5.9(b) displays the full liquid jet double ionization spectrum of water as solid black trace. It is notably less structured than the vapor phase spectrum. The fitted energy region is scaled by a factor of 3 for better visibility. The same features can be found in (a) and (b) albeit broadened and of lower contrast to the scattering background. For (b) the

vapor phase fit function was augmented by an additional Gaussian. The vapor phase fit results were used as input parameters and constraints were set especially on the two sets of double peaks to ensure comparability with the vapor phase spectrum. These constraints on the amplitudes of the double peaks, respectively, the ratio of their amplitudes, the energetic positions and width were chosen in a way that all fit parameters were allowed to to move within a small interval. The individual contributions are depicted as dashed lines and the additional Gaussian component is shown as solid blue trace. The additional Gaussian component is required to properly describe the signal around 30 eV double ionization energy of the condensed phase. It was tried to omit this additional Gaussian component, however, the respective fit could not converge. In other words: in contrast to water vapor, the double ionization of liquid water exhibits an increased number of coincidence counts at around 30 eV double ionization energy. Since all other components of the double ionization spectra could be identified in the vapor phase, the additional intensity can be tentatively assigned to 1h1h final states populated by inner valence ICD in liquid water.

To further test this claim, the energy sharing ratio of electron coincidences corresponding to the 1h1h final state were determined. It was previously established for water clusters of varying size that the detection of coincidence events comprised of an inner valence electron and a slow ICD electron are visible in the energy sharing ratio traces as an intensity redistribution at the side of highly antisymmetric energy sharing (see fig. 5.5). The energy sharing ratio $e_1/(e_1+e_2)$ for spectra obtained at different photon energies is displayed in figure 5.10. The black and red traces correspond to the sharing ratios of the liquid and vapor phase, re-

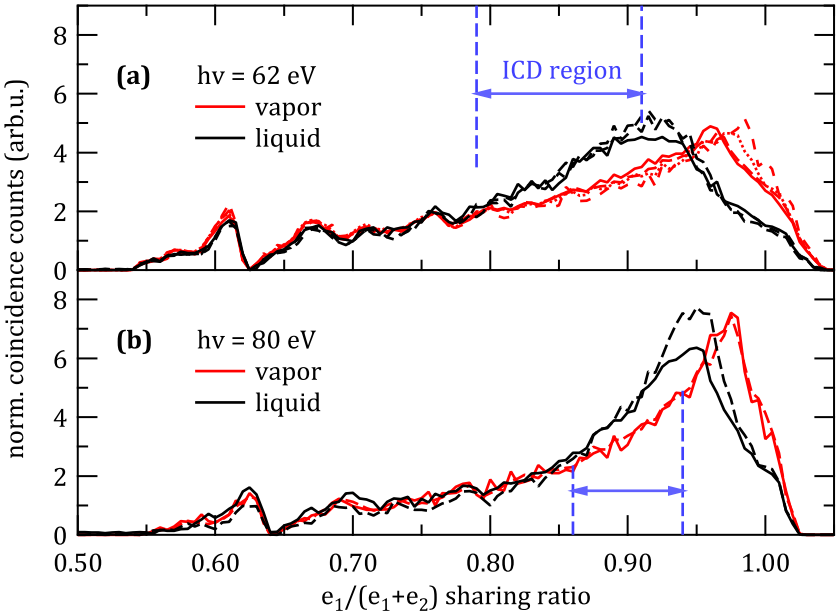

Figure 5.10: $e_1/(e_1+e_2)$ energy sharing ratio of the doubly ionized state at around 30 eV ionization energy for spectra taken at (a) 62 and (b) 80 eV photon energy. The red and black traces correspond to measurements of the vapor and the liquid jet, respectively. The blue dashed lines indicate the region relevant to coincidence events originating from the ICD process similar.

spectively. Each trace is normalized to unit area to enable qualitative comparison of the two phases. (a) was determined for spectra taken at 62 eV and (b) at 80 eV photon energy. In both panels, the region enclosed by the blue dashed lines indicates the region containing coincidences originating from the ICD process. When comparing the liquid jet and vapor traces the intensity is higher in the marked region, which in addition to the previously observed additional intensity in fig. 5.9(b) points towards the presence of ICD electrons.
For completeness, it should be noted that the energy sharing traces of the liquid jet exhibit a step-like feature at a value ~ 1.00, in contrast to the vapor phase. It is believed that this step is a result of the applied spectrometer settings. In the experiments the spectrometer was set to ensure that all emitted electrons, especially those of very low kinetic energy, were accelerated into the spectrometer. This was realized by setting accelerating potentials of $+3$ V to the spectrometer drift tube, -2 V to the permanent magnet and a bias voltage on the liquid jet itself. Specifically the jet bias voltage, which was set to -2 eV, leads to differences between jet and vapor spectra. The water jet is conductive due to a small amount of sodium chloride added in preparation of the liquid jet[2]. Therefore, electrons emitted from the liquid surface experience a potential of around 2 V, the vapor phase however is not conductive. So, electrons emitted from the vapor phase experience a lower potential than the one's emitted from the jet. In order to verify that the observed intensity in the energy sharing ratio in the ICD relevant region is real, rather than an artifact of the jet bias voltage, an analogous analysis was performed for spectra recorded in a different beamtime were no bias was applied to the liquid jet. The results are shown in figures 5.11 and 5.12 for water vapor and liquid spectra recorded at 100 eV photon energy. The applied fit function was akin to the one for the previously shown spectra measured at 80 eV photon energy, however, the number of Gaussians was adjusted to reflect the extended energy range. Again, the data treatment comprises of carefully fitting the well structured vapor phase spectrum (a) followed by constrained fitting of the liquid jet spectrum (b) using the previous fit results as input parameters. As seen for the preceding example (see fig. 5.9(b)) for optimal fit results of the liquid jet spectrum an additional Gaussian contribution indicated by the blue trace is required, which is assigned to the ICD process. However, the intensity and width of the ICD signature is lower compared to fig. 5.9(b). Overall, the liquid jet double ionization spectrum at 100 eV appears slightly more structured, especially in the region of 30 eV double ionization energy. The double peak structure associated with the electron impact ionization is apparent, which indicates a relatively high gas phase contribution.
The $e_1/(e_1+e_2)$ energy sharing ratio (fig. 5.12) of the double ionization signal around 30 eV double ionization energy was determined for the two spectra with the vapor phase as red and the liquid phase as black trace. Both traces are normalized to unit area. Similar to the spectra measured at 80 eV it shows an asymmetric shape with the electron e_1 predominantly having the higher kinetic energy. It should be emphasized that the step associated with the jet bias in fig. 5.10 is absent in the present traces as no bias voltage was applied. Here, the blue dashed lines again indicate the area in which coincidences of electron e_1 with and ICD

[2]In photoelectron spectroscopic experiments a pure water spectrum actually refers to a very diluted aqueous solution of 0.05 mol/l of sodium chloride. It is added in order to avoid charging of the liquid jet upon ionization.

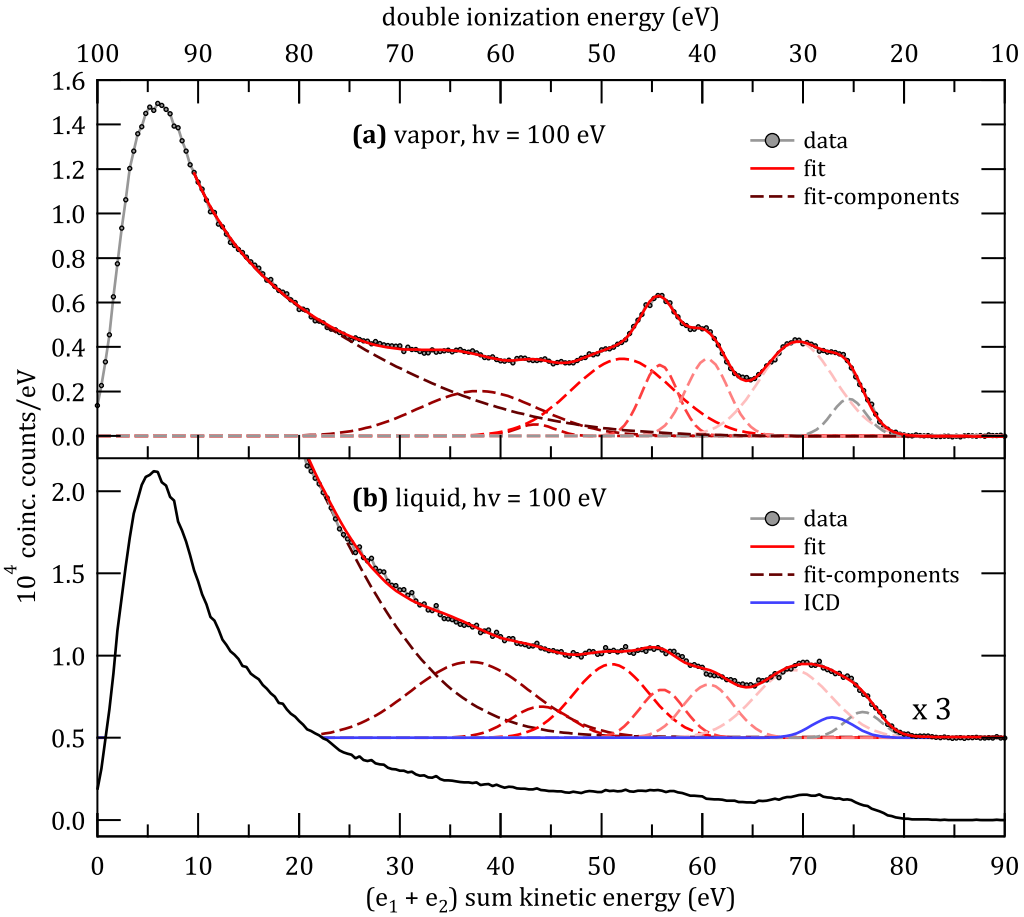

Figure 5.11: Comparison of the double ionization spectra of (a) water vapor and (b) liquid water taken at 100 eV photon energy. The fits are shown as solid red traces with its individual components shown as dashed 'reddish' traces. For the liquid jet spectrum (b) an additional peak (see blue trace) was required to obtain reasonable results. Consistent with the results in fig. 5.9 the additional peak is assigned to the ICD process.

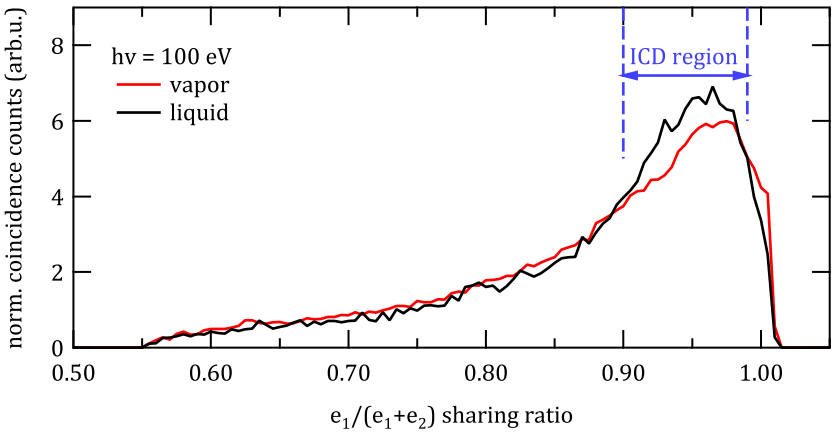

Figure 5.12: $e_1/(e_1+e_2)$ energy sharing ratio of the doubly ionized state at around 30 eV ionization energy for spectra taken at 100 eV photon energy. The red and black traces correspond to measurements of the vapor and the liquid jet, respectively. The blue dashed lines indicate the region relevant to coincidence events originating from the ICD process.

electron of about 1 to 6 eV kinetic energy are expected. The direct comparison of the two traces reveals an additional intensity within the marked ICD region. This observation is in line with the preceding results in fig. 5.10, which suggests that the additional signal is not an artifact of the jet potential. But it rather corroborates the assumption that the additional intensity can be credited to the inner valence ICD process taking place in solution.

In conclusion, the double ionization spectrum of a water liquid jet was measured for the first time. In a comprehensive comparison with the double ionization spectra of gaseous water, water clusters of varying size, and water vapor the different signal contribution to the liquid jet spectrum could be identified. The comparison of the gas phase and cluster spectra was straightforward and yielded distinct signatures of direct double ionization of gaseous water molecules and ICD as the non-local autoionization mechanism of the condensed phase. Whereas, the interpretation of the water vapor and liquid jet spectra was less clear. In the latter two, a spectral feature was apparent in the energy region associated with the inner valence ICD process. Since ICD is considered as a general electronic relaxation process, the emergence of a signature of ICD in liquid water is readily justifiable. However, the observation of a feature of similar shape in the vapor phase was not in line with the aforementioned process. A comparison of the gas phase reference by Feifel and Eland [28] with the vapor phase spectra suggested that newly observed signature is a result of the elevated sample density. Electrons emitted from one water molecule are capable to scatter on another molecule on their trajectory to the spectrometer and induce the emission of a second electron via electron impact ionization.
Transferred to the liquid jet double ionization spectra, a superposition of doubly ionized final states is observed resulting from two different mechanisms which are schematically depicted in figure 5.13. (a) illustrates the analogous process observed in the vapor phase spectra, namely the ionization of two non-interacting water molecules by absorption of a

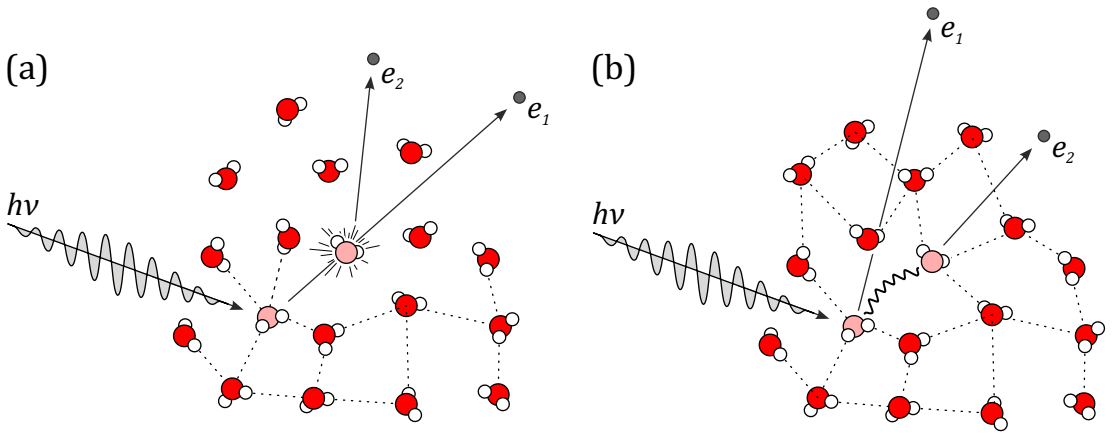

Figure 5.13: Processes leading to dicationic final states of similar energy in the double ionization spectrum of the water liquid jet. (a) shows the ionization of two water molecules in a single photoionization event by electron impact of the initially emitted liquid jet photoelectron with a water molecule in the surrounding vapor phase. (b) is the double ionization of two neighboring water molecules in the liquid phase by intermolecular energy transfer, namely ICD.

single photon. A water molecule in the liquid phase is photoionized, the resulting photoelectron carries enough excess energy to ionize a second water molecule in the dense vapor phase surrounding the liquid jet by electron impact. On the other hand, (b) depicts the ICD process in aqueous solution, in which the inner valence orbital $2a_1$ of one water molecule is photoionized leaving the molecule in an excited state. Subsequently, this molecule can energetically relax by transferring its energy to a neighboring molecule from where a second electron is emitted, typically of very low energy. It was possible to separate these two processes in a tentative analysis, which allows reporting the first experimental indication of the non-local decay mechanism in liquid water. A systematic examination of the coincident electron energy sharing ratio of the double ionization signature around 30 eV double ionization energy of water clusters, vapor and the liquid jet corroborated this interpretation.

Unlike for the results on water clusters in section 4.1.1, a quantitative analysis of the coincidence $2a_1$ signal to determine ICD efficiency is challenging due to the high vapor phase contribution to the spectra and the resulting overlap between ICD signal and the signature of double ionization via photoelectron impact. In order to briefly elaborate on the complication of determining the efficiency of the decay process in liquid water, the ICD efficiency α_{ICD}, which was introduced in equation 4.3, shall be revisited.

$$\alpha_{\mathrm{ICD}} = \frac{P(E_{\mathrm{ph}}, E_{\mathrm{ICD}})}{p(E_{\mathrm{ph}})}$$

Here, the efficiency as described for an ideal coincident electron spectroscopic experiment is given by the number of coincidences of photoelectrons and ICD electrons $P(E_{\mathrm{ph}}, E_{\mathrm{ICD}})$ related to the total number of electrons of the respective energy $p(E_{\mathrm{ph}})$. Under realistic conditions, various experimental uncertainties need to be considered as additional parameters, such as the finite detection efficiency of ICD electrons $\gamma(E_{\mathrm{ICD}})$ or the degree of condensation in a cluster beam c. While the parameter $\gamma(E_{\mathrm{ICD}})$ is still valid for the liquid jet spectra, the parameter c is obsolete. Instead the effects of inelastic scattering of photoelectrons and ICD electrons within the liquid jet might have to be taken into account. In addition, a parameter is required describing the signal attenuation, depending on the density of the vapor phase, which is strongly dependent on the temperature of the liquid jet, or in other words the equilibrium vapor pressure at the respective temperature. It is noteworthy that one of the key differences in the coincident experiments on the cluster beam and the liquid jet is the pressure in the interaction chamber. In the cluster experiments the pressure in the experimental chamber is usually in the range of 10^{-6} to lower 10^{-5} mbar and the cluster beam is skimmed, creating a rather dilute environment in the interaction region. Whereas for the liquid jet experiments the chamber pressure is at 10^{-4} to 10^{-3} mbar and especially the immediate surrounding vapor phase of the jet is at even higher pressure. It can be crudely approximated with the water vapor pressure at a set water temperature e.g., at 12 °C the equilibrium vapor pressure is around 14 mbar. So, the pressure difference between the two experiments spans about 6 to 7 orders of magnitude. Based on these considerations, an

attempt to quantify the ICD efficiency in liquid water would require a systematic investigation of the coincident electron spectra of a temperature controlled liquid jet thereby varying the amount of vapor phase in the probed volume. As of now, the presented results are of qualitative nature.

A different aspect of this first investigation of the liquid jet double ionization spectrum is that it enables a more detailed understanding of the background in the conventional photoelectron spectrum of liquid water, specifically in the inner valence region. In an early publication of the photoelectron spectrum of liquid water by Winter et al. [87] broad features in the extended valence spectrum in the range of 20 to 60 eV binding energy were attributed to photoelectrons loosing their energy by inducing quasi-optical transitions in the vapor phase. While this process appears plausible, the coincident double ionization signatures identified in the present work cover the same energy range when projected onto the photoelectron axis. It is therefore likely that single photon double ionization does contribute to the electron intensity observed in the extended valence spectrum of the water liquid jet.

Chapter 6

Electron Transfer Mediated Decay in Electrolyte Solutions

The focus of the following chapter is on electron spectroscopic experiments on aqueous solutions of inorganic ions. Upon photoionization of the respective cation the non-local process of electron transfer mediated decay (ETMD) can be triggered. The ETMD process was introduced and illustrated earlier in chapter 2.3.3. Briefly, ETMD is a non-local electronic relaxation mechanism. After initial photoionization of one atom or molecule, an electron of a second site is transferred and by the energy gained via this transfer a secondary electron — the ETMD electron — is emitted by the second atom or molecule. In this process the initial site recovers its initial electronic configuration; a fact which clearly distinguishes ETMD from intermolecular coulombic decay (ICD). The process was originally described in detail in references [7] and [202] and could be experimentally observed in various rare gas clusters[69, 93, 203–205]. Similar to other autoionization mechanisms, such as Auger decay and ICD, ETMD is a process of very general nature. In an early publication by Müller *et al.* the process was also predicted to take place in a hydrogen bonded environment, namely in microsolvated $Li^+(H_2O)_N$ clusters [206]. Therein, calculated single and double ionization spectra of $Li^+(H_2O)_N$, with $N \leq 5$, were presented, from which the occurence of ETMD subsequently to Li 1s photoionization could be inferred. Electronic relaxation via ETMD is typically of lower probability compared to other processes due to the required orbital overlap connected to the initial electron transfer step. The system of hydrated Li^+, however, presents a special case as ETMD is the only accessible relaxation pathway after Li 1s ionization. The Li cation lacks electrons of lower binding energy which could fill the 1s vacancy, however, the surrounding water molecules, predominantly those of the first solvation shell, are capable to do so. A detailed hole population analysis of the spectra revealed the existence of two distinguishable types of final states corresponding to a single H_2O^{2+} or two H_2O^+ cations, created in an ETMD(2) or ETMD(3) process, respectively.[1] The estimated lifetimes of the Li 1s excited states in the microsolvated system were comparable to the ones seen for ICD in rare gas clusters analogous in size, causing the ETMD process to be similarly efficient as ICD; a fact associated with ETMD being the single accessible decay channel [206].

[1] As introduced in section 2.3.3, the numbers in ETMD(2) and ETMD(3) denote the total number of molecular units involved in the decay process.

Solvated Li^+ was recently revisited in the experimental works of Unger *et al.* [207] and Pohl *et al.* [73]. These two publications describe the first observation of ETMD in the aqueous environment of a liquid jet. In the work by Unger and co-workers the signature of ETMD electrons was identified within the background of inelastically scattered photoelectrons emitted from a liquid jet of LiCl solution ionized with soft X-ray radiation. The measurements were performed using a hemispherical electron analyzer, resulting in autoionization spectra of relatively high noise level. Nevertheless, in conjunction with ab initio molecular dynamics simulations and calculated double ionization spectra it could be shown that the electron spectroscopic signature was a result from the ETMD process. Moreover, the results indicated a sensitivity of the ETMD energy distribution to the ion pairing motif in the electrolyte solution. Ion pairing describes the extent of interaction/association of typically two oppositely charged ions in solution. It is an important effect when studying ion mobility in solution and when considering the distribution of ions from bulk solution to the surface. From the results of Unger and co-workers [207] it is deduced that the reported ETMD spectrum of LiCl solution is dominated by formation of *solvent shared ion pairs* (SShIP). Furthermore, the calculated ETMD double ionization spectra suggested a critical dependence of the Li^+ cation's chemical surrounding, especially on the composition of the first and second solvation shell. The authors around Pohl *et al.* [73] performed follow-up experiments on Li^+ solutions employing the coincident electron detection scheme presented in section 3.4.1. In these experiments, for the first time electron-electron coincidence spectroscopy was applied to a liquid sample. Here, the emission of secondary ETMD electrons could be unambiguously assigned to the initially emitted Li 1s photoelectron, confirming the results of ref. [207]. Furthermore, applying the coincident electron detection scheme with a magnetic bottle electron spectrometer allowed for an improved electron collection efficiency and a strongly increased contrast between background and ETMD electron intensity. The spectra of two different Li salts were compared, namely lithium chloride (LiCl) and lithium acetate (LiOAc), which supposedly form two distinct ion pairing motifs in solution. In fact the ETMD electron distributions of LiCl and LiOAc show a significant difference in signal intensity at higher kinetic energy, which was attributed to the formation of *contact ion pairs* (CIP) in LiOAc solution, creating a solvation shell which incorporates the acetate counter ion. The counter ion thus strongly participates in the ETMD process due to an increased orbital overlap between the ions. Thereby, it could be experimentally shown that the ETMD electron spectrum is sensitive to ion pairing.

While the aforementioned theoretical and experimental results focus on the special case of the solvated monovalent Li^+ cation, the ETMD process is, as previously stated, a general phenomenon which was emphasized by the extensive theoretical investigation in ref. [15]. Therein, the X-ray induced photochemistry of metal ions in an aqueous environment was tracked, as metal centres are found in numerous biomolecules and enzymes where they fulfill catalytic functions [208]. These metal centres are, however, prone to inflict radiation damage to their molecular surrounding upon interaction with high energy photons. In ref. [15] the microsolvated Mg^{2+} cation was investigated. It was observed that Mg 1s core-level ionization is followed by a complex electronic deexcitation cascade. The main result is that the

electronic relaxation of the core-excited state proceeds along multiple pathways, combining an initial local Auger decay with subsequent steps by non-local autoionization mechanisms, namely ICD and ETMD. A schematic overview of these findings is shown in Fig. 6.1. While

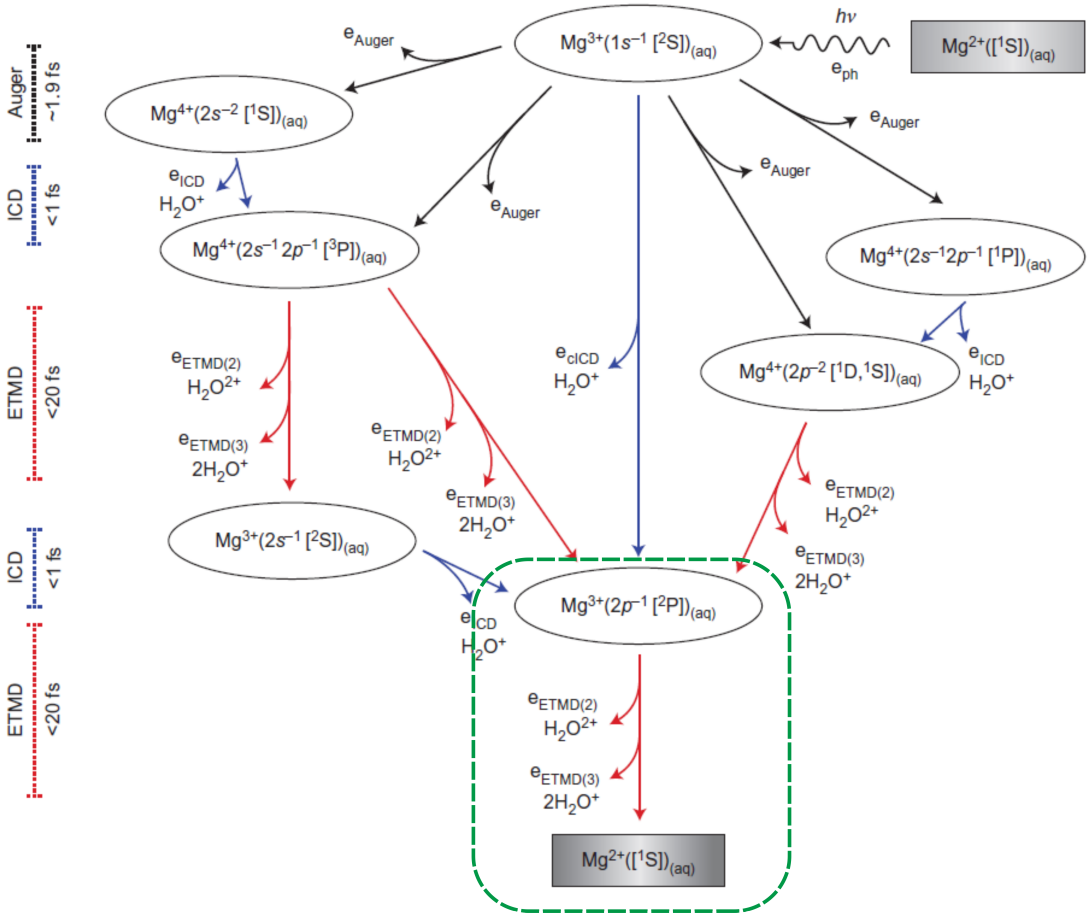

Figure 6.1: Schematic description of the electronic decay processes that take place after the core ionization of a hydrated Mg^{2+} cation. First, the intra-atomic Auger decay (black arrows) creates highly charged Mg^{4+} cations. Then, the energetic ions lose their excess energy by ICD. The Mg^{4+} ions with little excess energy undergo ETMD and become reduced. Computed electronic decay lifetimes for $Mg^{q+}(H_2O)_6$ clusters are shown on the left. The cascade continues until all the Mg^{4+} and Mg^{3+} ions revert to the original Mg^{2+} state in a sequence of ultrafast ICD (blue) and ETMD (red) steps. Accounting for the ionization of the water neighbours, the computed time for the complete cycle is 220 fs. Several reactive products, such as electrons, water cations and dications, are released, mainly from the first coordination shell of Mg^{2+}, as indicated by the arrows branching off the cascade pathways. e_{ph}, photoelectron. Taken from ref.[15].

the electronic relaxation cascade only lasts about 220 fs, the magnesium cation undergoes several changes of its oxidation state and finally ends up in its initial configuration. The vicinity of the magnesium cation, however, is drastically changed by the decay cascade. The emitted ETMD and ICD electrons are typically of relatively low kinetic energy and therefore highly reactive [13]. Furthermore, high reactivity is also associated with the oxidized water molecules and their reaction products. This behaviour of the magnesium cation in an hydrated environment and the multitude of competing relaxation pathways makes it especially relevant for radiation chemistry.

Since the ETMD process always requires an electron transfer step, rather than an energy transfer like in ICD and Auger decay, it is usually less efficient compared to those processes. However, fig. 6.1 shows an energetic situation (green dashed box), in which ETMD is the only accessible relaxation mechanism, much like in the previously discussed investigations of Li^+ solutions. The experiments compiled in this chapter focus on this part of the cascade process, namely the deexcitation of the inner valence ionized magnesium cation in the varying chemical environment of different counter ions. The purpose of this investigation was twofold: substantiating the general nature of the ETMD process, by experimentally showing that it is not restricted to the special case of solvated Li^+ ions[2] and further exploring the capabilities of coincident electron spectroscopy on liquid samples.

Experiments were conducted at the UE112 PGM-1 beamline at the BESSY II synchrotron radiation facility using a vacuum setup combining a magnetic bottle time-of-flight electron spectrometer with a liquid microjet, which was briefly described in section 3.5. The UE112 PGM-1 beamline provided synchrotron radiation in the VUV to soft X-ray range, which was the range required for the inner valence photoionization of Mg^{2+} cations in solution to induce secondary electron emission via ETMD. Ionization of the Mg 2p state creates the $Mg^{3+}(2p^{-1})$ excited state which can decay via ETMD electron emission (see green dashed box in fig. 6.1). Energetically, EMTD(2) and ETMD(3) are possible, involving two or three molecular entities. The respective processes are illustrated in eq. 6.1 and 6.2.

$$Mg^{2+} \cdot L_n \xrightarrow[-e_{h\nu}]{h\nu} Mg^{3+}(2p^{-1}) \cdot L_n \xrightarrow[-e_{ETMD(2)}]{} Mg^{2+} \cdot L_{n-1} + L^{2+} \tag{6.1}$$

$$Mg^{2+} \cdot L_n \xrightarrow[-e_{h\nu}]{h\nu} Mg^{3+}(2p^{-1}) \cdot L_n \xrightarrow[-e_{ETMD(3)}]{} Mg^{2+} \cdot L_{n-2} + 2\,L^{+} \tag{6.2}$$

Here, L_n denotes the ligands of the first coordination shell of the magnesium cation, namely H_2O or the respective anion. The investigated magnesium salt solutions were prepared using magnesium chloride ($MgCl_2$), magnesium acetate ($Mg(OAc)_2$) and magnesium nitrate ($Mg(NO_3)_2$). These salts were chosen due to their good solubility in water, which is beneficial to conduct liquid jet experiments, and due to their different surface propensities and ion pairing motifs. According to the theoretical and experimental investigation by Götte and co-workers, in $MgCl_2$ solutions the two ions show a high surface propensity, with the chloride (Cl^-) anion localized at the water surface and the Mg^{2+} cation in the subsurface region, forming a SShIP with the counter ion [210]. In solutions of $Mg(OAc)_2$ the surface propensity is more pronounced combined with the formation of CIP [211] and in $Mg(NO_3)_2$ solutions the ions are predominantly found in the bulk, showing no clear picture of ion pairing [211, 212]. Figure 6.2 schematically summarizes these properties. Here, a drawing of a hypothetical water interface is depicted containing $Mg(OAc)_2$, $MgCl_2$ or $Mg(NO_3)_2$. The surface propensity of the different ions is indicated by their placement relative to the surface and

[2] In fact in very recent electron spectroscopic experiments on various different electrolyte solutions, hints of the non-local processes ICD and ETMD could be observed, which are most likely part of complex deexcitation cascades from excited deep core levels [209].

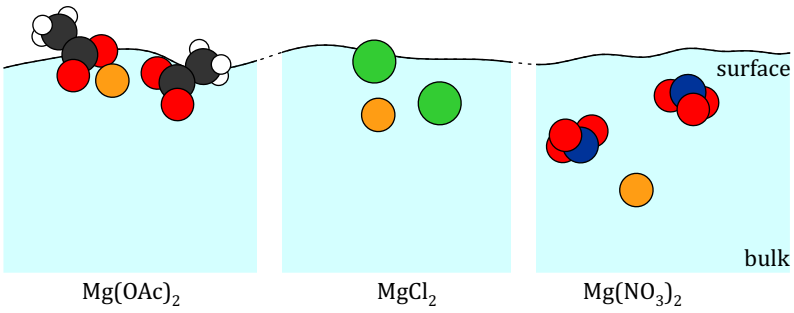

Figure 6.2: Illustration of the surface propensity and ion pairing motif of the different magnesium salts in aqueous solution based on the experimental and theoretical results in references [210], [211] and [212].

their supposed ion pairing is qualitatively illustrated by the distances between Mg^{2+} (orange) and the respective counter ion. Considering the differences in surface propensity and ion pairing, the chemical surrounding of the solvated Mg^{2+} ion, specifically its first solvation shell, and its localization in reference to the water surface are different for the respective counter ions. As the ETMD process is inherently dependent on orbital overlap of neighboring molecules, a change in the chemical surrounding of the initially excited site should be reflected in the ETMD electrons as well. Furthermore, the electrons emitted in the autoionization processes are subject to scattering processes, which limit its mean free path. The ETMD signature will, therefore, depend on the surface propensity.

As a general reminder and rule of thumb, autoionization takes place once the binding energy of a singly ionized initial state of a given system exceeds the double ionization energy. Under this condition it is energetically favourable to emit a secondary electron to reach a final state of lower energy. In the case of ETMD the final state is distributed over one or two molecules in the vicinity of the initial state. For ETMD in magnesium salt solutions, the initial state is the Mg 2p orbital and the final states can be any inner and outer valence molecular orbitals of liquid water and the states of the respective anions in aqueous solution. Energies for all of these states were available from the literature, except for the ionization potential of the acetate anion in solution, for which no reference could be found. The first ionization potential of the aqueous acetate was determined analogous to the method described in ref. [213]. The result is depicted in fig. 6.3. Here, an outer valence spectrum of pure water (black) and the corresponding spectrum of 1 M $Mg(OAc)_2$ solution (red) are shown on the kinetic energy (bottom) and binding energy scale (top). The acetate signal is clearly visible by its intensity below 10 eV binding energy. The spectra were normalized to the liquid water $1b_1$ molecular orbital, subsequently subtracted and fitted with a single gaussian, which is displayed as a grey shaded area. The resulting first ionization potential of the acetate anion in aqueous solution is 9.5(2) eV, which compares well with the ionization potentials of other typical anions in solution [213].
Table 6.1 summarizes all ionization potentials relevant to the ETMD processes in the respective Mg^{2+} solution. On the left side of tab. 6.1 is the initial state, namely the Mg^{2+} 2p orbital and on the right are the potential final states of liquid water and the individual anions in

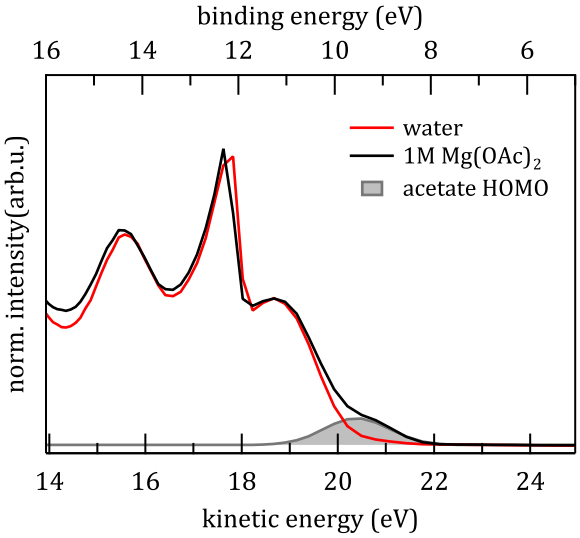

Figure 6.3: Photoelectron spectrum of water (red) and 1 molar solution of magnesium acetate (black). The additional peak at low binding energy is identified as the first ionization potential of the acetate anion at a binding energy of 9.5(2) eV.

Table 6.1: Initial and final states of inner valence ETMD in $Mg(OAc)_2$, $MgCl_2$ and $Mg(NO_3)_2$ aqueous solutions. *a* Literature value taken from ref. [74]. *b* Ionization potential measured within this work. *c* Taken from ref. [87] and [214]. *d* Taken from ref. [213]. All presented IPs refer to the liquid phase or the aqueous solution.

ETMD initial state			ETMD final states		
	state	IP (eV)		state	IP (eV)
Mg^{2+}	$2p_{3/2}$	55.51(48)[a]	H_2O (liq.)	$1b_1$	11.16(4)[c]
	$2p_{1/2}$	55.79(48)[a]		$3a_1$	13.50(10)[c]
				$1b_2$	17.34(4)[c]
				$2a_1$	30.90(6)[c]
			CH_3COO^-	HOMO	9.5(2)[b]
			Cl^-	HOMO	9.60(7)[c]
			NO_3^-	HOMO	9.35[d]

aqueous solution. From these values a rough estimation of the width of the ETMD electron energy distribution can be made as the difference of the initial state E_i and the final states E_{f1} and E_{f2}.

$$E_{ETMD} \approx E_i - E_{f1} - E_{f2}, \tag{6.3}$$

with E_i the vertical ionization potential of the Mg 2p state for the aqueous cation and E_{f1}/E_{f2} can be any of the ionization potentials given in table 6.1. From this estimate an energy distribution of zero to 30 eV kinetic energy is expected for ETMD in aqueous magnesium salt solution. This is of course only a rough estimate, neglecting repulsive interaction of the

electron holes in close proximity and the polarization screening of the charges by the surrounding water molecules The previous results of Pohl *et al.* show this estimate to be in reasonable agreement with the measured spectra [73].

In separate experiments on the SOL^3 experimental station (see section 3.5) at the BESSY II UE52-SGM beamline the proposed surface propensities of the different magnesium salt solutions was verified in order to corroborate the predictions in the literature [210–212]. These proposed surface propensities were obtained in separate theoretical calculations, in part, combined with *sum frequency generation* (SFG) spectroscopy of the water OH stretching region (3000–3800 cm^{-1}) [210, 212], which is an inherently interface sensitive technique, yet indirect, as only the ion's effects on the interfacial water structure is probed. However, using element-specific X-ray photoelectron spectrosopy the different magnesium salt solutions could be probed directly. For this purpose, the Mg 2p photoelectron spectra of $Mg(OAc)_2$, $MgCl_2$ and $Mg(NO_3)_2$ solutions were recorded at 210 and 585 eV kinetic energy. Since the electron mean free path length increases with increasing kinetic energy, the photoelectron spectra of higher kinetic energy are more sensitive to the bulk of the solutions. All spectra were recorded at an angle of $\sim 55\,^\circ$ between the linear polarization vector of the synchrotron radiation and the electron spectrometer and were later normalized to the acquisition time, the atomic photoionization cross sections taken from calculations [215] and the current of the refocusing mirror of the beamline. For each photoline the normalized area was determined, followed by the ratio of low and high kinetic energy of the individual photoelectron signal. The resulting ratios are summarized in table 6.2. The values are rounded to one decimal

Table 6.2: Surface propensity trends of $Mg(OAc)_2$, $MgCl_2$ and $Mg(NO_3)_2$ aqueous solutions determined from the ratio of the Mg 2p photoelectron signal at low and high kinetic energy. The individual solutions were prepared at 2 M concentration.

	$Mg(OAc)_2$	$MgCl_2$	$Mg(NO_3)_2$
ratio of Mg 2p signal	2.0	1.4	1.0

point. Clearly, the ratio of Mg 2p photoelectrons is decreasing from left to right, thereby following the proposed trend for the surface propensity of $Mg(OAc)_2 > MgCl_2 > Mg(NO_3)_2$. These results yield a qualitative picture of the the surface propensity of the different magnesium salts. A quantitative determination of the surface propensities would require the measurement of the photon flux for the individual photon energies and a high degree of stability of the liquid jet position checked between each measurement. Such an experiment was outside the scope of this thesis.

So far, the coincident experiments on Li^+ solutions focused on ETMD transitions of higher kinetic energies as those carry information about the solvation shell of the cation i.e., its ion pairing situation. Said experiments were carried out within the frame of this work using the same setup for electron-electron coincidence measurements on liquid jet samples[3]. In these,

[3]These experiments were a collaborative effort and were part of the thesis of Marvin N. Pohl. [216]

a retardation voltage of about -20 V was applied to the drift tube of the magnetic bottle TOF electron spectrometer to ensure reasonable energy resolution of the ETMD electron distribution. This setting is suitable for the detection of electrons of about 20 eV kinetic energy or higher. However, in the case of ETMD in magnesium salt solutions, encouraged by the quantitative results on inner valence ICD in water clusters, the focus was on the determination of the autoionization efficiency. Given the estimates following table 6.1 this required the simultaneous measurement of photoelectrons and secondary electrons of near zero kinetic energy and higher. This was realised by carefully applying a small negative potential to the liquid jet and use of an acceleration voltage of a few volts in the spectrometer drift tube.
Quantifying the ETMD efficiency from coincident electron spectra follows the same approach presented in references [92] and [105] for Ne clusters and pure H_2O clusters, respectively. Analogous to the previous discussions in section 4.1.1, for an ideal experiment the ETMD efficiency or branching ratio α_{ETMD} is described by the number of coincident events of photoelectrons and ETMD electrons $P(E_{\mathrm{ph}}, E_{\mathrm{ETMD}})$ divided by the total rate of electrons of the respective energy $p(E_{\mathrm{ph}})$.[4]

$$\alpha_{\mathrm{ETMD}} = \frac{P(E_{\mathrm{ph}}, E_{\mathrm{ETMD}})}{p(E_{\mathrm{ph}})}. \tag{6.4}$$

To come to quantitative results for actual experimental conditions, the finite detection efficiency for ETMD electrons $\gamma(E_{\mathrm{ETMD}})$ has to be considered:

$$\alpha_{\mathrm{ETMD}} = \frac{P(E_{\mathrm{ph}}, E_{\mathrm{ETMD}})}{p(E_{\mathrm{ph}})} \frac{1}{\gamma(E_{\mathrm{ETMD}})}. \tag{6.5}$$

In contrast to previous experiments on clusters the degree of condensation c is omitted for the liquid jet experiments. Another noticeable difference to the experiments on cluster and gas phase targets with the magnetic bottle spectrometer is the reduced acceptance angle, as electrons emitted with directional components into the direction opposite to the spectrometer will not to be detected. Furthermore, the influence of losses due to inelastic scattering is neglected as it is not yet known how it could be quantified.
The detection efficiency $\gamma(E_{\mathrm{ETMD}})$ was estimated using the non-coincident and coincident electron spectra of the water O 1s core level. A corresponding set of spectra is shown in figure 6.4. Here, (a) contains the non-coincident time-of-flight photoelectron spectrum of a 2 M $MgCl_2$ solution recorded at 550 eV photon energy. (b) displays the accompanying two dimensional electron spectrum of coincident events in which exactly two electrons were detected within one bunch period. The arrival time of the faster electron e_1 is the horizontal axis and the vertical axis assigns the arrival time of the second electron e_2 at the detector. In fig. 6.4(a) the photoelectron intensity enclosed with the red lines corresponds to the region-of-interest (ROI) for Auger electrons and O 1s core level electrons. Since the Auger decay results from initial O 1s ionization the electron correlation map shows a coincidence of Auger and core level electrons, which is indicated here by the two dimensional ROI. $\gamma(E_{\mathrm{ETMD}})$ was

[4] See equation 4.3 for comparison with the inner valence ICD efficiency.

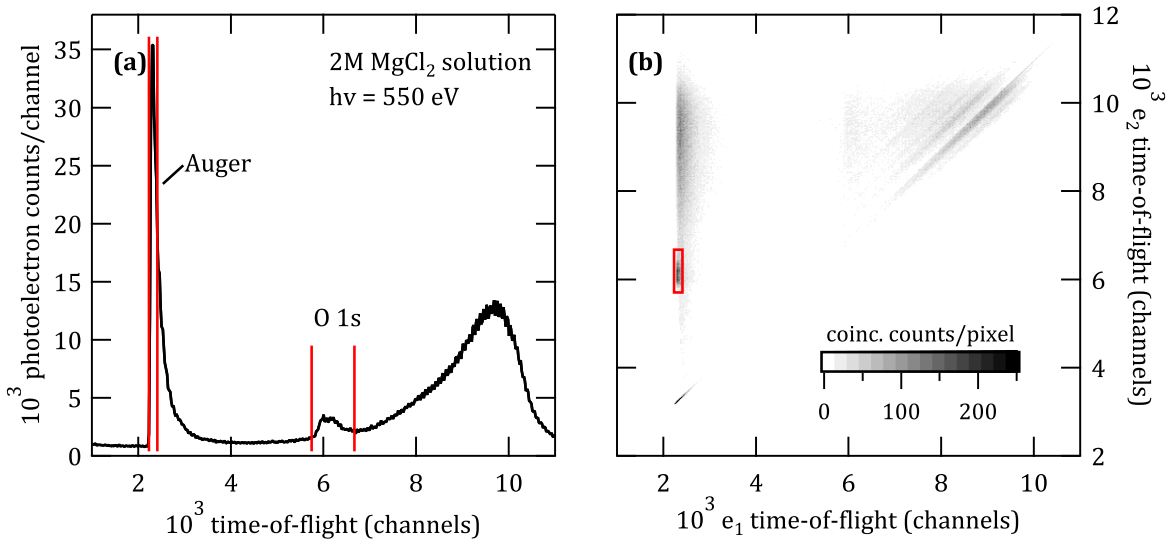

Figure 6.4: (a) non-coincident and (b) coincident time-of-flight electron spectra. The electron counts enclosed in the red regions was used for estimating the detection efficiency $\gamma(E_{\mathrm{ETMD}})$.

determined from the number of coincident O 1s electrons divided by the number of non-coincident O 1s electrons. This procedure was performed for a number of spectra of pure water and magnesium salt solutions recorded at 550 and 600 eV photon energy. The derived values for $\gamma(E_{\mathrm{ETMD}})$ were stable resulting in an averaged value of $\gamma(E_{\mathrm{ETMD}}) = 0.16(4)$ for spectra taken with an accelerating voltage set to the spectrometer drift tube (see below).
At this point it is not known what other processes might influence the efficiency of the ETMD process. Based on the results on inner valence ICD in water clusters, it is possible that photoinduced nuclear dynamics might affect the decay, since this could lead to changes in the solvation shell geometry accompanied with changes in the required orbital overlap for the ETMD process. Radiative electronic relaxation (fluorescence) is less likely due to the low Z of all involved atoms. In general, the transition matrix elements describing the decay are yet unknown. A property, however, which is likely to affect the ETMD efficiency is the different surface/interface propensity of the different ions.

In the following paragraphs, energy resolved and time-of-flight electron spectra of $Mg(OAc)_2$ solution are shown for concentrations of 1 to 3 M (mol/L), measured at different photon energies. The use of different spectrometer settings emphasizes some aspects of liquid jet spectroscopy using a magnetic bottle electron spectrometer. Additionally, the quantification of non-coincident and coincident Mg 2p counts required to obtain the ETMD efficiency for all magnesium salt solutions is illustrated.
In figure 6.5 all spectra of $Mg(OAc)_2$ aqueous solution are compiled. In every panel the upper traces contains the photoelectron spectrum, or more precisely all events in which a single electron is detected, whereas the lower traces displays the corresponding coincident electron spectrum, in which exactly two electrons were detected within one single bunch period. The coincident spectra show the first electron of the two-electron coincidence, the

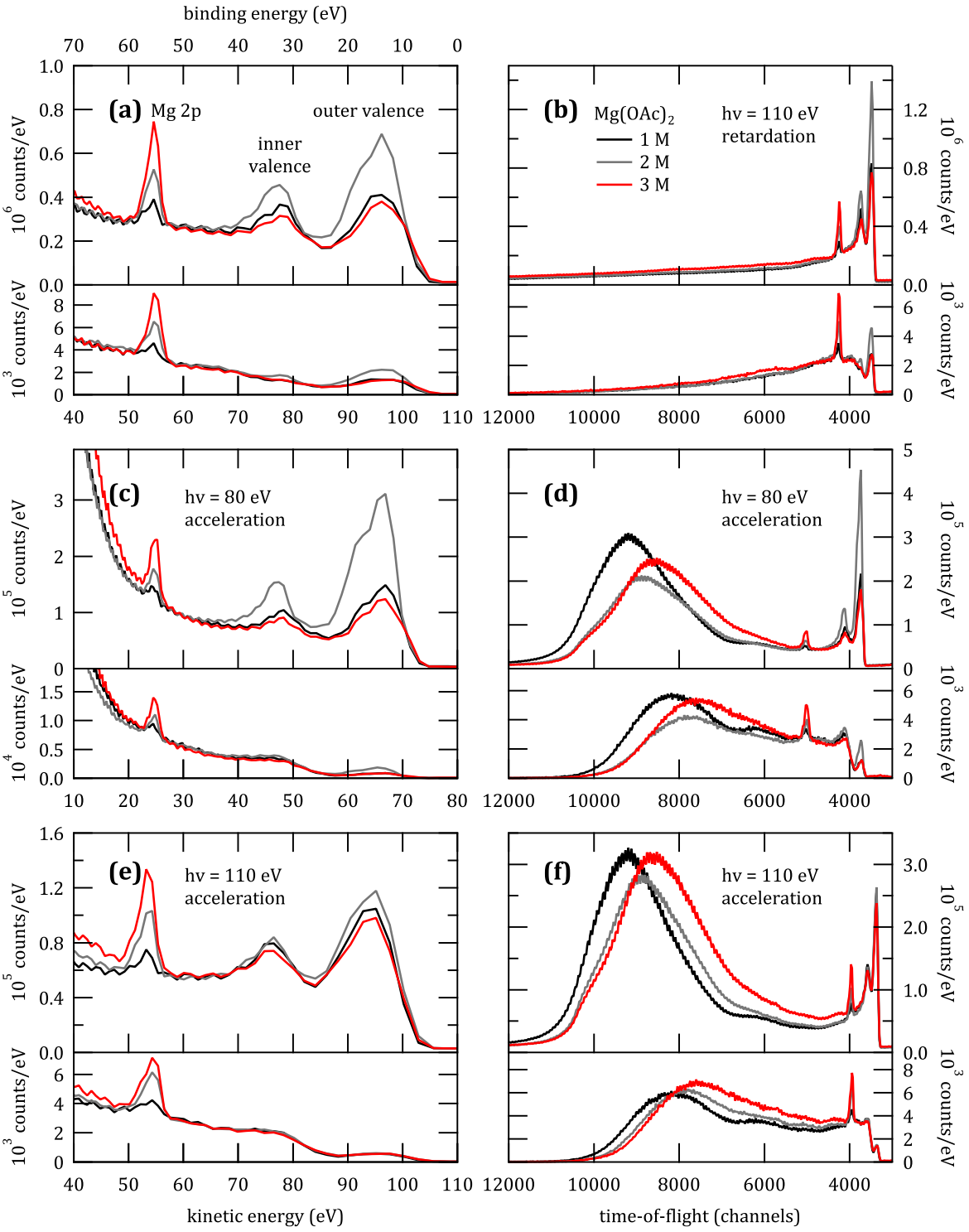

Figure 6.5: Compilation of photoelectron (upper panel) and coincident (lower panel) electron spectra of magnesium acetate solutions in the energy and time domain taken at 80 and 110 eV photon energy. (a) and (b) show the spectra recorded with a retardation voltage of -10 eV applied to the magnetic bottle drift tube. (c) to (f) are the spectra recorded an acceleration voltage of $+3$ V at the drift tube and a jet bias of -2 V. All spectra were normalized to the area between 40 and 50 eV on the binding energy axis of the 1 M traces to ease comparison.

faster electron. Panels (a) and (b) show the extended valence spectra in the energy (left) and time domain[5] (right) of magnesium acetate solutions measured at 110 eV photon energy and a retardation/deceleration voltage of −10 V at the spectrometer drift tube. (c) and (d) correspond to the spectra measured at 80 eV using an acceleration voltage of +3 V in the drift tube and a jet bias voltage of −2 V to ensure detection of all emitted electrons down to zero kinetic energy. (e) and (f) analogously depict the spectra under accelerating conditions at 110 eV photon energy. For comparison, each set of spectra was normalized to match the signal intensity of the spectrum at 1 M concentration (black traces) between 40 to 50 eV binding energy. The vertical axes are, therefore, only valid for the spectra of low concentration. It should be noted, that all spectra in fig. 6.5 exhibit a signal oscillation. This oscillation is an artifact in all spectra of Mg^{2+} solutions presented in this chapter. An oscillation of unknown origin with a period of approximately 2 ns was picked up by the measurement electronic.
Immediately apparent in all spectra is the intensity variation of the outer valence region of 0 to 40 eV binding energy for the 2 M spectra (gray trace). This is probably due to a different ratio of gaseous and liquid phase caused by slightly different alignment of the liquid jet in front of the analyzer entrance. Additionally, the increasing electrolyte concentration reduces the vapor pressure [217], affecting the gas-to-liquid ratio. This kind of behaviour is known within the liquid jet community and can be minimized by carefully and systematically conducting the experiments and, if necessary, can typically be accounted for by careful data analysis. As can be seen in the energy spectra in fig. 6.5 the energy region of interest around the Mg 2p state at about 55 eV binding energy shows a relatively stable signal intensity throughout all measurements.
In general, the spectra with decelerating spectrometer settings in (a) and (b) compare well. At first glance, the non-coincident intensity of the Mg 2p state approximately linearly follows the increase in concentration. This trend can also be recognized in fig. 6.5(c). However, in contrast to the spectra with deceleration voltage a difference in the scattering background greater than 60 eV binding energy (lower kinetic energy) is noticeable. This difference is more pronounced in the time-of-flight data in (d) in the region between channel numbers 6000 and 10000 which correspond to scattered electrons of relatively low kinetic energy. This signature is absent in the spectra with retardation voltage as electrons of about 10 eV kinetic energy or lower are not capable to reach the detector. It is noticeable that the distribution of scattered electrons varies for all spectra, which is not unexpected when comparing liquid jet spectra. However, also the position of the secondary electron cut-off i.e., the time-of-flight of near zero energy electrons, is shifted towards higher channel numbers for the spectra with 1 M concentration. This kind of behavior could be associated with different potential of the liquid jet surface. Sources for such a potential could be electrokinetic charging by friction between the sample solution and the glass capillary or the formation of a molecular surface dipole layer. This behavior is also visible in figures. 6.5(e) and (f) for the spectra taken with 110 eV photon energy and at accelerating spectrometer settings.
In an attempt to quantify the differences in the inelastic scattering background and a general

[5]The time-of-flight in this experiment is recorded in TDC channels with a bin with of 60 ps. From this the physical time-of-flight can be easily inferred up to a fixed but unknown offset. The region displayed on the righthand side of fig. 6.5 amounts to a time window of 540 ns.

examination of the stability of the liquid jet experiments with a magnetic bottle spectrometer, the center of gravity[6] was determined for a number of magnesium salt solutions and pure water. Since the inelastic scattering background is a rather broad vaguely structured spectral feature a physically meaningful fit function is difficult to express. Thus the center of gravity of low kinetic energy electrons between 0 and 10 eV, which approximately corresponds to the electron signal between channel 6600 and 12000, is a reasonable quantity to track qualitative changes in the energy distribution. Figure 6.6 depicts the center of gravity of the secondary electron background in the non-coincident photoelectron spectra of the respective magnesium salt solutions and pure water, measured at 70, 80 and 110 eV photon energy. While for $Mg(NO_3)_2$, $MgCl_2$ and water the center of gravity fluctuates around 3.6 eV

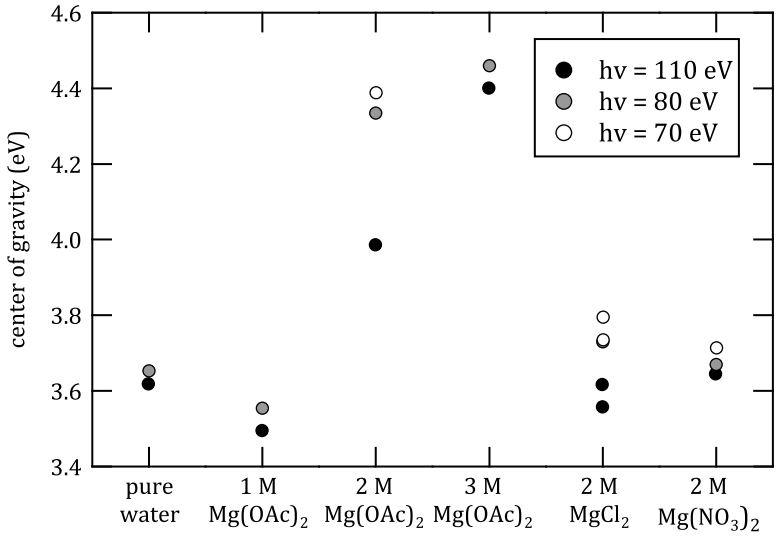

Figure 6.6: Compilation of the center of gravity for different magnesium salt solutions measured at 110 (black), 80 (gray) and 70 eV (red) with acceleration.

kinetic energy, the value for $Mg(OAc)_2$, especially for 2 and 3 M concentration, unequivocally differs. The center of gravity is shifted towards higher kinetic energy, indicating a higher negative potential at the liquid-gas interface. The shift is approximately 0.8 eV which is on the same order of magnitude of workfunction shifts caused by molecular adsorption on solid surfaces in surface science experiments [218]. The observation of the shift only affecting the low energy electrons while the energetic positions of the extended valence states are unaltered resembles molecular adsorption in surface science. In such experiments, changes in the workfunction of a metal surface can be attributed to changes in the surface dipole i.e., the charge distribution at the surface [219]. When applying this concept to the liquid-vapor interface it appears reasonable to encounter a different surface dipole in electrolyte solutions of supposedly high surface propensity compared to pure water. Furthermore, the possibility of a so-called streaming potential resulting from electrokinetic charging should also be discussed. Liquid jet studies in references [180] and [181] characterized the streaming potential of simple electrolyte solutions and reported a dependency on the concentration and the flow rate. Therein, the general trend was that the magnitude of the streaming potential

[6]The center of gravity C of a curve $g(x)$ can be defined as $C = \sum(x \cdot g(x)) / \sum(g(x))$.

is largely suppressed to about 0.1 eV for 30 mM electrolyte concentration or higher. Therefore, a contribution of the streaming potential to the total surface potential should not be excluded, but given the range concentration from 1 to 3 M it is not expected to be a major source for the observed shift in the low kinetic energy electrons.
At this point a detailed discussion of the spread in the values in fig. 6.6 for the different solutions in comparison to pure water should be refrained from. The topic of the workfunction is, although recently reported on in reference [182], still not well understood. Though the results in fig. 6.6 unambiguously show an effect in the secondary electron distribution depending on the solute and solute concentration, a more systematic series of measurements solely focused on quantification of the secondary electron cut-off in liquid jet experiments would be required.

In order to quantify the ETMD efficiency α_{ETMD} following equation 6.5, the number of non-coincident and coincident Mg 2p counts was determined for all magnesium salts. The fit procedure to determine these quantities is displayed in figure 6.7. Herein, (a) shows the photoelectron signal (upper panel) and coincident signal (lower panel) of the Mg 2p state

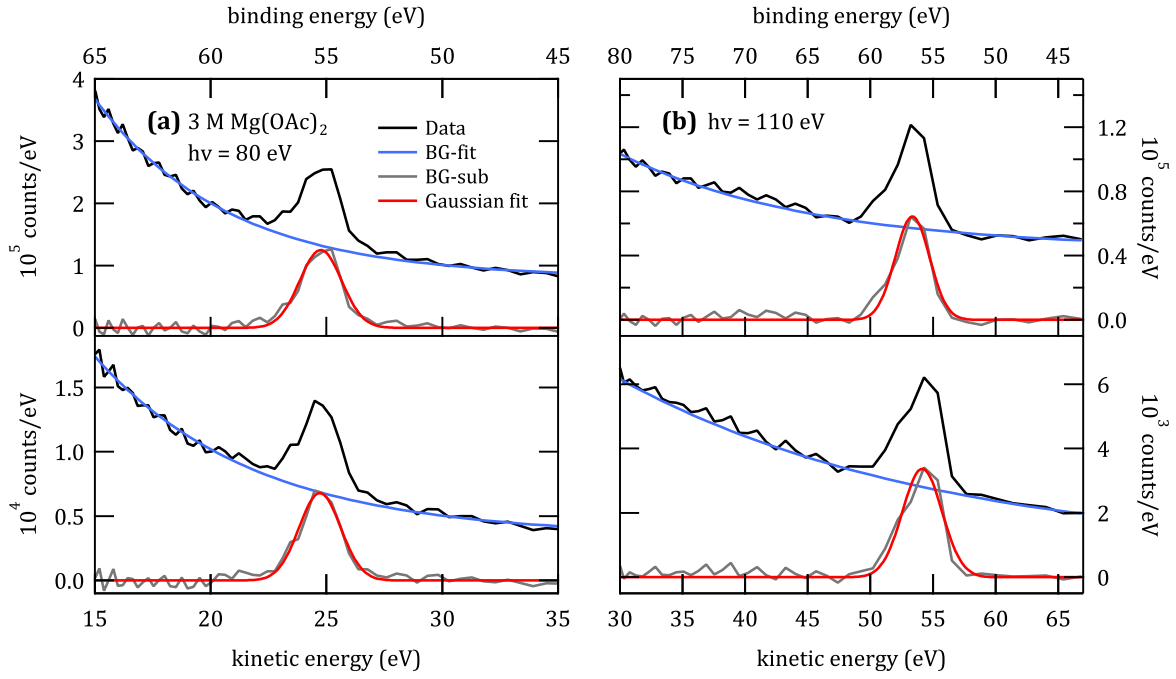

Figure 6.7: Example of fit procedure to determine the number of non-coincident (upper panel) and coincident (lower panel) Mg 2p counts of a 3 M $Mg(OAc)_2$ solution. (a) shows the spectra recorded at 80 eV photon energy and (b) the same set of data obtained at 110 eV photon energy. In both cases an acceleration voltage of +3 V was set to the drift tube of the spectrometer and a bias voltage of −2 V on the liquid jet to ensure the detection of electrons down to near zero kinetic energy. A curved background (blue traces) around the Mg 2p signal was determined and subtracted (gray traces). The Mg 2p counts were determined within 2σ of a Gaussian fit (red traces) to the background subtracted spectrum.

of a 3 M solution of $Mg(OAc)_2$ recorded at 80 eV photon energy and +3 V acceleration voltage. (b) shows the same spectra measured at 110 eV photon energy. The black traces correspond to the untreated data of the non-coincident and coincident Mg 2p electron counts, respectively. The background of each of these spectra, shown as blue traces, was fitted using an exponential decay or polynomial. Subtraction of the curved background resulted in the gray traces, which were subsequently fitted to using a single Gaussian distribution (red trace). In each case, the quality of the individual fits was checked by inspecting the residuals (not shown). The number of non-coincident and coincident Mg 2p electrons ($p(E_{ph})$ and $P(E_{ph}, E_{ETMD})$) were then determined within 2σ of the background-free Mg 2p signal.
The described procedure was carried out for all measured magnesium salt solutions and the resulting efficiencies are graphically depicted in figure 6.8. The figure shows the Mg 2p

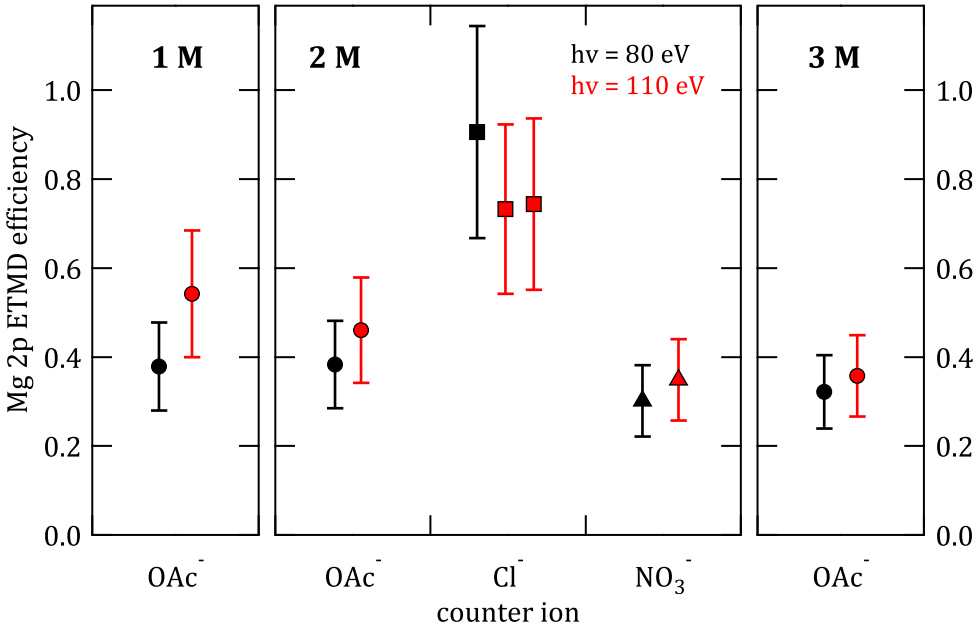

Figure 6.8: Compilation of the Mg 2p ETMD efficiency in $Mg(OAc)_2$, $MgCl_2$ and $Mg(NO_3)_2$ solutions. The black symbols refer to the measurements at 80 eV and the red symbols to the analogous measurements at 110 eV photon energy and accelerating spectrometer settings. The error bars shown here represent the standard deviation due to stochastic errors.

ETMD efficiencies of aqueous solutions of $Mg(OAc)_2$, $MgCl_2$ and $Mg(NO_3)_2$ at concentrations varying from 1 to 3 M. These efficiencies were determined with the procedure outlined above for the measurements at 80 eV (black symbols) and 110 eV (red symbols) photon energy applying an acceleration voltage to the spectrometer. Immediately, two observations stand out. The ETMD efficiency for $Mg(OAc)_2$ shows no clear concentration dependence, but rather stays constant between 0.3 to 0.4 for the values determined at 80 eV. For the $Mg(OAc)_2$ ETMD efficiency at 110 eV a variation between 0.3 to 0.5 is observed for the covered range of concentrations. More importantly, the comparison between the different salt solutions at 2 M concentration shows a clear trend. The efficiency for NO_3^- is slightly lower with respect to OAc^- and significantly higher for Cl^- ($NO_3^- < OAc^- \ll Cl^-$). This behavior is clearly visible at both photon energies.

The same analysis was performed for the equivalent magnesium salt spectra measured with a deceleration voltage of −10 V. In this case, however, only the raw efficiency (see eq. 6.4) could be determined. Unfortunately, for the spectra with retardation the detection efficiency γ could not be determined, so a direct quantitative comparison of the ETMD efficiencies is not possible. The raw efficiencies and actual efficiencies of all measurements are compiled in table 6.3. From this table, it is possible to compare the raw efficiencies determined for

Table 6.3: Compilation of Mg 2p ETMD efficiencies according to equations 6.4 and 6.5 for aqueous solutions of $Mg(OAc)_2$, $MgCl_2$ and $Mg(NO_3)_2$.

			acceleration		retardation	
Solution	c (mol/L)	$h\nu$ (eV)	raw	α_{ETMD}	raw	α_{ETMD}
$Mg(OAc)_2$	1	80	0.060	0.38(10)		
	2	80	0.061	0.38(10)		
	3	80	0.051	0.32(8)		
	1	110	0.086	0.54(14)	0.0074	
	2	110	0.073	0.46(12)	0.0095	
	3	110	0.057	0.36(9)	0.0129	
$MgCl_2$	2	80	0.144	0.91(24)		
	2	110	0.117	0.73(19)	0.0102	
	2	110	0.119	0.74(19)	0.0131	
$Mg(NO_3)_2$	2	80	0.048	0.30(8)		
	2	110	0.056	0.35(2)	0.0093	

measurements at 110 eV with acceleration and retardation settings of the spectrometer. It should be noted, however, that the count rate ratios measured with retardation are one order of magnitude smaller than with acceleration. The retardation voltage acts as a high pass filter only allowing the detection of electrons with kinetic energy of about 10 eV or higher. Nonetheless, in the comparison of the different counter ions at 2 M a similar hierarchy $NO_3^- < OAc^- < Cl^-$ is observed.

The results for inner valence ETMD in $Mg(OAc)_2$ solution at 80 and 110 eV look similar. While the efficiency at 80 eV appears constant, the efficiency at 110 eV appears to be decreasing with increasing concentration. It can be speculated, that this behavior is connected to the varying potential at the liquid jet surface for different acetate concentrations. Comparison of non-coincident and non-coincident time-of-flight spectra in figures 6.5(d) and 6.5(f) shows a stronger mismatch in the onset of the secondary electron signal at around 10000 channels for the spectra taken at 110 eV. The onset of the secondary electron signal is at higher channel numbers, which relate to lower kinetic energies, for the 1 M acetate solution compared to the higher concentrations. Therefore, the width of the spectrum for the low concentration is broader. From this follows that more electrons of low kinetic energy contribute to the coincident Mg 2p signal, which could lead to a slightly higher apparent ETMD efficiency for the 1 M magnesium acetate solution measured at 110 eV. Further, the different shape of the secondary electron distribution, characterized by the center of gravity (see fig. 6.6) will lead to some uncertainties in the ETMD efficiency, as this shape also influences the background

subtracted underneath the Mg 2p signal. Taking the results in tab. 6.3 and the spectral shape and onset of the secondary electrons into account the inner valence ETMD efficiency can be assumed constant for 1 to 3 M concentration at around 0.4 ± 0.1. A constant ETMD efficiency for $Mg(OAc)_2$ can be rationalized by considering the results in ref. [211], wherein the density profile suggests a distinct surface propensity for $Mg(OAc)_2$ with the ions forming contact ion pairs directly at the water surface. The authors of ref. [211] observed this behavior for concentrations from 0.5 to 2 M, which leads to the plausible assumption that the concentration range covered in this work features the same behavior. In addition, the ETMD process is thought to be highly sensitive to the distance due to the required orbital overlap [7]. In the experiment, the average internuclear distance between the ETMD subunits is unaffected by the increasing concentration due to the formation of contact ion pairs. Due to the strong surface propensity of $Mg(OAc)_2$ the ETMD electrons likely emerge directly from the liquid/vapor interface of the liquid jet, which makes an influence of inelastic scattering between the different concentrations less likely.

At this point, the raw ETMD efficiency for the measurements with -10 V retardation will be discussed briefly. For these spectra the coincident detection efficiency γ could not be determined, which does not allow a quantitative comparison with the results from previous beamtimes. In the spectra measured with retardation voltage any electrons of kinetic energies below $\sim$10 eV are exempt from detection, leading to a drastically reduced raw efficiency, which in this case is about one order of magnitude smaller. However, it should be possible to draw some conclusions from this data. Firstly, it should be pointed out that the raw efficiency at -10 V retardation follows the same trend of $NO_3^- < OAc^- < Cl^-$ as seen for the spectra measured with acceleration. Yet, the differences between the individual values are less drastic, compared to measurements with acceleration. The second observation is that the raw efficiency (see table 6.3) actually shows an increase with increasing $Mg(OAc)_2$ concentration. The spectra at 110 eV photon energy and -10 V retardation voltage (see fig. 6.5(a) and (b)) appear to be measured under stable conditions and have been analyzed consistently by the procedure outlined above, which suggests that the observed concentration dependence is real. Assuming the detection efficiencies for the two spectrometer settings — retardation and acceleration — are comparable a qualitative comparison of the raw efficiencies is possible. It is safe to assume that ETMD electrons, akin to photoelectrons, emitted from the liquid jet, will undergo inelastic scattering processes to a degree determined by their point of origin with respect to the surface. Therefore, the coincident electron signal of the ETMD electrons should be especially sensitive to the surface propensity of the Mg^{2+} ion. Using a retardation voltage and omitting the low kinetic energy ETMD electrons primarily results in the detection of unscattered ETMD electrons from the liquid jet surface i.e., the measurement with retardation voltage is more surface sensitive. In this case, an increase in concentration, respectively the surface concentration, of $Mg(OAc)_2$(aq) will also lead to an increase in the raw ETMD efficiency, due to the higher number of Mg^{2+} ions available for ETMD. This increased surfaces sensitivity, would also account for smaller differences in raw efficiencies between the different counter ions, as the individual surface propensities would contribute stronger to the respective coincident signal intensity.

A second scenario of more speculative nature would be concentration dependent changes in the immediate vicinity of the Mg^{2+} cation which might lead to a modulation of the internuclear distances between ETMD-relevant subunits. For instance, in references [220] and [211] formation of small clusters of $Mg(OAc)_2$ complexes was observed. Within a small cluster e.g., consisting of one or two magnesium-bridged acetate–acetate pairs, at the water surface the Mg^{2+} ion would have a slightly higher number of counter ions in its vicinity. This could lead to a higher probability to undergo ETMD with OAc^- and thus a higher number of ETMD electrons with higher kinetic energy originating from the liquid surface. In turn, the interaction with surrounding water molecules would decrease leading to lower number of low energy ETMD electrons. The overall number of emitted ETMD electrons should, however, be approximately constant. This would be reflected in the constant ETMD efficiency in the spectra measured with accelerating settings.
Finally, the experimentally observed hierachy of the ETMD efficiency at 2 M concentration following $NO_3^- < OAc^- \ll Cl^-$ is discussed. Starting with the $Mg(NO_3)_2$ solutions, the difference in ETMD efficiency compared to the other solutions is readily explained by recognition of its surface propensity. The theoretical results of Minofar and co-workers implied a low surface propensity for both ions, compared to $Mg(OAc)_2$ [211]. Based on these results the nitrate salt was explicitly chosen as a sample, having the distinct surface sensitivity of coincident photoelectron spectroscopy due to the limited probing depth in mind. It is therefore reassuring to observe the lowest ETMD efficiency in the magnesium nitrate solution.
Regarding the distinctly higher ETMD efficiency of $MgCl_2$ compared to $Mg(OAc)_2$, this result is surprising. A reason for this behavior is less clear than for the nitrate solution and can only be speculated about. The density profiles resported in references [210] and [211] place the Mg^{2+} cation at the liquid/vapor interface for both solutions. The particular counter ion is at the surface, but in contrast to the formation of CIPs in $Mg(OAc)_2$, in $MgCl_2$ solution the Mg^{2+} SShIPs are formed with the cation fully coordinated by water in the first shell and the counter ion in the second solvation shall. In other words, the immediate surrounding, the solvation shell structure, of the Mg^{2+} ion is noticeably different in both cases. In the detailed discussion of the theoretical results of Unger *et al.* on LiCl solutions [207], which were also characterized by SShIPs, it is explicitly stated that the $3a_1$ molecular orbital of the solvation shell water has the highest contribution to the spectral intensity of the ETMD electron distribution due to its maximized overlap with the ETMD initial state. Transferring this to $MgCl_2$, whose first solvation shell is supposedly comprised of six water molecules, suggests that the ETMD process following Mg 2p ionization will be dominated by transitions involving the water molecules that form its solvation shell. Assuming the ETMD transitions involving water indeed have the highest probability, the situation of the fully solvated Mg^{2+} ion at the liquid jet surface would result in the highest measurable ETMD efficiency. In contrast, $Mg(OAc)_2$, while similarly located at the liquid surface, exhibits a substantially different solvation shell due to the formation of CIPs with up to two acetate anions in the first solvation shell. Each acetate can replace either one water molecules or even two water molecules from the solvation shell by acting as a bidentate ligand. Therefore, for the hydrated magnesium acetate not only the number of water molecules is reduced, but also the total number of

molecules in the first solvation shell, which constitute the most readily accessible subunits for the ETMD process. Thus, the ETMD efficiency is reduced compared to the magnesium chloride case.

In conclusion, the results on different magnesium salt solutions yield new insight into the ETMD process of ionic species in aqueous environment but also on the difficulty of performing liquid jet photoelectron spectroscopy with focus on low kinetic energy electrons.
By performing measurements following the predictions of ref. [15] the general nature of the ETMD process and its importance in more realistic systems could be emphasized. Furthermore, these experiments constitute a first attempt to quantify the ETMD efficiency in such an environment. It could be shown that the efficiency is influenced by the individual counter ions and their respective surface propensity, but not significantly by the concentration. The efficiency is at around 0.3 to 0.4 for $Mg(OAc)_2$ and $Mg(NO_3)_2$ solutions but is strongly enhanced for $MgCl_2$ solution by a factor of two. It is the last point, which is somewhat unexpected. A speculative explanation could be given in considering the obvious differences in the structure of the first solvation shell between systems consisting of SShIPs or CIPs, a point corroborated by the theoretical results in ref. [207]. Müller *et al.* also stated that the ETMD(3) process is probably less efficient than ETMD(2) [206]. On the other hand, ETMD(3) can access a higher number of final states. This is, of course, a point which cannot be answered from the experiments. It is, however, possible that differences in the solvation shell structure influence the ratio of the two types of ETMD processes. Additionally, it is not clear which parameter other than the surface propensity and solvation structure affect the ETMD efficiency. Known from our recent results on ICD [105], it is possible that ultrafast nuclear dynamics also limit the ETMD efficiency. Therefore, for more insight into this matter theoretical expertise is required.

Chapter 7

Summary and Conclusion

This thesis presents experimental results studying non-local electronic decay processes in a hydrogen bonded environment; to be more specific, in an aqueous environment. Motivated by the recognition of these processes as viable mechanisms to inflict biomolecular damage by ionizing radiation, a detailed investigation of these phenomena in water, as the universal solvent, is indispensable. The main focus of this work is the quantitative description of ICD and ETMD after inner valence photoionization. In addition, some experiments focus on the utilization of non-local phenomena to investigate the hydrogen bond strength in different systems. In the following paragraphs a brief summary of the most important results is given:

Inner Valence ICD in Water Clusters and Water-Formaldehyde Clusters

Water clusters of varying average cluster size were produced using supersonic expansion and subsequently photoionized using XUV synchrotron radiation. Analogous to the results by Mucke and co-workers [12], the photoelectrons and secondary electrons produced by light matter interaction were detected in coincidence using a magnetic bottle time-of-flight electron spectrometer. This type of measurement enables the unambiguous detection of inner valence ICD following the ionization of the water $2a_1$ level in the cluster. The efficiency of this decay was determined for water clusters ranging from 5 to about 250 water molecules on average as the ratio of coincident $2a_1$ electrons to all detected $2a_1$ electrons. The major experimental results are, firstly, an increase of ICD efficiency with increasing cluser size, due to the growing number of neighboring water units accessible for ICD. Secondly, the efficiency is considerably below 100 %, in sharp contrast to the isoelectronic neon clusters [92]. An experimental and theoretical comparison of clusters of normal H_2O and the heavier D_2O could identify photoinduced proton transfer on the timescale of the ICD process as the limiting factor for the ICD efficiency.
Additionally, similar measurements were performed on mixed clusters produced by supersonic co-expansion of a water-formaldehyde mixture. The expansion parameters were chosen similar to those for the water clusters. Outer valence and core level spectra used to estimate the degree of condensation in the cluster beam suggest the formation of mixed clusters. The calculated single and double ionization spectra of the water-formaldehyde dimer indicates that the ICD process is an open relaxation channel following inner valence ionization [118]. In the coincident electron spectra the ICD channel as well as an intramolecular

decay, similar to the Auger process, could be observed. A comparison of the autoionization efficiencies of pure water clusters with the mixed clusters shows a drastically lower efficiency for the latter under identical expansion conditions. These results suggest that the ICD process in water has a limited probability in the immediate presence of the carbonyl group.

Proton Mediated Charge Separation: Non-Local Electronic Relaxation after Core Excitation

A non-local contribution to the O 1s Auger electron spectrum of liquid water was identified by Thürmer et al. [18] by an isotope effect between H_2O and D_2O and attributed to a charge separation of the dicationic final state by photoinduced proton transfer. This isotope effect was called proton transfer mediated charge separation (PTM-CS). In a number of experiments at the CoESCA endstation for surface science experiments at the BESSY II synchrotron facility, similar O 1s Auger spectra were recorded for thick films of amorphous ice, also called amorphous solid water (ASW) — typically used as an analog to liquid water in surface science experiments. The comparison of Auger spectra for normal and heavy water unambiguously revealed the PTM-CS signature at liquid nitrogen temperature.
Since it could be established that the PTM-CS process is, by definition, sensitive to proton transfer or in other words to hydrogen bonding [143], in a systematic investigation of liquid jet O 1s Auger spectra of binary mixtures of water and cryoprotecting molecules the potential of the PTM-CS signature to study hydrogen bonding was explored. The molecules glycerol and dimethyl sulfoxide (DMSO) are frequently used for cryopreservation of organic materials, as they drastically lower the freezing point of water and inhibit crystallization. This property is often associated with the influence of the co-solvent on the existing hydrogen bond network of water. By carefully comparing the Auger spectra of pure water, water-glycerol and water-DMSO at different concentrations with their deuterated counter parts, it could be shown that the co-solvents indeed lower the overall strength of the hydrogen bond network in solution. However, the two cryoprotecting molecules seem to interact differently with the water hydrogen bond network.

Single photon Double Ionization of Liquid Water

The combination of the liquid jet with a magnetic bottle time-of-flight electron spectrometer was used for the first investigation of the double ionization spectrum of pure water using the coincident detection scheme. In order to identify the individual signal contributions to the liquid jet spectrum, the literature on the non-interacting water molecule in the gas phase was studied, followed by a systematic examination of the double ionization spectra for water clusters of different size and double ionization spectra of the vapor phase surrounding the liquid jet. In the case of gas phase water and water clusters the signal contributions of molecular double ionization and ICD, which is a signature of the condensed phase, are well separated. At elevated pressure as in the vapor phase or in the liquid an additional contribution of double ionization via electron impact ionization by outer valence photoelectrons

is observed. The contribution of double ionization via photoelectron impact is relatively pronounced and energetically coincides with the final states observed in the ICD process. After careful analysis of the recorded double ionization spectra at different photon energies it was, however, possible to qualitatively separate the two processes, thus finding the first experimental clues for the occurence of ICD in liquid water.

Electron Transfer Mediated Decay in Electrolyte Solutions

Different Mg^{2+} containing electrolyte solutions were investigated by combining the well established liquid jet technique with coincident electron detection using a magnetic bottle time-of-flight electron spectrometer intended for this purpose. Stumpf et al. identified the non-local processes ICD and ETMD to play a major role in the de-excitation cascade of core ionized magnesium ions in aqueous solution in an extensive theoretical study [15]. Towards the end of the cascade ETMD is the only accessible deexcitation channel. This particular channel could be selectively probed by photoionization of the Mg 2p level. The resulting Mg $2p^{-1}$ excited state decays by secondary electron emission with energies of near zero to 30 eV kinetic energy, involving its immediate surrounding. The efficiency of this ETMD process was determined as the ratio of coincident Mg 2p electrons to total number of Mg 2p electrons for the magnesium salts $Mg(OAc)_2$, $MgCl_2$ and $Mg(NO_3)_2$. All three salts exhibit a different surface propensity as well as different degrees of interactions between the counter ions i.e., different ion pairing. The ETMD efficiency of these solutions follows $Mg(NO_3)_2 < Mg(OAc)_2 \ll MgCl_2$. This order can on the one hand be justified by the different surface propensity and the inherent surface sensitivity of the coincident electron detection. On the other hand, the contrasting structure of the metal ion's first hydration shell specifically between $Mg(OAc)_2$ and $MgCl_2$ appears to play a crucial role for the efficiency of the decay.

Conclusion

The objective of this thesis was the investigation of autoionization processes with a particular focus on the non-local decay mechanisms ICD and ETMD in an aqueous environment in order to assess their relevance in radiation chemistry and biology. For this purpose the respective autoionization efficiency was quantified for different systems. In the case of inner valence ICD in pure water clusters and binary water-carbonyl clusters the ICD efficiency is dependent on the system size and limited to few tens of percent due to nuclear dynamics of the hydrogen bond network within the femtosecond lifetime of the excited state. For ETMD following the photoionization of the Mg 2p state in Mg^{2+} aqueous solutions a significant increase of the ETMD efficiency from few tens of percent up to 90 percent was observed for Mg^{2+} close to the liquid–vapor interface and a fully solvated coordination shell. These results present two extreme cases in which the interactions of the hydrogen bond network can either limit (ICD) or enhance (ETMD) the probability to emit secondary electrons. Nevertheless, it is shown that both processes are viable sources for radiation damage in aqueous media upon X-ray irradiation. In addition, a comparison of the double ionization spectra of

water clusters and liquid water revealed a signature which was tentatively attributed to inner valence ICD in liquid water. The observation of this signature emphasizes the relevance of ICD in biological conditions.
Furthermore, it was shown that the Auger electron spectrum can be a viable spectroscopic tool to investigate the hydrogen bond network of aqueous systems. The charge delocalization in the excited state via proton transfer dynamics (PTM-CS) is evident as an isotope effect in the spectra of the normal and deuterated system. The intensity of this isotope effect can be used to measure of the relative strength of the hydrogen bond network.

Chapter 8

Outlook

Regarding the quantitative results on ICD following the inner valence ionization of the $2a_1$ state in water clusters, a size dependence could be clearly shown. While the efficiency was below unity for all the cluster sizes measured it is not clear, whether the ICD efficiency would become 1 at larger or infinite system size i.e., bulk water. Potential energy curves calculated for the water dimer embedded in a polarizable continuum to estimate the impact of an infinite hydrogen bond network suggested the ICD process to be open at all geometries along the hydrogen bond coordinate. In order to check the validity of this model, additional measurements of inner valence ICD for extended system size are desirable. This constitutes a connection between the cluster experiments and the double ionization spectra of the water liquid jet (see 4.1.1 and 5). While signs of inner valence ICD were present in the liquid jet spectra the high amount of water vapor surrounding the jet hampers the a closer investigation of ICD in liquid water. However, eliminating the vapor phase should give spectroscopic access to the $2a_1$ ICD signature in bulk water. This could possibly be achieved by using an amorphous ice film deposited onto a cooled wire, thus mimicking the experimental geometry encountered by combination of the liquid jet with the magnetic bottle spectrometer. This approach was recently realized by Hikosaka and co-workers to measure coincident electron spectra following the core level ionization [71]. A simple cryostat for cooling of a metal wire was built, but as of now it has not been tested.
Furthermore, the study of mixed molecular clusters should be expanded to other organic molecules containing different functional groups. Similar to the results of clusters of water and formaldehyde, a few measurements were performed on water-methanol clusters, the results were however inconclusive. A combination of systematic measurements of different mixed systems, ideally as a function of cluster size, and theoretical support would improve the understanding of ICD in a biomolecular context.

Since measurement of Auger electron spectra is well established as an analytical method in surface materials science, it is only natural to utilize the isotope effect observed in the Auger electron distributions of hydrogen bonded systems i.e., PTM-CS, as a tool to investigate hydrogen bonding. In fact, recent publications on this matter started to explore the sensitivity of the PTM-CS signature to different variables such as hydrogen bond strength of different constituents, size and confinement effects in hydrogen bonded clusters and the temperature of the system [113, 143, 144, 221]. Based on the results in this thesis further

experiments on ice would be desirable. For instance, instead of amorphous ice and liquid water, in which the average number of hydrogen bonds per water molecule is lower than 4 (see 2.4), in hexagonal ice the PTM-CS signature would likely be more pronounced due to the higher degree of order in the crystalline arrangement. Other measurements to pursue would be the PTM-CS's sensitivity towards different salts and salt concentrations as it is known that the addition of salt can have strong effects on the overall hydrogen bond network in water.

The utilization of a coincident detection scheme would be an interesting approach to investigate the PTM-CS signature of bimolecular samples e.g., condensed layers containing two different molecules such as water and another organic molecule which can form hydrogen bonds. Such an experiment could make use of the two ArTOF analyzers of the CoESCA setup to characterize the initial state for every individual core level decay by recording photoelectron–Auger electron coincidence spectra similar to previous experiments in reference [75]. A first attempt to measure the O 1s-Auger electron coincidences for amorphous ice was made during the second beamtime at the CoESCA endstation. The results of this measurement are shown in figure 8.1. The coincidence map in fig. 8.1(b) shows events of

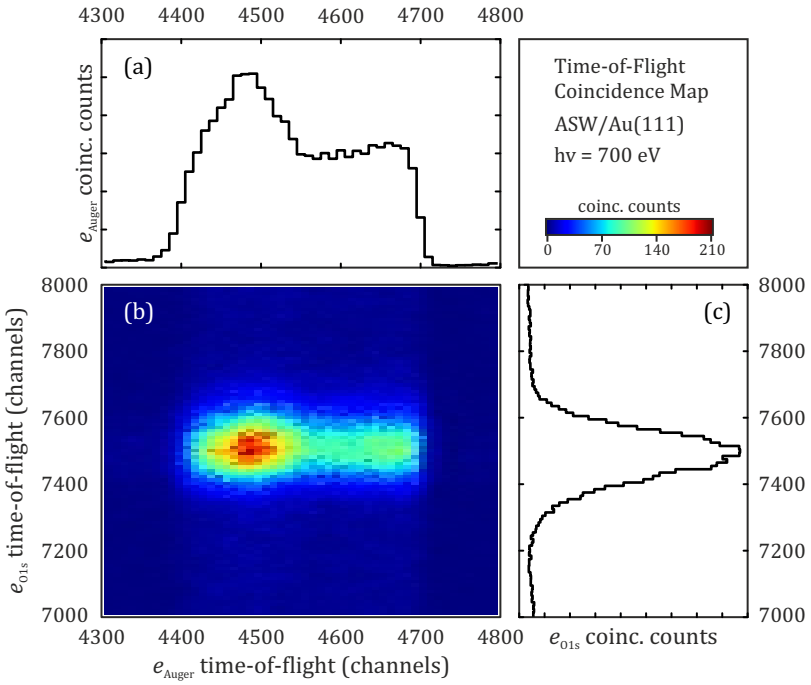

Figure 8.1: Coincident measurement of photoelectron and Auger-electron of ASW using the CoESCA's two ArTOF analyzers. (b) is the two-dimensional map showing the correlation of photo- and Auger-electrons. (a) is the coincident Auger spectrum and (c) is the corresponding O 1s core level as a function of arrival time at the respective detectors.

electrons arriving at the two ArTOF electron analyzers with the y-axis corresponding to the O 1s photoelectron and the x-axis to the coincident KVV-Auger electron. The data is given in time-of-flight in the form of channel position at the detector. Traces (a) and (c) are the projections onto the horizontal and vertical axes and correspond to the coincident Auger signal and O 1s photoline, respectively. The data is presented in the time-of-flight domain, meaning a high channel number equals a lower kinetic energy and vice versa. The energy

window of the Auger spectrum covers the range of 480 to 530 eV kinetic energy i.e., mostly the leading peak of the Auger electron distribution. The energy range of the O 1s peak on the other hand is fully covered in the energy window. This preliminary data is qualitatively comparable with the recent results of Hikosaka and co-workers [71]. The presented two-dimensional spectrum was recorded for about 9 hours, which indicates that these coincident measurements at the CoESCA endstation are time-demanding but feasible.

The results on the ETMD efficiency in electrolyte solutions were surprising, especially the difference between $Mg(OAc)_2$ and $MgCl_2$ solutions. While the interpretation regarding the different solvation shell structures of the Mg^{2+} cation is plausible, theoretical support would be beneficial to corroborate this claim. It should be mentioned that apart from the different magnesium salt solutions, similar measurements were performed for lithium and aluminium salts. In all these solutions ETMD could be detected. They were, however, measured using other spectrometer settings and, therefore, do not allow for a quantitative comparison. Given the complex electronic relaxation cascade following core-level photoionization of Mg^{2+} presented by Stumpf et al. [15], this relaxation could potentially be measured using coincident electron detection. It would be interesting to find out whether the contributions of the different autoionization processes are discernable and, if so, whether there is a preferred pathway along the cascade.

Acknowledgements

This thesis would not have been possible without the support I got from all the people I have met and worked with over the last years. I am immensely grateful for everyone's help.

First of all I would like to thank my supervisor Uwe Hergenhahn for making this thesis possible. Thanks to him I was able to set foot into the ICD community. Coming from different scientific backgrounds, we had to find a common language to talk about science. On multiple occasions he patiently took the time to find a common ground so that I could learn and grow. I am very grateful that he shared his great knowledge on photoelectron spectroscopy with me.
I also want to acknowledge Gerard Meijer, who took on the role of my second supervisor without hesitation and provided me with office space and the inspiring work environment at the Fritz Haber Institute. This climate was an enormous help for me during the writing process. Numerous people were an essential part of this environment. Bernd Winter lend me his ear and offered advice countless times, which means a lot to me. I would like to thank the whole AG Pagel and in particular Kim Greis and Carla Kirschbaum with whom I ended up sharing my office. They were very warm and welcoming which was exactly what I was looking for. If I could take them with me to any other office, I would do so. Great thanks goes out to all the people of the Molecular Physics department, especially Maike Lettow, Rayoon Chang, Johannes Bischoff, Sebastian Malerz and Nicole Walter.

All the experiments presented in this thesis have been a collaborative effort involving many people. All of these different people deserve acknowledgement.
Firstly, I want to mention Marvin Pohl and Robert Seidel. I was lucky to meet them the day I started as a doctoral student, which also happened to be my very first liquid jet beamtime. Over the last years they shared their liquid jet experience with me during numerous beamtimes and, of course, quite a bit of chocolate.
I was very glad to collaborate with Olle Björneholm and his group on a number of projects. He has a very kind and comforting personality and was open to share his knowlegde. Once witnessing his reaction of pure joy over a piece of Sachertorte was priceless. A big thanks to Isaak Unger for his help in multiple beamtimes. Having him around turned the night shifts at Soleil into an enjoyable experience. I am very thankful for Geethanjali Gopakumar. We shared the struggles of writing a thesis together, the many abrupt changes of ups and downs. I thank her for gently nudging me and making sure to keep going forward with the thesis. I am deeply grateful for Clara-Magdalena Saak's life lessons in silliness and seriousness. Since our very first beamtime together she has been an inspiring science person, a friend and an emotional support to me. I cannot quantify the amount of gratitude she deserves for everything.
The continuous collaboration with the Björneholm group would not have happened without Melanie Mucke. I want to thank her for the support in numerous beamtimes, for introducing me to molecular clusters and teaching me how to use the setup she build.

The AG Ehresmann from the university of Kassel was a regular visitor at BESSY II. Just meeting them and working with them, especially with Andreas Hans, Christian Ozga and Xaver Holzapfel, was always a pleasure. On multiple occasions I worked with Florian Trinter. He was always eager to do experiments and keen to help out when more manpower was required. His enthusiasm for fundamental science is infectious.
I also like to thank Caspar Lant, who joined me for a few months as an intern. When he arrived in the group, I suddenly had to teach him about the science and experiments I did, which was a very valuable experience for me. All the experiments would not have been possible without the support of the beamline scientists and, of course, the many people working in the mechanical workshop and in the user support at BESSY II. I especially want to thank Ronny Golnak for his help on so many occasions, and Ieva Bidermane and Torsten Leitner for their support at the CoESCA experimental endstation.
I also want to thank the Leibniz Institute of Surface Engineering, in particular Bernd Abel and Evgeny Lugovoy, for their the support. Lastly, I thank the Research Unit FOR 1789 'Intermolecular and Interatomic Coulombic Decay' for its financial support.

NEUER KUCHEN; ALLES WIEDER AUF NULL.

Clara-Magdalena Saak

Bibliography

[1] P. L. Geissler et al. "Autoionization in liquid water". In: *Science* 291.5511 (2001), pp. 2121–2124. DOI: 10.1126/science.1056991.

[2] M. Nič et al., eds. *IUPAC Compendium of Chemical Terminology*. IUPAC, June 2009. DOI: 10.1351/goldbook.

[3] S. Hofmann. *Auger- and X-Ray Photoelectron Spectroscopy in Materials Science*. Springer Berlin Heidelberg, 2013. DOI: 10.1007/978-3-642-27381-0.

[4] L. Meitner. "Über die β-Strahl-Spektra und ihren Zusammenhang mit der γ-Strahlung". In: *Zeitschrift für Physik* 11.1 (Dec. 1922), pp. 35–54. DOI: 10.1007/bf01328399.

[5] P. Auger. "Sur l'effet photoélectrique composé". In: *Journal de Physique et le Radium* 6.6 (1925), pp. 205–208. DOI: 10.1051/jphysrad:0192500606020500.

[6] L. S. Cederbaum, J. Zobeley, and F. Tarantelli. "Giant Intermolecular Decay and Fragmentation of Clusters". In: *Physical Review Letters* 79.24 (1997), pp. 4778–4781. DOI: 10.1103/PhysRevLett.79.4778.

[7] J. Zobeley, R. Santra, and L. S. Cederbaum. "Electronic decay in weakly bound heteroclusters: Energy transfer versus electron transfer". In: *The Journal of Chemical Physics* 115.11 (Sept. 2001), pp. 5076–5088. DOI: 10.1063/1.1395555.

[8] T. Jahnke et al. "Interatomic and Intermolecular Coulombic Decay". In: (2020).

[9] J. D. Watson and F. H. C. Crick. "Molecular Structure of Nucleic Acids: A Structure for Deoxyribose Nucleic Acid". In: *Nature* 171.4356 (Apr. 1953), pp. 737–738. DOI: 10.1038/171737a0.

[10] A. Nilsson and L. G. M. Pettersson. "The structural origin of anomalous properties of liquid water". In: *Nature Communications* 6.1 (Dec. 2015). DOI: 10.1038/ncomms9998.

[11] T. Jahnke et al. "Ultrafast energy transfer between water molecules". In: *Nature Physics* 6.2 (2010), pp. 139–142. DOI: 10.1038/nphys1498.

[12] M. Mucke et al. "A hitherto unrecognized source of low-energy electrons in water". English. In: *Nature Physics* 6.2 (Jan. 2010), pp. 143–146. DOI: 10.1038/Nphys1500.

[13] B Boudaiffa et al. "Resonant formation of DNA strand breaks by low-energy (3 to 20 eV) electrons". In: *Science* 287.5458 (2000), pp. 1658–1660. DOI: 10.1126/science.287.5458.1658.

[14] W. C. Chumlea et al. "Total body water data for white adults 18 to 64 years of age: The Fels Longitudinal Study". In: *Kidney International* 56.1 (July 1999), pp. 244–252. DOI: 10.1046/j.1523-1755.1999.00532.x.

[15] V. Stumpf, K. Gokhberg, and L. S. Cederbaum. "The role of metal ions in X-ray-induced photochemistry". In: *Nature Chemistry* 8.3 (2016), pp. 237–241. DOI: 10.1038/nchem.2429. arXiv: 1505.02079.

[16] J. Yano et al. "X-ray damage to the Mn4Ca complex in single crystals of photosystem II: A case study for metalloprotein crystallography". In: *Proceedings of the National Academy of Sciences* 102.34 (Aug. 2005), pp. 12047–12052. DOI: 10.1073/pnas.0505207102.

[17] F. Wolf. "Chemistry and biochemistry of magnesium". In: *Molecular Aspects of Medicine* 24.1-3 (Feb. 2003), pp. 3–9. DOI: 10.1016/s0098-2997(02)00087-0.

[18] S. Thürmer et al. "On the nature and origin of dicationic, charge-separated species formed in liquid water on X-ray irradiation". In: *Nature Chemistry* 5.7 (2013), pp. 590–596. DOI: 10.1038/nchem.1680.

[19] H. Hertz. "Über einen Einfluss des ultravioletten Lichtes auf die electrische Entladung". In: *Annalen der Physik und Chemie* 267.8 (1887), pp. 983–1000. DOI: 10.1002/andp.18872670827.

[20] A. Einstein. "Über einen die Erzeugung und Verwandlung des Lichtes betreffenden heuristischen Gesichtspunkt". In: *Annalen der Physik* 322.6 (1905), pp. 132–148. DOI: 10.1002/andp.19053220607. arXiv: arXiv:1011.1669v3.

[21] T Koopmans. "Über die Zuordnung von Wellenfunktionen und Eigenwerten zu den Einzelnen Elektronen Eines Atoms". In: *Physica* 1.1-6 (Jan. 1934), pp. 104–113. DOI: 10.1016/S0031-8914(34)90011-2.

[22] S. Hüfner. *Very High Resolution Photoelectron Spectroscopy*. Ed. by Stefan Hüfner. Vol. 715. Lecture Notes in Physics. Berlin, Heidelberg: Springer Berlin Heidelberg, 2007. ISBN: 978-3-540-68130-4. DOI: 10.1007/3-540-68133-7.

[23] K. Siegbahn. "Electron Spectroscopy for Chemical Analysis (E.S.C.A.)" In: *Philosophical Transactions of the Royal Society A: Mathematical, Physical and Engineering Sciences* 268.1184 (Nov. 1970), pp. 33–57. DOI: 10.1098/rsta.1970.0060.

[24] L. Hedin and J.D. Lee. "Sudden approximation in photoemission and beyond". In: *Journal of Electron Spectroscopy and Related Phenomena* 124.2-3 (July 2002), pp. 289–315. DOI: 10.1016/S0368-2048(02)00060-9.

[25] K. L. Reid. "Photoelectron Angular Distributions". In: *Annual Review of Physical Chemistry* 54.1 (Oct. 2003), pp. 397–424. DOI: 10.1146/annurev.physchem.54.011002.103814.

[26] D. Rolles et al. "Size effects in angle-resolved photoelectron spectroscopy of free rare-gas clusters". In: *Physical Review A* 75.3 (Mar. 2007). DOI: 10.1103/physreva.75.031201.

[27] S. Thürmer et al. "Photoelectron Angular Distributions from Liquid Water: Effects of Electron Scattering". In: *Physical Review Letters* 111.17 (Oct. 2013). DOI: 10.1103/physrevlett.111.173005.

[28] J.H.D. Eland and R. Feifel. *Double Photoionisation Spectra of Molecules*. Vol. 1. Oxford University Press, Mar. 2018. ISBN: 9780198788980. DOI: 10.1093/oso/9780198788980.001.0001.

[29] R. Santra, J. Zobeley, and L. Cederbaum. "Electronic decay of valence holes in clusters and condensed matter". In: *Physical Review B* 64.24 (Nov. 2001), p. 245104. DOI: 10.1103/PhysRevB.64.245104.

[30] R. Santra and L. S Cederbaum. "Non-Hermitian electronic theory and applications to clusters". In: *Physics Reports* 368.1 (Sept. 2002), pp. 1–117. DOI: 10.1016/S0370-1573(02)00143-6.

[31] U. Hergenhahn. "Interatomic and intermolecular coulombic decay: The early years". In: *Journal of Electron Spectroscopy and Related Phenomena* 184.3-6 (Apr. 2011), pp. 78–90. DOI: 10.1016/j.elspec.2010.12.020.

[32] T Jahnke. "Interatomic and intermolecular Coulombic decay: the coming of age story". English. In: *Journal of Physics B: Atomic, Molecular and Optical Physics* 48.8 (2015), p. 082001. DOI: 10.1088/0953-4075/48/8/082001.

[33] G. D. Scholes. "Long-Range Resonance Energy Transfer in Molecular Systems". In: *Annual Review of Physical Chemistry* 54.1 (Oct. 2003), pp. 57–87. DOI: 10.1146/annurev.physchem.54.011002.103746.

[34] T. Jahnke et al. "Experimental separation of virtual photon exchange and electron transfer in interatomic coulombic decay of neon dimers". In: *Physical Review Letters* 99.15 (2007), pp. 1–4. DOI: 10.1103/PhysRevLett.99.153401.

[35] M. Pernpointner, N. V. Kryzhevoi, and S. Urbaczek. "Possible electronic decay channels in the ionization spectra of small clusters composed of Ar and Kr: A four-component relativistic treatment". In: *The Journal of Chemical Physics* 129.2 (July 2008), p. 024304. DOI: 10.1063/1.2952272.

[36] F. Mallamace et al. "The anomalous behavior of the density of water in the range 30 K $\leq$ T $\leq$ 373 K". In: *Proceedings of the National Academy of Sciences* 104.47 (Nov. 2007), pp. 18387–18391. DOI: 10.1073/pnas.0706504104.

[37] L. Korson, W. Drost-Hansen, and F. J. Millero. "Viscosity of water at various temperatures". In: *The Journal of Physical Chemistry* 73.1 (Jan. 1969), pp. 34–39. DOI: 10.1021/j100721a006.

[38] *CRC Handbook of Chemistry and Physics, 100th Edition*. Taylor & Francis Ltd., June 21, 2019. 1700 pp. ISBN: 113836729X.

[39] Y. Maréchal. "The Hydrogen Bond: Formation, Thermodynamic Properties, Classification". In: *The Hydrogen Bond and the Water Molecule*. Elsevier, 2007, pp. 3–24. DOI: 10.1016/B978-044451957-3.50002-0.

[40] C. T. Nemes, C. J. Laconsay, and J. M. Galbraith. "Hydrogen bonding from a valence bond theory perspective: the role of covalency". In: *Physical Chemistry Chemical Physics* 20.32 (2018), pp. 20963–20969. DOI: 10.1039/c8cp03920h.

[41] D. Iwanenko and I. Pomeranchuk. "On the Maximal Energy Attainable in a Betatron". In: *Physical Review* 65.11-12 (June 1944), pp. 343–343. DOI: 10.1103/PhysRev.65.343.

[42] F. R. Elder et al. "Radiation from Electrons in a Synchrotron". In: *Physical Review* 71.11 (June 1947), pp. 829–830. DOI: 10.1103/PhysRev.71.829.5.

[43] D. H. Tomboulian and P. L. Hartman. "Spectral and Angular Distribution of Ultraviolet Radiation from the 300-Mev Cornell Synchrotron". In: *Physical Review* 102.6 (June 1956), pp. 1423–1447. DOI: 10.1103/PhysRev.102.1423.

[44] V. Schmidt. *Electron Spectrometry of Atoms using Synchrotron Radiation*. Cambridge: Cambridge University Press, 1997. ISBN: 9780511524561. DOI: 10.1017/CBO9780511524561.

[45] C. Nordling, E. Sokolowski, and K. Siegbahn. "Precision Method for Obtaining Absolute Values of Atomic Binding Energies". In: *Physical Review* 105.5 (1957), pp. 1676–1677. DOI: 10.1103/physrev.105.1676.

[46] D. W. Turner and M. I. Al Jobory. "Determination of Ionization Potentials by Photoelectron Energy Measurement". In: *The Journal of Chemical Physics* 37.12 (Dec. 1962), pp. 3007–3008. DOI: 10.1063/1.1733134.

[47] H. Siegbahn and K. Siegbahn. "ESCA applied to liquids". In: *Journal of Electron Spectroscopy and Related Phenomena* 2.3 (Jan. 1973), pp. 319–325. DOI: 10.1016/0368-2048(73)80023-4.

[48] M. Faubel, S. Schlemmer, and J. P. Toennies. "A molecular beam study of the evaporation of water from a liquid jet". In: *Zeitschrift für Physik D Atoms, Molecules and Clusters* 10.2-3 (June 1988), pp. 269–277. DOI: 10.1007/BF01384861.

[49] M. Faubel, B. Steiner, and J. P. Toennies. "Photoelectron spectroscopy of liquid water, some alcohols, and pure nonane in free micro jets". In: *The Journal of Chemical Physics* 106.22 (1997), pp. 9013–9031. DOI: 10.1063/1.474034.

[50] K. R. Wilson et al. "Investigation of volatile liquid surfaces by synchrotron x-ray spectroscopy of liquid microjets". In: *Review of Scientific Instruments* 75.3 (2004), pp. 725–736. DOI: 10.1063/1.1645656.

[51] H. Haberland, ed. *Clusters of Atoms and Molecules*. Vol. 52. Springer Series in Chemical Physics. Berlin, Heidelberg: Springer Berlin Heidelberg, 1994. ISBN: 978-3-642-84331-0. DOI: 10.1007/978-3-642-84329-7.

[52] H. Haberland, K. Kleinermann, and F. Träger. "Cluster". In: *Lehrbuch der Experimentalphysik Band 5: Gase, Nanosysteme, Flüssigkeiten*. 2nd Ed. de Gruyter, 2008. Chap. Cluster, pp. 817–963. ISBN: 978-3-11-019814-0.

[53] M. Rondelli et al. "Exploring the Potential of Different-Sized Supported Subnanometer Pt Clusters as Catalysts for Wet Chemical Applications". In: *ACS Catalysis* 7.6 (June 2017), pp. 4152–4162. DOI: 10.1021/acscatal.7b00520.

[54] M. Sierka et al. "Unexpected Structures of Aluminum Oxide Clusters in the Gas Phase". In: *Angewandte Chemie International Edition* 46.18 (Apr. 2007), pp. 3372–3375. DOI: 10.1002/anie.200604823.

[55] O. F. Hagena. "Nucleation and growth of clusters in expanding nozzle flows". In: *Surface Science* 106.1-3 (1981), pp. 101–116. DOI: 10.1016/0039-6028(81)90187-4.

[56] O. F. Hagena. "Condensation in free jets: Comparison of rare gases and metals". In: *Zeitschrift für Physik D Atoms, Molecules and Clusters* 4.3 (1987), pp. 291–299. DOI: 10.1007/BF01436638.

[57] C. Bobbert et al. "Fragmentation and reliable size distributions of large ammonia and water clusters". In: *The European Physical Journal D* 19.2 (May 2002), pp. 183–192. DOI: 10.1140/epjd/e20020070.

[58] S. Barth. "Untersuchung des Interatomaren Coulomb-Zerfalls in schwach gebundenen Systemen". PhD thesis. Technische Universität Berlin, 2007.

[59] S. Barth et al. "Valence ionization of water clusters: From isolated molecules to bulk". In: *Journal of Physical Chemistry A* 113.48 (2009), pp. 13519–13527. DOI: 10.1021/jp906113e.

[60] L. Belau et al. "Vacuum Ultraviolet (VUV) Photoionization of Small Water Clusters". In: *The Journal of Physical Chemistry A* 111.40 (Oct. 2007), pp. 10075–10083. DOI: 10.1021/jp075263v.

[61] B. L. Yoder et al. "Sizer for Neutral Weakly Bound Ultrafine Aerosol Particles Based on Sodium Doping and Mass Spectrometric Detection". In: *The Journal of Physical Chemistry Letters* 2.20 (Oct. 2011), pp. 2623–2628. DOI: 10.1021/jz201086v.

[62] J. Shu et al. "Light Scattering of Ultrafine Silica Particles by VUV Synchrotron Radiation". In: *Nano Letters* 5.6 (June 2005), pp. 1009–1015. DOI: 10.1021/nl050315i.

[63] M. Mucke. "Employing electron-electron coincidence techniques to investigate the autoionisation of clusters". PhD Thesis. TU Berlin, 2011. DOI: 10.14279/depositonce-2853.

[64] R.F Post. "The magnetic mirror approach to fusion". In: *Nuclear Fusion* 27.10 (Oct. 1987), pp. 1579–1739. DOI: 10.1088/0029-5515/27/10/001.

[65] P Kruit and F H Read. "Magnetic field paralleliser for 2π electron-spectrometer and electron-image magnifier". In: *Journal of Physics E: Scientific Instruments* 16.4 (Apr. 1983), pp. 313–324. DOI: 10.1088/0022-3735/16/4/016.

[66] O. Cheshnovsky et al. "Magnetic time-of-flight photoelectron spectrometer for mass-selected negative cluster ions". In: *Review of Scientific Instruments* 58.11 (Nov. 1987), pp. 2131–2137. DOI: 10.1063/1.1139475.

[67] T. Tsuboi et al. "Magnetic bottle electron spectrometer using permanent magnets". In: *Review of Scientific Instruments* 59.8 (1988), pp. 1357–1362. DOI: 10.1063/1.1139722.

[68] J.H.D. Eland. "Double photoionisation spectra of methane, ammonia and water". In: *Chemical Physics* 323.2-3 (Apr. 2006), pp. 391–396. DOI: 10.1016/j.chemphys.2005.09.047.

[69] E. Fasshauer et al. "Theoretical and experimental investigation of Electron Transfer Mediated Decay in ArKr clusters". In: *Chemical Physics* 482 (2017), pp. 226–238. DOI: 10.1016/j.chemphys.2016.09.006.

[70] F. Buchner et al. "Time-resolved photoelectron spectroscopy of liquids". In: *Review of Scientific Instruments* 81.11 (Nov. 2010), p. 113107. DOI: 10.1063/1.3499240.

[71] Y. Hikosaka et al. "Electron emission relevant to inner-shell photoionization of condensed water studied by multi-electron coincidence spectroscopy". In: *Journal of Electron Spectroscopy and Related Phenomena* 213 (2016), pp. 17–21. DOI: 10.1016/j.elspec.2016.10.006.

[72] M. Mucke et al. "Performance of a short "magnetic bottle" electron spectrometer". In: *Review of Scientific Instruments* 83.6 (June 2012), p. 063106. DOI: 10.1063/1.4729256.

[73] M.N. Pohl et al. "Sensitivity of electron transfer mediated decay to ion pairing". In: *Journal of Physical Chemistry B* 121.32 (2017), pp. 7709–7714. DOI: 10.1021/acs.jpcb.7b06061.

[74] G. Öhrwall et al. "Charge dependence of solvent-mediated intermolecular Coster-Kronig decay dynamics of aqueous ions". In: *Journal of Physical Chemistry B* 114.51 (2010), pp. 17057–17061. DOI: 10.1021/jp108956v.

[75] T Arion et al. "Conformational and nuclear dynamics effects in molecular Auger spectra: fluorine core-hole decay in CF 4". In: *Journal of Physics B: Atomic, Molecular and Optical Physics* 47.12 (June 2014), p. 124033. DOI: 10.1088/0953-4075/47/12/124033.

[76] R. Seidel et al. "Advances in liquid phase soft-x-ray photoemission spectroscopy: A new experimental setup at BESSY II". In: *Review of Scientific Instruments* 88.7 (July 2017), p. 073107. DOI: 10.1063/1.4990797.

[77] A. Lindblad et al. "A multi purpose source chamber at the PLEIADES beamline at SOLEIL for spectroscopic studies of isolated species: Cold molecules, clusters, and nanoparticles". In: *Review of Scientific Instruments* 84.11 (Nov. 2013), p. 113105. DOI: 10.1063/1.4829718.

[78] R. Ovsyannikov et al. "Principles and operation of a new type of electron spectrometer - ArTOF". In: *Journal of Electron Spectroscopy and Related Phenomena* 191 (2013), pp. 92–103. DOI: 10.1016/j.elspec.2013.08.005.

[79] K. Holldack et al. "Single bunch X-ray pulses on demand from a multi-bunch synchrotron radiation source". In: *Nature Communications* 5.May (2014), pp. 1–7. DOI: 10.1038/ncomms5010.

[80] J. Zobeley, L. S. Cederbaum, and F. Tarantelli. "Highly excited electronic states of molecular clusters and their decay". In: *The Journal of Chemical Physics* 108.23 (June 1998), pp. 9737–9750. DOI: 10.1063/1.476448.

[81] T. Jahnke et al. "Experimental Observation of Interatomic Coulombic Decay in Neon Dimers". In: *Physical Review Letters* 93.16 (Oct. 2004), p. 163401. DOI: 10.1103/PhysRevLett.93.163401.

[82] S. Marburger et al. "Experimental Evidence for Interatomic Coulombic Decay in Ne Clusters". In: *Physical Review Letters* 90.20 (May 2003), p. 203401. DOI: 10.1103/PhysRevLett.90.203401.

[83] Y. Morishita et al. "Experimental Evidence of Interatomic Coulombic Decay from the Auger Final States in Argon Dimers". In: *Physical Review Letters* 96.24 (June 2006), p. 243402. DOI: 10.1103/PhysRevLett.96.243402.

[84] M. Lundwall et al. "Self-assembled heterogeneous argon/neon core-shell clusters studied by photoelectron spectroscopy". In: *The Journal of Chemical Physics* 126.21 (June 2007), p. 214706. DOI: 10.1063/1.2735607.

[85] E. Alizadeh, T.M. Orlando, and L. Sanche. "Biomolecular Damage Induced by Ionizing Radiation: The Direct and Indirect Effects of Low-Energy Electrons on DNA". In: *Annual Review of Physical Chemistry* 66.1 (2015), pp. 379–398. DOI: 10.1146/annurev-physchem-040513-103605.

[86] X. Ren et al. "Experimental evidence for ultrafast intermolecular relaxation processes in hydrated biomolecules". In: *Nature Physics* (2018), p. 1. DOI: 10.1038/s41567-018-0214-9.

[87] B. Winter et al. "Full Valence Band Photoemission from Liquid Water Using EUV Synchrotron Radiation". In: *Journal of Physical Chemistry A* 108.14 (2004), pp. 2625–2632. DOI: 10.1021/jp030263q.

[88] D Reedy et al. "Dissociation dynamics of the water dication following one-photon double ionization. II. Experiment". In: *Physical Review A* 98.5 (Nov. 2018), p. 053430. DOI: 10.1103/PhysRevA.98.053430.

[89] K. Schnorr et al. "Time-resolved measurement of interatomic coulombic decay in Ne2". In: *Physical Review Letters* 111.9 (2013), pp. 1–5. DOI: 10.1103/PhysRevLett.111.093402.

[90] F. Trinter et al. "Evolution of interatomic coulombic decay in the time domain". In: *Physical Review Letters* 111.9 (2013), pp. 1–5. DOI: 10.1103/PhysRevLett.111.093401.

[91] G. Öhrwall et al. "Femtosecond Interatomic Coulombic Decay in Free Neon Clusters: Large Lifetime Differences between Surface and Bulk". In: *Physical Review Letters* 93.17 (Oct. 2004). DOI: 10.1103/physrevlett.93.173401.

[92] M. Förstel, T. Arion, and U. Hergenhahn. "Measuring the efficiency of interatomic coulombic decay in Ne clusters". In: *Journal of Electron Spectroscopy and Related Phenomena* 191 (Dec. 2013), pp. 16–19. DOI: 10.1016/j.elspec.2013.11.002.

[93] M. Förstel et al. "Long-Range Interatomic Coulombic Decay in ArXe Clusters: Experiment and Theory". In: *The Journal of Physical Chemistry C* 120.40 (Oct. 2016), pp. 22957–22971. DOI: 10.1021/acs.jpcc.6b06665.

[94] P. Morin and C. Miron. "Ultrafast dissociation: An unexpected tool for probing molecular dynamics". In: *Journal of Electron Spectroscopy and Related Phenomena* 185.8-9 (Sept. 2012), pp. 259–266. DOI: 10.1016/j.elspec.2012.06.002.

[95] I. Hjelte et al. "Evidence for ultra-fast dissociation of molecular water from resonant Auger spectroscopy". In: *Chemical Physics Letters* 334.1-3 (Feb. 2001), pp. 151–158. DOI: 10.1016/s0009-2614(00)01434-2.

[96] M. Odelius. "Information Content in O[1s] K-edge X-ray Emission Spectroscopy of Liquid Water". In: *The Journal of Physical Chemistry A* 113.29 (July 2009), pp. 8176–8181. DOI: 10.1021/jp903096k.

[97] M. Odelius. "Molecular dynamics simulations of fine structure in oxygen K-edge x-ray emission spectra of liquid water and ice". In: *Physical Review B* 79.14 (Apr. 2009), p. 144204. DOI: 10.1103/PhysRevB.79.144204.

[98] N. Sisourat et al. "Interatomic electronic decay driven by nuclear motion". In: *Physical Review Letters* 105.17 (2010), pp. 2–5. DOI: 10.1103/PhysRevLett.105.173401.

[99] P. Slavíček et al. "Proton-transfer mediated enhancement of nonlocal electronic relaxation processes in X-ray irradiated liquid water". In: *Journal of the American Chemical Society* 136.52 (2014), pp. 18170–18176. DOI: 10.1021/ja5117588.

[100] S. Hartweg et al. "Size-Resolved Photoelectron Anisotropy of Gas Phase Water Clusters and Predictions for Liquid Water". In: *Physical Review Letters* 118.10 (2017), pp. 1–6. DOI: 10.1103/PhysRevLett.118.103402. arXiv: 1612.02338.

[101] P. Slavíček et al. "Relaxation Processes in Aqueous Systems upon X-ray Ionization: Entanglement of Electronic and Nuclear Dynamics". In: *J Phys Chem Lett* 7.2 (Jan. 2016), pp. 234–243. DOI: 10.1021/acs.jpclett.5b02665.

[102] O. Svoboda et al. "Reaction selectivity in an ionized water dimer: nonadiabatic ab initio dynamics simulations". In: *Physical Chemistry Chemical Physics* 15.27 (2013), p. 11531. DOI: 10.1039/c3cp51440d.

[103] U. Buck and M. Winter. "Electron bombardment induced fragmentation of size selected neutral (D2O)n clusters". In: *Zeitschrift für Physik D Atoms, Molecules and Clusters* 31.4 (1994), pp. 291–297. DOI: 10.1007/BF01445010.

[104] T. P. Martin, ed. *Large Clusters of Atoms and Molecules*. Springer Netherlands, 1996. DOI: 10.1007/978-94-009-0211-4.

[105] C. Richter et al. "Competition between proton transfer and intermolecular Coulombic decay in water". In: *Nature Communications* 9.1 (2018), p. 4988. DOI: 10.1038/s41467-018-07501-6.

[106] A Kivimäki et al. "Intensities of the xenon N_{4,5}OO Auger electron spectrum revisited". In: *J. El. Spectr. Rel. Phenom.* 101–103 (1999), pp. 43–47. DOI: 10.1016/S0368-2048(98)00470-8.

[107] K. Kimura. *Handbook of HeI photoelectron spectra of fundamental organic molecules: ionization energies, ab initio assignments, and valence electronic structure for 200 molecules*. Japan Scientific Societies Press, 1981.

[108] L. Karlsson et al. "Isotopic and vibronic coupling effects in the valence electron spectra of H2 16O, H2 18O, and D2 16O". In: *The Journal of Chemical Physics* 62.12 (June 1975), pp. 4745–4752. DOI: 10.1063/1.430423.

[109] S. Y. Truong et al. "Photo-double ionization of water studied by threshold photoelectrons coincidence spectroscopy". In: *Chemical Physics Letters* 474.1-3 (2009), pp. 41–44. DOI: 10.1016/j.cplett.2009.04.036.

[110] O. Marsalek et al. "Chasing charge localization and chemical reactivity following photoionization in liquid water". In: *Journal of Chemical Physics* 135.22 (2011). DOI: 10.1063/1.3664746.

[111] T. Miteva, S. Kazandjian, and N. Sisourat. "On the computations of decay widths of Fano resonances". In: *Chemical Physics* 482 (2017), pp. 208–215. DOI: 10.1016/j.chemphys.2016.08.014.

[112] E. Alizadeh and L. Sanche. "Precursors of solvated electrons in radiobiological physics and chemistry". In: *Chemical Reviews* 112.11 (2012), pp. 5578–5602. DOI: 10.1021/cr300063r.

[113] D. Hollas et al. "Aqueous Solution Chemistry of Ammonium Cation in the Auger Time Window". In: *Scientific Reports* 7.1 (2017), pp. 1–10. DOI: 10.1038/s41598-017-00756-x.

[114] A. Ghosh, S. Pal, and N. Vaval. "Study of interatomic Coulombic decay of Ne(H 2 O) n (n = 1,3) clusters using equation-of-motion coupled-cluster method". In: *The Journal of Chemical Physics* 139.6 (Aug. 2013), p. 064112. DOI: 10.1063/1.4817966.

[115] D. J. Wales et al. *The Cambridge Cluster Database*. URL: http://www-wales.ch.cam.ac.uk/CCD.html.

[116] L. B. Skinner et al. "Benchmark oxygen-oxygen pair-distribution function of ambient water from x-ray diffraction measurements with a wide Q -range". In: *The Journal of Chemical Physics* 138.7 (Feb. 2013), p. 074506. DOI: 10.1063/1.4790861.

[117] B. Winter and M. Faubel. "Photoemission from liquid aqueous solutions". In: *Chemical Reviews* 106.4 (Apr. 2006), pp. 1176–1211. DOI: 10.1021/cr040381p.

[118] S. D. Stoychev, A. I. Kuleff, and L. S. Cederbaum. "Intermolecular Coulombic decay in small biochemically relevant hydrogen-bonded systems". In: *Journal of the American Chemical Society* 133.17 (2011), pp. 6817–6824. DOI: 10.1021/ja200963y.

[119] J. J. R. Frausto da Silva and R. J. P. Williams. *The Biological Chemistry of the Elements*. Oxford University Press, Aug. 16, 2001. 600 pp. ISBN: 0198508484.

[120] *Römpp Chemie Lexikon*. Thieme Verlag (online).

[121] H. Hasse and G. Maurer. "Vapor—liquid equilibrium of formaldehyde-containing mixtures at temperatures below 320 K". In: *Fluid Phase Equilibria* 64 (Jan. 1991), pp. 185–199. DOI: 10.1016/0378-3812(91)90013-w.

[122] J. D. Bozek et al. "Vibrationally resolved resonant Auger spectroscopy of formaldehyde at the C 1s-1π2* resonance". In: *Chemical Physics* 289.1 (2003), pp. 149–161. DOI: 10.1016/S0301-0104(02)01050-9.

[123] W. L. Jolly, K. D. Bomben, and C. J. Eyermann. "Core-electron binding energies for gaseous atoms and molecules". English. In: *Atomic Data and Nuclear Data Tables* 31.3 (1984), pp. 433–493. DOI: 10.1016/0092-640X(84)90011-1.

[124] G. Öhrwall et al. "The electronic structure of free water clusters probed by Auger electron spectroscopy". In: *Journal of Chemical Physics* 123.5 (2005). DOI: 10.1063/1.1989319.

[125] M. Hochlaf and J. H D Eland. "Single and double photoionizations of methanal (formaldehyde)". In: *Journal of Chemical Physics* 123.16 (2005). DOI: 10.1063/1.2090227.

[126] R. A. Kumpf and J. R. Damewood. "Interaction of formaldehyde with water". In: *The Journal of Physical Chemistry* 93.11 (June 1989), pp. 4478–4486. DOI: 10.1021/j100348a019.

[127] H. Fukunaga and K. Morokuma. "Cluster and solution simulation of formaldehyde-water complexes and solvent effect on formaldehyde $^1(n,\pi^*)$ transition". In: *The Journal of Physical Chemistry* 97.1 (Jan. 1993), pp. 59–69. DOI: 10.1021/j100103a013.

[128] G. F. Velardez et al. "Ab Initio Study of the Structures and $\pi^* \leftarrow n$ Electronic Transition in Formic Acid-(Water)$_n$ (n= 3, 4, and 5) Hydrogen Bonded Complexes". In: *The Journal of Physical Chemistry A* 105.38 (Sept. 2001), pp. 8769–8774. DOI: 10.1021/jp0100295.

[129] B. Nelander. "Infrared spectrum of the water formaldehyde complex in solid argon and solid nitrogen". In: *The Journal of Chemical Physics* 72.1 (Jan. 1980), pp. 77–84. DOI: 10.1063/1.438922.

[130] B. Bengt Nelander. "A matrix isolation study of the water-formaldehyde complex. The far-infrared region". In: *Chemical Physics* 159.2 (Jan. 1992), pp. 281–287. DOI: 10.1016/0301-0104(92)80077-9.

[131] M. Suto, X. Wang, and L. C. Lee. "Fluorescence from VUV excitation of formaldehyde". In: *The Journal of Chemical Physics* 85.8 (Oct. 1986), pp. 4228–4233. DOI: 10.1063/1.451793.

[132] C.-M. Saak. "Molecular Interaction in Aqueous Solutions : Effects of Temperature and Solutes on Surface Structure and Hydrogen Bonding in Water". PhD thesis. Uppsala University, Molecular and Condensed Matter Physics, 2019, p. 90. ISBN: 978-91-513-0721-3.

[133] R. R. Rye and J. E. Houston. "Molecular Auger spectroscopy". In: *Accounts of Chemical Research* 17.1 (Jan. 1984), pp. 41–47. DOI: 10.1021/ar00097a007.

[134] R. E. Weber and W. T. Peria. "Use of LEED Apparatus for the Detection and Identification of Surface Contaminants". In: *Journal of Applied Physics* 38.11 (Oct. 1967), pp. 4355–4358. DOI: 10.1063/1.1709128.

[135] W. E. Moddeman et al. "Determination of the K—LL Auger Spectra of N 2 , O 2 , CO, NO, H 2 O, and CO 2". In: *The Journal of Chemical Physics* 55.5 (Sept. 1971), pp. 2317–2336. DOI: 10.1063/1.1676411.

[136] H. Siegbahn, L. Asplund, and P. Kelfve. "The Auger electron spectrum of water vapour". In: *Chemical Physics Letters* 35.3 (1975), pp. 330–335. DOI: 10.1016/0009-2614(75)85615-6.

[137] P. S. Miedema, W. Quevedo, and M Fondell. "The variable polarization undulator beamline UE52 SGM at BESSY II". In: *Journal of large-scale research facilities JLSRF* 2 (May 2016). DOI: 10.17815/jlsrf-2-79.

[138] B. Bernd Winter et al. "Hydrogen bonding in liquid water probed by resonant Auger-electron spectroscopy". In: *The Journal of Chemical Physics* 127.9 (Sept. 2007), p. 094501. DOI: 10.1063/1.2770457.

[139] O. Björneholm et al. "Between vapor and ice: Free water clusters studied by core level spectroscopy". In: *The Journal of Chemical Physics* 111.2 (July 1999), pp. 546–550. DOI: 10.1063/1.479334.

[140] R. Sankari et al. "Vibrationally resolved O 1s photoelectron spectrum of water". In: *Chemical Physics Letters* 380.5-6 (Oct. 2003), pp. 647–653. DOI: 10.1016/j.cplett.2003.08.108.

[141] G. Zundel and H. Metzger. "Energiebänder der tunnelnden Überschuß-Protonen in flüssigen Säuren. Eine IR-spektroskopische Untersuchung der Natur der Gruppierungen $H_5O_2^+$". In: *Zeitschrift für Physikalische Chemie* 58.5_6 (Apr. 1968), pp. 225–245. DOI: 10.1524/zpch.1968.58.5_6.225.

[142] I. Isaak Unger et al. "Ultrafast Proton and Electron Dynamics in Core-Ionized Hydrated Hydrogen Peroxide: Photoemission Measurements with Isotopically Substituted Hydrogen Peroxide". In: *The Journal of Physical Chemistry C* 118.50 (July 2014), pp. 29142–29150. DOI: 10.1021/jp504707h.

[143] C.-M. Saak et al. "Proton dynamics in molecular solvent clusters as an indicator for hydrogen bond network strength in confined geometries". In: *Physical Chemistry Chemical Physics* (2020). DOI: 10.1039/c9cp06661f.

[144] C.-M. Saak et al. "Site-specific X-ray induced dynamics in liquid methanol". In: *Physical Chemistry Chemical Physics* (2019). DOI: 10.1039/C9CP02063B.

[145] T. Hama and N. Watanabe. "Surface Processes on Interstellar Amorphous Solid Water: Adsorption, Diffusion, Tunneling Reactions, and Nuclear-Spin Conversion". In: *Chemical Reviews* 113.12 (Oct. 2013), pp. 8783–8839. DOI: 10.1021/cr4000978.

[146] T. Loerting et al. "How many amorphous ices are there?" In: *Physical Chemistry Chemical Physics* 13.19 (2011), p. 8783. DOI: 10.1039/c0cp02600j.

[147] P. G. Debenedetti and H. E. Stanley. "Supercooled and Glassy Water". In: *Physics Today* 56.6 (June 2003), pp. 40–46. DOI: 10.1063/1.1595053.

[148] J. D. Smith, R. J. Saykally, and P. L. Geissler. "The effects of dissolved halide anions on hydrogen bonding in liquid water." In: *Journal of the American Chemical Society* 129.45 (Nov. 2007), pp. 13847–56. DOI: 10.1021/ja071933z.

[149] C. A. Angell. "Insights into Phases of Liquid Water from Study of Its Unusual Glass-Forming Properties". In: *Science* 319.5863 (Feb. 2008), pp. 582–587. DOI: 10.1126/science.1131939.

[150] N. G. Petrik, A. G. Kavetsky, and G. A. Kimmel. "Electron-Stimulated Production of Molecular Oxygen in Amorphous Solid Water". In: *The Journal of Physical Chemistry B* 110.6 (Feb. 2006), pp. 2723–2731. DOI: 10.1021/jp055173v.

[151] Q.-B. Lu et al. "Structural and temperature effects on Cl- yields in electron-induced dissociation of CF2Cl2 adsorbed on water ice". In: *Chemical Physics Letters* 342.1-2 (July 2001), pp. 1–6. DOI: 10.1016/s0009-2614(01)00569-3.

[152] U. Bovensiepen. "Ultrafast electron transfer, localization and solvation at ice–metal interfaces: Correlation of structure and dynamics". In: *Progress in Surface Science* 78.3-4 (Jan. 2005), pp. 87–100. DOI: 10.1016/j.progsurf.2005.06.001.

[153] J. Zhao et al. "Solvated Electrons on Metal Oxide Surfaces". In: *Chemical Reviews* 106.10 (Oct. 2006), pp. 4402–4427. DOI: 10.1021/cr050173c.

[154] D. Wegkamp. "Ultrafast electron dynamics and the role of screening." PhD thesis. Freie Universität Berlin, 2014. eprint: http://www.diss.fu-berlin.de/diss/receive/FUDISS_thesis_000000099417.

[155] S. B. King et al. "Trapped Electrons at the Amorphous Solid Water/Vacuum Interface as Possible Reactants in a Water Splitting Reaction". In: *J. Phys. Chem. C* 121.13 (2017), pp. 7379–7386. DOI: 10.1021/acs.jpcc.7b01459.

[156] K. Christmann. *Introduction to Surface Physical Chemistry*. 1st ed. Topics in Physical Chemistry 1. Steinkopff-Verlag Heidelberg, 1991. ISBN: 978-3-7985-0858-3,978-3-662-08009-2.

[157] B. Baron and F. Williams. "X-ray photoelectron spectroscopy of amorphous ice". In: *The Journal of Chemical Physics* 64.9 (May 1976), pp. 3896–3897. DOI: 10.1063/1.432672.

[158] A. Křepelová et al. "Adsorption of Acetic Acid on Ice Studied by Ambient-Pressure XPS and Partial-Electron-Yield NEXAFS Spectroscopy at 230–240 K". In: *The Journal of Physical Chemistry A* 117.2 (Jan. 2013), pp. 401–409. DOI: 10.1021/jp3102332.

[159] E.-S. Moon and H. Heon Kang. "Metastable hydronium ions in UV-irradiated ice". In: *The Journal of Chemical Physics* 137.20 (Nov. 2012), p. 204704. DOI: 10.1063/1.4768418.

[160] D. Coulman et al. "Excitation, deexcitation, and fragmentation in the core region of condensed and adsorbed water". In: *The Journal of Chemical Physics* 93.1 (July 1990), pp. 58–75. DOI: 10.1063/1.459560.

[161] R. S. Smith, C. Huang, and B. D. Kay. "Evidence for Molecular Translational Diffusion during the Crystallization of Amorphous Solid Water". In: *The Journal of Physical Chemistry B* 101.32 (Aug. 1997), pp. 6123–6126. DOI: 10.1021/jp963278f.

[162] A. Luzar and D. Chandler. "Hydrogen-bond kinetics in liquid water". In: *Nature* 379.6560 (Jan. 1996), pp. 55–57. DOI: 10.1038/379055a0.

[163] K. J. Tielrooij et al. "Cooperativity in Ion Hydration". In: *Science* 328.5981 (May 2010), pp. 1006–1009. DOI: 10.1126/science.1183512.

[164] J. Grdadolnik, F. Merzel, and F. Avbelj. "Origin of hydrophobicity and enhanced water hydrogen bond strength near purely hydrophobic solutes". In: *Proceedings of the National Academy of Sciences* 114.2 (Jan. 2017), pp. 322–327. DOI: 10.1073/pnas.1612480114.

[165] R. G. LeBel and D. A. I. Goring. "Density, Viscosity, Refractive Index, and Hygroscopicity of Mixtures of Water and Dimethyl Sulfoxide." In: *Journal of Chemical & Engineering Data* 7.1 (Jan. 1962), pp. 100–101. DOI: 10.1021/je60012a032.

[166] G. J. Morris et al. "The high viscosity encountered during freezing in glycerol solutions: Effects on cryopreservation". In: *Cryobiology* 52.3 (June 2006), pp. 323–334. DOI: 10.1016/J.CRYOBIOL.2006.01.003.

[167] L. B. Lane. "Freezing Points of Glycerol and Its Aqueous Solutions." In: *Industrial & Engineering Chemistry* 17.9 (Sept. 1925), pp. 924–924. DOI: 10.1021/ie50189a017.

[168] R. N. Havemeyer. "Freezing Point Curve of Dimethyl Sulfoxide—Water Solutions". In: *Journal of Pharmaceutical Sciences* 55.8 (Aug. 1966), pp. 851–853. DOI: 10.1002/jps.2600550822.

[169] A. Baudot and V. Odagescu. "Thermal properties of ethylene glycol aqueous solutions". In: *Cryobiology* 48.3 (June 2004), pp. 283–294. DOI: 10.1016/j.cryobiol.2004.02.003.

[170] J. F. Carpenter and J. H. Crowe. "The mechanism of cryoprotection of proteins by solutes". In: *Cryobiology* 25.3 (June 1988), pp. 244–255. DOI: 10.1016/0011-2240(88)90032-6.

[171] J. L. Dashnau et al. "Hydrogen Bonding and the Cryoprotective Properties of Glycerol/Water Mixtures". In: *The Journal of Physical Chemistry B* 110.27 (July 2006), pp. 13670–13677. DOI: 10.1021/jp0618680.

[172] J. J. Towey and L. Dougan. "Structural examination of the impact of glycerol on water structure". In: *Journal of Physical Chemistry B* 116.5 (Feb. 2012), pp. 1633–1641. DOI: 10.1021/jp2093862.

[173] J.E. Lovelock. "Het mechanism of the protective action of glycerol against haemolysis by freezing and thawing". In: *Biochimica et Biophysica Acta* 11 (Jan. 1953), pp. 28–36. DOI: 10.1016/0006-3002(53)90005-5.

[174] J. E. Lovelock and M. W. H. Bishop. "Prevention of Freezing Damage to Living Cells by Dimethyl Sulphoxide". In: *Nature* 183.4672 (May 1959), pp. 1394–1395. DOI: 10.1038/1831394a0.

[175] K.-I. Oh et al. "Quantifying Hydrogen-Bond Populations in Dimethyl Sulfoxide/Water Mixtures". In: *Angewandte Chemie International Edition* 56.38 (Sept. 2017), pp. 11375–11379. DOI: 10.1002/anie.201704162.

[176] A. K. Soper and A. Luzar. "A neutron diffraction study of dimethyl sulphoxide–water mixtures". In: *The Journal of Chemical Physics* 97.2 (July 1992), pp. 1320–1331. DOI: 10.1063/1.463259.

[177] A. K. Soper and A. Luzar. "Orientation of Water Molecules around Small Polar and Nonpolar Groups in Solution: A Neutron Diffraction and Computer Simulation Study". In: *The Journal of Physical Chemistry* 100.4 (Jan. 1996), pp. 1357–1367. DOI: 10.1021/jp951783r.

[178] A. Puzenko et al. "Relaxation Dynamics in Glycerol-Water Mixtures: I. Glycerol-Rich Mixtures". In: *The Journal of Physical Chemistry B* 109.12 (Mar. 2005), pp. 6031–6035. DOI: 10.1021/jp0445122.

[179] N. Ottosson et al. "Photoelectron spectroscopy of liquid water and aqueous solution: Electron effective attenuation lengths and emission-angle anisotropy". In: *Journal of Electron Spectroscopy and Related Phenomena* 177.2-3 (Mar. 2010), pp. 60–70. DOI: 10.1016/j.elspec.2009.08.007.

[180] N. Preissler et al. "Electrokinetic Charging and Evidence for Charge Evaporation in Liquid Microjets of Aqueous Salt Solution". In: *The Journal of Physical Chemistry B* 117.8 (Feb. 2013), pp. 2422–2428. DOI: 10.1021/jp304773n.

[181] Naoya Kurahashi et al. "Photoelectron spectroscopy of aqueous solutions: Streaming potentials of NaX (X = Cl, Br, and I) solutions and electron binding energies of liquid water and X-". In: *The Journal of Chemical Physics* 140.17 (May 2014), p. 174506. DOI: 10.1063/1.4871877.

[182] G. Olivieri et al. "Quantitative ionization energies and work functions of aqueous solutions". In: *Physical Chemistry Chemical Physics* 18.42 (2016), pp. 29506–29515. DOI: 10.1039/c6cp05682b.

[183] R. R. Rye et al. "Chemical-state effects in Auger electron spectroscopy". In: *The Journal of Chemical Physics* 69.4 (Aug. 1978), pp. 1504–1512. DOI: 10.1063/1.436777.

[184] K. W. Nebesny and N. R. Armstrong. "Reactions of clean lithium surfaces with sulfur dioxide: molecular Auger line-shape analysis and reaction kinetics". In: *Langmuir* 1.4 (July 1985), pp. 469–477. DOI: 10.1021/la00064a013.

[185] A. Luzar and D. Chandler. "Structure and hydrogen bond dynamics of water–dimethyl sulfoxide mixtures by computer simulations". In: *The Journal of Chemical Physics* 98.10 (May 1993), pp. 8160–8173. DOI: 10.1063/1.464521.

[186] J.-H. Guo et al. "Molecular Structure of Alcohol-Water Mixtures". In: *Physical Review Letters* 91.15 (Oct. 2003). DOI: 10.1103/physrevlett.91.157401.

[187] R. K. Lam, J. W. Smith, and R. J. Saykally. "Communication: Hydrogen bonding interactions in water-alcohol mixtures from X-ray absorption spectroscopy". In: *The Journal of Chemical Physics* 144.19 (May 2016), p. 191103. DOI: 10.1063/1.4951010.

[188] A. Vishnyakov, A. P. Lyubartsev, and A. Laaksonen. "Molecular Dynamics Simulations of Dimethyl Sulfoxide and Dimethyl Sulfoxide-Water Mixture". In: *The Journal of Physical Chemistry A* 105.10 (Mar. 2001), pp. 1702–1710. DOI: 10.1021/jp0007336.

[189] J. Tomlinson-Phillips et al. "Structure and Dynamics of Water Dangling OH Bonds in Hydrophobic Hydration Shells. Comparison of Simulation and Experiment". In: *The Journal of Physical Chemistry A* 115.23 (June 2011), pp. 6177–6183. DOI: 10.1021/jp111346s.

[190] P. N. Perera et al. "Observation of water dangling OH bonds around dissolved nonpolar groups". In: *Proceedings of the National Academy of Sciences* 106.30 (July 2009), pp. 12230–12234. DOI: 10.1073/pnas.0903675106.

[191] Q. Du, E. Freysz, and Y. R. Shen. "Surface Vibrational Spectroscopic Studies of Hydrogen Bonding and Hydrophobicity". In: *Science* 264.5160 (May 1994), pp. 826–828. DOI: 10.1126/science.264.5160.826.

[192] O. Björneholm et al. "Water at Interfaces". In: *Chemical Reviews* 116.13 (May 2016), pp. 7698–7726. DOI: 10.1021/acs.chemrev.6b00045.

[193] A. M. Schrader et al. "Communication: Contrasting effects of glycerol and DMSO on lipid membrane surface hydration dynamics and forces". In: *The Journal of Chemical Physics* 145.4 (July 2016), p. 041101. DOI: 10.1063/1.4959904.

[194] P. J. Richardson et al. "Spectrum and decay of the doubly charged water ion". In: *The Journal of Chemical Physics* 84.6 (1986), pp. 3189–3194. DOI: 10.1063/1.450808.

[195] D. Winkoun et al. "One- and two-step double photoionisation processes in valence shells of H2O". In: *Journal of Physics B: Atomic, Molecular and Optical Physics* 21.8 (1988), pp. 1385–1394. DOI: 10.1088/0953-4075/21/8/011.

[196] J. C. Severs et al. "Triplet-state energies of H2O2+: a combined experimental and theoretical study". In: *Chemical Physics* 175.2-3 (1993), pp. 467–473. DOI: 10.1016/0301-0104(93)85173-6.

[197] H. Sann et al. "Electron Diffraction Self-Imaging of Molecular Fragmentation in Two-Step Double Ionization of Water". In: *Physical Review Letters* 106.13 (Mar. 2011), p. 133001. DOI: 10.1103/PhysRevLett.106.133001.

[198] I. B. Müller and L. S. Cederbaum. "Ionization and double ionization of small water clusters". In: *The Journal of Chemical Physics* 125.20 (2006), p. 204305. DOI: 10.1063/1.2357921.

[199] M. H. Elkins, H. L. Williams, and D. M. Neumark. "Isotope effect on hydrated electron relaxation dynamics studied with time-resolved liquid jet photoelectron spectroscopy". In: *The Journal of Chemical Physics* 144.18 (May 2016), p. 184503. DOI: 10.1063/1.4948546.

[200] J. Hummert et al. "Femtosecond Extreme Ultraviolet Photoelectron Spectroscopy of Organic Molecules in Aqueous Solution". In: *The Journal of Physical Chemistry Letters* 9.22 (Nov. 2018), pp. 6649–6655. DOI: 10.1021/acs.jpclett.8b02937.

[201] C. Dal Cappello, R. El M'Khanter, and P. Lamy. "Double Ionization of Helium by Electron Impact: A Study of the Two-Step Mechanism". In: *Coincidence Studies of Electron and Photon Impact Ionization*. Boston, MA: Springer US, 1997, pp. 77–83. DOI: 10.1007/978-1-4757-9751-0_8.

[202] C. Buth, R. Santra, and L. S. Cederbaum. "Impact of interatomic electronic decay processes on Xe 4d hole decay in the xenon fluorides". In: *The Journal of Chemical Physics* 119.20 (Nov. 2003), pp. 10575–10584. DOI: 10.1063/1.1620502.

[203] M. Förstel et al. "Autoionization Mediated by Electron Transfer". In: *Physical Review Letters* 106.3 (Jan. 2011), p. 033402. DOI: 10.1103/PhysRevLett.106.033402.

[204] K. Sakai et al. "Electron-Transfer-Mediated Decay and Interatomic Coulombic Decay from the Triply Ionized States in Argon Dimers". In: *Physical Review Letters* 106.3 (Jan. 2011), p. 033401. DOI: 10.1103/PhysRevLett.106.033401.

[205] D. You et al. "Charge transfer to ground-state ions produces free electrons". In: *Nature Communications* 8.1 (Jan. 2017). DOI: 10.1038/ncomms14277.

[206] I. B. Müller and L. S. Cederbaum. "Electronic decay following ionization of aqueous Li+microsolvation clusters". In: *Journal of Chemical Physics* 122.9 (2005). DOI: 10.1063/1.1854118.

[207] I. Unger et al. "Observation of electron-transfer-mediated decay in aqueous solution". In: *Nature Chemistry* 9.7 (2017), pp. 708–714. DOI: 10.1038/nchem.2727.

[208] Cl Andreini et al. "Metal ions in biological catalysis: from enzyme databases to general principles". In: *JBIC Journal of Biological Inorganic Chemistry* 13.8 (July 2008), pp. 1205–1218. DOI: 10.1007/s00775-008-0404-5.

[209] Geethanjali Gopakumar. Personal conversation. July 2019.

[210] L. Götte et al. "Solvent-Shared Ion Pairs at the Air–Solution Interface of Magnesium Chloride and Sulfate Solutions Revealed by Sum Frequency Spectroscopy and Molecular Dynamics Simulations". In: *The Journal of Physical Chemistry A* 121.34 (Aug. 2017), pp. 6450–6459. DOI: 10.1021/acs.jpca.7b05600.

[211] B. Minofar et al. "Propensity for the air/water interface and ion pairing in magnesium acetate vs magnesium nitrate solutions: Molecular dynamics simulations and surface tension measurements". In: *Journal of Physical Chemistry B* 110.32 (2006), pp. 15939–15944. DOI: 10.1021/jp060627p.

[212] W. Hua, D. Verreault, and H. C. Allen. "Surface Electric Fields of Aqueous Solutions of NH_4NO_3, $Mg(NO_3)_2$, $NaNO_3$, and $LiNO_3$: Implications for Atmospheric Aerosol Chemistry". In: *The Journal of Physical Chemistry C* 118.43 (Oct. 2014), pp. 24941–24949. DOI: 10.1021/jp505770t.

[213] R. Seidel, B. Winter, and S. E. Bradforth. "Valence Electronic Structure of Aqueous Solutions: Insights from Photoelectron Spectroscopy". In: *Annual Review of Physical Chemistry* 67.1 (2016), pp. 283–305. DOI: 10.1146/annurev-physchem-040513-103715.

[214] B. Winter et al. "Electron Binding Energies of Aqueous Alkali and Halide Ions: EUV Photoelectron Spectroscopy of Liquid Solutions and Combined Ab Initio and Molecular Dynamics Calculations". In: *Journal of the American Chemical Society* 127.19 (May 2005), pp. 7203–7214. DOI: 10.1021/ja042908l.

[215] J. J. Yeh and I. Lindau. "Atomic subshell photoionization cross sections and asymmetry parameters: $1 \leqslant Z \leqslant 103$". In: *Atomic Data and Nuclear Data Tables* 32.1 (Jan. 1985), pp. 1–155. DOI: 10.1016/0092-640x(85)90016-6.

[216] M. N. Pohl. "Intermolecular Electronic Decay in Aqueous Solutions: A Liquid-Phase Photoelectron Spectroscopy Study". PhD thesis. Freie Universität Berlin, Department of Physics, 2018.

[217] G. Wedler. *Lehrbuch der Physikalischen Chemie (German Edition)*. Wiley-VCH, 2005. ISBN: 978-3-527-31066-1.

[218] U. Bovensiepen, C. Gahl, and M. Wolf. "Solvation Dynamics and Evolution of the Spatial Extent of Photoinjected Electrons in D 2 O/Cu(111)". In: *The Journal of Physical Chemistry B* 107.33 (2003), pp. 8706–8715. DOI: 10.1021/jp034654g.

[219] H. J. Lee, A. C. Jamison, and T. R. Lee. "Surface Dipoles: A Growing Body of Evidence Supports Their Impact and Importance". In: *Accounts of Chemical Research* 48.12 (Nov. 2015), pp. 3007–3015. DOI: 10.1021/acs.accounts.5b00307.

[220] A. Wahab et al. "Ultrasonic velocities, densities, viscosities, electrical conductivities, raman spectra, and molecular dynamics simulations of aqueous solutions of Mg(OAc)2 and Mg(NO3)2: Hofmeister effects and ion pair formation". In: *Journal of Physical Chemistry B* 109.50 (2005), pp. 24108–24120. DOI: 10.1021/jp053344q.

[221] C.-M. Saak et al. "Temperature Dependence of X-Ray Induced Auger Processes in Liquid Water". In: *The Journal of Physical Chemistry Letters* (Mar. 2020). DOI: 10.1021/acs.jpclett.0c00158.

IT IS PITCH BLACK. YOU ARE LIKELY TO BE EATEN BY A GRUE.

> WHAT IS A GRUE?

THE GRUE IS A SINISTER, LURKING PRESENCE IN THE DARK PLACES OF THE EARTH. ITS FAVORITE DIET IS ADVENTURERS, BUT ITS INSATIABLE APPETITE IS TEMPERED BY ITS FEAR OF LIGHT. NO GRUE HAS EVER BEEN SEEN BY THE LIGHT OF DAY, AND FEW HAVE SURVIVED ITS FEARSOME JAWS TO TELL THE TALE.

Dave Lebling, Zork I: The Great Underground Empire